Downloaded from orbit.dtu.dk on: May 05, 2023

DTU Library

Theory of dual probes on graphene structures

Settnes, Mikkel

Publication date:
2015

Document Version
Publisher's PDF, also known as Version of record

Link back to DTU Orbit

Citation (APA):
Settnes, M. (2015). *Theory of dual probes on graphene structures*. DTU Nanotech.

General rights
Copyright and moral rights for the publications made accessible in the public portal are retained by the authors and/or other copyright owners and it is a condition of accessing publications that users recognise and abide by the legal requirements associated with these rights.

- Users may download and print one copy of any publication from the public portal for the purpose of private study or research.
- You may not further distribute the material or use it for any profit-making activity or commercial gain
- You may freely distribute the URL identifying the publication in the public portal

If you believe that this document breaches copyright please contact us providing details, and we will remove access to the work immediately and investigate your claim.

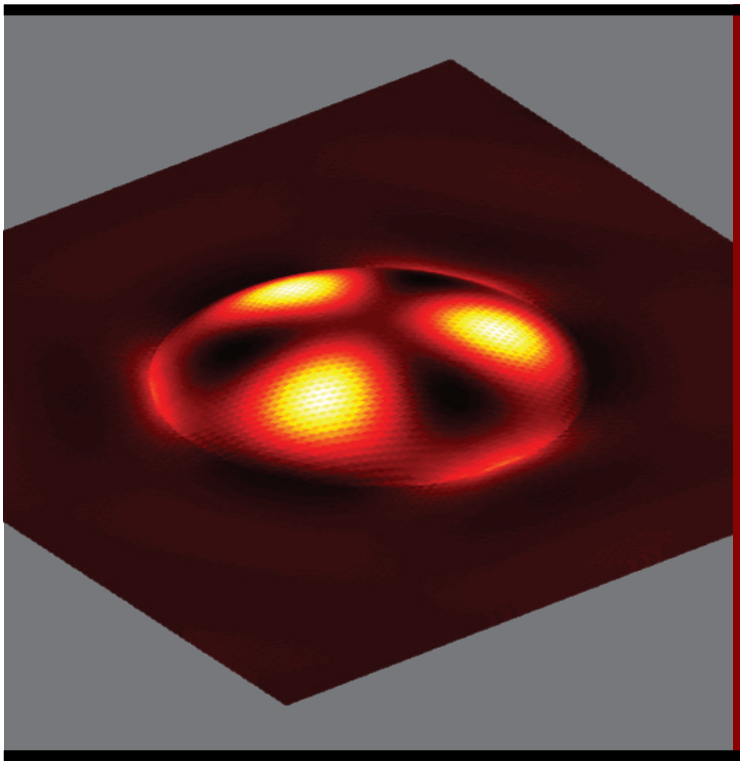

Theory of dual probes on graphene nanostructures

Mikkel Settnes
PhD Thesis June 2015

DTU Nanotech
Department of Micro- and Nanotechnology

Theory of dual probes on graphene nanostructures

Mikkel Settnes

Ph.D. Thesis

June 2015

DTU Nanotech
Institut for Mikro- og Nanoteknologi

Supervisors:
Stephen R. Power
Dirch H. Petersen
Antti-Pekka Jauho

Abstract

This thesis concerns the development of theoretical and computational methods for multi-probe systems and their application to nanostructured graphene. Recent experimental advances emphasize the usefulness of multi-probe techniques when analyzing the electrical properties of nanoscale samples. The multi-probe setup, however, is conceptually different from the standard calculation setups which either disregard the effects of the probes altogether or use probes connected at the edge of a finite device region. In the multi-probe setup, on the other hand, the device region is infinite and extends all around the local probes. This necessitates a reformulation of the conventional calculation methods allowing for the description of non-periodic structures embedded within infinite samples.

The two-dimensional material graphene, is a highly interesting system for multi-probe characterization as graphene is purely surface and exhibits a wide range of highly intriguing electronic properties. Using a dual probe setup, we demonstrate the application of the developed formalism to a number of different graphene-based systems. The conductance between the two probes in either scanning or spectroscopy mode, shows quantum interference patterns around impurities or crystalline edges. These interferences can be used to reveal important information about the scattering processes taking place. The thesis furthermore discusses nanostructuring such as perforations or local gating. We show how single states or modes and their interplay gives rise to resonances in the dual probe conductance and can be associated with vortex-like current patterns either guiding or suppressing the current.

We further address the effect of strain in graphene when subjected to mechanical deformations giving rise to so-called pseudomagnetic fields. Here we investigate strained graphene bubbles ("pseudomagnetic dots") directly from tight binding, effectively going beyond the Dirac approximation. In this way, we study the local density of states of different pseudomagnetic dots in real space and show Friedel-type oscillations caused by the finite size of the dots, sublattice polarization and Landau quantization. Additionally, we use the dual probe conductance to demonstrate the current guiding ability of the pseudomagnetic fields leading to preferential scattering directions responsible for the observed pseudomagnetic focusing and anti-focusing effects.

Resumé - Danish

Denne afhandling omhandler udvikling af teori og beregningsmetoder til multi-probe systemer and disses anvendelse for nanostruktureret grafén. Nye eksperimentelle teknikker har demonstreret brugen af multi-probe teknikker til karakterisering af materialer på nanoskala. Metoder til at beskrive multi-probe systemer er imidlertidig grundlæggende forskellige fra standard beregningsmæssige metoder, der som oftest enten negligere effekten af proberne eller benytter prober som kobler til kanten et endeligt system. Multi-probe systemer vil på den anden side have uendelige udstrækning omkring de lokale prober. Dette nødvendiggør en omformulering af konventionelle beregningsmetoder som gør det muligt at beskrive ikke-periodiske strukturer i et uendeligt system

Todimensionale materialer som grafén er et yderst interessant system at karakterisere ved hjælp af multi-probe metoder da grafén udelukkende er overflade og besidder en lang række interessante elektriske egenskaber. Vi demonstrerer anvendelsen af de udviklede metoder for en række forskellige grafén systemer ved at bruge en dobbelt-probe opstilling. Konduktansen mellem de to prober i enten scanning eller spektroskopi tilstand, viser kvante interferensmønstre omkring urenheder og krystallinske kanter. Disse interferenser kan bruges til at analyserer spredningsprocesserne som finder sted. Afhandlingen diskuterer desuden nanostrukturering såsom perforeringer eller lokale elektriske felter. Vi viser hvordan enkelte tilstande eller modes og deres interaktion giver anledning til resonanser i dobbelt-probe konduktansen og er forbundet med vortex mønstre i strømmen der enten leder eller blokerer.

Endvidere beskriver vi effekten af mekanisk deformation af grafén, der giver anledning til såkaldte pseduomagnet felter. Vi undersøger grafén deformationer med en "Tight-binding"-model der går ud over Dirac approksimationen. På denne måde analyserer vi den lokale tilstandstæthed af forskellige pseudomagnetiske deformationer og viser effekter såsom undergitter polarisering, Landau kvantisering og Friedel svingninger forårsaget af den endelige størrelse af deformationerne. Derudover bruger vi dobbelt-probe konduktansen til at vise hvordan det pseudomagnetiske felt kan lede strømmens retning og skabe præferentielle spredningsretninger der udmønter sig i fokusering eller anti-fokusering af strømmen.

Preface

This thesis is submitted in partial fulfillment of the requirements for obtaining the Ph.D. degree at the Technical University of Denmark (DTU). The work presented in this thesis was carried out between April 2012 and June 2015 at DTU Nanotech and was financed jointly by DTU and the Danish National Research Foundation.

The Ph.D. project was supervised by Post. Doc. Stephen R. Power, Senior Researcher Dirch H. Petersen and Professor Antti-Pekka Jauho. Firstly, I would like to thank Antti for providing an open and motivating research environment where ideas could always be pursued even if they sometimes strayed far from the original plan. I thank Dirch for sharing his knowledge of "real-world" experimental details and for many motivating discussion on and off-topic. I am very grateful that Stephen choose to become part of the supervising team as his enthusiasm, critique and comments on everything from physics to English grammar have been invaluable for the outcome. In addition to my supervisors, I have had the chance to interact with a lot of knowledgeable people during the past three years without whom it would not have been the same enjoyable time and I sincerely hope I do not forget anyone below.

At first it has been a pleasure working in the "Theoretical Nanotechnology and Nanoelectronics" group where present and former members have provided a relaxed yet productive working environment. A special thanks to Mads Brandbyge and Tue Gunst for valuable comments and suggestions throughout the entire Ph.D. period. Going beyond the everyday research group I have also been so fortunate to be part of the Center for Nanostructured Graphene (CNG) where numerous lectures, seminars and "late-night" discussions have been a constant source of inspiration. Also I sincerely thank Anders Mølbjerg, Per Kær Nielsen and Jesper Mørk for a fruitful collaboration at the start of my Ph.D. period. Even though the details of my work within quantum optics did not make it to the thesis, it has been a satisfactory experience to finish the work and see it published.

Outside DTU I would like to thank the group of Christoph Tegenkamp at the University of Hannover for letting me visit although the duration of the stay was limited this time around. Especially, I thank Jens Baringhaus for nice collaboration and for showing me "my" theoretical setup in real life. I am also very grateful to Stephan Roche for hosting my visit to the Catalan Institute of Nanoscience and Nanotechnology (ICN2) in Barcelona and the entire Barcelona group, Nicolas Leconte, Jose "Eduardo" B. Vargas, Dinh van Tuan, David Soriano and Aron W. Cummings for making my stay successful both personally and scientifically. During my stay in Barcelona I also had the good fortune to meet Stefan Hummel and Jani Kotakoski from the University of Vienna which I thank for inspiring

discussions on the experimental realization of the dual-STM setup and for participating in applications for future funding. Additionally, I thank François Peeters, Vitor M. Pereira and Niels-Asger Mortensen for accepting to serve in the evaluation committee of my thesis.

Finally, I thank my friends and family for continuously reminding me that there are important things in life which are *not* hexagonally shaped.

Mikkel Settnes
June 2015

List of publications

Paper A:
Mikkel Settnes, Per Kaer, Anders Moelbjerg and Jesper Mork
Auger Processes Mediating the Nonresonant Optical Emission from a Semiconductor Quantum Dot Embedded Inside an Optical Cavity
Phys. Rev. Lett. **111**, 067403 (2013)

Paper B:
Anders Moelbjerg, Mikkel Settnes, Per Kaer and Jesper Mork
Far-off-resonant coupling between a semiconductor quantum dot and an optical cavity
Proceedings of 2014 Conference on Lasers and Electro-Optics (CLEO), (2014),IEEE

Paper I:
Mikkel Settnes, Stephen R. Power, Dirch H. Petersen and Antti-Pekka Jauho
Theoretical Analysis of a Dual-Probe Scanning Tunneling Microscope Setup on Graphene
Phys. Rev. Lett. **112**, 096801 (2014)

Paper II:
Mikkel Settnes, Stephen R. Power, Dirch H. Petersen and Antti-Pekka Jauho
Dual-probe spectroscopic fingerprints of defects in graphene
Phys. Rev. B **90**, 035440 (2014)

Paper III:
Mikkel Settnes, Stephen R. Power, Jun Lin, Dirch H. Petersen and Antti-Pekka Jauho
Patched Green's function techniques for two-dimensional systems: Electronic behavior of bubbles and perforations in graphene
Phys. Rev. B **91**, 125408 (2015)

Paper IV:
Mikkel Settnes, Stephen R. Power, Jun Lin, Dirch H. Petersen and Antti-Pekka Jauho
Bubbles in graphene - a computational study
Journal of Physics: Conference Series (JPCS) (2015)

Paper V:
Mikkel Settnes, Stephen R. Power and Antti-Pekka Jauho
Pseudomagnetic fields and triaxial strain in graphene
In preparation

Paper VI:
Mikkel Settnes, Nicolas Leconte, Jose E. B. Vargas , Antti-Pekka Jauho and Stephan Roche
Conductivity of large scale strain manipulation in graphene
In preparation

Paper VII:
Jens Baringhaus, Mikkel Settnes, Johannes Aprojanz, Antti-Pekka Jauho and Christoph Tegenkamp
Electron diffraction barriers in ballistic epitaxial graphene nanoribbons
In preparation

All papers have been published/prepared during my PhD. Papers I-VI are discussed in this PhD thesis and papers I-IV are included as appendices.

Contents

Abstract i

Resumé - Danish iii

Preface v

List of publications vii

1 Introduction 3

1.1 Graphene . . . 3

1.2 Dual probe setups . . . 5

1.3 Outline of the thesis . . . 7

2 Theoretical multi-probe models using quantum mechanics 9

2.1 Problems faced by theoretical modeling . . . 9

2.2 Method 1: Integral Green's function method . . . 11

2.2.1 Real space graphene Green's function . . . 13

2.2.2 Stationary phase approximation . . . 16

2.2.3 Summary of method 1 . . . 22

2.3 Solution 2: Patched Green's function method . . . 24

2.3.1 Boundary self energy . . . 25

2.3.2 Real space pristine Green's function . . . 27

2.3.3 Adaptive recursion for device region . . . 28

2.3.4 Summary of method 2 . . . 34

2.4 Probe model . . . 35

3 Dual probe on graphene 37

3.1 Dual-STM using stationary phase approximation . . . 37
3.2 Scanning mode . . . 41
3.2.1 Pristine graphene . . . 41
3.2.2 Vacancies . . . 43
3.2.3 Crystalline edges . . . 48
3.3 Spectroscopy mode . . . 50
3.3.1 Pristine graphene . . . 50
3.3.2 Simple impurities . . . 53
3.4 Summary . . . 57

4 Dual probe investigation of nanostructures in graphene 59
4.1 Graphene antidots . . . 59
4.1.1 Dual probe spectroscopy . . . 60
4.1.2 Bond currents . . . 62
4.2 Locally gated dots . . . 66
4.2.1 Local gate in Dirac approximation . . . 67
4.2.2 Local density of states . . . 70
4.2.3 Transmission and bond currents . . . 72
4.3 Summary . . . 76

5 Strain fields with pseudomagnetic effects 77
5.1 Strain using a tight binding approach . . . 78
5.2 Pseudomagnetic field from strain field . . . 78
5.3 Constant pseudomagnetic field using triaxial strain . . . 79
5.3.1 Pseudo Landau Levels . . . 81
5.3.2 Sublattice splitting of the zeroth pseudo Landau level . . . 82
5.3.3 Rotation of triaxial strain . . . 84
5.3.4 Finite size effects . . . 87
5.4 Finite inhomogeneous strain field . . . 87
5.5 Local density of states in inhomogeneous strain fields . . . 93
5.5.1 Sublattice polarization . . . 93
5.5.2 Pseudo Landau levels and Friedel oscillations in clamped bubbles . . . 94

5.5.3 Comparison of membrane and non-linear plate models for gas inflated bubbles . . . 98
5.6 Transport through individual pseudomagnetic dots . . . 101
5.6.1 Gauss height profile . . . 101
5.6.2 Membrane bubble model . . . 105
5.6.3 Pseudomagnetic valley filtering . . . 107
5.6.4 Finite triaxial strain . . . 109
5.7 Pseudomagnetic dot arrays . . . 112
5.7.1 Kubo-Greenwood propagation methods - a quick safari . . . 112
5.7.2 Superlattice of nanobubbles . . . 116
5.8 Summary . . . 121

6 Leaving the phase coherent regime: a mean field approach to disorder 123
6.1 Mean field theory for disorder . . . 123
6.2 Green's function in the Coherent Potential Approximation (CPA) . . . 125
6.3 Transport using vertex corrections (CPA-VC) . . . 127
6.3.1 Summary of CPA-VC Technique . . . 129
6.4 Graphene nanoribbon with nitrogen doping . . . 130
6.4.1 Symmetric nitrogen doping . . . 130
6.4.2 Asymmetric nitrogen doping . . . 132
6.4.3 Computational cost . . . 134
6.4.4 Scaling behavior of resistance . . . 135
6.5 Summary . . . 136

7 Summary & Outlook 137

A Plate theory 143
Paper I . . . 149
Paper II . . . 157
Paper III . . . 167
Paper IV . . . 181

Bibliography 186

Abbreviations list

Abbreviations	Description
(A/Z)GNR	(Armchair/Zigzag) Graphene Nanoribbon
BZ	Brillouin Zone
CVD	Chemical Vapor Deposition
CPA	Coherent Potential Approximation
VC	Vertex-Correction
DFT	Density Functional Theory
(L)DOS	(Local) Density of States
LCA	Low Concentration Approximation
NECPA	Non-Equillibrium Coherent Potential Approximation
NEGF	Non-Equillibrium Green's Function
PGF	Patched Green's Function
PMF	Pseudomagnetic Field
pLL	pseudo Landau Level
RGF	Recursive Green's Function
SPA	Stationary Phase Approximation
SSA	Single-Site Approximation
STM	Scanning Tunneling Microscope
TEM	Transmission Electron Microscope

CHAPTER 1

Introduction

"What could we do with layered structures with just the right layers? What would the properties of materials be if we could really arrange the atoms the way we want them?"

— Richard Feynman, (1918-1988)

Since Richard Feynman's highly praised lecture in 1959 [1] the quest of nanotechnology has been a continuous miniaturization. The more than 50 year old speculation of materials containing an exact number of layers is no longer a visionary thought but an experimental fact [2]. In fact, the two dimensional carbon material, graphene, contains only a single layer and the electron waves propagate through this single layer, which makes them accessible to various scanning probe methods. So what does happen when we can manipulate an individual layer on the nanoscale? And how can we detect the properties on a similar nanoscale?

1.1 Graphene

Carbon is a very versatile element and depending on the hybridization of the individual bonds, we can experience cabon based materials in a variety of forms in all dimensions. This ranges from the large class of hydrocarbons which compose the majority of the biological materials providing the energy for the modern technological society to pure carbon materials like diamonds or graphite, both of which are widely used throughout the industry. The variety is not limited to macroscale materials because we find carbon nanomaterials in all dimensions like fullerene molecules (0D), carbon nanotubes (1D), graphene (2D) and nano-diamonds (3D), see Fig. 1.1. This versatility, with each form exhibiting different chemical and physical properties, makes carbon nanostructures an important component in the field of nanoscience and nanotechnology. In this thesis, we focus on the remarkable properties of the two-dimensional form, *graphene*.

Like most good ideas, it all started with a pencil. Using the famous scotch tape

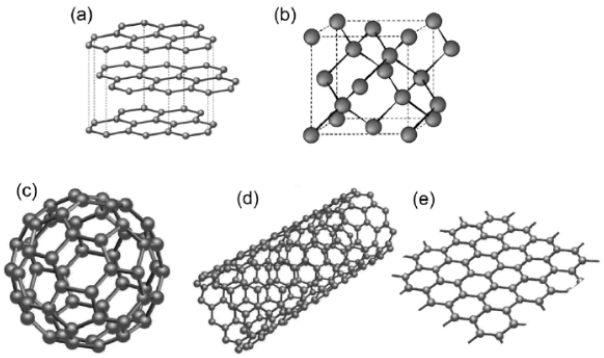

Figure 1.1: Carbon materials with macroscale structures like (a) graphite and (b) diamonds and the lower dimensional structures like (c) fullerenes (C_{60}), (d) carbon nanotubes and (e) graphene. Picture adapted form [3].

method, graphene can be derived from the graphite in our pencils by simply peeling of a single layer. Graphene has been presented as the miracle material of the twenty-first century. The one-atom-thick carbon material combines a number of highly attractive properties never seen before in one material: extreme mechanical strength, exceptionally high electronic and thermal conductivity, impermeability to gases, optical transparency *etc.*. [4, 5]

Theoretically graphene has been studied for many years [6, 7] and thought of as the fundamental building block of carbon structures like graphite, fullerenes or carbon nanotubes. After the experimental realization in 2004 [8], however, it became clear that graphene is also a material in itself. Fundamental for many of the striking features of graphene, is the relativistic-like linear energy spectrum making quasiparticles in graphene behave like massless fermions. This gives rise to relativistic effects like the half integer Quantum Hall effect [9, 10] and the Klein tunneling effect which lets electrons with normal incidence pass through infinitely large potential barriers with a probability of one [11]. We do not review all the remarkable properties of graphene and their origin as several extensive reviews [12, 13], roadmaps [4, 14] and a couple of text books [15, 16] exist describing the general properties of graphene. On the other hand, a few properties relevant for this work should be mentioned here.

The first is the exceptional electronic quality of graphene allowing electrons to travel long distances without scattering, hence making quantum interference effects visible [17–20]. Second, is the similarity between photons and electrons in graphene [21, 22] which inspires the pursuit of devices analogous of optical devices. This includes nanopatterning or gating to create an electron analogue photonic crystals [23], waveguides [24, 25] and optical cavities [22, 26]. Third, is the remarkable connection between mechanical deformation of graphene and its electronic, optical and phononic properties [27, 28]. For example, it has been shown that strain allows for the formation of local gauge fields mimicking the effect of a strong magnetic field [29]. Fourth, due to the massless carriers and little scattering, quantum effects in graphene have been shown to be very robust and can even survive at

room temperature [30].

Even though this thesis focuses on graphene, we should also briefly mention the other two dimensional materials [2, 31, 32]. Although graphene was the first truly two dimensional crystal isolated, a variety of 2D materials have been realized covering properties from insulators to semi- and superconductors [33]. In this way, we do not consider graphene as a single unique material, but rather as a spectacular example of a whole class of 2D materials with different properties and compositions [34]. Moreover, the ability to control the number and composition of layers could significantly modify the properties of the new layered materials.

1.2 Dual probe setups

A vital part of the miniaturization process is the ability to *see* and measure at the nanoscale. Fundamental studies of nanomaterials can only continue through a continued downscaling of characterization techniques [35].

Since its development, the Scanning Tunneling Microscope (STM) [36, 37] has been the most important tool to investigate the electronic structure of nanoscale surfaces. Nanometer scale STM measurements, yielding both local density of states (LDOS) and topographic details, are extensively used to study graphene both theoretically [38–46] and experimentally [47–52]. A conventional STM has a single probe, therefore, its main function is to image the structure of a sample and it cannot be used to measure the lateral transport. However, a double probe setup with STM-like probes allows for measuring the lateral transport by utilizing the two probes as contact electrodes [53]. This type of STM or similar probes that only couple very locally to the sample is seen in contrast to the commonly used invasive macroscopic probes.

During the past decade multi-probe systems have been developed to avoid the need of fixed macroscopic contacts and enable nanoscale transport measurements [35, 53–56]. Multi-probe measurements have been used to characterize several systems: nanowires [58, 59], carbon nanotubes [60], graphene nanoribbons [61], anisotropic transport [57], grain boundaries both in graphene [62, 63] and other materials [64], and monolayer and bilayer graphene of varying quality [65–69]. Multi-probe systems are useful to study different length-scales as the probe pitch is changed from the commercially available μm-scale [55] to the state-of-the-art multi-probe STM techniques [59, 61, 65, 70] allowing for tip separations down to a couple of hundred nanometers, see Fig. 1.2.

As we move towards actual nanoscale transport, different physical principles come into play. The large probe pitch is still well described by classical electrostatic theory [71], but when the probe pitch is smaller than the phase coherence length, we enter the mesoscopic regime governed by quantum mechanics [72] where classical theory is predicted to break down. There are needs for theoretical and computational methods including quantum mechanical effects to describe such dual-STM probe systems on the nanoscale

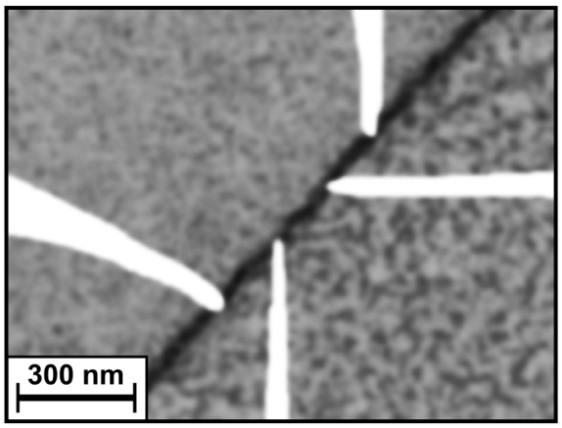

Figure 1.2: A scanning electron microscopy image of a four STM-probe setup on a graphene nanoribbon. The picture is courtesy of J. Baringhaus.

and what system properties that can be analyzed using this type of setup. Developing such a theoretical framework and describing the dual probe setup in the coherent transport regime is the overall goal of this thesis.

"There's plenty room at the bottom."

— Richard Feynman, (1918-1988)

1.3 Outline of the thesis

We address the fundamental miniaturization question of *dual probes* in the phase coherent regime and how these can be used to study nanoscale transport properties. In this context graphene is an excellent candidate to investigate. In contrast to subsurface two-dimensional electron systems, where the environment is less accessible to nanoscale surface probes, the electrons propagate at the surface of graphene giving the unique opportunity to probe the electronic behavior using scanning probe methods. In this way, the thesis first focuses on the development of the necessary theoretical framework to study dual probe setups while including the effect of quantum mechanics. Secondly, we apply these methods to graphene systems containing simple defects and nanostructures such as local gating and strain engineering. The remainder of the thesis is organized as follows:

Chapter 2 (Paper I, II, III):
We develop a theoretical framework to treat multi-probe setups and nanostructures in a graphene system. As the STM-like probes are required to be finite, local and placed on an *infinite* sample, we have to modify the standard Green's function approach to capture these important characteristics. We present two approaches: The first is based on an *integral Green's function* approach to the pristine system. Due to its analytical origin it is computationally effective, however, it does not scale to treat larger nanostructures. The second approach, although more computationally expensive, is able to treat large disordered or nanostructured regions. This method, denoted the *patched Green's function method*, relies on a self-energy approach to describe the infinite part of the system.

Chapter 3 (Paper I,II):
The theoretical framework based on the *integral Green's function method* is used to treat the two fundamental modes of a dual-STM setup: the scanning and the spectroscopy mode. We exemplify both methods using pristine graphene and simple defects such as adatoms or vacancies, observing effects like conductance anisotropy between armchair and zigzag directions as well as quantum interference around defects and crystalline edges.

Chapter 4 (Paper II, III, unpublished):
Turning to more complicated nanostructures using the *patched Green's function method*, we show how the dual probe setup can be used to describe transport effects for perforations and local gating of the graphene sheet. The perforation shows Fano-like resonances in the dual probe transmission, caused by localized states at the zigzag components of the edges. Here the current forms vortices effectively increasing the size of the perforation. Furthermore we demonstrate how a circularly gated region exhibits features like focusing and resonant scattering creating quasi bound states. We show that these resonances can turn forward scattering on and off effectively suppressing the Klein tunneling effect at certain energies.

Chapter 5 (Paper III, IV , V , VI):

We study inhomogeneous strain fields which give rise to pseudomagnetic fields. A constant pseudomagnetic field is created by a triaxial strain profile and we observe pseudo Landau quantization due to this field. Moreover, we investigate pseudo-Landau levels in rotationally symmetric strain fields with clamped edges. In these systems, the pseudo-Landau levels mixes with strong Friedel-type oscillations caused by the size quantization from the edges. These competing effects make a clear identification of pseudo-Landau levels difficult at best. Moreover, we use the dual probe setup to analyze the current flow in various types of local strain fields ("pseudomagnetic dots") demonstrating effects like current focusing or splitting, preferential direction scattering, increased backscattering and snake-like currents. Finally, we extend the analysis to arrays of pseudomagnetic dots and consider the effect on the conductivity of large scale samples using the Kubo-Greenwood formalism.

Chapter 6 (unpublished):
We consider possible extensions of the theoretical framework to treat systems outside the phase coherent regime. This requires the introduction of disorder or dephasing mechanisms. We propose an approach based on the coherent potential approximation to obtain an effective medium including disorder effects. To calculate the transmission through this effective medium, we present a vertex correction scheme and show how this can be used in case of a standard two terminal setup for a graphene nanoribbon.

Chapter 7:
We evaluate the progress made in the thesis and summarize the main results. In addition, we discuss possible extensions and some possible next steps for investigations made in the thesis.

CHAPTER 2

Theoretical multi-probe models using quantum mechanics

In this chapter we aim to develop a theoretical framework for multi-probe setups which is able to include quantum effects. Firstly, we notice that geometry plays an important role in the case of STM-like probes as, in contrast to the standard calculation setup, a local probe does not only couple to the sample at the edge. Furthermore, the relative positions of the probes are important. These characteristics need to be captured by a theoretical model. We therefore disregard formalisms that calculate the native material properties without including the effects of the probes and their positions. Instead, we choose a Landauer-Bütikker formalism as it allows us to include the geometrical factors.

We will not derive the framework of non-equilibrium Green's functions (NEGF) or the Landauer-Bütikker formalism, instead we refer to textbooks as Datta [72] or Haug & Jauho [73] for thorough treatment or to the short introduction in Ref. [74]. Instead, this chapter focuses on how to utilize the NEGF framework to make numerical calculations for systems containing multiple local probes.

The chapter opens with a discussion of the challenges in comparison to the standard two terminal ("Lead-Device-Lead") approach. Next, we present two methods able to deal with these specific challenges. The first approach is particularly efficient when only a limited amount of disorder is present. The second approach, although computationally more expensive, is able to deal with arbitrary size of defects and is therefore the more general of the two methods.

2.1 Problems faced by theoretical modeling

In the Landauer-Büttiker formalism the current flow between two electrodes is expressed in terms of the probability that an electron can pass from one electrode through the conductor and into the second electrode. In this way, the zero temperature conductance is connected to the transmission $\mathcal{T}$ as $\mathcal{G} = \frac{2e^2}{h}\mathcal{T}$. Using the non-equilibrium Green's function

formalism [72–75] the transmission probability can be calculated as

$$\mathcal{T} = \mathrm{Tr}\big[\boldsymbol{G}_D^\dagger \boldsymbol{\Gamma}_R \boldsymbol{G}_D \boldsymbol{\Gamma}_L\big], \tag{2.1}$$

where $\mathrm{Tr}\big[\,\cdot\,\big]$ is the trace over all states in the device region, $\boldsymbol{G}_D$ is the Green's function (GF) for the device Hamiltonian and $\boldsymbol{\Gamma}_{L/R}$ is the imaginary part of the lead self-energy describing the scattering into the left and right lead.

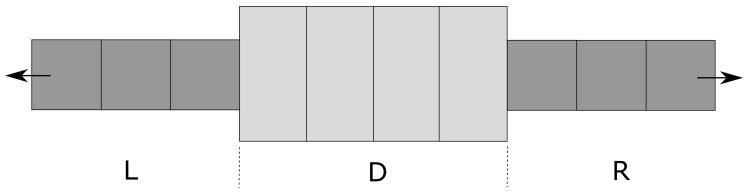

Figure 2.1: Generic two probe system which couples the left (L) and right (R) leads to an intermediate device region (D).

In the standard NEGF framework transport is considered through a lead-device-lead setup as shown in Fig. 2.1. Here a voltage drop is applied between the left (L) and right (R) leads causing a current to flow through the central device region (D). In this setup, the device Hamiltonian is finite in the transport direction, but can be repeated periodically in the transverse direction using a Bloch scheme. Although the device is finite in the transport direction, the leads are typically taken as semi-infinite chains of repeated cells, which in turn can be constructed using recursive schemes [76]. The device Hamiltonian is defined on a local basis set meaning that each basis orbital has a finite range. This can be in a form of a phenomenological tight binding Hamiltonian or obtained using Density Functional Theory (DFT) with a local atomic orbital basis set [75]. In both cases, the GF for the device region can be calculated using so-called recursive Green's function methods (RGF) [77]. Although variants of the method can be used for arbitrary geometries and multiple leads, [78–80] the method remains limited to finite-width or periodic systems.

Now we turn to the dual-STM setup shown schematically in Fig. 2.2. Here the device region becomes the entire two-dimensional sheet making the device Hamiltonian infinite. Moreover, the local probes exclude periodicity making the Hamiltonian including the STM-like probes non-periodic. However, the standard setup in Fig. 2.1 requires semi-infinite leads in the transport direction and periodicity in the transverse direction in order to describe a two-dimensional system. As the standard approach is not directly applicable, this chapter presents two alternative methods to treat the dual probe setup with an infinite and non-periodic device region.

Method 1 exploits the fact that we only need a limited part of the full real space GF to calculate the transmission between different local probes. The real space GF for a pristine infinite system can often be calculated using a combination of analytical and integral methods which we will show in the case of graphene. Afterwards, using a Dyson equation approach to add any real space perturbations, we obtain exactly the full GF elements needed for transport calculations.

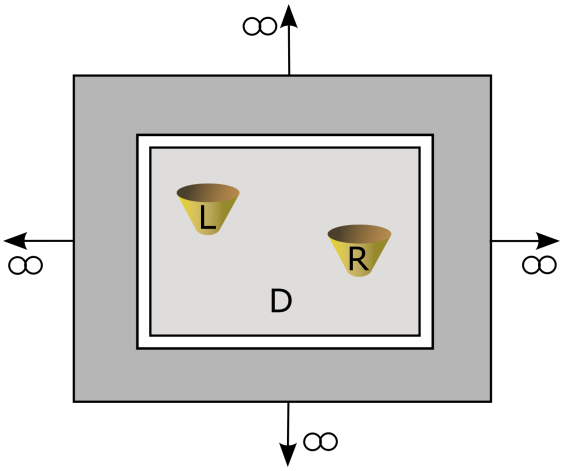

Figure 2.2: Generic dual probe system with finite probes coupling to an infinite system.

Method 2 uses a self-energy approach to reduce the infinite Hamiltonian to a finite one while including the infinite degree of freedom through a finite self-energy. The idea is similar to the one used for the leads in the standard setup discussed above. We show how to construct a self-energy in order to take into account the infinite part of the system (dark gray in Fig. 2.2). With the inclusion of this self-energy, the device Hamiltonian can afterwards be treated by an efficient recursive scheme which is also presented. This approach can treat the local electronic and transport properties of very large systems embedded within an infinite two-dimensional sheet, something that has not previously been possible.

2.2 Method 1: Integral Green's function method

The first approach to treat an infinite two dimensional system with local probes relies on an evaluation of the pristine real space GF. Such a GF can often be calculated for pristine systems using a combination of analytical and integral methods making this approach computationally effective as long as the system does not deviate too much from pristine. Throughout this thesis we will focus on graphene, but the method is extendable to all other two dimensional materials where the real space GF for the pristine material is obtainable in a similar manner.

Considering a dual-STM setup (see Fig. 2.3) with two probes placed at $\boldsymbol{r}_1$ and $\boldsymbol{r}_2$, the transmission in Eq. (2.1) becomes

$$\mathcal{T}_{12} = \mathrm{Tr}\big[G^\dagger(\boldsymbol{r}_1,\boldsymbol{r}_2)\Gamma_2(\boldsymbol{r}_2)G(\boldsymbol{r}_2,\boldsymbol{r}_1)\Gamma_1(\boldsymbol{r}_1)\big], \tag{2.2}$$

where $G(\boldsymbol{r}_1,\boldsymbol{r}_2)$ is Green's function connecting $\boldsymbol{r}_1$ and $\boldsymbol{r}_2$ and $\Gamma_{1/2}$ is the imaginary part

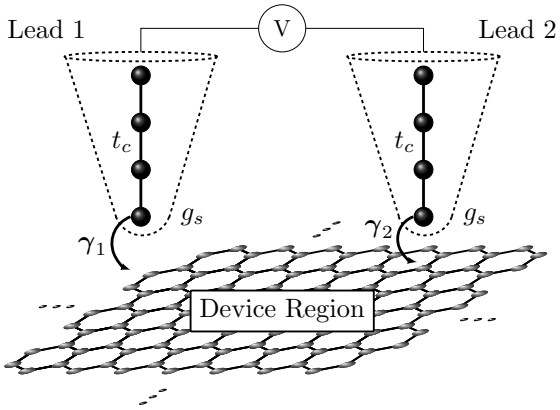

Figure 2.3: Setup sketch including the leads modelled as one dimensional chains with a hopping t_c between the sites. The surface Green's functions g_s are indicated together with the coupling $\boldsymbol{\gamma}^{1/2}$ between the lead and the graphene sample. The specific probe models will be elaborated in Section 2.4.

of the lead self-energies, $\Gamma_{1/2}(E) = \mathrm{i}\big(\Sigma_{1/2} - \Sigma_{1/2}^{\dagger}\big)$. The exact form of the self-energies, $\Sigma_{1/2}$, is postponed until Section 2.4.

We note from Eq. (2.2) that we only need the GF elements between the sites coupling to the probes. Hence, even though the device is infinite, we only need a finite number of real space GF elements for the system. In the next section we will discuss how to obtain the pristine real space GF of an infinite graphene sheet which we will denote $\boldsymbol{G}^0$. To go from a pristine system to include defects, probes or other perturbations, we use the Dyson equation:

$$\boldsymbol{G} = \boldsymbol{G}^0 + \boldsymbol{G}^0\boldsymbol{V}\boldsymbol{G} = \big(\mathbf{1} - \boldsymbol{G}^0\boldsymbol{V}\big)^{-1}\boldsymbol{G}^0, \tag{2.3}$$

where $\boldsymbol{V}$ is the matrix representation of the perturbation. Any local perturbation (*e.g.*, adatoms, vacancies, coupling to leads) can be included using this technique. Accurate parametrizations for many of these perturbations can be obtained using density functional theory [15, 81].

We note that the dimension of the $\boldsymbol{V}$-matrix is determined by the number of the modified sites. Thus, for N modified sites one needs to solve a $N \times N$ system, and the computational cost thus follows the number of defect and contact sites, rather than the sample size which is usual for RGF methods.

All perturbations to the pristine lattice are added in real space, as opposed to describing them with additional terms in the reciprocal space Hamiltonians. This ensures that modifications are added only locally and are not repeated via periodic boundary conditions. The approach is well suited to situations where the majority of the sample is pristine, as unmodified graphene is computationally 'free'.

2.2.1 Real space graphene Green's function

In this section, we want to determine the real space GF for pristine graphene. In graphene, the four valence electrons are conveniently modeled by the tight binding sp^2-orbital model. The sp^2 hybridization (or σ-orbitals) in the plane are responsible for the bonding and electrons in these orbitals occupy lower energies than the remaining out-of-plane π-orbital [15]. Therefore, we can accurately describe transport properties by a nearest neighbor orthonormal tight binding Hamiltonian with zero onsite energy

$$\boldsymbol{H} = \sum_{<i,j>} t\hat{c}_i^\dagger \hat{c}_j + h.c, \tag{2.4}$$

where the sum $< i, j >$ runs over all nearest neighbour pairs and the carbon-carbon hopping integral is $t \approx -2.7$ eV. The graphene hexagonal lattice can be split into two triangular sublattices, which we denote A and B, where neighboring sites reside on opposite sublattices connected with vectors, see Fig. 2.4.

$$\delta_1 = a_0\big(-\frac{\sqrt{3}}{2}, -\frac{1}{2}\big), \quad \delta_2 = a_0\big(\frac{\sqrt{3}}{2}, -\frac{1}{2}\big), \quad \delta_3 = a_0\big(0, 1\big), \tag{2.5}$$

where $a_0 = 0.142$ nm is the carbon-carbon distance. Using Bloch functions, the Hamiltonian can be rewritten in reciprocal space as [12, 82]

$$\boldsymbol{H_k} = t\begin{pmatrix} 0 & f(\boldsymbol{k}) \\ f^*(\boldsymbol{k}) & 0 \end{pmatrix}, \tag{2.6}$$

where the matrix form arises from sublattice indexing within a 2 atom unit cell and we have used the definition $f(\boldsymbol{k}) = 1 + \mathrm{e}^{\mathrm{i}\boldsymbol{k}\cdot\boldsymbol{a}_1} + \mathrm{e}^{\mathrm{i}\boldsymbol{k}\cdot\boldsymbol{a}_2}$, with the lattice vectors $\boldsymbol{a}_1 = a_0(-\sqrt{3}, 3)/2$

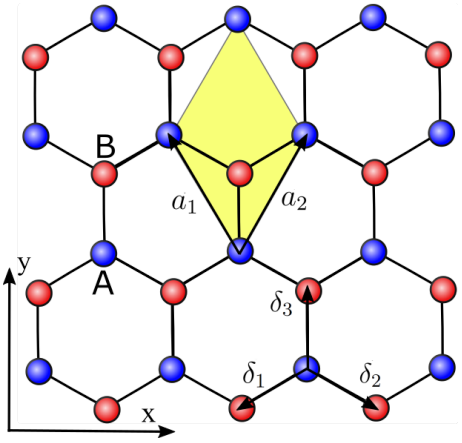

Figure 2.4: Graphene lattice with two superimposed triangular sublattices A (blue) and B (red) with unit vectors $\boldsymbol{a}_1$, $\boldsymbol{a}_2$ and nearest neighbor vectors δ_1, δ_2 and δ_3. The yellow area indicates the unit cell containing two atoms.

and $\boldsymbol{a}_2 = a_0(\sqrt{3}, 3)/2$. With this definition of the unit vectors we have the armchair direction along the y-axis (and zigzag along the x-axis).

The eigenenergies and eigenstates of the system are easily obtained from this form of the Hamiltonian, and transforming back to real space allows us to write the desired Green's function between sites i and j as [83, 84]

$$G^0_{ij}(z) = \frac{1}{\Omega_{BZ}} \int \mathrm{d}^2\boldsymbol{k} \frac{N_{ij}(z, \boldsymbol{k}) \mathrm{e}^{\mathrm{i}\boldsymbol{k}\cdot(\boldsymbol{r}_j - \boldsymbol{r}_i)}}{z^2 - t^2|f(\boldsymbol{k})|^2}, \tag{2.7}$$

where $z = E + \mathrm{i}0^+$ is the energy, Ω_{BZ} is the area of the first Brillouin zone. The position of the unit cell containing site i is denoted by $\boldsymbol{r}_i = m_i\boldsymbol{a}_1 + n_i\boldsymbol{a}_2$, with m_i and n_i being integers.

Finally we use the definition $N_{ij}(z, \boldsymbol{k}) = z$, when i and j are on the same sublattice and $N_{ij}(z, \boldsymbol{k}) = tf(\boldsymbol{k})$ if i is on the A sublattice and j is on the B sublattice and $N_{ij}(z, \boldsymbol{k}) = tf^*(\boldsymbol{k})$ when i is on B and j on A.

$$N(z, \boldsymbol{k}) = \begin{pmatrix} z & tf(\boldsymbol{k}) \\ tf^*(\boldsymbol{k}) & z \end{pmatrix}. \tag{2.8}$$

To simplify the notation we introduce the dimensionless k-vectors

$$k_A = 3k_y a_0/2, \tag{2.9a}$$
$$k_Z = \sqrt{3}k_x a_0/2, \tag{2.9b}$$

such that $f(k_A, k_Z) = 1 + 2\cos\left(k_Z\right)\mathrm{e}^{\mathrm{i}k_A}$, and write the separation vector in terms of the lattice vectors

$$\boldsymbol{r} = \boldsymbol{r}_j - \boldsymbol{r}_i = m\boldsymbol{a}_1 + n\boldsymbol{a}_2. \tag{2.10}$$

Inserting this into Eq. (2.7) gives

$$G^0_{ij}(z, \boldsymbol{r}) = \frac{1}{2\pi^2} \int \mathrm{d}k_A \int \mathrm{d}k_Z N_{ij}(z, k_A, k_Z) \times \frac{\mathrm{e}^{\mathrm{i}k_A(m+n) + \mathrm{i}k_Z(m-n)}}{z^2 - t^2\left(1 + 4\cos^2(k_Z) + 4\cos(k_A)\cos(k_Z)\right)}. \tag{2.11}$$

where the integration is over the BZ zone. Eq. (2.11) can be solved using a two-dimensional numerical integration, but as we require Eq. (2.11) for each Green's function element individually, we wish to increase the performance by doing one integration analytically using complex contour techniques. The choice of first integration variable is important and below we treat the two different choices – namely *armchair* (k_A) and *zigzag* (k_Z).

Armchair direction

Following the approach of Ref. [84], we use k_A as the complex variable and consider the integral

$$I_A = \int_{-\pi}^{\pi} \mathrm{d}k_A \frac{N_{ij}(z, k_A, k_Z)\mathrm{e}^{\mathrm{i}k_A(m+n)+\mathrm{i}k_Z(m-n)}}{z^2 - t^2\big(1 + 4\cos^2(k_Z) + 4\cos(k_A)\cos(k_Z)\big)}. \tag{2.12}$$

The pole, q, of the denominator is given by

$$q = \cos^{-1}\left[\frac{\frac{z^2}{t^2} - 1 - 4\cos^2\left(k_Z\right)}{4\cos\left(k_Z\right)}\right]. \tag{2.13}$$

Contours in the positive half plane correspond to the situation $m + n \geq 0$ and the sign of the pole must be selected carefully to ensure that it lies within the integration contour, *i.e.* $\mathrm{Im}(q) > 0$.

The residue of a function $f(z) = \frac{g(z)}{h(z)}$ at a pole z_0 is given by $\mathrm{Res}(f(z))_{z=z_0} = \frac{g(z_0)}{h'(z_0)}$, where $h'(z)$ is the derivative of h. The residue of the integrand in Eq. (2.12) becomes

$$\mathrm{Res}\big(I_A\big) = \frac{N_{ij}(z, q, k_Z)\mathrm{e}^{\mathrm{i}q(m+n)+\mathrm{i}k_Z(m-n)}}{4t^2\sin(q)\cos(k_z)} \tag{2.14}$$

Using the residue theorem we finally reduce Eq. (2.11) to

$$G^0_{ij}(z, \boldsymbol{r}) = \frac{\mathrm{i}}{4\pi t^2}\int_{-\frac{\pi}{2}}^{\frac{\pi}{2}} \mathrm{d}k_Z \frac{N_{ij}(z, q, k_Z)\mathrm{e}^{\mathrm{i}q(m+n)+\mathrm{i}k_Z(m-n)}}{\cos\left(k_Z\right)\sin\left(q\right)}, \tag{2.15}$$

with q given by Eq. (2.13).

Zigzag direction

Following the same approach as for the armchair direction we use a different Brillouin zone and consider the integral

$$I_Z = \int_{-\pi}^{\pi} \mathrm{d}k_Z \frac{N_{ij}(z, k_A, k_Z)\mathrm{e}^{\mathrm{i}k_A(m+n)+\mathrm{i}k_Z(m-n)}}{z^2 - t^2\big(1 + 4\cos^2(k_Z) + 4\cos(k_A)\cos(k_Z)\big)}. \tag{2.16}$$

We again go to the complex plane and use the residue theorem. This time there are two poles in the denominator,

$$\cos(q) = -\frac{1}{2}\left(\cos(k_A) \pm \sqrt{\frac{z^2}{t^2} - \sin^2(k_A)}\right), \tag{2.17}$$

Each pole must have its overall sign chosen to ensure it lies within the contour. The residue for these poles can be calculated in a similar manner as for the armchair direction:

$$\mathrm{Res}(I_Z) = \frac{1}{4t^2}\sum_q \frac{N_{ij}(z,k_A,q)\mathrm{e}^{\mathrm{i}k_A(m+n)+\mathrm{i}q(m-n)}}{\sin(2q)+\sin(q)\cos(k_A)} \tag{2.18}$$

Using the residue theorem reduces the total integral Eq. (2.11)

$$G^0_{ij}(z,\boldsymbol{r}) = \frac{\mathrm{i}}{4\pi t^2}\sum_q \int_{-\frac{\pi}{2}}^{\frac{\pi}{2}} \mathrm{d}k_A \frac{N_{ij}(z,q,k_Z)\mathrm{e}^{\mathrm{i}k_A(m+n)+\mathrm{i}q(m-n)}}{\sin(2q)+\sin(q)\cos(k_A)}, \tag{2.19}$$

with q given by Eq. (2.17).

Even though Eq. (2.15) and Eq. (2.19) give identical results for the GF, the zigzag direction (Eq. (2.19)) proves most stable in the numerical evaluations of the final integral. Furthermore, the above expressions can be generalized to include, for example, second nearest neighbor terms [85] and uniaxial strains [86].

2.2.2 Stationary phase approximation

Above we have shown how the first integral in the GF calculation could be done using complex contour methods. The results in Eqs. (2.15) and (2.19) only contain a one dimensional integral which in general needs to be evaluated numerically. However, in certain cases we can make approximations to solve for a closed analytical form of the GF [84].

We note that the remaining integrand of both Eqs. (2.15) and (2.19) contains an exponential factor of the form $\mathrm{e}^{\mathrm{i}\boldsymbol{k}\cdot\boldsymbol{r}}$, where $\boldsymbol{r} = m\boldsymbol{a}_1 + n\boldsymbol{a}_2$. Therefore the integrand will oscillate rapidly if the distance between the two sites is great enough. This observation is key to performing the remaining integration in the limit of large separations, as the rapid oscillations do not contribute significantly towards the final value of the integral [84].

If we consider an integral of the general form

$$I(x) = \int \mathrm{d}y f(y)\mathrm{e}^{\mathrm{i}\phi(y)x}. \tag{2.20}$$

The integrand oscillates with a varying phase $\phi(y)$ and for large values of x the parts having different phase will tend to cancel when performing the integration over y. The region with the largest contribution will therefore correspond to y values where $\phi(y)$ is constant. This leads to the so-called Stationary Phase Approximation (SPA) where we replace the integrand of Eq. (2.20) with a Taylor expansion around the stationary points y_0. The stationary points are determined by

$$\left.\frac{\mathrm{d}\phi}{\mathrm{d}y}\right|_{y_0} = 0, \tag{2.21}$$

such that the phase term becomes

$$\phi(y) \approx \sum_{y_0} \left(\phi(y_0) + \frac{1}{2} \frac{\mathrm{d}^2\phi}{\mathrm{d}^2 y}\bigg|_{y_0} (y - y_0)^2 + \cdots \right). \tag{2.22}$$

Note that the first order Taylor expansion term is zero per definition of the stationary point.

If we now furthermore assume that the function $f(y)$ is slowly varying about each stationary point then a stationary point will contribute to the integral with the value

$$\begin{aligned} I_{y_0}(x) &= \int \mathrm{d}y f(y_0) \mathrm{e}^{\mathrm{i}\left[\phi(y_0) + \phi''(y_0)(y-y_0)^2\right]x} \\ &= f(y_0)\mathrm{e}^{\mathrm{i}\phi(y_0)x} \int \mathrm{d}y \mathrm{e}^{\mathrm{i}\phi''(y_0)(y-y_0)^2 x} \\ &= f(y_0)\mathrm{e}^{\mathrm{i}\phi(y_0)x} \sqrt{\frac{2\mathrm{i}\pi}{\phi''(y_0)x}}. \end{aligned} \tag{2.23}$$

Below we use Eq. (2.23) to consider the GF for graphene between sites on the same sublattice separated in either the armchair or zigzag direction.

Armchair direction

First we consider the GF between two sites on the same sublattice and separated by a vector in the armchair direction. For armchair separation we have $m = n$ and from Eq. (2.15) we obtain

$$G^0_{ij}(z, \boldsymbol{r}) = \frac{\mathrm{i}z}{4\pi t^2} \int_{-\frac{\pi}{2}}^{\frac{\pi}{2}} \mathrm{d}k_Z \frac{\mathrm{e}^{\mathrm{i}q(m+n)}}{\cos\left(k_Z\right)\sin\left(q\right)} \tag{2.24}$$

The special choice of separation and contour integration direction has led to the simple functional form of Eq. (2.24). Comparing with Eq. (2.20) we note that the phase term is simply given by the pole of the contour integral Eq. (2.13). Inserting Eq. (2.13) into $\frac{\mathrm{d}q}{\mathrm{d}k_Z}\Big|_{k_Z^0}$ the solution for the stationary points becomes

$$k_Z^0 = 0, \pm\cos^{-1}\left(\frac{\sqrt{t^2 - z^2}}{2t}\right) \tag{2.25}$$

Although both solutions are valid, only one of them yields a real value of the pole q for a given energy. If q is complex the integrand in Eq. (2.24) vanishes for large separations *i.e.* large values of $m + n$. In consequence, we only consider the solution giving rise to real q values for a given energy

$$k_Z^0 = \begin{cases} \pm\cos^{-1}\left(\frac{\sqrt{t^2-z^2}}{2t}\right), & \text{if } |z| < |t| \\ 0, & \text{if } |z| > |t|. \end{cases} \tag{2.26}$$

For the case $|z| = \pm|t|$ we must consider both contributions.

The wavevector q can now be expanded in a Taylor series around the relevant stationary point k_Z^0. Keeping only terms up to second order we get from Eq. (2.22)

$$q(k_Z) \approx q(k_Z^0) + \frac{1}{2}\frac{\mathrm{d}^2 q}{\mathrm{d}^2 k_Z}\bigg|_{k_Z^0}(k_Z - k_Z^0)^2 = \mathcal{Q}(z) + \mathcal{W}(z)(k_Z - k_Z^0)^2, \tag{2.27}$$

where

$$\mathcal{Q}(z) = \begin{cases} \pm\cos^{-1}\left(-\sqrt{1-\frac{z^2}{t^2}}\right), & \text{if } |z| < |t|, \\ \pm\cos^{-1}\left(\frac{z^2-5t^2}{4t^2}\right), & \text{if } |z| > |t|, \end{cases} \tag{2.28}$$

and

$$\mathcal{W}(z) = \begin{cases} \pm\frac{z^2+3t^2}{2z\sqrt{t^2-z^2}}, & \text{if } |z| < |t|, \\ \pm\frac{z^2+3t^2}{2\sqrt{(t^2-z^2)(z^2-9t^2)}}, & \text{if } |z| > |t|. \end{cases} \tag{2.29}$$

The sign of $\mathcal{Q}(z)$ must be chosen as earlier to ensure that it lies within the integration contour. Additionally the correct sign of $\mathcal{W}(q)$ must be determined by its correspondence to the curvature of q at the stationary points.

Substituting Eq. (2.27) into Eq. (2.24) using the expression Eq. (2.23) yields the Green's function

$$\begin{aligned} G_{ij}^0(z,\boldsymbol{r}) &= \frac{\mathrm{i}z}{4\pi t^2}\sum_{k_Z^0}\frac{\mathrm{e}^{\mathrm{i}\mathcal{Q}(z)(m+n)}}{\cos(k_Z^0)\sin(\mathcal{Q}(z))}\int_{-\frac{\pi}{2}}^{\frac{\pi}{2}}\mathrm{d}k_Z \mathrm{e}^{\mathrm{i}\mathcal{W}(z)(k_Z-k_Z^0)^2(m+n)} \\ &= \frac{\mathrm{i}z}{4\pi t^2}\sum_{k_Z^0}\sqrt{\frac{\mathrm{i}\pi}{\mathcal{W}(z)(m+n)}}\frac{\mathrm{e}^{\mathrm{i}\mathcal{Q}(z)(m+n)}}{\cos(k_Z^0)\sin(\mathcal{Q}(z))}, \end{aligned} \tag{2.30}$$

where the choice of k_Z^0 is determined by the considered energy regime. Using definitions of $\mathcal{Q}$ and $\mathcal{W}$ we simplify the expression and, after some algebra, for $z > 0$ we arrive at

$$\begin{aligned} G_{ij}^{\mathrm{spa,ac}}(z,\boldsymbol{r}) = \sqrt{\frac{2}{\mathrm{i}\pi}}\frac{1}{\sqrt{m+n}}\frac{1}{\sqrt{(z^2+3t^2)\sqrt{t^2-z^2}}} \\ \times\begin{cases} -\mathrm{i}\sqrt{z}\mathrm{e}^{\mathrm{i}\mathcal{Q}(z)(m+n)} & \text{if } |z| < |t|, \\ \frac{z}{(z^2-9t^2)^{1/4}}\mathrm{e}^{\mathrm{i}\mathcal{Q}(z)(m+n)} & \text{if } |z| > |t|. \end{cases} \end{aligned} \tag{2.31}$$

Fig. 2.5 shows the real and imaginary parts of the GF for the case $m+n = 40$ calculated both using the analytical expression Eq. (2.31) and a numerical evaluation of the integral Eq. (2.15). We note an excellent agreement between the two methods over the entire energy interval considered. We furthermore test the validity of the analytical expression by calculating $|G^0 - G^{SPA}|/|G^0|$ as a function of separation distance for specific energies,

see Fig. 2.6. The deviation between the numerical and analytical decreases with increasing distance between the two sites. In addition, the analytical expression is more accurate for higher energies, but even for small energies the deviation is less than 5% for distances above $40a_0$ and decreases rapidly with increased separation.

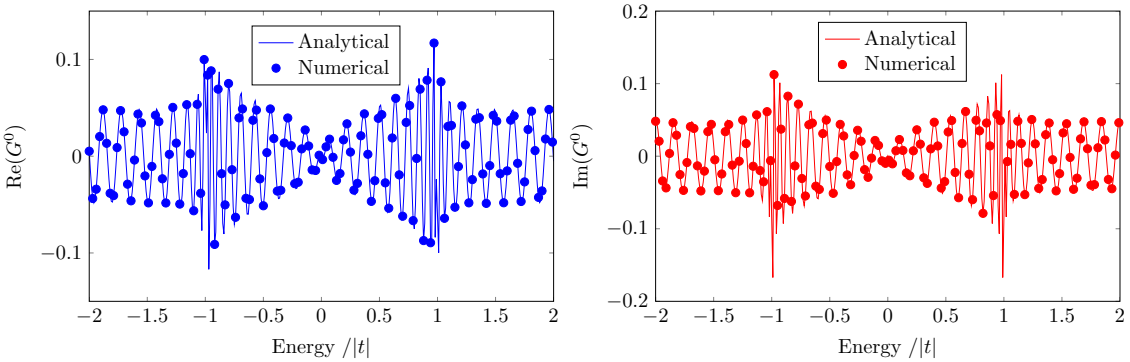

Figure 2.5: Real (Left) and imaginary (Right) part of the Green's function calculated using both the analytical expression, Eq. (2.31), and the numerical evaluation of the Green's function integral in Eq. (2.15) for the armchair separation $m + n = 40$.

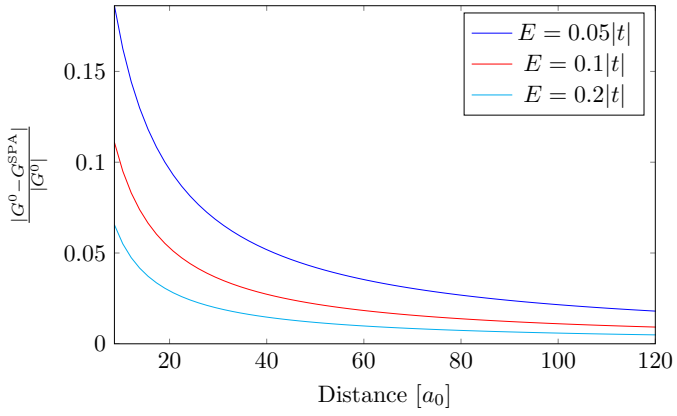

Figure 2.6: The percentage difference between the analytical SPA expression and the numerical integral as a function of separation distance along the armchair direction.

Zigzag direction

Next, we consider the GF between two sites on the same sublattice, but separated along the zigzag direction. For zigzag separations $m = -n$ and using Eq. (2.19) we obtain

$$G^0_{ij}(z,\boldsymbol{r}) = \frac{\mathrm{i}z}{4\pi t^2}\sum_q \int_{-\frac{\pi}{2}}^{\frac{\pi}{2}} \mathrm{d}k_A \frac{\mathrm{e}^{\mathrm{i}q(m-n)}}{\sin(2q)+\sin(q)\cos(k_A)}, \tag{2.32}$$

Now using the same approach as for the armchair direction above we determine the stationary points from the condition $\left.\frac{\mathrm{d}q}{\mathrm{d}k_A}\right|_{k_A^0}$,

$$k_A^0 = 0. \tag{2.33}$$

The stationary points in the zigzag direction are independent of energy. Expanding the wavevector q, Eq. (2.13), in a Taylor series around the stationary points while keeping only terms up to second order we get

$$q(k_A) \approx q(k_A^0) + \frac{1}{2}\left.\frac{\mathrm{d}^2 q}{\mathrm{d}^2 k_A}\right|_{k_A^0}(k_A - k_A^0)^2 = \mathcal{Q}(z) + \mathcal{W}(z)(k_A - k_A^0)^2, \tag{2.34}$$

where

$$\mathcal{Q}^+(z) = \pm\cos^{-1}\left(-\frac{t+z}{2t}\right), \tag{2.35a}$$

$$\mathcal{Q}^-(z) = \pm\cos^{-1}\left(\frac{-t+z}{2t}\right), \tag{2.35b}$$

and

$$\mathcal{W}^+(z) = \pm\frac{t}{2z}\frac{t+z}{\sqrt{(3t+z)(t-z)}}, \tag{2.36a}$$

$$\mathcal{W}^-(z) = \pm\frac{t}{2z}\frac{t-z}{\sqrt{(3t-z)(t+z)}}, \tag{2.36b}$$

Using the Taylor expansion and the general integral solution Eq. (2.23) we get after some algebraic manipulations

$$\begin{aligned} G^{\mathrm{spa,zz}}_{ij}(z,\boldsymbol{r}) &= \frac{\mathrm{i}z}{4\pi t^2}\sum_{\alpha=\pm}\sqrt{\frac{\mathrm{i}\pi}{\mathcal{W}^\alpha(m-n)}}\frac{\mathrm{e}^{\mathrm{i}Q^\alpha(z)(m-n)}}{\sin(2Q^\alpha(z))+\sin(Q^\alpha(z))\cos(k_A^0)}, \\ &= \sqrt{\frac{1}{2\mathrm{i}\pi(m-n)}}\left(\sqrt{\frac{z}{|t|(t+z)}}\frac{\mathrm{e}^{\mathrm{i}\mathcal{Q}^+(z)(m-n)}}{((3t+z)(t-z))^{1/4}}\right. \\ &\quad \left. + \sqrt{\frac{z}{|t|(t-z)}}\frac{\mathrm{e}^{\mathrm{i}\mathcal{Q}^-(z)(m-n)}}{((3t-z)(t+z))^{1/4}}\right). \end{aligned} \tag{2.37}$$

Similarly to the armchair direction, Fig. 2.7 shows both the real and imaginary parts of the GF calculated using both a numerical evaluation of Eq. (2.19) and the analytical expression Eq. (2.37). We note a very good agreement between the two approaches, validating the analytical expression for the GF along the zigzag direction at large distances.

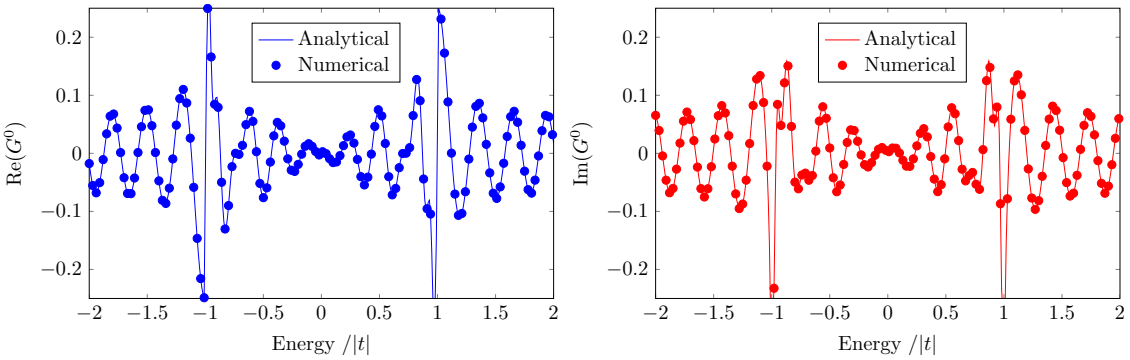

Figure 2.7: Real (Left) and imaginary (Right) part of the Green's function calculated using both the analytical expression, Eq. (2.37), and the numerical evaluation of the Green's function integral in Eq. (2.19) for the zigzag separation $m + n = 40$.

Simple SPA form

The analytic expressions in Eqs. (2.31) and (2.37) are valid throughout the entire energy range compared to analytical expressions for the GF relying on the Dirac approximation which are only valid at small energies. The advantage of the SPA expressions is obvious when considering energy scales outside the linear dispersion regime but the approach is also useful when considering distance-dependent properties. This is seen when expressing Eqs. (2.31) and (2.37) in a more concise form [84],

$$\mathcal{G}_{ij}^{\mathrm{spa}}(z) = \frac{\mathcal{A}(z)\mathrm{e}^{\mathrm{i}\mathcal{Q}(z)\Delta}}{\sqrt{d_{ij}}}, \tag{2.38}$$

where d_{ij} is the distance between two sites and $\mathcal{A}$ and $\mathcal{Q}$ are given by Eqs. (2.37) and (2.31) for $z > 0$ we collect the simple form and corresponding coefficients at the end of this section.

In Eq. (2.38) the energy and distance dependent features of the GF are clearly identified. So even in the case where the coefficient $\mathcal{A}$ is not particularly simple, the expression above can be used to draw qualitative arguments. Combined with the ability to clearly isolate the distance dependence in the GF allows us to perform a more transparent investigation of the properties of graphene.

The simple form in Eq. (2.38) will be especially useful to explain the qualitative effects when considering local probes and interference patterns arising from defect scattering in Chapter 3. It is specifically suited for this as the distance between the probes and defects exceeds tens of nanometers and therefore resides in the regime where the SPA approximation is a very close match to the numerically evaluated GF.

2.2.3 Summary of method 1

Integral Green's function method

We treat a multiprobe setup where the device region is infinite. Using a combination of analytical and integral methods to obtain the pristine GF's for an infinite system (see below), we can add defects and probes locally within the infinite system.

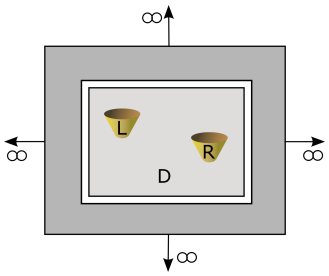

The transmission is calculated using the standard formula

$$\mathcal{T}_{12} = \mathrm{Tr}\left[G^\dagger(\boldsymbol{r}_1,\boldsymbol{r}_2)\Gamma_2(\boldsymbol{r}_2)G(\boldsymbol{r}_2,\boldsymbol{r}_1)\Gamma_1(\boldsymbol{r}_1)\right], \tag{2.39}$$

and defects are added using a Dyson equation

$$\boldsymbol{G} = \left(\mathbf{1} - \boldsymbol{G}^0\boldsymbol{V}\right)^{-1}\boldsymbol{G}^0. \tag{2.40}$$

Pristine Green's function for graphene: armchair

$$G^0_{ij}(z,\boldsymbol{r}) = \frac{\mathrm{i}}{4\pi t^2}\int_{-\frac{\pi}{2}}^{\frac{\pi}{2}} \mathrm{d}k_Z \frac{N_{ij}(z,q,k_Z)\mathrm{e}^{\mathrm{i}q(m+n)+\mathrm{i}k_Z(m-n)}}{\cos\left(k_Z\right)\sin\left(q\right)}, \tag{2.41}$$

$$\cos(q) = \frac{\frac{z^2}{t^2} - 1 - 4\cos^2\left(k_Z\right)}{4\cos\left(k_Z\right)}, \tag{2.42}$$

Pristine Green's function for graphene: zigzag

$$G^0_{ij}(z,\boldsymbol{r}) = \frac{\mathrm{i}}{4\pi t^2}\sum_q \int_{-\frac{\pi}{2}}^{\frac{\pi}{2}} \mathrm{d}k_A \frac{N_{ij}(z,q,k_Z)\mathrm{e}^{\mathrm{i}k_A(m+n)+\mathrm{i}q(m-n)}}{\sin(2q)+\sin(q)\cos(k_A)} \tag{2.43}$$

$$\cos(q) = -\frac{1}{2}\left(\cos(k_A) \pm \sqrt{\frac{z^2}{t^2} - \sin^2(k_A)}\right). \tag{2.44}$$

Stationary phase approximation(SPA): armchair

The Green's function of graphene can be approximated using the SPA for the armchair direction

$$\mathcal{G}_{ij}^{\mathrm{spa}}(z) = \frac{\mathcal{A}(z)\mathrm{e}^{\mathrm{i}\mathcal{Q}(z)d_{ij}}}{\sqrt{d_{ij}}} \tag{2.45a}$$

where d_{ij} is the distance between two sites.

Coefficients

$$\mathcal{Q}(z) = \pm\cos^{-1}\left(-\sqrt{1-\frac{z^2}{t^2}}\right) \tag{2.45b}$$

$$\mathcal{A}(z) = -\frac{1+\mathrm{i}}{\sqrt{\pi}}\frac{\sqrt{z}}{\sqrt{(z^2+3t^2)\sqrt{t^2-z^2}}} = -(1+\mathrm{i})|\mathcal{A}(z)| \tag{2.45c}$$

Stationary phase approximation (SPA): zigzag

The Green's function of graphene can be approximated using the SPA for the zigzag directions yielding a sum of two terms

$$\mathcal{G}_{ij}^{\mathrm{spa}}(z) = \sum_{\eta=\pm}\frac{\mathcal{A}^{\pm}(z)\mathrm{e}^{\mathrm{i}\mathcal{Q}^{\pm}(z)d_{ij}}}{\sqrt{d_{ij}}} \tag{2.46a}$$

where d_{ij} is the distance between two sites.

Coefficients

$$\mathcal{Q}^{+}(z) = \pm\cos^{-1}\left(\frac{-t-z}{2t}\right) \tag{2.46b}$$

$$\mathcal{Q}^{-}(z) = \pm\cos^{-1}\left(\frac{-t+z}{2t}\right) \tag{2.46c}$$

$$\mathcal{A}^{+}(z) = -\frac{1+\mathrm{i}}{\sqrt{4\pi}}\sqrt{\frac{z}{|t|(t+z)}}\frac{1}{\left[(3t+z)(t-z)\right]^{1/4}} = -(1+\mathrm{i})|\mathcal{A}^{+}(z)| \tag{2.46d}$$

$$\mathcal{A}^{-}(z) = -\frac{1+\mathrm{i}}{\sqrt{4\pi}}\sqrt{\frac{z}{|t|(t-z)}}\frac{1}{\left[(3t-z)(t+z)\right]^{1/4}} = -(1+\mathrm{i})|\mathcal{A}^{-}(z)| \tag{2.46e}$$

2.3 Solution 2: Patched Green's function method

The second approach to treat an infinite two dimensional sheet is based on the construction of a self-energy term that takes into account the extended parts of the system and is published in Paper III [87]. The self-energy describes the extended parts of the system in between finite device 'patches'. The device patches are described by a Hamiltonian, $\boldsymbol{H}_D$, which may include disorder, deformations, mean field terms, (non)uniform magnetic fields or leads *etc.* . We therefore consider the computational setup schematically shown in the left panel of Fig. 2.8, where a device region is embedded within an extended two dimensional system by applying a self energy term, Σ_B. To treat this setup, we need two things: first, we need to construct Σ_B and, secondly, we need an efficient way to describe the device region while taking Σ_B into account. Furthermore, the treatment of the device should be able to consider arbitrary geometries, including mutually disconnected patches within the extended system, as shown in the right panel of Fig. 2.8.

We describe the method in three steps:

1: Derivation of the boundary self energy term, Σ_B, in terms of the pristine lattice GFs.

2: Calculation of the real-space GF needed in the self energy calculation. We use graphene as an example.

3: Implementation of an adaptive RGF method to build the device region(s) efficiently while including the self energy term(s) Σ_B.

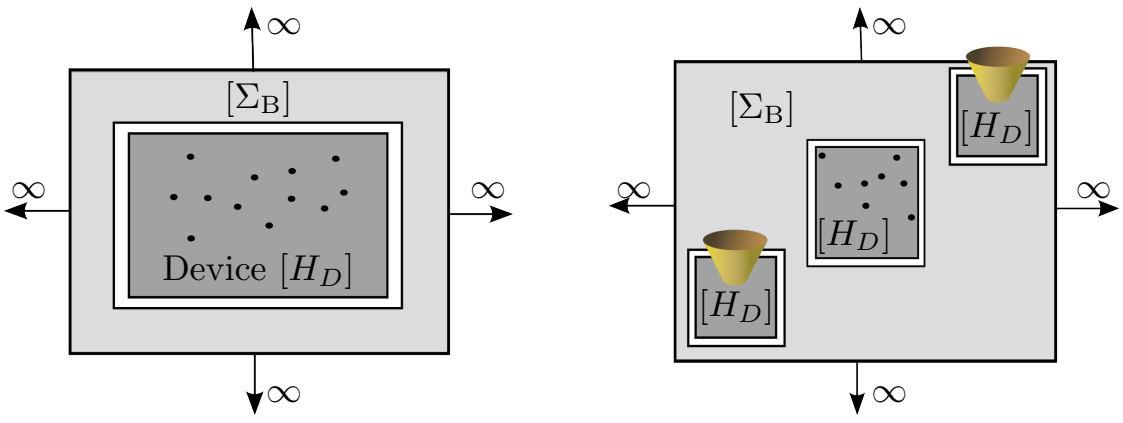

Figure 2.8: The left panel shows a schematic of a computational setup containing a finite device 'patch' , described by $\boldsymbol{H}_D$, embedded within an extended system described by the self energy $\boldsymbol{\Sigma}_B$. The right panel shows a computational setup containing several device 'patches' of interest.

2.3.1 Boundary self energy

To construct the boundary self energy describing the extended region in Fig. 2.8, we consider the simple graphene example in Fig. 2.9a. Here a central device region, indicated by the dashed square, is embedded into an extended sheet. In this example both the extended area and the device region are assumed to be graphene-based, but the following arguments are general to any two dimensional material. We consider a division of the system into two parts: sites in the device (D) or sites in the extended sheet region. Furthermore, we subdivide the extended sheet into boundary sites (B) which are indicated by blue in Fig. 2.9 and have a non-zero Hamiltonian element coupling them to the device region, or 'sheet' sites which do not couple to the device region. Within a nearest-neighbour tight-binding Hamiltonian, the boundary sites in Fig. 2.9a are shown by blue symbols and have non-zero couplings to the device sites indicated by red symbols. We can now write the Hamiltonian for the entire system, in block matrix form, as

$$\boldsymbol{H} = \begin{pmatrix} \boldsymbol{H}_{D,D} & \boldsymbol{V}_{D,B} & 0 \\ \boldsymbol{V}_{B,D} & \boldsymbol{H}_{B,B} & \boldsymbol{V}_{B,\text{sheet}} \\ 0 & \boldsymbol{V}_{\text{sheet},B} & \boldsymbol{H}_{\text{sheet}} \end{pmatrix}, \tag{2.47}$$

where the "light" shaded part of Eq. (2.47) represents an infinite Hamiltonian. The connections between device and sheet, (i.e. between the red and blue symbol sites in Fig. 2.9) are contained in the off-diagonal blocks $\boldsymbol{V}_{D,B}$ and $\boldsymbol{V}_{B,D}$.

We aim to replace the infinite Hamiltonian $\boldsymbol{H}$ with a finite effective Hamiltonian, $\boldsymbol{H}_{\text{eff}} = \boldsymbol{H}_{D,D} + \boldsymbol{\Sigma}_B$, which takes into account the extended sheet using a self energy

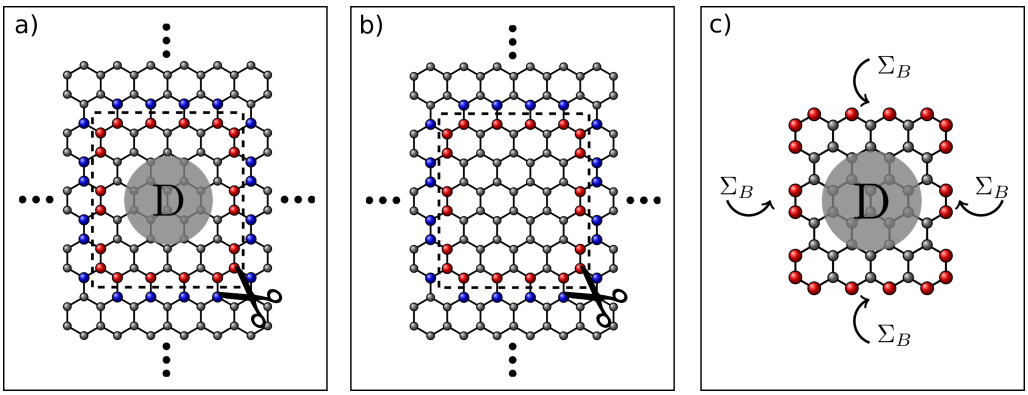

Figure 2.9: a) Shows the desired device region, indicated by the dashed square, embedded within an extended system. Red symbols are the edge of the device and blue symbols indicate sites in the surrounding sheet that couples to the device. We obtain the disconnected system discussed in the text by removing the couplings that cross the dashed line. b) Shows the corresponding pristine system. Again the disconnected system is obtained by removing couplings along the dashed line. c) Illustrates how the effect of the extended sheet on the device region is taken into account by the self energy, see Eq. (2.50).

term $\boldsymbol{\Sigma}_B$. To do this, we consider the *connected* system in panel a) of Fig. 2.9, and a disconnected system formed by removing the Hamiltonian elements $\boldsymbol{V}_{D,B}$ and $\boldsymbol{V}_{B,D}$, corresponding to removing couplings crossing the dashed line in Fig. 2.9a. The GFs of the connected ($\boldsymbol{G}^{(\mathrm{con})}$) and disconnected ($\boldsymbol{G}^{(\mathrm{dis})}$) systems can be related via the Dyson equation, and in particular we can write the GF of the connected device region as

$$\boldsymbol{G}^{(\mathrm{con})}_{D,D} = \boldsymbol{G}^{(\mathrm{dis})}_{D,D} + \boldsymbol{G}^{(\mathrm{dis})}_{D,D}\boldsymbol{V}_{D,B}\boldsymbol{G}^{(\mathrm{con})}_{B,D}. \tag{2.48}$$

Applying the Dyson equation again to obtain $\boldsymbol{G}^{(\mathrm{con})}_{B,D}$ and inserting this into Eq. (2.48) allows us to simplify,

$$\boldsymbol{G}^{(\mathrm{con})}_{D,D} = \left(E\mathbf{1} - \boldsymbol{H}_{D,D} - \boldsymbol{\Sigma}_B\right)^{-1}, \tag{2.49}$$

where the self energy term is given by

$$\boldsymbol{\Sigma}_B = \boldsymbol{V}_{D,B}\boldsymbol{G}^{(\mathrm{dis})}_{B,B}\boldsymbol{V}_{B,D}. \tag{2.50}$$

We note that the self energy in Eq. (2.50) is independent of the considered device and depends only on GF matrix elements connecting sites in the pristine surrounding 'frame' that remains when the device is removed from the full system. We take advantage of this to temporarily replace the device with a corresponding pristine region of the same size, as shown in panel b) of Fig. 2.9. The self-energy required to incorporate the finite pristine region into an infinite, pristine sheet is the same self energy, $\boldsymbol{\Sigma}_B$, that is required in Eq. (2.49). We can therefore write the required GF matrix, $\boldsymbol{G}^{(\mathrm{dis})}_{B,B}$, in terms of the GF of the infinite pristine sheet, $\boldsymbol{G}^{(0)}$. These are related using the Dyson equation with a perturbation $-\boldsymbol{V}_{D,B}$,

$$\boldsymbol{G}^{(\mathrm{dis})}_{B,B} = \left(\mathbf{1} + \boldsymbol{G}^{(0)}_{B,D}\boldsymbol{V}_{D,B}\right)^{-1}\boldsymbol{G}^{(0)}_{B,B}. \tag{2.51}$$

The advantage of writing the self-energy in terms of the pristine sheet GFs, $\boldsymbol{G}^{(0)}_{B,B}$ and $\boldsymbol{G}^{(0)}_{B,D}$, becomes clear in the next section, where we demonstrate an efficient method to calculate these two terms. It is worth noting that $\boldsymbol{G}^{(0)}_{B,D}$ only needs to be calculated for the sites in D which connect to sites in B. These sites are indicated by red in Fig. 2.9 and are where the self-energy terms need to be added, as shown in Fig. 2.9c.

The calculation scheme for the patched Green's function approach

1: Calculate $\boldsymbol{G}^{(0)}_{B,B}$ and $\boldsymbol{G}^{(0)}_{B,D}$ for example using the methods outlined in Section 2.3.2.

2: Calculate $\boldsymbol{\Sigma}_B$ from Eq. (2.50) and Eq. (2.51).

3: The finite GF for the device region, $\boldsymbol{G}^{(\mathrm{con})}_{D,D}$, is given by Eq. (2.49) and can be treated using an adaptive RGF method, see Section 2.3.3.

We note that this approach does not require a specific geometric shape of the device, nor does the device region need to be contiguous. We can treat different non-connected patches in an extended system, as shown in the right panel of Fig. 2.8, by extending the set D to include sites inside each patch and similarly expanding B to include sites at the boundary of each patch. The method presented in this section is applicable to any system where the connected, pristine GFs are easily obtainable as demonstrated in the next section using a tight-binding description of graphene as an example.

2.3.2 Real space pristine Green's function

We now turn to the calculation of $\boldsymbol{G}^{(0)}_{B,B}$ and $\boldsymbol{G}^{(0)}_{B,D}$, as defined above. In this work we consider graphene in a nearest neighbor tight binding model, but the technique is easily generalized to other cases

In Section 2.2 we showed how the pristine GF for the graphene tight binding Hamiltonian

$$G^0_{ij}(z) = \frac{1}{\Omega_{BZ}} \int \mathrm{d}^2\boldsymbol{k} \frac{\mathrm{e}^{\mathrm{i}\boldsymbol{k}\cdot(\boldsymbol{r}_j - \boldsymbol{r}_i)}}{z^2 - t^2|f(\boldsymbol{k})|^2} \begin{pmatrix} z & tf(\boldsymbol{k}) \\ tf^*(\boldsymbol{k}) & z \end{pmatrix}, \tag{2.52}$$

could be calculated using complex contour methods. In this way, Eqs. (2.15) and (2.19) can be used to fill up the elements of $\boldsymbol{G}^{(0)}_{B,B}$ and $\boldsymbol{G}^{(0)}_{B,D}$ one at a time.

Since we need GF matrices of size $N_B \times N_B$ and $N_B \times N_D$, where N_D and N_B are the number of sites at the edge of the device region and in the region B, respectively, it could seem very ineffective to calculate one element at a time. However, the total number of GF

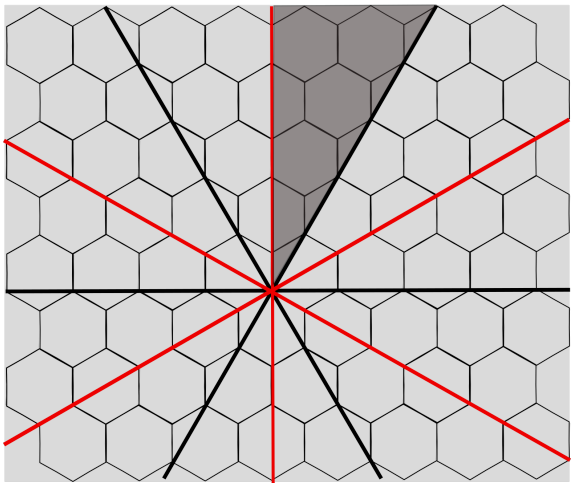

Figure 2.10: Illustrating the symmetries of the graphene lattice. Only 1/12 of the couplings (dark region) are unique and all other couplings can be found as rotation of this region.

elements to be calculated is greatly reduced by the symmetries of the pristine graphene lattice. The lattice itself is six-fold symmetric and each of these six identical wedges is in turn mirror symmetric, resulting in a 12-fold degeneracy of the GFs indexed by site separation vectors, see Fig. 2.10. Additionally, many of the required elements in $\boldsymbol{G}^{(0)}_{B,B}$ and $\boldsymbol{G}^{(0)}_{B,D}$ are identical. For instance, the onsite and nearest neighbor GF element appear many times, but only need to be calculated once. Taking the device region in Fig. 2.9 as example we have $N_D = N_B = 20$, yielding 400 individual elements for a brute force calculation. Instead, using symmetries and duplicates, we only need to calculate 38 and 42 elements when determining $\boldsymbol{G}^{(\mathrm{con})}_{B,B}$ and $\boldsymbol{G}^{(\mathrm{con})}_{B,D}$, respectively. The reduction becomes more significant for larger systems, as we generally only need to add the GF elements corresponding to the longest couplings. Consequently, only a small percentage of the GF elements need to be calculated individually and their values for frequently used separations and energies can be stored or reused to enable extremely fast calculation of the required self energies.

2.3.3 Adaptive recursion for device region

In this section we consider the device region where the boundary self energy can be added at the edge. The full GF of the device region is given by $\boldsymbol{G}_D = \left(E\mathbf{1} - \boldsymbol{H}_D - \boldsymbol{\Sigma}_B\right)^{-1}$, where we have simplified the notation from Eq. (2.49). From this GF both transport and local properties can be obtained. However, for most purposes we do not require every element of the Green's function matrix element in the device region, and so to avoid a time consuming full matrix inversion, various recursive or other decomposition methods are often applied [77, 80, 88–96].

This section outlines an adaptive recursion method which efficiently includes the boundary self energy as well as an arbitrary device region shape and configuration (and number) of leads. Alternative approaches have been developed to treat arbitrary shaped regions with multiple leads [78, 79, 94]. These so-called knitting-algorithms add single sites at a time. They rely on a complicated categorizing of sites into different intermediate updating blocks making the theory and implementation cumbersome. Hence, we use an approach similar to the ones in Refs. [88–90], and employ an adaptive partitioning of the Hamiltonian matrix in order to bring it into the desired tridiagonal form suitable for recursive methods.

Tridiagonalization

Calculating physical properties generally requires certain GFs connecting a specific set of sites in the device region. These sites of interest, for example, could be sites where we want to introduce defects, or couple to probes for transport calculations, or measure properties like the local density of states. We focus first on the general partitioning process, and then

demonstrate how it can be quickly modified to account for the edge self-energy terms. We begin by placing all these sites of interest into recursive cell 1, as shown by the red sites in Fig. 2.11. We emphasize that the cells in this process are not of a fixed size and may consist of arbitrary sites which are not necessarily connected. Cell 2 is determined by selecting all the remaining unpartitioned sites which couple directly to sites in cell 1 via a non-zero Hamiltonian matrix element. In the example in Fig. 2.11, this consists of nearest neighbor sites of those in cell 1, which are not themselves in cell 1. This process is repeated until all sites in the device region have been allocated a cell, and is demonstrated schematically in the panels of Fig. 2.11 where red sites indicate the current cell, and dark gray or white sites indicate sites added to the previous cell, or to earlier cells, respectively.

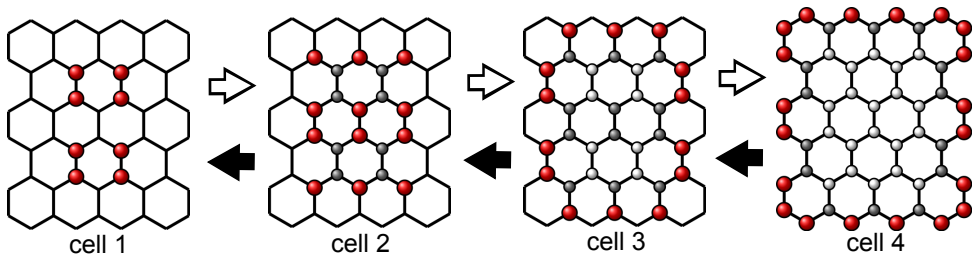

Figure 2.11: The partitioning of a small graphene sample where all sites of interest are located in cell 1. Cell 2 contains all the sites coupling to cell 1 but which are not themselves part of cell 1. Likewise cell 3 is the sites coupling to cell 2 and so on. The red sites are assigned to the current cell and the lines indicate the sites still to be assigned. The previous cell and all sites already added are indicated by gray and white, respectively. The recursive sweep starting at the final cell and ending in cell 1, indicated by filled arrows, gives the GFs connecting all sites of interest. We can also employ a second recursive sweep, as indicated by the white arrows, to obtain local properties everywhere within the device region.

Including the boundary self-energy

The method described above is a general way to obtain a tridiagonal matrix and we now return to the specific case where the recursive method needs to be adapted carefully to take the boundary self energy into account. In general $\mathbf{\Sigma}_B$ is a non-hermitian dense matrix connecting all edge sites of the device region. Therefore it is essential to assign all edge sites to the same cell. This principle is shown in Fig. 2.12. If cell $n-1$ contains sites which connect to an edge site, then cell n must contain not only the edge sites directly connecting to cell $n-1$, but also all other edge sites, as these are connected to each other via $\mathbf{\Sigma}_B$. In this way, the cell, $n+1$, must then contain all the sites connecting to cell n, *i.e.* also connecting to the edge, but not included in cell n. The full cell partitioning algorithm, including this step is summarized in the box below.

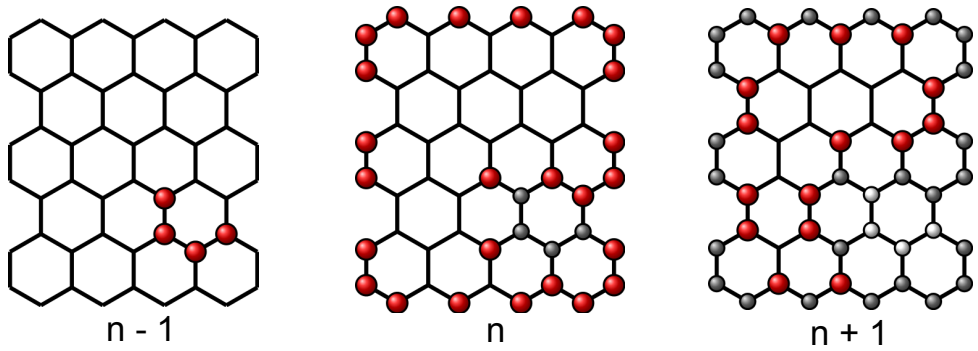

Figure 2.12: An example of the partitioning when the cell $n-1$ is connected to the edge, and we need to include the boundary self-energy, $\mathbf{\Sigma}_B$. In this case, all edge sites and self energy terms are included in cell n. The symbols are similar to Fig. 2.11.

General tridiagonalizing algorithm

Starting from cell $n = 1$ containing all sites of interest

1: Let $\{n\}$ denote all sites in cell n and $\{$"*unassigned*"$\}$ denote all sites not yet assigned to a cell.

2: Find all sites j for which $H_{nj} \neq 0$ where $n \in \{n\}$ and $j \in \{$"*unassigned*"$\}$. Denote these sites $\{n+1\}$.

2a: If $\{n+1\}$ contains an edge site, then all remaining edge sites are added to $\{n+1\}$.

3: Sites in $\{n+1\}$ are removed from $\{$"*unassigned*"$\}$

4: Repeat 1-3 until all sites are assigned to a cell.

Step 2a is included if we require an edge self energy term Σ_B.

Recursive calculation

After performing the tridiagonalization the Hamiltonian is now blocktridiagonal

$$\boldsymbol{H}_{D,D} = \begin{pmatrix} \boldsymbol{H}_{1,1} & \boldsymbol{V}_{1,2} & 0 & 0 & \\ \boldsymbol{V}_{2,1} & \boldsymbol{H}_{2,2} & \boldsymbol{V}_{2,n} & 0 & 0 \\ 0 & \boldsymbol{V}_{n,2} & \boldsymbol{H}_{n,n} & \boldsymbol{V}_{n,N-1} & \\ 0 & 0 & \boldsymbol{V}_{N-1,n} & \boldsymbol{H}_{N-1,N-1} & \boldsymbol{V}_{N-1,N} \\ 0 & 0 & 0 & \boldsymbol{V}_{N,N-1} & \boldsymbol{H}_{N,N} \end{pmatrix}, \tag{2.53}$$

where $\boldsymbol{H}_{n,n}$ is the Hamiltonian of the n-the cell and $\boldsymbol{V}_{n,n-1}$ is the coupling between cell n and $n-1$.

The form Eq. (2.53) enables a variation of the standard recursive algorithm [77] to calculate the GF of the different blocks. The recursive sweep to obtain the full GF of cell $n = 1$ is schematically shown in Fig. 2.13 where each block illustrates a block-matrix. Starting from the block belonging to cell $n = N$, we obtain the *full* GF for cell $n = 1$ (illustrated by dark gray). The light gray denotes blocks where a preliminary GF have been calculated. These GF blocks are used below to calculate all (off)diagonal GF blocks.

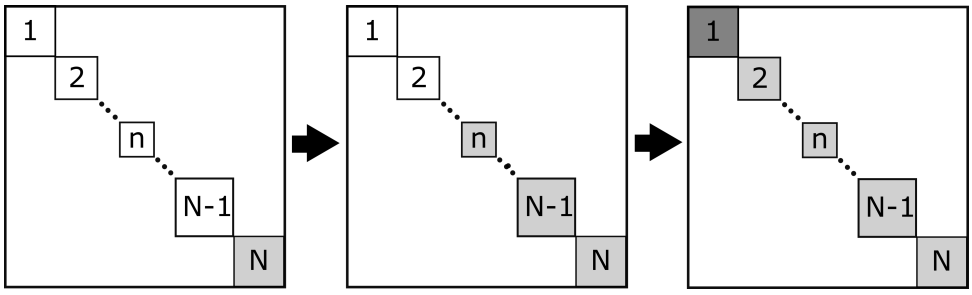

Figure 2.13: Recursive sweep going from cell $n = N$ to $n = 1$. Light gray indicate blocks that are stored for the reversed sweep and dark gray indicate blocks of the full GF.

Algorithm 1

First recursive sweep to obtain full GF of cell $n = 1$

$$\boldsymbol{g}_{N,N} = \left(E - \boldsymbol{H}_{N,N}\right)^{-1}, \tag{2.54a}$$

$$\boldsymbol{g}_{n,n} = \left(E - \boldsymbol{H}_{n,n} - \boldsymbol{V}_{n,n+1}\boldsymbol{g}_{n+1,n+1}\boldsymbol{V}_{n+1,n}\right)^{-1}, \tag{2.54b}$$

$$\boldsymbol{g}_{1,1} = \left(E - \boldsymbol{H}_{1,1} - \boldsymbol{V}_{1,2}\boldsymbol{g}_{2,2}\boldsymbol{V}_{2,1} - \sum_{m=1}^{M} \Sigma_{lead}^{m}\right)^{-1}. \tag{2.54c}$$

One of the $\boldsymbol{H}_{n,n}$ terms can include the boundary self energy, Σ_B. If we calculate transmission Σ_{lead}^{m} terms are included.

After the first sweep is complete, the fully connected GF of cell $n = 1$ is obtained as $\boldsymbol{G}_{1,1} = \boldsymbol{g}_{1,1}$. As all sites of interest are placed in this cell, we can now calculate observables involving these sites. For example we calculate transmission, $\mathcal{T}_{L,L'}$, between lead L and L' using these GFs.

$$\mathcal{T}_{L,L'}(E) = \mathrm{Tr}\big[\boldsymbol{G}_{L',L}\boldsymbol{\Gamma}^{L}_{L,L}\boldsymbol{G}^{\dagger}_{L,L'}\boldsymbol{\Gamma}^{L'}_{L',L'}\big], \tag{2.55}$$

where $\Gamma^{L} = \mathrm{i}(\Sigma^{L} - \Sigma^{L\dagger})$ and $\boldsymbol{G}_{L,L'}$ ($\boldsymbol{G}^{\dagger}_{L,L'}$) is the retarded (advanced) GF connecting the two leads L and L'. It is noted that the choice of sites in cell $n = 1$ is flexible and can be modified to a variety of calculation purposes *i.e.* not only transmission calculations.

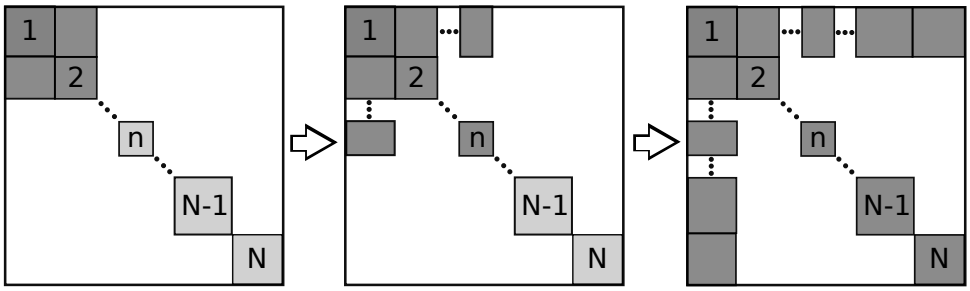

Figure 2.14: Reversed recursive sweep going from $n = 1$ to $n = N$ showing how this sweep can obtain both diagonal and off-diagonal blocks.

In order to obtain other blocks of the full GF, we need to *store* the preliminary GF matrices, $\boldsymbol{g}_{n,n}$, for each cell as we do the initial sweep from $n = N$ to $n = 1$. The stored blocks are shown in light gray on Fig. 2.13. We can use these stored blocks from the first sweep to obtain the diagonal blocks of the full GF, $\boldsymbol{G}_{n,n}$, using a reversed sweep from $n = 1$ to $n = N$, see Fig. 2.14. From these full diagonal blocks we can calculate the local density of states (LDOS) at a site i as $\rho_{ii} = -\mathrm{Im}\big(G_{ii}\big)/\pi$.

Algorithm 2

Algorithm for obtaining all full diagonal blocks

$$\boldsymbol{G}_{n,n} = \boldsymbol{g}_{n,n} + \boldsymbol{g}_{n,n}\boldsymbol{V}_{n,n-1}\boldsymbol{G}_{n-1,n-1}\boldsymbol{V}_{n-1,n}\boldsymbol{g}_{n,n}. \tag{2.56}$$

Finally, we want to obtain bond currents for the state leaving a lead L. This can be calculated by $J^{L}_{ij} = -H_{ij}\mathrm{Im}\big[\boldsymbol{G}_{i,1}\boldsymbol{\Gamma}^{L}_{1,1}\boldsymbol{G}^{\dagger}_{1,j}\big]/\hbar$. Remembering that the leads are assigned to cell $n = 1$, we need the off-diagonal blocks, $\boldsymbol{G}_{1,n}$ and $\boldsymbol{G}_{n,1}$, in order to obtain bond currents. Again we use the stored blocks from the first sweep to calculate the needed off-diagonals.

Algorithm 3

Algorithm for obtaining full off-diagonal blocks

$$\boldsymbol{G}_{1,n} = \boldsymbol{G}_{1,n-1}\boldsymbol{V}_{n-1,n}\boldsymbol{g}_{n,n}, \tag{2.57a}$$

$$\boldsymbol{G}_{n,1} = \boldsymbol{g}_{n,n}\boldsymbol{V}_{n,n-1}\boldsymbol{G}_{n-1,n}. \tag{2.57b}$$

We emphasize that the presented method is not unique to graphene systems, but can be employed to arbitrary tight-binding-like models. The method offers increased flexibility compared to the standard left-right recursive approach, [77] but keeps the operation count scaling $N_{\text{cell}} \times M^3$, where N_{cell} is the number of cells and M is the number of sites in each cell. We note that the cell size fluctuation is greater within the adaptive approach, so that the total operation count will also be higher by a factor dependent on the device aspect ratio and circumference. However, the larger number of matrix elements returned allow the system to be connected to multiple probes or as a patch in an extended system - options not available using a standard recursive sweep. The use of multiple patches within our framework, as illustrated in Fig. 2.8, can also significantly reduce the percentage of the system that needs to be built recursively. This removes the need for computationally expensive buffer zones, or k-space averaging techniques, that standard recursive GF techniques would require in attempting calculations of similar systems.

2.3.4 Summary of method 2

Patched Green's function (PGF) method

The patched Green's function approach treats device patches embedded within an extended two dimensional region. The extended part of the system is treated through a self-energy Σ_B entering the device area.

$$\boldsymbol{G}^{(\mathrm{con})}_{D,D} = \left(E\mathbf{1} - \boldsymbol{H}_{D,D} - \boldsymbol{\Sigma}_B\right)^{-1}, \tag{2.58}$$

The Hamiltonian for the device region can be tridiagonalized allowing for multiple probes to be placed at arbitrary positions. Using the tridiagonalized Hamiltonian, we treat the GF of the device region, $\boldsymbol{G}^{(\mathrm{con})}_{D,D}$, using an adaptive recursive method enabling calculation of local properties like LDOS and bond currents within large regions of an extended system.

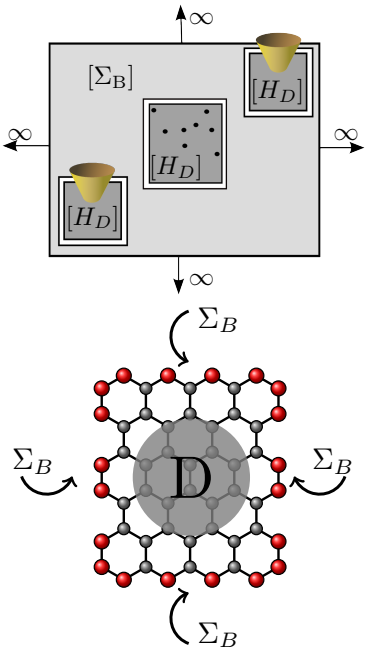

Boundary self-energy

The boundary is calculated as

$$\boldsymbol{\Sigma}_B = \boldsymbol{V}_{D,B}\boldsymbol{G}^{(\mathrm{dis})}_{B,B}\boldsymbol{V}_{B,D}. \tag{2.59a}$$

$$\boldsymbol{G}^{(\mathrm{dis})}_{B,B} = \left(\mathbf{1} + \boldsymbol{G}^{(0)}_{B,D}\boldsymbol{V}_{D,B}\right)^{-1}\boldsymbol{G}^{(0)}_{B,B}. \tag{2.59b}$$

For graphene we calculate $\boldsymbol{G}^{(0)}_{B,B}$ and $\boldsymbol{G}^{(0)}_{B,D}$ using

$$G^0_{ij}(z) = \frac{1}{\Omega_{BZ}}\int \mathrm{d}^2\boldsymbol{k}\frac{N_{ij}(z,\boldsymbol{k})\mathrm{e}^{\mathrm{i}\boldsymbol{k}\cdot(\boldsymbol{r}_j-\boldsymbol{r}_i)}}{z^2 - t^2|f(\boldsymbol{k})|^2}. \tag{2.60}$$

This integral can be treated through complex contour methods as describe in Section 2.2.

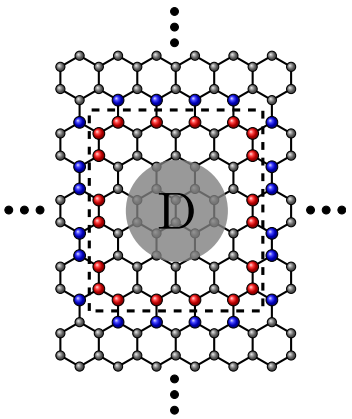

2.4 Probe model

We now return to the model of the probes and particularly the form of the lead self-energy. We assume that all probes are identical and generally described by a self-energy term of the form

$$\Sigma_{ij}^{1/2}(E) = \boldsymbol{V}_{is}^{1/2} g^s(E, \boldsymbol{r}_i - \boldsymbol{r}_j) \boldsymbol{V}_{sj}^{1/2}, \tag{2.61}$$

where $g^s(E, r)$ is a surface GF describing the electronic structure of the probe and $\boldsymbol{V}_{is}^{1/2}$ is the coupling matrix between the device site i and the probe. We note that if $\boldsymbol{V}^{1/2}$ is a scalar, the probe only couples to a single site in the device. We consider a structureless probe by using the surface GF of a single atomic chain

$$g^s(E) = \frac{E \pm \sqrt{E^2 - 4\gamma^2}}{2\gamma^2}. \tag{2.62}$$

where we chose the parameter $\gamma = |t|$ to give a constant DOS within the considered energy range.

The distance dependence of $g^s(\boldsymbol{r}_i - \boldsymbol{r}_j)$ in Eq. (2.61) is added by hand to avoid any unphysical coupling between lattice sites through the probe. We therefore add a $1/|\boldsymbol{r}_i - \boldsymbol{r}_j|$-dependence for the off-diagonal terms, as appropriate for a structureless three-dimensional free electron gas [97]. The distance dependence for the off-diagonal finally gives the GF,

$$g^s(E, \boldsymbol{r}_i - \boldsymbol{r}_j) = \delta_{ij} g^s(E) + (1 - \delta_{ij}) \frac{g^s(E)}{|\boldsymbol{r}_i - \boldsymbol{r}_j|}, \tag{2.63}$$

where $\boldsymbol{r}_i \neq \boldsymbol{r}_j$.

The probe self-energy given by Eq. (2.61) can be used to model general probes coupling to many sites in the sample. We use this model in Chapters 4 and 5 with probes coupling to an area of ~ 1 nm^2. For calculations on the dual-STM setup in Chapter 3 we are in the weak coupling regime outlined below.

Transmission in the weak coupling regime

In the weak coupling (STM) regime, we use the common Tersoff-Hamann approach [98–101] where each site couples to a single orbital at the tip of the probe. In this approach the coupling element becomes dependent of both the distance d_i and the angle θ_i between probe apex and site i.

$$V_{is} = V_0 w_i \mathrm{e}^{-d_i/\lambda} \cos\left(\theta_i\right), \tag{2.64}$$

where V_0 is a scaling factor, $w_i = \mathrm{e}^{-ad_i^2} / \sum_m \mathrm{e}^{-ad_m^2}$ is a normalization factor with parameters $\lambda = 0.85\text{Å}$ and $a = 0.6\text{Å}^{-2}$ chosen in accordance to Refs. [99] and [102].

Inserting this into the expression for the transmission in Eq. (2.39) gives the simple form of the transmission

$$\mathcal{T}_{12}(E) = \left(2\pi V_1 V_2 \rho_{lead}\right)^2 |G_{12}(E)|^2, \tag{2.65}$$

where $\rho_{lead} = -\mathrm{Im}(g_s)/\pi$ is the density of states of the probe which is slowly varying over the considered energy window, hence, the only energy dependence originates from the GF term. We furthermore note that the transmission scales with the couplings $\sim V_1^2 V_2^2$ which depend exponentially on the distance between the tip and the sample.

CHAPTER 3

Dual probe on graphene

The standard single-STM measurement yields direct information of the local density of states, and is a wide-spread method for analyzing nanoscale features on surfaces, including graphene flakes with impurities, vacancies, edges, or deliberate nanostructuring. In comparison, the transmission between two probes yields more information than what can be extracted from a single-STM probe measuring topography or local density of states. In this chapter, we apply the *integral Green's function method* presented in Section 2.2. We study the dual-STM setup for pristine graphene as well as for simple defects like vacancies and adatoms. These simple cases provide a very instructive introduction to the dual probe method and its analysis. In this regard, we first consider analytical calculations made using the SPA approximation for the high symmetry directions. Afterwards, these analytical results are compared to full numerical calculations. To distinguish the different results, we divide the results after the two distinct operation modes of the dual probe setup: scanning and spectroscopy.

- *The scanning mode* operates with one fixed and one movable probe to obtain images of the position dependent conductance between the probes. The results are published in Paper I.
- *The spectroscopy mode* uses fixed probe positions and instead vary the energy of the electrons propagating through the graphene sheet *i.e.* varying a gate. The results are published in Paper II.

3.1 Dual-STM using stationary phase approximation

In this section we consider the dual-STM transmission using the SPA expressions derived in Section 2.2.2. This analytical approximation to the GF along high symmetry directions provides simple analytical expressions showing the energy and distance dependencies of the transmission between the probes in the presence of impurities, see Fig. 3.1. The simple analytical expressions derived in this section will be compared to numerical calculations in the rest of this chapter.

For convenience we repeat the SPA expressions for separations between the i and j sites exceeding a few lattice spacings

$$G^{0,ac}_{ij,\mathrm{SPA}} = \frac{\mathcal{A}(E)\mathrm{e}^{\mathrm{i}\mathcal{Q}(E)d_{ij}}}{\sqrt{d_{ij}}}, \tag{3.1a}$$

$$G^{0,zz}_{ij,\mathrm{SPA}} = \sum_{\eta=\pm} \frac{\mathcal{A}^{\eta}(E)\mathrm{e}^{\mathrm{i}\mathcal{Q}^{\eta}(E)d_{ij}}}{\sqrt{d_{ij}}}, \tag{3.1b}$$

where $\mathcal{A}(E)$ is an energy dependent amplitude and $\mathcal{Q}(E)$ is the Fermi wavevector for armchair or zigzag separations. The coefficients are given in Section 2.2.2.

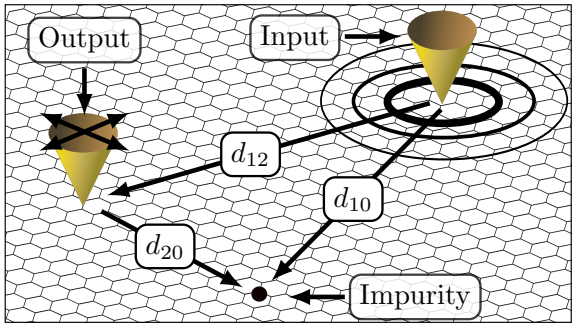

Figure 3.1: Schematic overview of a dual-probe STM setup. Current input and output probes and an impurity on site 0 are indicated together with their relative separations.

Pristine graphene

We first consider the case of pristine graphene without defects. This case is important to understand because any features for pristine graphene are superimposed on when we perturb the pristine system. In addition, the pristine case provide simple explanations for directional features in the dual-STM transmission explored using numerical techniques later in this chapter.

Inserting Eq. (3.1) into the transmission formula

$$\mathcal{T}_{12}(E) = \mathrm{Tr}\big[\boldsymbol{G}(E)\boldsymbol{\Gamma}_1(E)\boldsymbol{G}^{\dagger}(E)\boldsymbol{\Gamma}_2(E)\big], \tag{3.2}$$

gives the distance dependence of the transmission, $\mathcal{T}_{12} \propto 1/d_{12}$ for all directions.

Consider now the case when the separation between the two probes is in the armchair direction. Using Eq. (3.1a), we find that the transmission coefficient increases linearly with energy. This gives a linear increase of $\mathcal{T}^{(ac)} \propto |\mathcal{A}|^2/d_{12}$ with energy as $|\mathcal{A}|^2$ grows linearly with energy for low energies, see Section 2.2.2. On the other hand, $\mathcal{T}^{(ac)} \times d_{12}$ is constant as we change the probe positions.

The zigzag direction is more complicated because of the two terms in Eq. (3.1b),

$$\begin{aligned}\mathcal{T}_{12}^{(zz)} \times d_{12} &\propto \Big|\sum_{\eta=\pm} \mathcal{A}^{\eta} \mathrm{e}^{\mathrm{i}\mathcal{Q}^{\eta} d_{12}}\Big|^2 \\ &= 2|\mathcal{A}^{+}|^2 + 2|\mathcal{A}^{-}|^2 + 2|\mathcal{A}^{+}||\mathcal{A}^{-}|\mathrm{e}^{\mathrm{i}(\mathcal{Q}^{+}-\mathcal{Q}^{-})d_{12}} + 2a^{+}a^{-}\mathrm{e}^{-\mathrm{i}(\mathcal{Q}^{+}-\mathcal{Q}^{-})d_{12}} \\ &= 2|\mathcal{A}^{+}|^2 + 2|\mathcal{A}^{-}|^2 + 4|\mathcal{A}^{+}||\mathcal{A}^{-}|\cos\Big(\big[\mathcal{Q}^{+}-\mathcal{Q}^{-}\big]d_{12}\Big),\end{aligned} \tag{3.3}$$

where we have used the definition $\mathcal{A}^{\eta} = -(1+\mathrm{i})|\mathcal{A}^{\eta}|$ from Eq. (2.46). In addition to the linear increase with energy of the first two terms, we also find an oscillating term. The oscillation period decreases with increasing energy due to the energy dependence of $\mathcal{Q}^{+} - \mathcal{Q}^{-}$. We therefore expect a more rapid oscillation for higher values of the Fermi energy.

The absence of oscillations for the armchair direction compared to the oscillation in Eq. (3.3) is important when exploring directional effects using the dual-STM setup.

Simple impurities

Next we consider defects like vacancies and adatoms. To obtain an analytical treatment in this case let the defects be coupled to a group of sites denoted 0 and the probes coupled to sites denoted 1 and 2.

The GF for a graphene system with a perturbation can be calculated using the Dyson equation. Restating the Dyson equation using the t-matrix formalism

$$\boldsymbol{G}_{12} = \boldsymbol{G}^{0}_{12} + \boldsymbol{G}^{0}_{10}\mathbf{t}_{00}\boldsymbol{G}^{0}_{02}, \tag{3.4}$$

where

$$\mathbf{t}_{00} = \big(\mathbf{1} - \boldsymbol{V}_{00}\boldsymbol{G}^{0}_{00}\big)^{-1}\boldsymbol{V}_{00}. \tag{3.5}$$

Inserting this into Eq. (3.2) we obtain

$$\begin{aligned}\mathcal{T}_{12} &\propto \mathrm{Tr}\big[\big(\boldsymbol{G}_{12} + \boldsymbol{G}_{10}\mathbf{t}_{00}\boldsymbol{G}_{02}\big)\big(\boldsymbol{G}^{\dagger}_{12} + \boldsymbol{G}^{\dagger}_{02}\mathbf{t}^{\dagger}_{00}\boldsymbol{G}^{\dagger}_{10}\big)\big] \\ &= \mathrm{Tr}\Big[\boldsymbol{G}_{12}\boldsymbol{G}^{\dagger}_{12} + \big(\boldsymbol{G}_{10}\mathbf{t}_{00}\boldsymbol{G}_{02}\big)\big(\boldsymbol{G}_{10}\mathbf{t}_{00}\boldsymbol{G}_{02}\big)^{\dagger} \\ &\quad + 2\mathrm{Re}\Big\{(\boldsymbol{G}_{10}\mathbf{t}_{00}\boldsymbol{G}_{02})\boldsymbol{G}^{\dagger}_{12}\Big\}\Big].\end{aligned} \tag{3.6}$$

Eq. (3.6) is generally applicable, but if the probes and the defect couple to single sites all matrices reduce to scalar quantities and enable simple analytic expressions. For example, we use the SPA expression Eq. (3.1a), when both probes and defects are all collinear along the armchair direction, to calculate the change in transmission when a defect is introduced

$$\Delta\mathcal{T}_{12} = \mathcal{T}_{12} - \mathcal{T}^{0}_{12} \propto \frac{4|\mathcal{A}|^4}{d_{10}d_{20}}|t_{00}|^2 - \frac{2|\mathcal{A}|^3}{\sqrt{d_{10}d_{20}d_{12}}}\mathrm{Re}\Big\{(1+\mathrm{i})t_{00}\mathrm{e}^{\mathrm{i}\mathcal{Q}(d_{10}+d_{20}-d_{12})}\Big\}, \tag{3.7}$$

where $\mathcal{T}_{12}^0$ is the pristine transmission, d_{12} denotes the distance between the two probes, and d_{10} and d_{20} denote the distance between the defect site and probe 1 and 2, respectively.

A change in transmission occurs due to the backscattering at the defect. The size and form of $\Delta\mathcal{T}_{12}$ depend on the type of defect through t_{00}. Below we use Eq. (3.7) to consider two different situations: the case where the defect is in between the probes (case 1) and the case where the defect is *not* in between the probes (case 2).

Case 1: $\Delta\mathcal{T}^{(ac)}$ using SPA for $d_{12} = d_{10} + d_{20}$

Defect lies between the probes, *i.e.* $d_{12} = d_{10}+d_{20}$

$$\Delta\mathcal{T}_{12} \propto \frac{4|\mathcal{A}|^4}{d_{10}d_{20}}|t_{00}|^2 - \frac{2|\mathcal{A}|^3}{d_{20}\sqrt{d_{10}\left(1+\frac{d_{10}}{d_{20}}\right)}}\mathrm{Re}\Big\{(1+\mathrm{i})t_{00}\Big\}. \quad (3.8)$$

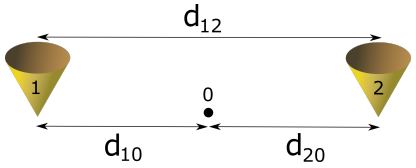

Case 2: $\Delta\mathcal{T}^{(ac)}$ using SPA for $d_{10} = d_{12} + d_{20}$

Defect on either side of the probes, *i.e.* $d_{10} = d_{12} + d_{20}$

$$\Delta\mathcal{T}_{12} \propto \frac{4|\mathcal{A}|^4}{d_{10}d_{20}}|t_{00}|^2 - \frac{2|\mathcal{A}|^3}{d_{20}\sqrt{d_{10}\left(\frac{d_{10}}{d_{20}}-1\right)}}\mathrm{Re}\Big\{(1+\mathrm{i})t_{00}\mathrm{e}^{2\mathrm{i}\mathcal{Q}d_{20}}\Big\}. \quad (3.9)$$

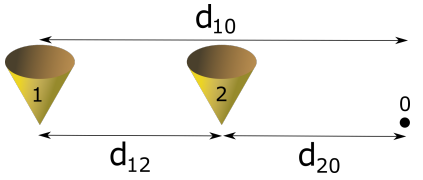

The result for the impurity on the other side of the probes ($d_{20} = d_{12} + d_{10}$) is obtained by interchanging 1 and 2.

The case described by Eq. (3.8) does not give rise to oscillations but resonances can occur depending on the transfer matrix t_{00}. On the other hand, the case in Eq. (3.9) gives rise to oscillations as we change either the energy by changing $\mathcal{Q}$ or the position by changing d_{20}. These oscillations are a consequence of quantum interference between the outgoing wave from the output probe and the wave scattered by the defect. Similar expressions as Eqs. (3.8) and (3.9) can be derived for the zigzag separation, but the simple form is complicated by the two interfering terms in Eq. (3.1b).

The behavior demonstrated in Eqs. (3.8) and (3.9) will be confirmed by numerical calculations performed in the remainder of this chapter. First, we vary d_{20} for a fixed energy and observe the $2Q$-oscillations from Eq. (3.9) by moving the output probe relative to the different defects in a so-called *scanning mode*. Secondly, we vary the energy in a *spectroscopy mode* where both probes are fixed.

3.2 Scanning mode

In this section we treat the setup shown in the schematic Fig. 3.2 exploring effects beyond the high symmetry directions. The input probe is fixed in position and we collect the propagating electron wave at the output probe. In this way, we scan the sample using the movable probe, calculating the transmission between the two STM probes at each position using the method based on the integral formulation for the Green's function, "*Integral Green's function method*", outlined in Chapter 2. This yields real space conductance maps, which form the main results of this section and also confirms the behavior predicted by the analytical SPA expressions derived previously. We use the real-space conductance maps to explore quantum interference effects near defects and edges in graphene as published in Paper I [103]. Fourier transforms of the real-space maps allow us to extract further details, and in particular they reveal information about intra and intervalley scattering due to the defects.

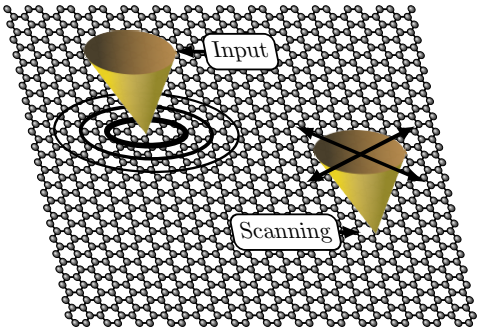

Figure 3.2: Artistic illustration of two STM probes. One probe is fixed and one is scanning across the sample obtaining the conductance between the probes for each position.

3.2.1 Pristine graphene

In Fig. 3.3 we show the real space conductance map for pristine graphene at $E_F = 0.5|t|$. Other Fermi energies show similar qualitative behavior, but lower E_F values require a larger scan area to obtain the same number of oscillation periods. Furthermore, the results are not very sensitive to the exact position of the stationary probe, with the exponential coupling generally ensuring that the probe primarily couples to a single site.

As shown in the previous section the transmission decays monotonically as $1/d_{12}$. Correcting for this geometrical decay yields the constant $\mathcal{T} \times d$ along the armchair directions, while oscillations occur for zigzag directions. The transmission in the zigzag direction was derived previously for strict single-site coupling as $\mathcal{T}_{12}^{(zz)} \times d_{12} \propto \cos\left(\left[\mathcal{Q}^+ - \mathcal{Q}^-\right] d_{12}\right)$. As we change the distance d_{12} between the probes the transmission exhibits oscillations with the wavevector $\mathcal{Q}^+ - \mathcal{Q}^-$. As seen in Fig. 3.3 this leads to both long and short range

oscillations. The long range oscillations depend on the Fermi wavelength as $\mathcal{Q}^+$ and $\mathcal{Q}^-$ represents the opposite sites of the Fermi surface in the zigzag direction.

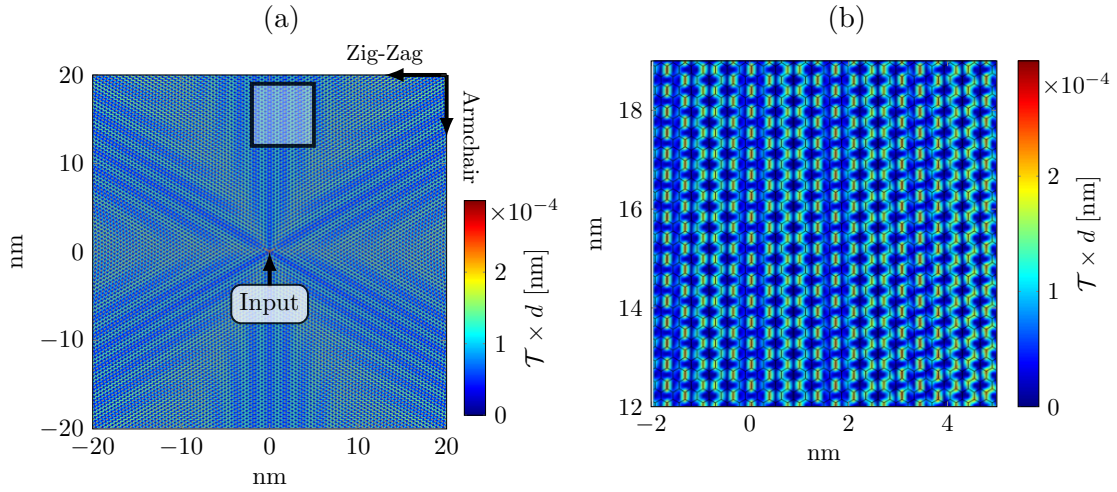

Figure 3.3: (a) The conductance map for pristine graphene with $E_F = 0.5|t|$. The fixed input probe is at the origin, and the map represents the conductance between the probes as a function of scanning probe position. The conductance has been multiplied by the inter-probe distance d_{12} to compensate for a geometric decay, see Eq. (3.1). (b) A magnification of the boxed area showing the short range oscillations.

The short range oscillation, on the other hand, is independent of E_F and inherent to quantities measured along the zigzag direction. In the zigzag direction $\mathcal{Q}^+(E_F) = \cos^{-1}\left(\frac{-t-E_F}{2t}\right)$ and $\mathcal{Q}^-(E_F) = -\cos^{-1}\left(\frac{-t+E_F}{2t}\right)$ can be approximated using the Taylor series expansion $\cos^{-1}(x) \approx \pi/2 - x$ and the interference term written as $\mathcal{Q}^+(E_F) - \mathcal{Q}^-(E_F) \approx= \pi + 1 \approx \frac{4\pi}{3}$. In this way, the transmission along the zigzag direction becomes $\mathcal{T}_{12}^{(zz)} \times d_{12} \approx \cos\left(\frac{4\pi}{3} d_{12}\right)$. Moreover, we notice that $d_{12} = na_0$ is discrete with n being an integer and a_0 being the graphene lattice vector. The cosine sampled at discrete values, $\frac{4\pi}{3}n$, is responsible for the three different type of sites which is evident in Fig. 3.4a. Here we observe that every third point follows the same oscillation curve giving rise to a large scale oscillations pattern caused by the interplay between these curves, see Fig. 3.4b.

These three different oscillation curves are the origin of the small scale oscillations and are a manifestation of the same mechanism observed for graphene nanoribbons with an armchair edge [104], where the transverse modes are along the zigzag direction.

Oscillations varying on the atomic scale tend to get canceled for probes coupling to many sites with different phases. However, the long range oscillations are more robust, particularly for small E_F, as the phase is constant over a wider range of sites and should thus be observable even for tips with a larger radius of curvature.

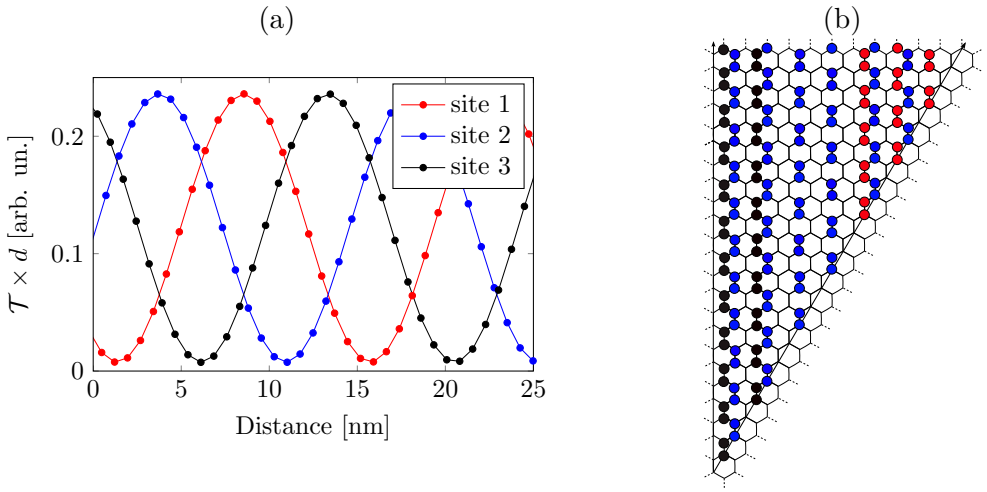

Figure 3.4: (a) The dual STM probe transmission in the zigzag direction separated in three groups of sites such that every third site belongs to the group "site 1". The three groups oscillate with the same large oscillation period determined by $\mathcal{Q}^+ - \mathcal{Q}^-$. (b) The circles represent high transmission values corresponding to the three group of sites from (a). The resulting real space pattern is responsible for the oscillations shown in the numerical calculations in Fig. 3.3.

3.2.2 Vacancies

We now turn to the case of simple vacancies in an otherwise pristine graphene sheet. The GF for a graphene system with a perturbation can be calculated using the Dyson equation as explained in Chapter 2,

$$G_{ij} = G^0_{ij} + \sum_{nm} G^0_{in} V_{nm} G_{mj}, \tag{3.10}$$

where V_{nm} is the perturbation matrix element between site n and m. For a vacancy at site n the perturbation reduces to $V_{nn} \to \infty$ and the solution for the full GF can be conveniently described in the t-matrix formalism as $G_{ij} = G^0_{ij} + G^0_{in} t_{nn} G^0_{nj}$ where $t_{nn} = -1/G^0_{nn}$, see Section 3.1.

Single-STM probe

The single probe STM measurement is a widely used tool to determine the nanoscale electronic properties of surfaces. The typical STM measurement yields information about the local density of states of the surface [37, 45]. STM measurements around a single vacancy have been studied thoroughly using experiments [47, 48, 105, 106] and theoretical calculations [39, 40, 107–109]. We will not provide a detailed discussion of these results. Instead, we give a short introduction to the main result regarding single STM real space scans to ease comparison with the dual probe results.

A standard way to analyze real space STM scans is to make the Fourier transform of the real space image [47, 48, 106]. This gives a representation of the wavevectors of the electrons around the vacancy. In Fig. 3.5 we show a sketch of the Brillouin zone of graphene including constant energy contours for an energy outside the linear regime (within the linear regime the constant energy contours are circular). The final $\boldsymbol{k}$-space map is derived from the Brillouin zone as the result of scattering between different parts of the Brillouin zone. The vacancy causes two types of scattering [12]: intra- and intervalley. Intravalley scattering involves wavevectors from the same valley and the resulting wavevector $\boldsymbol{q}_1 = \boldsymbol{k}_1 - \boldsymbol{k}_2 \sim 2\boldsymbol{q}_F$ is shown in red in Fig. 3.5. Likewise for the intervalley scattering which is between wavevectors from opposite valleys depicted in blue in Fig. 3.5. The resultant $\boldsymbol{k}$-space map revealed by Fourier transforming the real space map, gets the qualitative form shown in the right panel of Fig. 3.5.

Fig. 3.6 shows the result of a simulated STM scan around a vacancy. The numerical calculations use the *Integral Green's Function method* discussed in Chapter 2 with the difference that we only include a single STM probe. In Fig. 3.6 we identify both intra- and intervalley scattering signatures as sketched in Fig. 3.5. The inset A shows the small wavevectors arising from intravalley scattering resulting in $2\boldsymbol{q}_F$ oscillations. The intervalley scattering also causes $2\boldsymbol{q}_F$ oscillations, but by a qualitatively different scattering mechanism as evident from the full Fourier transform.

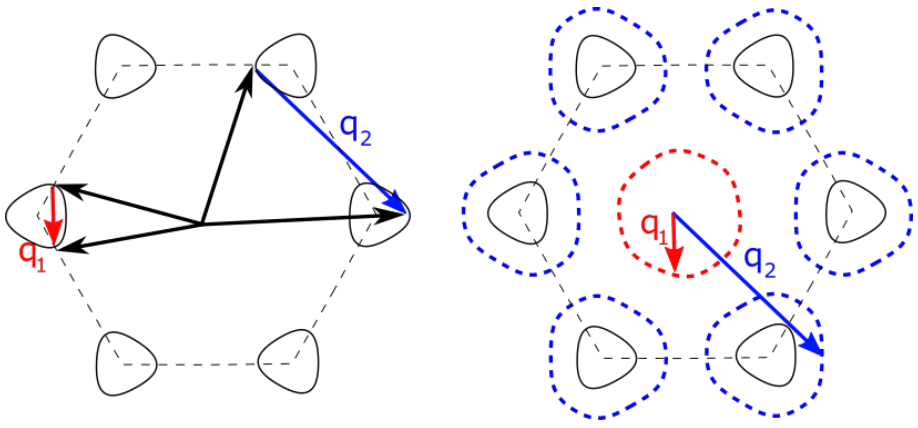

Figure 3.5: (Left) Schematic of the two dimensional Brillouin zone (dashed line). The constant energy contours (full line) are shown at the $\boldsymbol{K}$ and $\boldsymbol{K}'$ points, the energy shown is beyond the linear regime. The two scattering vectors are shown for both intra and intervalley scattering (black). Intravalley scattering vectors $\boldsymbol{q}_1$ (red) connect points on the same energy contour. Intervalley scattering $\boldsymbol{q}_2$ (blue) connects two points on different energy contours. (Right) The resultant Brillouin showing possible scattering processes with red and blue dashed curves corresponding to intra and intervalley processes, respectively. The pristine Brillouin zone from the left panel is show as reference.

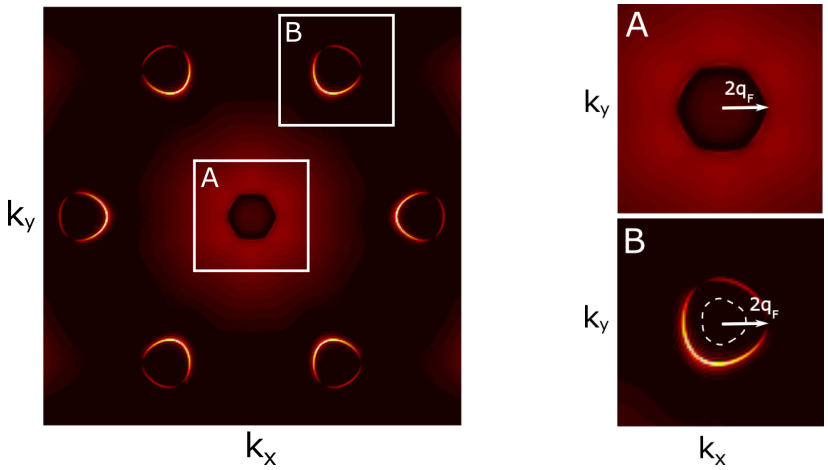

Figure 3.6: The Fourier transform of the calculated real space STM image around a vacancy (not shown). The Fourier transform pattern corresponds qualitatively to the map of scattering amplitudes in Fig. 3.5. The frames A and B correspond to zooms of the intra and intervalley areas of the Brillouin zone, respectively.

Dual-STM probes

We now return to the case of dual-STM probes where the real space maps correspond to the transmission between the two probes when the position of the output probe is varied. Accordingly, such scans yield more information than what can be extracted from LDOS obtained using a single STM probe.

Fig. 3.7 shows the relative change in transmission from the pristine lattice case when a single vacancy is introduced at the origin. The vacancy and fixed probe are separated along the armchair direction and the scanning probe measures conductance fluctuations in the region around the vacancy. Quantum interference effects are clearly visible in Fig. 3.7. The map for a zigzag separation of fixed probe and vacancy (not shown) looks qualitatively similar. To describe the oscillations we turn to the SPA expression derived in Section 3.1. The solution of the Dyson equation for a vacancy is $G_{ij} = g^0_{ij} + g^0_{i0} t_{00} g^0_{0j}$, where $t_{00} = -1/g^0_{00}$ is the t-matrix element of site 0 when $V_{00} \to \infty$. We consider the analytic solutions for the path shown by the dashed line in Fig. 3.7. We observe oscillations in region A, where the scanning probe is between the fixed probe and vacancy such that $d_{12} = d_{10} - d_{20}$. From Eq. (3.9) we find $\Delta\mathcal{T} \propto \mathcal{R}e\left[\mathcal{A}t_{00} \exp\left(2\mathrm{i}\mathcal{Q}d_{20}\right)/\sqrt{d_{10}d_{20}d_{12}}\right]$, which exhibits $2\mathcal{Q} \sim 2q_F$ oscillations. When the scanning probe is not between the fixed probe and the vacancy no oscillations occur and we observe a shadow in region B behind the defect due to scattering (see Eq. (3.8)).

The oscillations arise due to interferences between an incoming plane wave and the backscattered wave, analogous to optical interference effects. To analyze the pattern further, we consider the Fourier transform of the conductance map in the same way as for the single-STM calculations above.

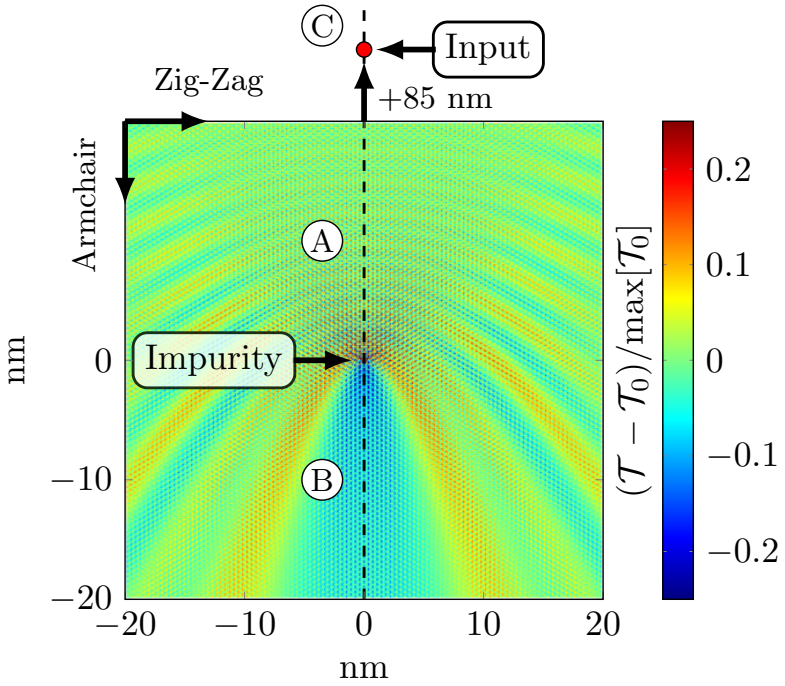

Figure 3.7: Real space map of $\mathcal{T} - \mathcal{T}0$, the difference between the transmission between In and Out probes with (T), and without (T0) the impurity, respectively. The scan is done at $E_F = 0.25|t|$ around a vacancy at $(0, 0)$. The fixed probe (outside the scan area) at $(0, 106)$ nm is separated from the impurity along the armchair direction.

Fig. 3.8 shows the Fourier transform of $\Delta\mathcal{T}$ for the single vacancy at different energies and positions of the fixed probe relative to a vacancy at the origin, with Panel (a) corresponding to Fig. 3.7. We notice a distinct double-ring feature arising from the interference fringes. The double-ring can be explained by considering backscattering of a plane wave. An incoming plane wave along the y direction is $\boldsymbol{k}_{in} = \pm\boldsymbol{e}_y$ where $\boldsymbol{e}_y$ is a unit vector in the y-direction. The wave is scattered at an angle θ, $\boldsymbol{k}_{sc} = \cos(\theta)\boldsymbol{e}_y + \sin(\theta)\boldsymbol{e}_x$. The interference between $\boldsymbol{k}_{in}$ and $\boldsymbol{k}_{sc}$ causes fringes parallel to $\boldsymbol{k}_{in} - \boldsymbol{k}_{sc}$ which makes an angle $\phi = \tan^{-1}\big[-\sin(\theta)/\big(\pm 1 - \cos(\theta)\big)\big]$ with the y-axis. Allowing all possible values of θ results in two circles with diameters of $2k_f$ centered on the y axis. Consequently, the ring shaped features are an image of $2k_f e^{i\phi}$ in the complex plane, for all possible values of ϕ and with the amplitude of double the Fermi wavevector.

Following the scattering analyzes, an incoming wave along the y-direction (armchair) gives the double-ring pattern in Fig. 3.8a. A plane wave along the y-direction only has a components of the wavevector along k_y direction, $\boldsymbol{k} = (0, k_y)$. This means that the inital state before scattering is at the top and bottom of the Fermi surface, indicated by red dots in Figs. 3.8f and 3.8g. Scattering from these points to all other points on either the same valley (intravalley, Fig. 3.8f) or the opposite valley (intervalley, Fig. 3.8g) gives rise to the scattering pattern shown at the bottom of Figs. 3.8f and 3.8g. The intravalley scattering

produces the short wavevector features at the center of the Fourier transform (and at all reciprocal lattice vectors), while the intervalley scattering yields the large wavevector features at the $\boldsymbol{K}$ and $\boldsymbol{K}'$-points. Figs. 3.8a and 3.8b correspond to an energy in the linear dispersion regime whereas 3.8c and 3.8d show an energy with trigonal warping, thus leading to the Fourier signatures sketched by the diagrams of Fig. 3.8f-g.

In Fig. 3.8 we see additional fine structure due to deviations from the ideal picture of a plane incoming wave. A broader range of incoming k-vectors increases the part of the Fermi surface which can act as an initial state. This effect is more pronounced for incoming waves along the zigzag direction where even a small broadening of the incoming k-vector allows a larger part of the Fermi surface to act as an initial state. Similar calculations performed for a Gaussian shaped charge distribution, modeling a trapped charge, find that the scattering fingerprint is qualitatively similar to that of the single vacancy. This is in contrast to single-probe LDOS measurements, where the intervalley scattering fingerprint vanishes for extended defects[43, 110].

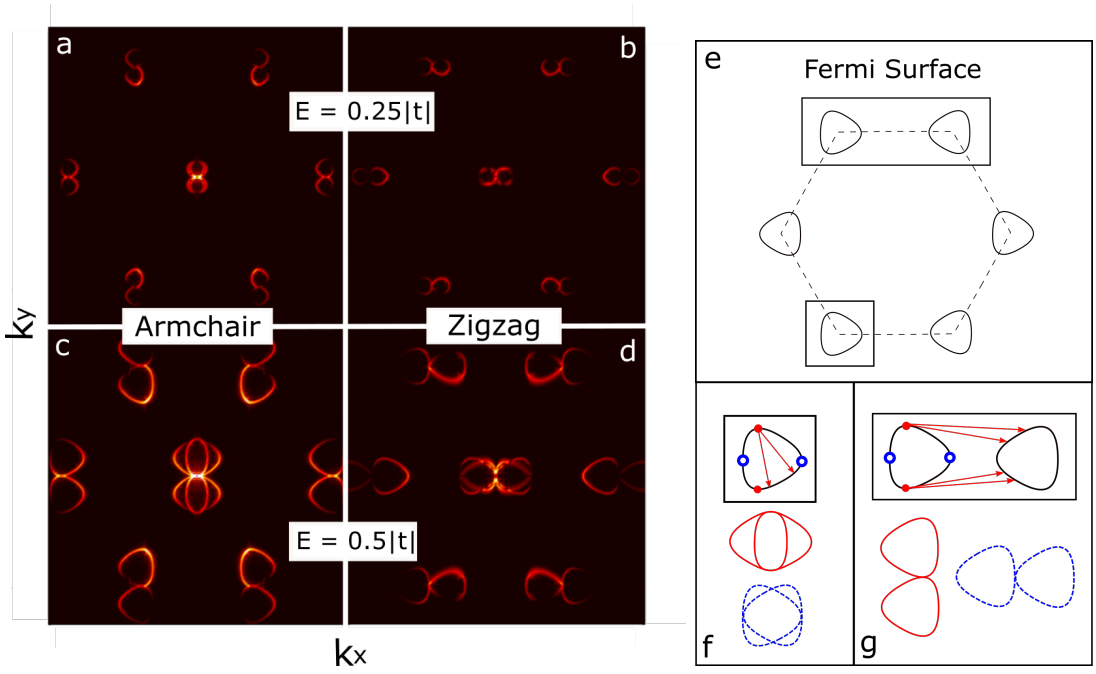

Figure 3.8: Fourier transform of the real-space map of $\Delta\mathcal{T}$ for a single vacancy separated from the fixed probe along the armchair ((a) and (c)), and zigzag ((b) and (d)) directions. Energy is in the linear regime ($E = 0.25|t|$) in (a) and (b), and beyond the linear regime ($E = 0.5|t|$) in (c) and (d). (e) The Fermi surface of graphene beyond the linear regime. (f)-(g) Scattering diagrams for intra- and intervalley scattering.

3.2.3 Crystalline edges

We now turn to the case of crystalline edges. The GF for the semi infinite system with an armchair edge, S^0_{ac}, is calculated from the pristine GF with the method of images, as described in Ref. [111]

$$S^{ac}_{ij}(z) = G^0_{ij}(z) - G^0_{ij'}(z), \tag{3.11}$$

where G^0 is the GF for the pristine infinite system and the site j' is the image of the original site j around the mirror axis along the armchair edge. G^0 is calculated using the complex contour methods discussed in Chapter 2 and S^{ac} takes the place of the full GF used in the Dyson equation and transmission formula. The zigzag edge does not posses the same mirror symmetry and we therefore use a direct inversion scheme to calculate the GF for the semi infinite system containing a zigzag edge.

We briefly present the central result of a single probe STM measurement to ease comparison with the dual probe situation. Fig. 3.9a shows a simulation of an STM measurement near a crystalline armchair edge. It clearly shows localization of the electronic density of states along the C-C bond and parallel to the edge. This results in a characteristic interference pattern, whose shape depends on the edge structure rather than the electron energy. Following the approach from last section, we make the Fourier transform of the real space image. The result for an armchair edge is shown in Fig. 3.9b and for a zigzag edge in Fig. 3.9c. Comparing the result for the armchair and zigzag edge, we notice that the zigzag edge does not give rise to intervalley scattering as also shown by Raman experiments [112]. This arises due to the termination of the different edges. The armchair edge consists of both sublattices and therefore mixes valley whereas the zigzag edge consists of a single sublattice. As a consequence, it does not mix valleys (intervalley scattering). For a thorough discussion of the single STM measurement near crystalline edges see Refs. [113] and [49].

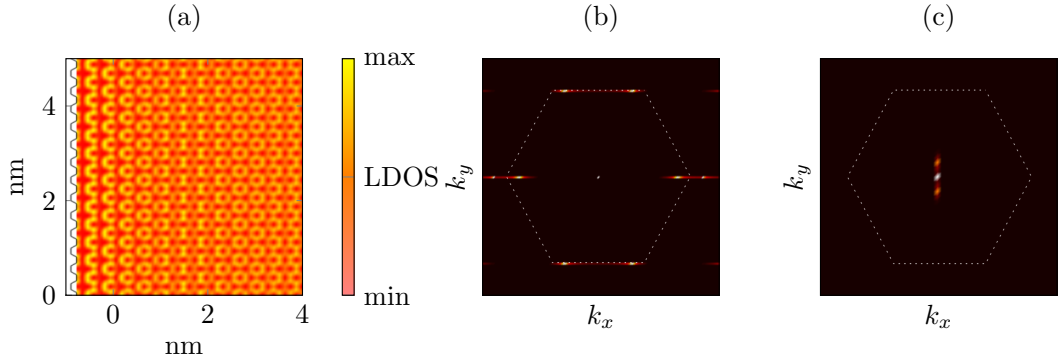

Figure 3.9: (a) Real space STM simulation near a crystaline armchair edge for $E_F = 0.15|t|$. (b-c) Fourier transform of STM simulation near armchair edge (b) and zigzag edge (c) for $E_F = 0.25|t|$. The outline of the first Brillouin zone is indicated in white.

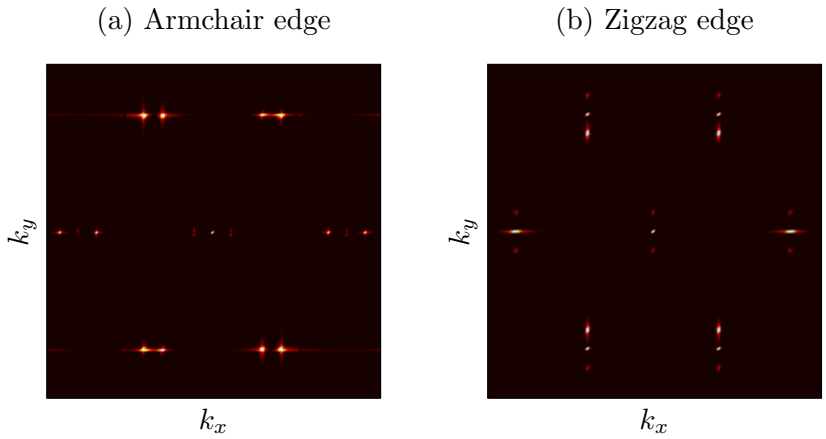

Figure 3.10: (a-b) The Fourier transform for an armchair (a) and zigzag edge (b) for $E_F = 0.25|t|$.

We now turn to the dual-STM setup. The conductance maps (not shown) reveal oscillations away from the edge arising from the interference between incoming and backscattered waves. In contrast to the single vacancy case, not all scattering angles are available due to the symmetries of the edges. In consequence, the double-rings reduce to points indicating the direction of propagation (zigzag for armchair edge and vice versa) as shown in Figs. 3.10a-b. The only qualitative difference is the direction of the incoming wave and hence the direction of the scattering fingerprint in $\boldsymbol{k}$-space. This is in sharp contrast to single-probe STM measurements, where the zigzag edge does not show an intervalley signal, see Fig. 3.9c. The dual-probe setup therefore opens the possibility of characterizing edges by its interference pattern as both edges are equally visible with different signatures.

3.3 Spectroscopy mode

In this section, we consider the setup shown schematically in Fig. 3.11. As opposed to the scanning mode discussed in the previous section, both probes are now fixed and we vary the energy of the propagating electrons. This places us in a situation between the single STM setup and the fixed macroscopic contacts.

The variation of the Fermi energy of the electrons could be obtained using a gate beneath the graphene or setting the potential of the graphene sheet relative to the probes using an additional probe. We still keep the dual-STM setup in the phase coherent regime at low temperature. In this regime, structural details, such as single-site scattering centers, edges, or grain boundaries, limit the conductance, such that quantum interference phenomena become visible in the transmission between the probes as published in Paper II [114]. We calculate the transmission numerically using the "*Integral Green's Function method*" discussed in Chapter 2 and use it to explore the directional effects of pristine graphene as well as the spectroscopic fingerprints of defects like vacancies and adatoms.

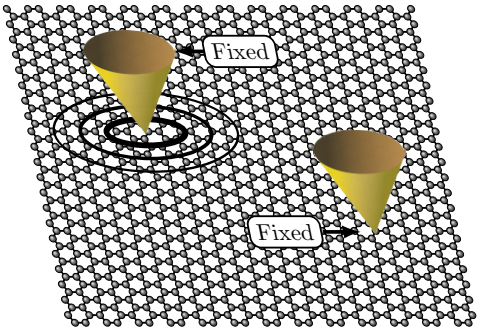

Figure 3.11: Artistic illustration of two STM probes where both probes are fixed in position.

3.3.1 Pristine graphene

In the case of pristine graphene, we again return to the SPA expressions for the transmission as derived in Section 3.1. For armchair separation between the probes, we get the linearly increasing transmission characteristic of graphene, $\mathcal{T}^{(ac)}(E) \propto |\mathcal{A}(E)|^2/d_{12}$, where d_{12} is the constant separation between the probes and $|\mathcal{A}(E)|^2$ grows linearly with energy for low energies, see Fig. 3.12b.

The zigzag direction is more complicated because of the two interfering terms in Eq. (3.3) caused by the two non-identical sides of the Fermi surface along the zigzag

direction. Here we repeat the result for reference

$$\mathcal{T}_{12}^{(zz)}(E) \times d_{12} \propto 2a^{+}(E)^2 + 2a^{-}(E)^2 + 4a^{+}(E)a^{-}(E)\cos\left(\left[\mathcal{Q}^{+}(E) - \mathcal{Q}^{-}(E)\right]d_{12}\right) \tag{3.12}$$

In addition to the linear increase of the first two terms, the last term oscillates with energy due to the energy dependence of $\mathcal{Q}^{+}(E) - \mathcal{Q}^{-}(E)$. The term $\mathcal{Q}^{+} - \mathcal{Q}^{-} \propto E$ if we expand the expressions for $\mathcal{Q}^{\pm}$ in Eq. (2.46) to lowest order. We therefore expect oscillations as a function of energy caused by the cosine term in Eq. (3.12). We clearly observe these oscillations in Fig. 3.12c where we plot the energy dependent transmission for a zigzag separation between the probes of $d_{12} \sim 50$ nm. The transmissions are calculated using both the SPA expressions Eq. (3.1) (dots) and using the Analytical GF method presented in Chapter 2 (line). We note an almost perfect match for all energies, which again confirms the validity of the SPA approach.

In Fig. 3.12d we consider an intermediate direction rotated $\theta \approx 11^{\circ}$ relative to the armchair direction. Consequently the oscillation period depends on the rotation angle θ, as defined in Fig. 3.12a. The oscillation is a consequence of the asymmetry of the Fermi surface in the given direction and is therefore a fingerprint of the crystalline direction between the probes. The GFs for all other separations (except armchair) have the same form as for the zigzag direction [84]. So the transmission generally takes a form qualitatively equivalent to Eq. (3.12) but with different expressions for $\mathcal{Q}^{+}$ and $\mathcal{Q}^{-}$, which depend on the direction of separation. In the limit of low energies we can expand the coefficients as $|\mathcal{A}(E)|^2 \propto E$ and $\left(\mathcal{Q}^{+}(E) - \mathcal{Q}^{-}(E)\right) \propto E^2/\nu(\theta)$. Here $\nu(\theta)$ is an oscillation period that depends on the angle θ defined in Fig. 3.12a. Accordingly $\theta = 0$ denotes armchair separation and $\theta = 30^{\circ}$ denotes zigzag separation between the probes. The energy dependence of the transmission in Eq. (3.12) now becomes

$$\mathcal{T}_{12} \propto E\cos\left(\frac{E^2 d_{12}}{\nu(\theta)} + \phi_{ph}\right), \tag{3.13}$$

where ϕ_{ph} is a phase factor, independent of the direction but dependent on the distance and the exact atoms coupling to the probes. If we plot $\mathcal{T}_{12}/E$ as a function of $d_{12}E^2$ we can determine the period $\nu(\theta)$ as the lowest full period of oscillation in the $\mathcal{T}_{12}/E$ vs $d_{12}E^2$ plot for the corresponding angle θ. In Fig. 3.12e, we plot $\nu(\theta)$ as a function of angle. Fig. 3.12e is the average of many individual calculations of $\nu(\theta)$ for separations ranging from 20 to 100 nm.

From Fig. 3.12e we conclude that $\nu(\theta)$ provides a fingerprint of the probe separation direction. Furthermore $\nu(\theta)$ enables us to determine the crystalline direction with a simple spectroscopic measurement provided we know the distance between the probes and the gate is kept sufficiently small for the expansions of $\mathcal{A}$ and $\mathcal{Q}^{\pm}$ to be valid.

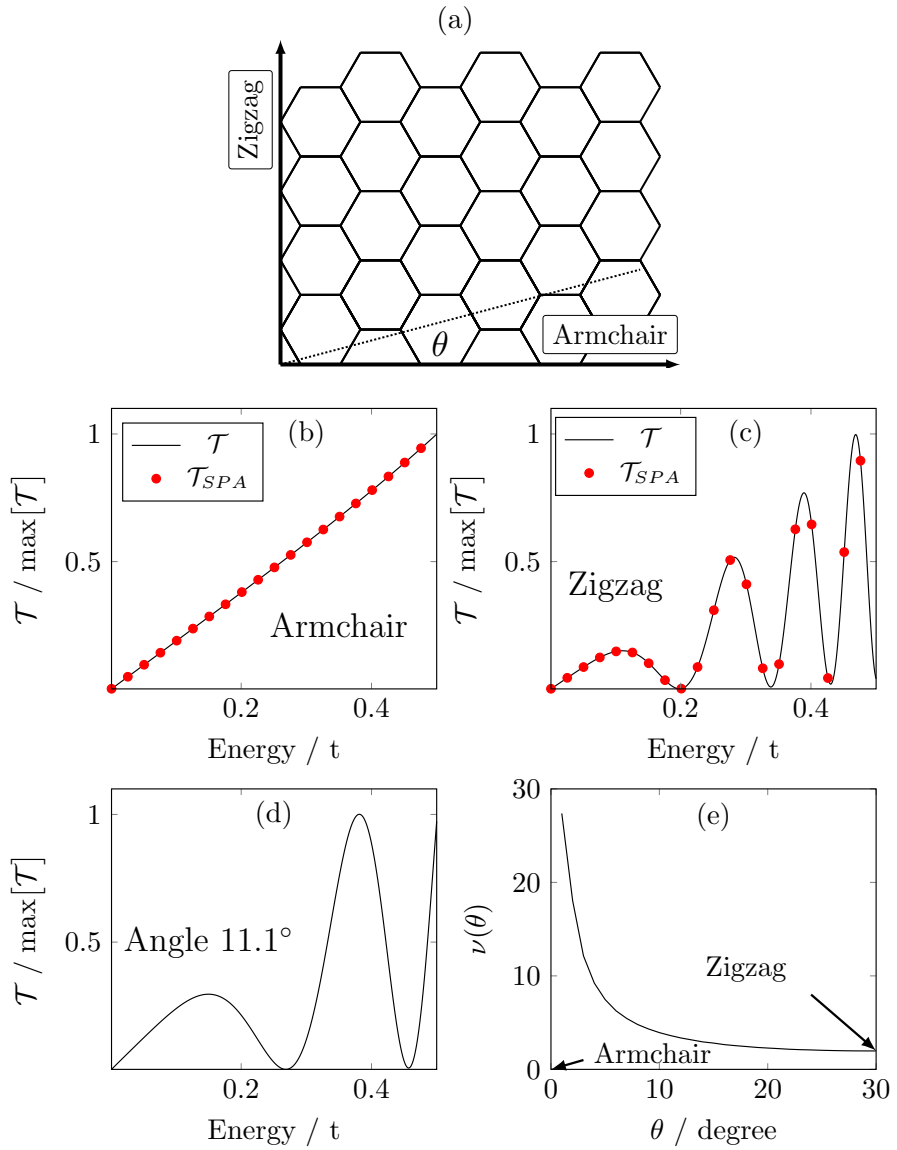

Figure 3.12: (a) Sketch of the pristine sample and the defintion of the rotation angle θ from the armchair direction. (b-d) The transmission as a function of energy between the two leads separated by 50 nm along (b) armchair, (c) zigzag and (d) rotated $\theta = 11.1°$ from the armchair direction. In (b) and (c) the transmission calculated using the SPA is indicated (red dots). (e) The oscillation period $\nu(\theta)$ (see main text for definition) is plotted against rotation angle θ. The curve is constructed by averaging over many individual calculations with distances ranging from 20 to 100 nm.

3.3.2 Simple impurities

Next we consider defects like vacancies and adatoms. In this case we get the full GF from the t-matrix formulation of the Dyson equation $\boldsymbol{G}_{12} = \boldsymbol{G}^0_{12} + \boldsymbol{G}^0_{10}\mathbf{t}_{00}\boldsymbol{G}^0_{02}$, where $\mathbf{t}_{00}$ is the t-matrix for a given type of impurity.

Vacancies are modeled as a change of the onsite energy, $V_{00} \to \infty$. On the other hand, adatoms are modeled with an energy-dependent self energy Σ^α, describing a resonant level with energy ϵ_α, coupled to the graphene sample with coupling constant γ_α, *i.e.* $V_{00} = \Sigma^\alpha_{00} = |\gamma_\alpha|^2/(E + \mathrm{i}0^+ - \epsilon_\alpha)$. To summarize the t-matrices become, [115, 116]

$$\text{Vacancy}: \; t_{00} = \frac{V_{00}}{1 - V_{00}G^0_{00}} \to -\frac{1}{G^0_{00}}. \tag{3.14a}$$

$$\begin{aligned}\text{Adatom}: \; t_{00} &= \frac{\Sigma^\alpha_{00}}{1 - \Sigma^\alpha_{00}G^0_{00}} = \left(\Sigma^{\alpha\,-1}_{00} - G^0_{00}\right)^{-1} \\ &= \frac{|\gamma_\alpha|^2}{E - \epsilon_\alpha - |\gamma_\alpha|^2 G^0_{00}}.\end{aligned} \tag{3.14b}$$

In this way, the adatom gives rise to a resonant level whose position is determined by both ϵ_α and γ_α. We choose parameters from Ref. [117] as $\epsilon_\alpha = -0.185|t|$ and $t_\alpha = 0.37|t|$. This gives a resonant level within the energy interval of consideration.

Fig. 3.13 shows the numerical result compared to the analytical expression derived in Section 3.1, see Eq. (3.8), for both a vacancy and an adatom. The impurities are located equidistant ($d_{10} = d_{20} = d_{12}/2$) from the two probes, where d_{10} (d_{20}) is the distance between probe 1 (2) and the impurity. As for the pristine case treated above, we observe

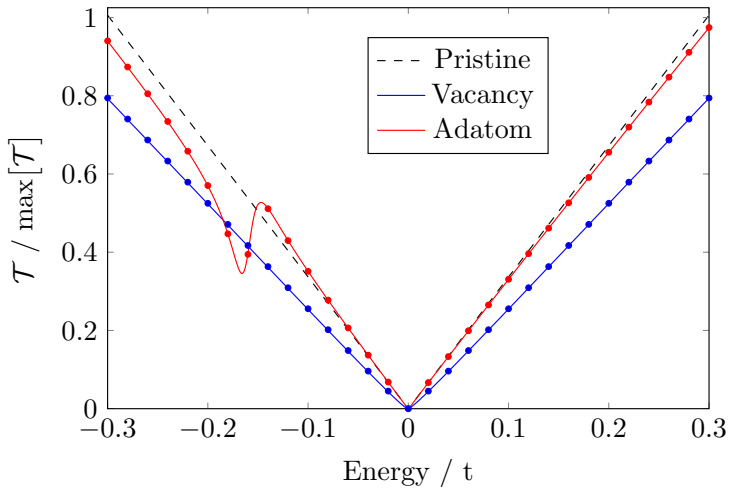

Figure 3.13: The transmission as a function of energy for pristine graphene (dashed), vacancy (red) and adatom (blue). The impurity is in between probes, which are separated by ~ 50 nm along the armchair direction. The dots denote a similar calculation using the SPA expression Eq. (3.8). The parameters for the adatom are chosen as in Ref. [117] as $\epsilon_\alpha = -0.185|t|$ and $t_\alpha = 0.37|t|$.

an almost perfect match between the analytic (symbols) and numerical (lines) results. The vacancy gives rise to an overall reduction in transmission due to scattering, while the adatom leads to a smaller reduction of transmission, except at the resonance. Here the level of the adatom interacts strongly with the continuum of the graphene states giving rise to the asymmetric Fano type resonance [118] observed at approximately −0.15 eV in Fig. 3.13. Similar results are obtained for the zigzag direction, but superimposed onto the characteristic zigzag oscillation discussed in the previous section.

Impurity positions

For the rest of this section we focus on the adatom as the vacancy was studied in detail using the scanning mode presented in Section 3.2. To investigate the influence of adatom position on the resonance, we move the adatom away from the high symmetry point between the probes. First, the adatom is moved along the line connecting the probes such that it is no longer equidistant from the probes. These positions are shown by the red and green squares in Fig. 3.14a. The corresponding dual-probe transmissions are shown in Fig. 3.14b and the change relative to the pristine graphene sheet is shown in

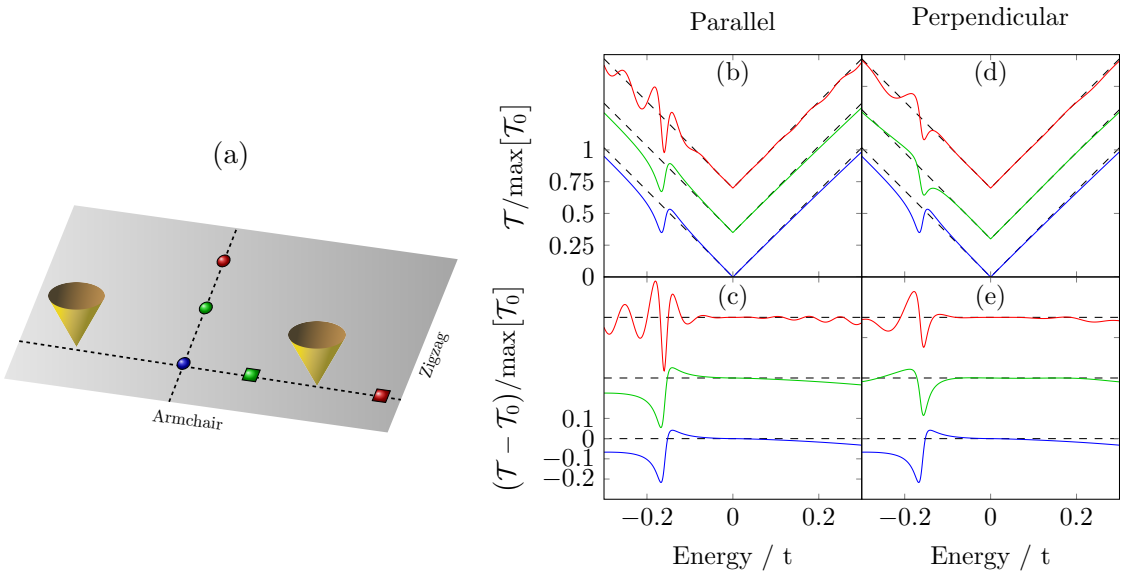

Figure 3.14: (a) Sketch illustrating the two probes separated along the armchair direction by $\sim$ 50 nm. The symbols refer to impurity positions. Blue is along the line of separation and equidistant of the probes. The green and red squares are moved relative to the blue site along the armchair direction (parallel) by 12.8 nm and 34 nm, respectively. The transmission for the parallel translation are shown in (b) and (c). The green and red circles are equidistant of the probes but moved along the zigzag direction (perpendicular) to 7.4 nm and 17.2 nm, respectively. The transmission function for impurities in these positions are shown in (d) and (e). The zero point for the curves has been translated for better distinction between curves.

Fig. 3.14c. Furthermore, both panels include the transmission for the equidistant impurity (blue curve) for comparison. Likewise Figs. 3.14d and 3.14e show the corresponding transmissions as the adatom is moved perpendicular to the line separating the probes while keeping the impurity equidistant to the probes.

First, we consider the parallel case (Figs. 3.14b-c). Here the adatom is either in-between the probes, yet closer to one of them (green square in Fig. 3.14a), or to the far side of one of the probes (red square in Fig. 3.14a). The Fano-type resonance is present for both positions and only the form changes. However, when the impurity does not lie between the probes (red square), additional oscillations arise. This can be understood by comparing Eqs. (3.8) and (3.9) where the difference is the term $\exp\left[2i\mathcal{Q}(E)d_{20}\right]$ introducing interference between the incoming wave from the input probe and the backscattered wave from the impurity. This term gives rise to energy dependent oscillations through the energy dependence of $\mathcal{Q}(E)$. The same type of "additional" oscillations are present for the perpendicular direction and especially for the red circle position (Figs. 3.14d-e). In this case, we have to consider the interference between the emitted wave and the scattered wave returning from the impurity in the direction of the second probe. These oscillations have the same origin as those investigated in real space in Section 3.2 while scanning one probe around the impurity.

Configurational average

In an experimental setup, individual defects or adatoms can be difficult to locate. This makes investigations of many randomly scattered defects important. We fix the two probes with an armchair separation of 50 nm and place adatoms randomly with varying concentration. The averaged transmissions are shown in Fig. 3.15. The transmission is almost unchanged at energies away from the resonance, despite the oscillations caused by individual impurity positions shown in Fig. 3.14. This shows that the oscillations, induced by interference between incoming and scattered waves, tend to average out for many defects. However, the resonance feature survives configurational averaging as is evident from Fig. 3.15. The signal is enhanced on resonance and an overall Fano type resonance is present in Fig. 3.15b with a height that scales with impurity concentration. This suggests that the dual-probe setup can detect the type (position of resonant level) and concentration (peak height) of adatoms on the surface of a graphene sample without the need of scanning the exact position of the impurity as required for a single probe measurement. This is in line with the suggested applications of graphene as a gas sensor [119, 120]. In the case of random vacancies we see an overall decrease in the transmission following the impurity concentration. In this case a zero energy peak is present due to localization effects around vacancies. This feature has been described in several works addressing the LDOS [40, 44, 121].

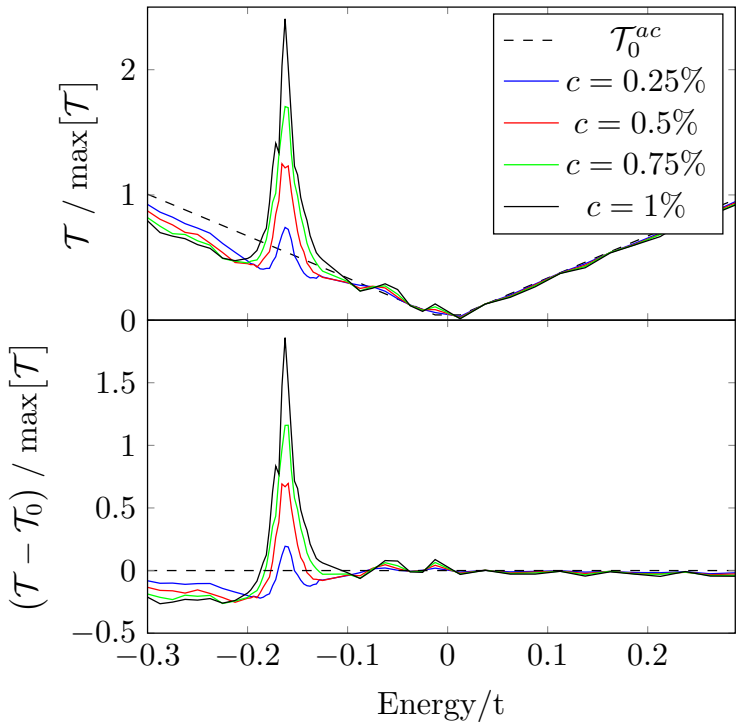

Figure 3.15: (a) Configuration averaged transmission as a function of energy. (b) The difference between the averaged transmission and the pristine transmission. We place impurities in a 50×85 nm rectangle around the probes. The unequal sides are chosen to take into account the probe separation direction. The curves are made from averaging $2 \cdot 10^4$ configurations.

3.4 Summary

Scanning mode

The dual-probe setup in scanning mode offers new flexibility to study directional transport effects in nanosystems beyond the reach for a single STM probe experiment. Using one probe in scanning mode while fixing the other, we are able to compute real space conductance maps using the Analytical GF method presented in Chapter 2.

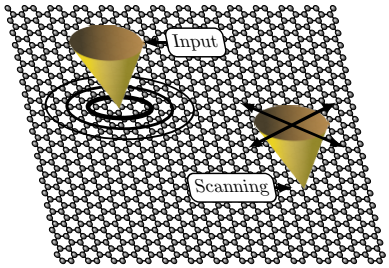

The resulting real space maps show anisotropic behavior depending on the underlying crystal direction and quantum interferences around defects and crystalline edges.

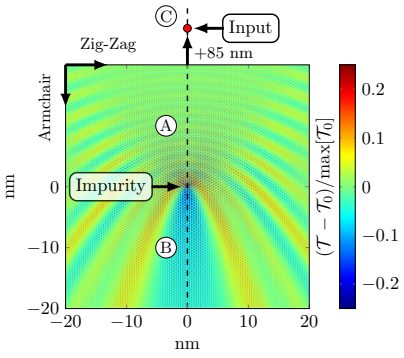

An efficient way of analyzing the real space maps is to perform the Fourier transform, which can be used to extract information of intra- and intervalley scattering processes.

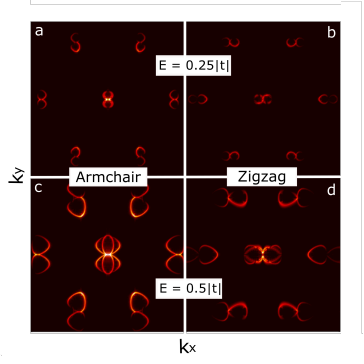

Spectroscopy mode

A dual-STM setup with fixed probes and a probe separation distance in the nanometer range, makes it possible to obtain local transport properties at the nanoscale by varying the electron energy.
This allowed us to study directional transport effects, not directly attainable using macroscopic contacts or single-STM measurements. Furthermore, we considered the spectroscopic fingerprints of local perturbations such as vacancies and adatoms. In particular, we observe Fano-type resonances in the spectroscopic fingerprint arising from resonant states in adatoms. The resonance is shown to be a dominant feature in the dual probe spectroscopy compared to the single probe.

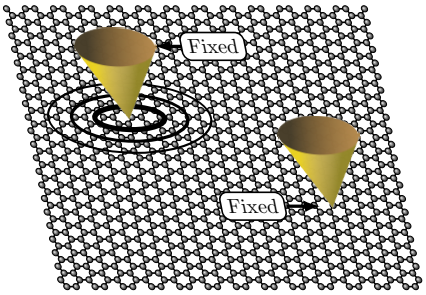

CHAPTER 4

Dual probe investigation of nanostructures in graphene

In the previous chapter, we introduced the two fundamental operation modes of a dual probe setup in the case of simple defects. We now extend the discussion to more complex defects or nanostructures. Many applications require deliberate nanostructuring of the graphene in order to engineer its electronic structure. The *integral Green's Function method* used in the previous chapter is only useful for moderately sized perturbations to the pristine system. However, the *patched Green's function method* (PGF) introduced in Chapter 2 is able to treat sizeable defects while allowing for calculation of local electronic and transport properties. The PGF method enables us to study the effect of individual perturbations within an infinite system without edges or periodic properties.

We first consider the spectroscopic response of a single perforation ("antidot") in an otherwise pristine graphene sheet. These results are published as parts of Paper II and III [87, 114]. Secondly, we consider the situation of local gating. Here we apply a local gate to create a scattering region or "dot" and calculate the effect of an incoming wave emitted from one of the two probes.

4.1 Graphene antidots

In this section, we investigate local transport properties near antidots (*i.e.* perforations) in a graphene sheet [23]. Periodic arrays of antidots have been studied as a way to open a bandgap in graphene [23, 122–124] or to obtain waveguiding effects [24, 125]. Antidots can be fabricated using a variety of experimental techniques like block copolymer [64, 126, 127] or electron beam lithography, [128–130]. Unfortunately, these fabrication processes inevitably lead to disorder and imperfect edges. Several studies show that the electronic structure of an antidot is closely related to the exact edge geometry [114, 122, 125] which may be controllable by heat treatment [129, 131], or selective etching [130, 132].

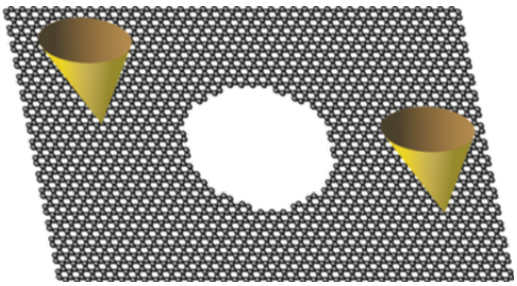

Figure 4.1: Schematic illustration of a dual probe setup around a perforation in a graphene sheet.

Here we consider a single antidot and its effect on the nanoscale current flow in the system. A single graphene antidot has been considered as a nanopore for DNA sensing [133, 134] and recent studies of antidots in a magnetic field have shown the Aharonov-Bohm effect for conducting edge states around single antidot[135]. This makes the single antidot a fundamentally interesting system and not only a building block of periodic arrays. The PGF method allows us to study a single antidot with an experimentally realizable size [120, 126, 134] with no influence from periodic repetition or finite sample effects. In fact, we demonstrate the treatment of experimental structures found from high resolution transmission electron microscope (TEM) images using pattern recognition. [136, 137]

4.1.1 Dual probe spectroscopy

We consider three possible edge geometries for antidots: zigzag, armchair or circular, the last contains an alternating sequence of armchair and zigzag edges, see Fig. 4.2. We calculate the transmission for each antidot type placed between probes separated in the armchair direction (y-direction in Fig. 4.2). The result is shown in Fig. 4.3a. As expected the transmission is generally lowered by the introduction of a perforation. A notable

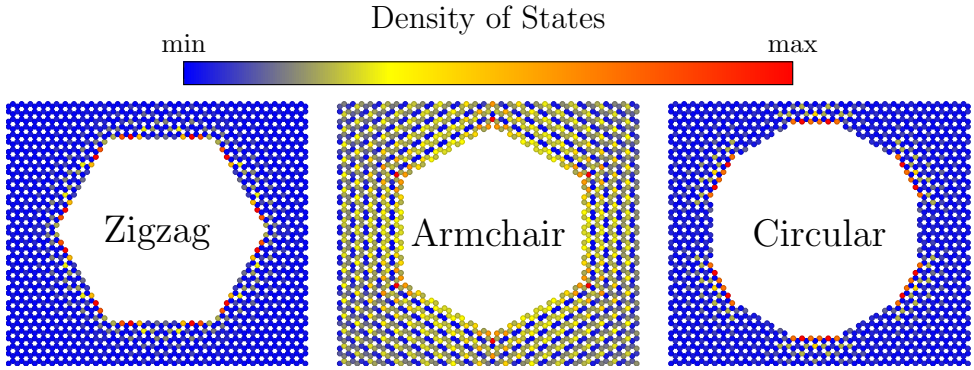

Figure 4.2: The density of states for $E = 0.028|t|$ around antidots with different edge structures as indicated. The maps are individually scaled.

difference between the antidot types is a transmission dip present for the circular, and particularly zigzag, type antidots. This dip resembles the Fano type resonance observed for single adatoms in the previous chapter, see Fig. 3.13. Fig. 4.3a suggests that the resonant feature is connected to the zigzag edges, as the circular antidot consists of a mixture of zigzag and armchair edges. We therefore map the local density of states on sites around the antidot at the energy of the transmission dip (see Fig. 4.2). The DOS is localized around the zigzag edges as known for nanoribbons or antidot lattices [123, 125]. The localized states, being essentially dispersionless, resemble a single level and therefore create a Fano type resonance in the transmission. In addition, we notice a difference between the resonance of the circular and zigzag antidot on Fig. 4.3a. The resonance of the pure zigzag edge has a sharper feature than the mixed edge (circular antidot). This leads to the conclusion that the resonance features can be related to the amount of zigzag edge present. Calculations performed with antidots of varying size (not shown) yield

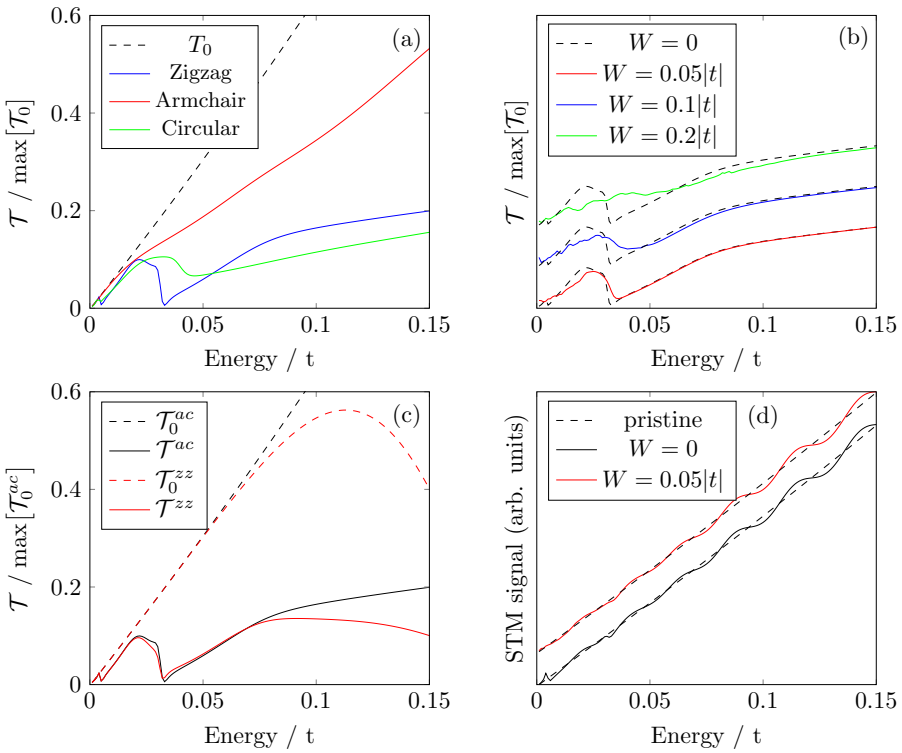

Figure 4.3: (a) The transmission for probes separated along the armchair direction ($\sim$ 50 nm) for zigzag, armchair and circular antidots. The antidot structures are shown in Fig. 4.2. (b) Transmission for the same zigzag antidot as (a) including disorder of varying strength. Each curve is an average of 50 different configurations and have been shifted relatively to each other. (c) The transmission for the same zigzag antidot as (a), with probe separations ($\sim$ 50 nm) along armchair and zigzag direction. (d) Single probe spectroscopy of zigzag antidot with the same probe position as (a). Calculation both with and without disorder is included. The curves have been shifted relatively to each other.

qualitatively the same result, but the position of the dip feature changes depending on the length of the zigzag edge present. This in turn can be used as a fingerprint to determine the edge profile of antidots and other nanostructures.

In Fig. 4.3b the robustness of the signal against edge disorder is investigated. We add a onsite potential, chosen randomly within $[-W, W]$, to the two rows of atoms around the antidot. Fig. 4.3b shows the transmission for different disorder strengths averaged over several configurations. For weak edge disorder the resonance feature persists whereas it vanishes for higher disorder strengths as expected because high disorder tends to destroy the localized edge state giving rise to the resonance in the first place.

Next we consider the separation direction between the probes. The exact direction between the probes should not have a great impact on the spectroscopic fingerprints, if the dual-probe setup is to be a useful tool for characterization of larger nanostructures, such as antidots. Therefore we compare the transmission for both zigzag and armchair probe separations in Fig. 4.3c and note very similar behavior at low energies. We considered several non-symmetric positions (not shown) all exhibiting the resonant feature in the same position.

Finally, we compare the single and dual probe spectroscopy of the zigzag antidot. Fig. 4.3d shows the single probe spectroscopy both without disorder and including a weak disorder. The single probe position is the same as one of the probes in Fig. 4.3a. We notice small oscillations due to the symmetry breaking caused by the presence of the antidot. This is the same kind of Friedel oscillations arising around single vacancies [44]. Without disorder the localized state is barely visible in Fig. 4.3d, but the small resonance vanishes at a disorder strength where it is clearly visible in the dual probe spectroscopy (*cf.* Fig. 4.3b). Consequently the transmission signal from the dual probe setup yields considerably more information about defect induced transport processes than the single probe measurement.

4.1.2 Bond currents

The antidot size considered above is in line with previous work [122, 123, 125]. However, the *patched Green's function* approach presented in Chapter 2 allows for calculation of properties like transmission, LDOS and bond currents for notably larger systems. In this section we investigate the nanoscale current flow around antidots of realizable sizes [120, 126, 134]. We discuss the Fano type resonance observed above for larger antidots an extend the study to antidot geometries found in high resolution transmission electron microscope (TEM) images [136, 137].

First, we consider a zigzag-edged antidot with side length $R = 48a \sim 12$ nm, where $a = \sqrt{3}a_0 = 2.46$ Å. This is comparable to experimental sizes where sub-20-nm feature sizes have been reported [64, 126, 127, 134]. The antidot is in-between two probes placed 200 nm apart, as shown schematically in the inset of Fig. 4.4a. The main panel of Fig. 4.4a shows the transmission as a function of energy for this dual probe setup. We note the

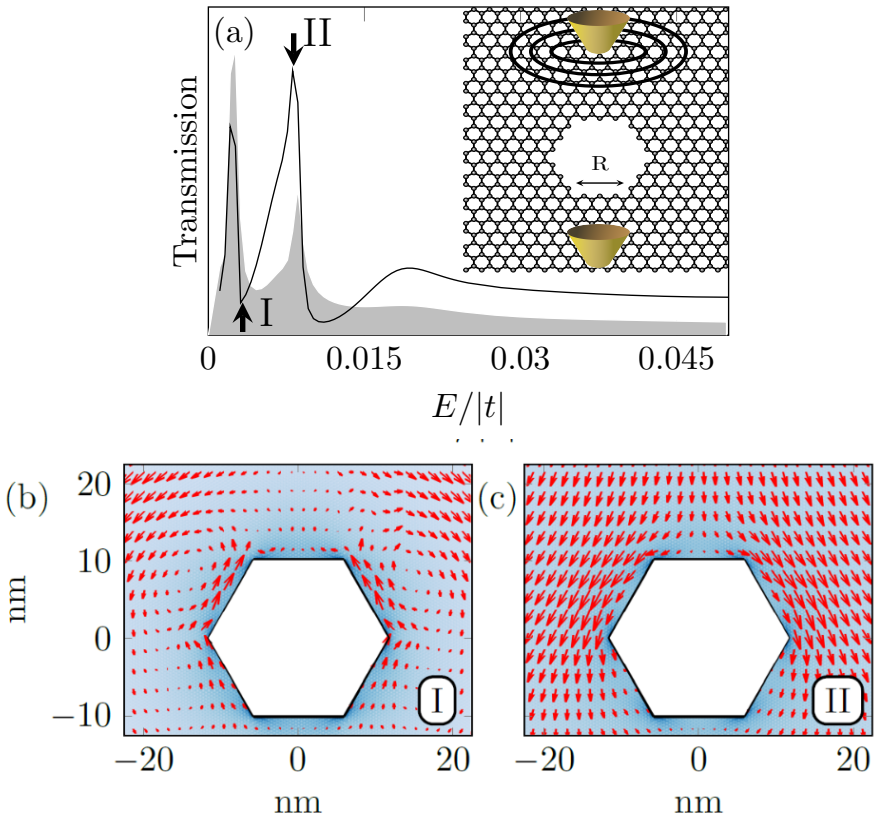

Figure 4.4: (a) The transmission as a function of energy for a dual probe setup with an antidot in between the probes as schematically shown in the inset. The distance between the probes are 200 nm and the antidot with purely zigzag edges has side length $R = 48a_0 \sim 6.8$ nm. The shaded area corresponds to the LDOS around the edge of the antidot. (b-c) The bond currents at the highlighted energies in (a). The size of the arrows corresponds to the magnitude of the bond current.

distinct transmission peaks. As explained above the peaks are related to localized states along the zigzag edges. As a consequence, we notice the correspondence between the peaks in the transmission and the peaks in the LDOS around the edge, see shaded area in Fig. 4.4a. The presence of several peaks is a consequence of the longer zigzag edge segment compared to the antidot used in Fig. 4.3.

Next, we calculate the bond currents from the top lead. The bond currents around the zigzag antidot for the energies indicated in Fig. 4.4a are shown in Figs. 4.4b-c. It is clear that the transmission dips are related to vortex like current paths. These vortex paths create a larger "effective size" of the antidot at this energy which is characterized by a region around the antidot avoided by the current flow. On the other hand, at the transmission peaks when the current passes near to the antidot edge minimizing the backscattering caused by the antidot.

The antidot considered in Fig. 4.4, although of realistic size, is an idealization, as

experimental perforations will inevitably contain imperfections. To consider a more realistic case, we turn to a perforation observed in experimental TEM images. The original TEM image is shown in Fig. 4.5e. Using pattern recognition [136, 137] the positions of the individual carbon atoms can be identified and result in the lattice shown in Fig. 4.5f. We surround the experimentally obtained atomic positions with pristine graphene, see Fig. 4.5a, to allow for calculations using the *patched Green's function* method. The positions of the two probes are indicated in Fig. 4.5a, however, they are separated by 200 nm in the actual calculation to ensure the assumption of a plane incoming wave.

The transmission between the two probes are shown in Fig. 4.5b together with the DOS of the edge atoms in the antidot. Even though the antidot edge is very irregular it still contains zigzag segments. These zigzag segments give rise to localized states as usual, however, since the length of segments vary, the resonance energy of the localized states are different for the different segments. This causes the broadening of the peaks in the density of states as observed in Fig. 4.5b. As a result the Fano-type resonances in the transmission are also significantly broadened. Considering the two energies I and II in Fig. 4.5b corresponding to "dips" in the transmission, we calculate the bond currents and the DOS around the antidot, see Fig. 4.5c-d. The DOS is indicated by the lightblue colormap in Fig. 4.5c-d and we clearly observe a larger DOS at certain segments of the antidot edge for both I and II. Comparing with the spatial bond current maps, we find that the edge segments with high DOS cause vortex patterns qualitatively similar to those observed for the pristine edges, see Fig. 4.4. In turn these vortex patterns are responsible for the additional backscattering causing the transmission dips. In this way, dip I corresponds to a vortex pattern at the left side of the antidot, see Fig. 4.5c, whereas the dip at II is caused by a vortex pattern at the bottom of the antidot, see Fig. 4.5d. The electrons at different energies experience a different effective perforation size and shape caused by these vortices. This type of irregular scattering causes most of the current to flow around the antidot either along the "top" or "bottom" edge of the antidot. If we could control such irregularities, we could imagine controlling the direction of the current flow by designing asymmetric scatterers causing a preferred scattering direction.

The results presented in this section also prove another important development. Instead of experiments trying to replicate idealized theoretical systems, we here demonstrate that high resolution experimental techniques can act as a starting point for theoretical calculations. This potentially allows for a better understanding of the electronic structure and transport properties of nanostructures when theoretical calculations can be made on the exact structures studied experimentally.

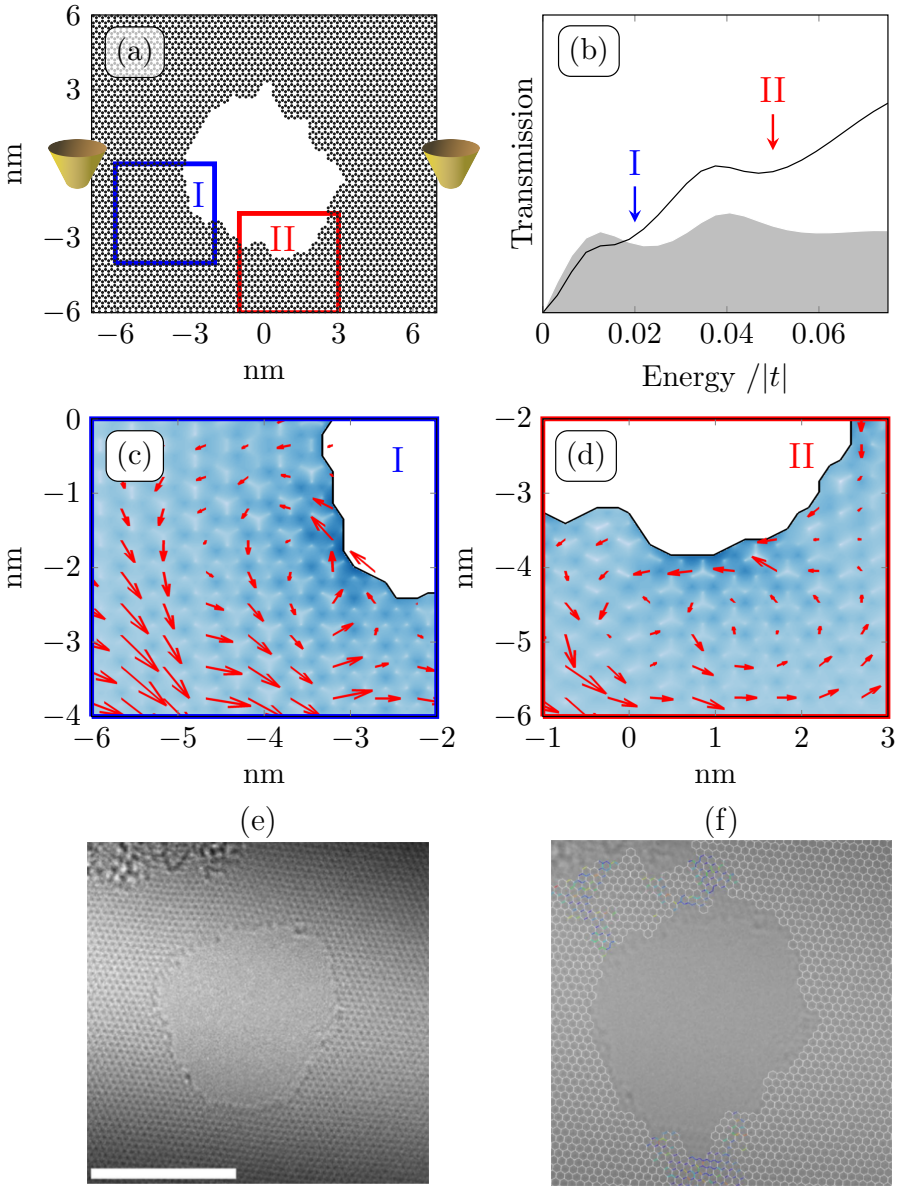

Figure 4.5: An actual perforation is obtained from high resolution TEM images through pattern recognition and we consider the vortex like current paths forming around the perforation at certain energies. (a) Shows the structure of the perforation as well as an indication of the probe position (in the actual calculations the probes are 200 nm apart). The indicated areas correspond to the zooms in (c) and (d). (b) The transmission for the dual probe setup. The shaded area indicates the average LDOS around the edge of the antidot. Furthermore, the energies I and II correspond to the energies used on (c) and (d), respectively. (c-d) Bond current maps taken at the energies I and II, respectively, and at the positions indicated on (a). (e) Actual high resolution TEM image adapted from [137]. The scale bar is 5 nm. (f) The same image as (e) overlayed with graphene lattice constructed using pattern recognition. Note that the graphene lattice has been rotated in (a) to have armchair direction along the y-direction. Picture is adapted from [137].

4.2 Locally gated dots

The antidot studied in the previous section modified the electronic structure by removing part of the graphene sheet. A different route to obtain external control of the properties is to apply external electrical fields. Locally and spatially varying electrical fields provide a unique opportunity to tune the potential landscape by forming p-n junctions. In graphene the linear dispersion making the quasiparticles behave like massless relativistic particles,photons, gives rise to peculiar effects for such p-n junctions. Most notably is perhaps the Klein-tunneling [11] or electron focusing described by a negative refractive index in an optical analogue [21]. The p-n junction takes the role of the intersection between two materials with different refractive index therefore guiding the electrons [138]. Moreover, optical effects like waveguiding have been studied both theoretically [139, 140] and experimentally [25]. The ability to create local gates has also been used to realize the equivalent of optical cavities in ballistic graphene devices [22, 26, 141].

This section focuses on the circular p-n junction which gives rise to effects like caustics [142] or quasi bound states [143–146] affecting the scattering from the gated region. Many of the theoretical predictions use the Dirac approximation which inherently contain the "photon-like" behavior of graphene electrons. Instead, the *patched Green's function method* allows us to study locally gated regions within a tight binding approach, while using the two probes as emitter and collector of electrons. In this way, the dual probe setup combines the ability to study electron waves in an infinite medium (graphene sheet) with the ability to analyze directional effects like preferred scattering directions without the assumptions of the low energy Dirac Hamiltonian. The multiple patches connected through the self-energy allow us to place one probe very far away (+250 nm) from the gated region ensuring that the incoming electron wave closely resembles a plane wave. Furthermore, it allows for an analysis both of the local electronic structure using LDOS maps and the electron scattering using real space bond current maps.

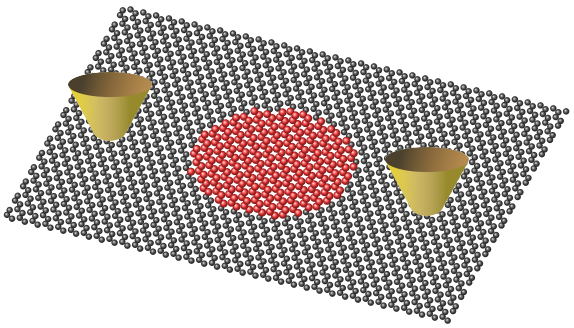

Figure 4.6: Artistic illustration of a dual probe setup around a locally gated region.

4.2.1 Local gate in Dirac approximation

We first consider a circularly gated region within the low energy Dirac approximation. This allows for an analytical solution of the scattering problem which is used in the analysis of the numerical results at the end of this section. We first consider the Dirac model for a circularly gated dot to determine the form of the wavefunctions inside and outside the gated region. Starting from the the Dirac Hamiltonian $\mathcal{H}$ without any perturbation,

$$\mathcal{H} = -\mathrm{i}\hbar v_F \sigma \cdot \boldsymbol{\nabla} = -\mathrm{i}\hbar v_F \begin{pmatrix} 0 & -\mathrm{i}\partial_x - \partial_y \\ -\mathrm{i}\partial_x + \partial_y & 0 \end{pmatrix}, \tag{4.1}$$

we rewrite the problem in polar coordinates (r, θ),

$$\partial_x = \cos(\theta)\partial_r - \frac{1}{r}\sin(\theta)\partial_\theta = \frac{1}{2}\left(\mathrm{e}^{\mathrm{i}\theta} + \mathrm{e}^{-\mathrm{i}\theta}\right)\partial_r - \frac{1}{r}\frac{1}{2\mathrm{i}}\left(\mathrm{e}^{\mathrm{i}\theta} - \mathrm{e}^{-\mathrm{i}\theta}\right)\partial_\theta, \tag{4.2a}$$

$$\partial_y = \sin(\theta)\partial_r + \frac{1}{r}\cos(\theta)\partial_\theta = \frac{1}{2\mathrm{i}}\left(\mathrm{e}^{\mathrm{i}\theta} - \mathrm{e}^{-\mathrm{i}\theta}\right)\partial_r + \frac{1}{r}\frac{1}{2}\left(\mathrm{e}^{\mathrm{i}\theta} + \mathrm{e}^{-\mathrm{i}\theta}\right)\partial_\theta. \tag{4.2b}$$

The derivatives from Eq. (4.1) become

$$-\mathrm{i}\partial_x \pm \partial_y = \mathrm{e}^{\pm\mathrm{i}\theta}\left(-\mathrm{i}\partial_r \pm \frac{1}{r}\partial_\theta\right). \tag{4.3}$$

Finally inserting into the Dirac Hamiltonian while adding the circularly symmetric gating,

$$\mathcal{H} = -\mathrm{i}\hbar v_F \sigma \cdot \boldsymbol{\nabla} + V\Theta(R-r) = \hbar v_F \begin{pmatrix} \tilde{V}\Theta(R-r) & \mathrm{e}^{-\mathrm{i}\theta}(-\mathrm{i}\partial_r - \frac{1}{r}\partial_\theta) \\ \mathrm{e}^{\mathrm{i}\theta}(-\mathrm{i}\partial_r + \frac{1}{r}\partial_\theta) & \tilde{V}\Theta(R-r) \end{pmatrix}, \tag{4.4}$$

where $\Theta(R-r)$ is the Heavyside step function, $\tilde{V} = V/\hbar v_F$ and $\sigma = [\sigma_x, \sigma_y]$ with $\sigma_{x/y}$ being the Pauli spin matrices. Introducing a rotational symmetric ansatz for the spinor

$$|\Psi\rangle = \mathrm{e}^{\mathrm{i}m\theta}\begin{pmatrix} a(r) \\ \mathrm{e}^{\mathrm{i}\theta}\mathrm{i}b(r) \end{pmatrix}, \tag{4.5}$$

we insert into the Dirac equation, $\mathcal{H}|\Psi\rangle = E|\Psi\rangle$

$$1: \quad a(r)\tilde{V}\mathrm{e}^{\mathrm{i}m\theta}\Theta(R-r) + \mathrm{e}^{-\mathrm{i}\theta}\left(-\mathrm{i}\partial_r - \frac{1}{r}\partial_\theta\right)\mathrm{i}b(r)\mathrm{e}^{\mathrm{i}(m+1)\theta} = \frac{E}{\hbar v_F}\mathrm{e}^{\mathrm{i}m\theta}a(r), \tag{4.6a}$$

$$2: \quad \mathrm{e}^{\mathrm{i}\theta}\left(-\mathrm{i}\partial_r + \frac{1}{r}\partial_\theta\right)a(r)\mathrm{e}^{\mathrm{i}m\theta} + \mathrm{i}\tilde{V}b(r)\mathrm{e}^{\mathrm{i}(m+1)\theta}\Theta(R-r) = \frac{E}{\hbar v_F}\mathrm{e}^{\mathrm{i}(m+1)\theta}\mathrm{i}b(r). \tag{4.6b}$$

These equation can be reduced to

$$1: \quad \left(\partial_r + \frac{(m+1)}{r}\right)b(r) = \left(\frac{E}{\hbar v_F} - \tilde{V}\Theta(R-r)\right)a(r), \tag{4.7a}$$

$$2: \quad -\left(\partial_r - \frac{m}{r}\right)a(r) = \left(\frac{E}{\hbar v_F} - \tilde{V}\Theta(R-r)\right)b(r), \tag{4.7b}$$

The system of equations, Eq. (4.7), is equivalent to a second order equation in either $a(r)$ or $b(r)$.

$$\left(r^2\partial_r^2 + r\partial_r - m^2\right)a(r) = -r^2\left(\frac{E}{\hbar v_F} - \tilde{V}\Theta(R-r)\right)^2 a(r), \tag{4.8}$$

$b(r)$ fulfills a similar equation with $m \to m+1$. Using $\tilde{k} = \left|E/\hbar v_F - \tilde{V}\Theta(R-r)\right|$ we can finally write the second order equation for $a(r)$ as

$$\left(r^2\partial_r^2 + r\partial_r + (\tilde{k}^2r^2 - m^2)\right)a(\tilde{k}r) = 0. \tag{4.9}$$

Eq. (4.9) is formally equivalent to the Bessel equation. In conclusion, we find the wavefunctions in the presence of a circularly gated dot to be either Bessel functions of the first kind $J_m(\tilde{k}r)$ or Hankel functions of first kind $H_m^{(1)}(\tilde{k}r)$. The exact wavefunction in the different regions are determined by the applied boundary conditions as shown below.

Scattering from circular gated region in Dirac approximation

Above we solved for the wavefunction in the presence of a circularly gated dot and we now turn to the scattering caused by this dot on an incoming plane wave. To solve the scattering problem inside and outside the gated region, we assume an incoming plane wave along the x-direction ($\propto \mathrm{e}^{ikx}$) and consider the scattered wave inside and outside the gated region following the approach of Ref. [144]. As the asymptotic form of the Hankel solution is $H_m(z \to \infty) \propto \frac{1}{z}\mathrm{e}^{iz}$ this solution correspond to an outgoing wave. Consequently, the scattered wave outside the gated region is expanded using Hankel functions of the first kind while the wave inside are expanded using Bessel functions.

$$|\Psi^{\text{incoming}}\rangle = \frac{1}{\sqrt{2}}\begin{pmatrix}\mathrm{e}^{\mathrm{i}kx}\\ \mathrm{e}^{\mathrm{i}kx}\end{pmatrix} = \frac{1}{\sqrt{2}}\sum_{m=-\infty}^{\infty}\mathrm{i}^m\begin{pmatrix}J_m(kr)\mathrm{e}^{\mathrm{i}m\theta}\\ \mathrm{i}J_{m+1}(kr)\mathrm{e}^{\mathrm{i}(m+1)\theta}\end{pmatrix}, \tag{4.10a}$$

$$|\Psi^{\text{scat,out}}\rangle = \frac{1}{\sqrt{2}}\sum_{m=-\infty}^{\infty}c_m^r\mathrm{i}^m\begin{pmatrix}H_m^{(1)}(kr)\mathrm{e}^{\mathrm{i}m\theta}\\ \mathrm{i}H_{m+1}^{(1)}(kr)\mathrm{e}^{\mathrm{i}(m+1)\theta}\end{pmatrix}, \tag{4.10b}$$

$$|\Psi^{\text{scat,in}}\rangle = \frac{1}{\sqrt{2}}\sum_{m=-\infty}^{\infty}c_m^t\mathrm{i}^m\begin{pmatrix}J_m(qr)\mathrm{e}^{\mathrm{i}m\theta}\\ \mathrm{i}J_{m+1}(qr)\mathrm{e}^{\mathrm{i}(m+1)\theta}\end{pmatrix}, \tag{4.10c}$$

where $k = E/\hbar v_F$ and $q = \left|E/\hbar v_F - \tilde{V}\right|$. c_m^r and c_m^t are scattering coefficient to be determined by the boundary conditions are the edge of the gated region ($r = R$).

The continuity of the wavefunction requires

$$|\Psi^{\text{incoming}}\rangle + |\Psi^{\text{scat,out}}\rangle = |\Psi^{\text{scat,in}}\rangle, \tag{4.11}$$

for $r = R$. The requirement needs to be fulfilled for each angular momentum m leading to

$$J_m(kR) + c_m^r H_m^{(1)}(kR) = c_m^t J_m(qR), \tag{4.12a}$$

$$J_{m+1}(kR) + c_m^r H_{m+1}^{(1)}(kR) = c_m^t J_{m+1}(qR). \tag{4.12b}$$

Solving this system of equations yields the scattering coefficients

$$c_m^t = \frac{J_{m+1}(kR)H_m^{(1)}(kR) - J_m(kR)H_{m+1}^{(1)}(kR)}{H_m^{(1)}(kR)J_{m+1}(qR) - H_{m+1}^{(1)}(kR)J_m(qR)} \tag{4.13a}$$

$$c_m^r = \frac{J_{m+1}(kR)J_m(qR) - J_m(kR)J_{m+1}(qR)}{H_m^{(1)}(kR)J_{m+1}(qR) - H_{m+1}^{(1)}(kR)J_m(qR)} \tag{4.13b}$$

Using symmetries of the Bessel (and Hankel) functions $J_{-m} = (-1)^m J_m$ we see that $c_{-m}^{r/t} = c_{m-1}^{r/t}$.

The results of this section provide analytic expressions to help analyze the numerical results presented below. An important quantity is the ratio between the wavenumber inside and outside the gated region, $N = q/k = |\tilde{E} - \tilde{V}|/|\tilde{E}|$, where $\tilde{E} = E/\hbar v_F$ which determines the behavior of the electron wave when passing through the dot region. A small E results in a large N value while $E \to V$ results in $N \to 0$. In consequence, low E leads to sharp resonances which broaden and overlap for larger energies.

For a large dot radius compared to the wavelength of the electrons, the scattering shows features known from ray optics. Refraction inside the gated region gives rise to caustics, which are studied in details in Ref. [142], including a ray-optical model. In this case the boundary of the gated region acts as a lens focusing the electrons resulting in a focusing of the electron flow [144].

Instead, we focus on the situation where both the radius and energy are small. For specific values of E and R, resonances appear in a_m^r. Dependent on the parameters, several of these resonances may appear. Below we consider these resonances and their effect on the current flow by comparing the analytic solution to numerical calculations using the full tight binding model.

4.2.2 Local density of states

We consider a gated region with parameters $R = 10$ nm and $V = 0.1|t|$, where t is the carbon-carbon hopping integral. Numerical calculation using the *patched Green's function* method allows us to determine two qualitatively different spatial profiles in the LDOS, corresponding to two resonant modes shown in Fig. 4.7. These are the only resonances clearly resolved for the chosen set of parameters. We clearly notice the difference at the center. Here the mode in Fig. 4.7a is finite whereas the mode in Fig. 4.7b vanishes at $r = 0$. Furthermore, we observe a large difference in magnitude between the two.

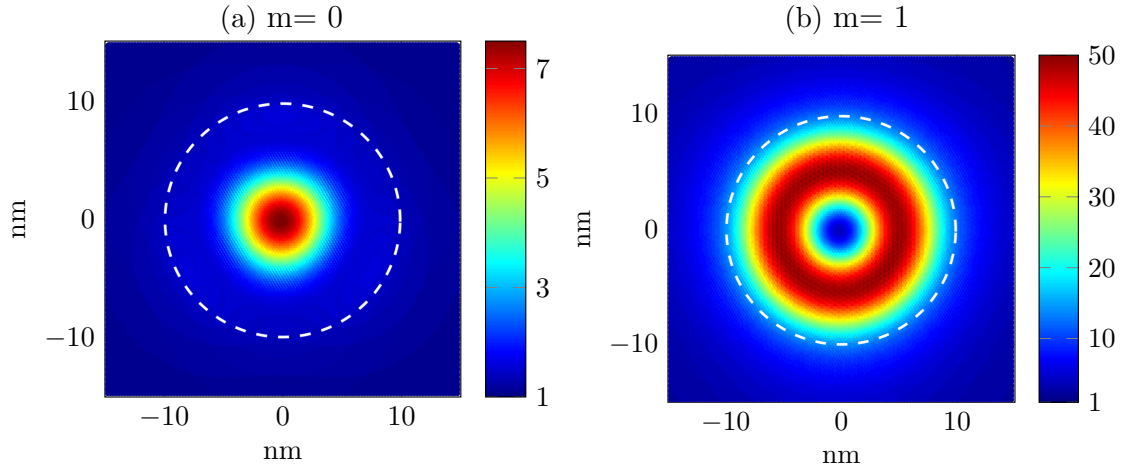

Figure 4.7: Real space map of the local density of states for the (a) $m = 0$ ($E = 0.002|t|$) and (b) $m = 1$ mode ($E = 0.012|t|$) for $V = 0.1|t|$. The local gated region for $R = 10$ nm is indicated with the white dashed line.

Comparing the calculation in Fig. 4.7 with the analytic solution in Eqs. (4.10) and (4.13), we first use Eq. (4.10c) to determine the electron density n within the gated region as $n = \mathbf{\Psi}^\dagger \mathbf{\Psi} = \langle \Psi | \Psi \rangle$,

$$n \propto |c_m^t|^2 \big(J_m^2(qr) + J_{m+1}^2(qr) \big). \tag{4.14}$$

From Eq. (4.14) we note that the $m = 0$ mode gives rise to a finite electron density at $r = 0$ because of the $J_0^2(qr)$ term. On the other hand, the $m = 1$ mode does not contain such a term and consequently gives rise to a vanishing electron density at $r = 0$. From this, we conclude that the gated dot contains two resonances corresponding to a $m = 0$ and a $m = 1$ mode. These two modes give rise to the different spatial profiles of the LDOS in Fig. 4.7. The $m = 0$ and $m = 1$ modes and the interference between them cause the different behavior of the incoming electrons which is investigated below.

Probability current

Next, we study the probability current in the gated region. The probability current or flux describes the change in the probability of finding an electron at a given position. It is therefore similar to the bond currents and comparable to the net flow of current at a given point.

The probability current can be calculated from the spinors as $J_i = \mathbf{\Psi}^\dagger \sigma_i \mathbf{\Psi} = \langle \Psi | \sigma_i | \Psi \rangle$ [12]. Using polar coordinates we get the radial and angular component

$$j_r = \Psi^\dagger \big(\sigma_x \cos(\theta) + \sigma_y \sin(\theta)\big)\Psi = \Psi^\dagger \begin{pmatrix} 0 & \mathrm{e}^{-\mathrm{i}\theta} \\ \mathrm{e}^{\mathrm{i}\theta} & 0 \end{pmatrix} \Psi, \tag{4.15a}$$

$$j_\theta = \Psi^\dagger \big(\sigma_y \cos(\theta) - \sigma_x \sin(\theta)\big)\Psi = \Psi^\dagger \begin{pmatrix} 0 & -\mathrm{i}\mathrm{e}^{-\mathrm{i}\theta} \\ \mathrm{i}\mathrm{e}^{\mathrm{i}\theta} & 0 \end{pmatrix} \Psi. \tag{4.15b}$$

Using the ansatz for a rotationally symmetric spinor, Eq. (4.5),

$$|\Psi\rangle = \mathrm{e}^{\mathrm{i}m\theta} \begin{bmatrix} a(r) \\ \mathrm{e}^{\mathrm{i}\theta}\mathrm{i}b(r) \end{bmatrix}, \tag{4.16}$$

we insert into Eq. (4.15),

$$j_r^{m,m'} = \mathrm{i}\mathrm{e}^{\mathrm{i}(m-m')\theta} \Big[a^*(r)b(r) - a(r)b^*(r) \Big], \tag{4.17a}$$

$$j_\theta^{m,m'} = \mathrm{e}^{\mathrm{i}(m-m')\theta} \Big[a^*(r)b(r) + a(r)b^*(r) \Big]. \tag{4.17b}$$

For the radial component we use Eq. (4.10c) for the wavefunction inside the gated region,

$$j_r^{m,m'} = -\frac{1}{2}\mathrm{e}^{\mathrm{i}(m-m')\theta} \big[{c_{m'}^t}^* c_m^t J_{m'}(qr) J_{m+1}(qr) - {c_{m'}^t}^* c_m^t J_m(qr) J_{m'+1}(qr) \big] \tag{4.18}$$

$$\tag{4.19}$$

Exploiting the fact that $c_{-m}^t = c_{m-1}^t$, we can collect $m' = -(m+1)$ and $m = -(m'+1)$ terms to obtain

$$j_r^m \propto |c_m^t|^2 \big[J_{m+1}^2(qr) + J_m^2(qr) \big] \cos\big((2m+1)\theta\big). \tag{4.20}$$

We can derive a similar expression for the angular component,

$$j_\theta^m \propto |c_m^t|^2 \big[J_{m+1}^2(qr) - J_m^2(qr) \big] \sin\big((2m+1)\theta\big) \tag{4.21}$$

For the $m = 0$ mode we analyze Eqs. (4.20) and (4.21) in detail. We observe that j_r^0 is zero when $\theta = \frac{\pi}{2}n$ with n being an integer. The resulting vertical $j_r^0 = 0$ line is indicated in Fig. 4.8. Similarly, j_θ^0 is zero when $\theta = \pi n$ giving rise to a horizontal $j_\theta^0 = 0$ line or when r attains a value such that $J_{m+1}^2(qr) = J_m^2(qr)$ giving rise to a circular $j_\theta^0 = 0$ curve. We note that the total current field needs to be perpendicular to both the $j_r^0 = 0$ and $j_\theta^0 = 0$ curves. Furthermore, the current is incoming from the left due to the placement of

the probes, so we conclude that the current field of the $m = 0$ mode must contain a vortex pattern as the one shown by the red arrows in Fig. 4.8. By symmetry arguments, this vortex pattern must be symmetric around the x-axis and tends to confine the electrons in the gated region when this mode is activated.

Similar analysis can be done for the m-th mode giving rise to a pattern containing $2(m+1)$ vortices. Below, we study these vortex patterns and their effect on the transmission through the gated region using numerical calculations in a dual probe setup.

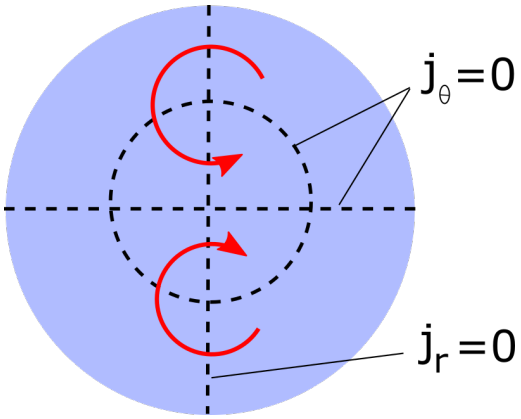

Figure 4.8: Schematic of the $m = 0$ mode of the gated region. From Eqs. (4.20) and (4.21) we see that $j_r = 0$ on $y = 0$ and $j_\theta = 0$ on $x = 0$. In addition, the radial dependence of j_θ leads to a circle with $j_\theta = 0$. The intersection of these lines causes vortices guiding electrons through the center of the gated region. The figure is adapted from [144].

4.2.3 Transmission and bond currents

In this section, we use the *patched Green's function* method to calculate the transmission between two probes placed on either side of the gated region (radius $R = 10$ nm and gate strength $V = 0.1|t|$). Earlier, we demonstrated that this gated region contains two modes ($m = 0$ and $m = 1$). We place the dot in between the probes such that the input probe is 250 nm away from the dot while the second probe is 20 nm on the opposite side, see schematic in Fig. 4.9. This ensures that the incoming wave is almost a perfect plane wave.

The transmission between the probes is shown in Fig. 4.9 together with the average LDOS within the gated region. We observe a notable Fano-type resonance [144] in the transmission where a small variation in energy can lead to a large change in transmission and even give rise to a suppression of the Klein tunneling effect at the energy highlighted by the circle in Fig. 4.9. To analyze these features, we calculate the bond current leaving the far probe. In Fig. 4.10a-c the bond current maps are shown for the highlighted energies in Fig. 4.9 and are represented schematically in the bottom of Fig. 4.9. The size of the bond current is given by the colormap and the direction is indicated by the direction of

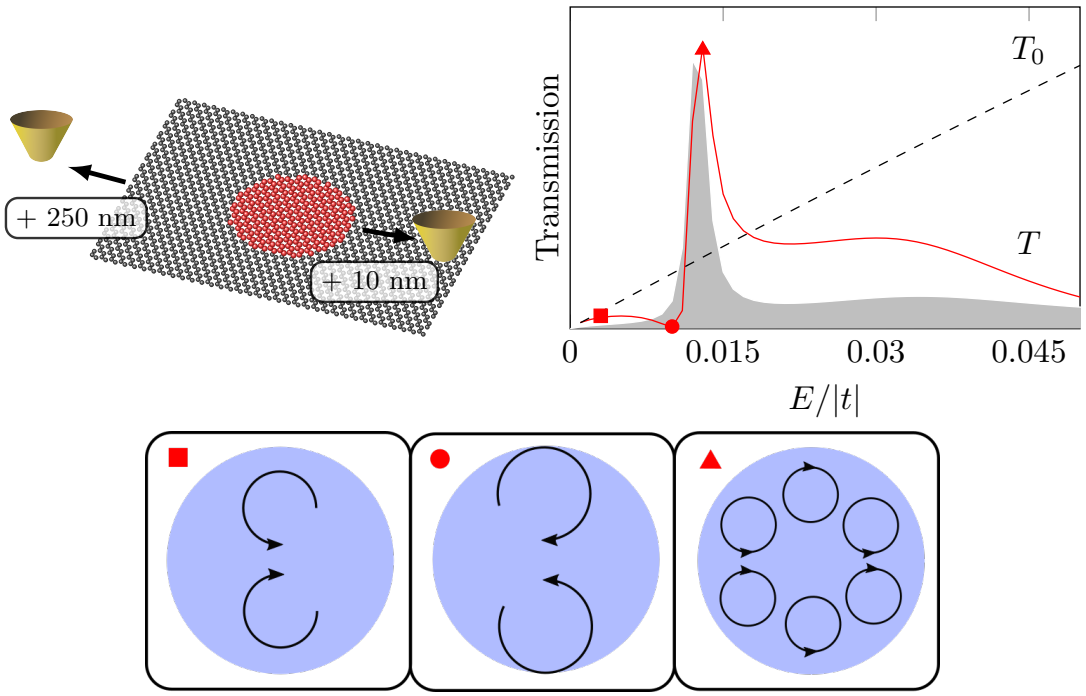

Figure 4.9: (Top) A sketch of the dual probe setup with two probes $\sim$ 250 nm apart with a gated circular region in between. The right panel shows the transmission between the probes. The shaded area corresponds to the average LDOS within the gated region. The marks correspond to the bottom schematics. Parameters $R = 10$ nm and $V = 0.1|t|$. (Bottom) Schematics showing the two vortices of the $m = 0$ mode (square), two counterpropagating vortices backscattering the current (circle) and the six vortices of the $m = 1$ mode (triangle).

the arrows. In addition the bond current maps, Fig. 4.10 also shows directional scattering defined as the size of the bond currents relative to the pristine value as a function of the angle ϕ with the horizontal axis where $\phi = 0$ corresponds to the right hand side of the region, *i.e.* $\big|J(R+\delta r,\phi)\big|/\big|J_0(R+\delta r,\phi)\big|$ where we use $\delta r = 5$ nm in Fig. 4.10d-e.

The behavior at the energy highlighted by a square, is caused by the vortex pattern shown in Fig. 4.10a. This vortex pattern consists of two vortices focusing the current through the gated region. This is consistent with the analytic treatment of the $m = 0$ mode using Eqs. (4.20) and (4.21) leading to the schematic in Fig. 4.8. As the two vortices are in the same direction as the incoming current the $m = 0$ mode focuses the current somewhat as it passes through the gated region. This focusing is also evident from the directional scattering in Fig. 4.10d. Here we clearly see the increased current at $\phi = 0°$ caused by the focusing nature of the vortices. Likewise the suppression around $\phi = \pm 90°$ is caused by the backwards current flow in the vortex pattern at this angle.

The previous analytical analysis of Eqs. (4.20) and (4.21) predicted a vortex pattern with $2(m + 1)$ vortices for the m'th mode. We confirm this prediction by the numerical

calculations when considering the bond current map in Fig. 4.10c belonging to the energy highlighted by a triangle in Fig. 4.9. Here we clearly observe the six predicted vortices of the $m = 1$ mode. The $m = 1$ mode gives three preferred scattering directions $\phi = 0$ and $\phi \approx \pm 120^\circ$ as evident from Fig. 4.10f which should be seen in contrast to the single preferred scattering direction caused by the two vortices of the $m = 0$ mode. The preferred directions correspond to "outgoing" channels between neighboring vortices where both vortices cause an outward current flow. Similarly, the suppressed directions are caused by "in-going" channels. In addition, we observe that the current at the $m = 1$ mode is greatly enhanced compared to the pristine system demonstrating the strong resonance at $m = 1$ already observed in relation to the magnitude of the LDOS.

At last we consider the interference between the $m = 0$ and $m = 1$ mode which is responsible for the suppression of the transmission at the energy highlighted by a circle in Fig. 4.9. This interference leads to the inversion of the $m = 0$ vortex pattern, as clearly visible in Fig. 4.10b. Two counterpropagating vortices block the current flow through the gated region and increases the backscattering. This vortex pattern dramatically changes the preferred scattering direction going from the focusing of the $m = 0$ mode at $\phi = 0^\circ$ to suppression at $\phi = 0^\circ$, see Fig. 4.10e. Instead the current is increased along directions corresponding to the outwards flow in the two vortices ($\phi \approx \pm 120^\circ$).

The analysis of the current flow through the gated region is schematically summarized in Fig. 4.9 showing the transition from the focusing vortex pattern of the $m = 0$ mode, to the six vortices of the $m = 1$ which cause three preferred scattering directions and greatly enhance the current through the gated region. The numerical calculations have clearly shown the formation of the analytically predicted features which interplay give rise to two counterpropagating vortices suppressing the current flow and causing the Fano-type resonance in the transmission spectrum.

Similar to the antidots case, we have demonstrated the ability of this type of nanostructuring to alter the current flow at the nanoscale. In both cases we observed how the interplay between single states or modes is the origin of vortex patterns causing Fano-type resonances in the transmission able to act as switches by manipulating the energy or gating. The formation of vortices gives rise to preferred current directions either by increasing the scattering by certain parts of the nanosctructure (antidot) or by guiding the current along the vortex path effectively focusing the current (gated dot).

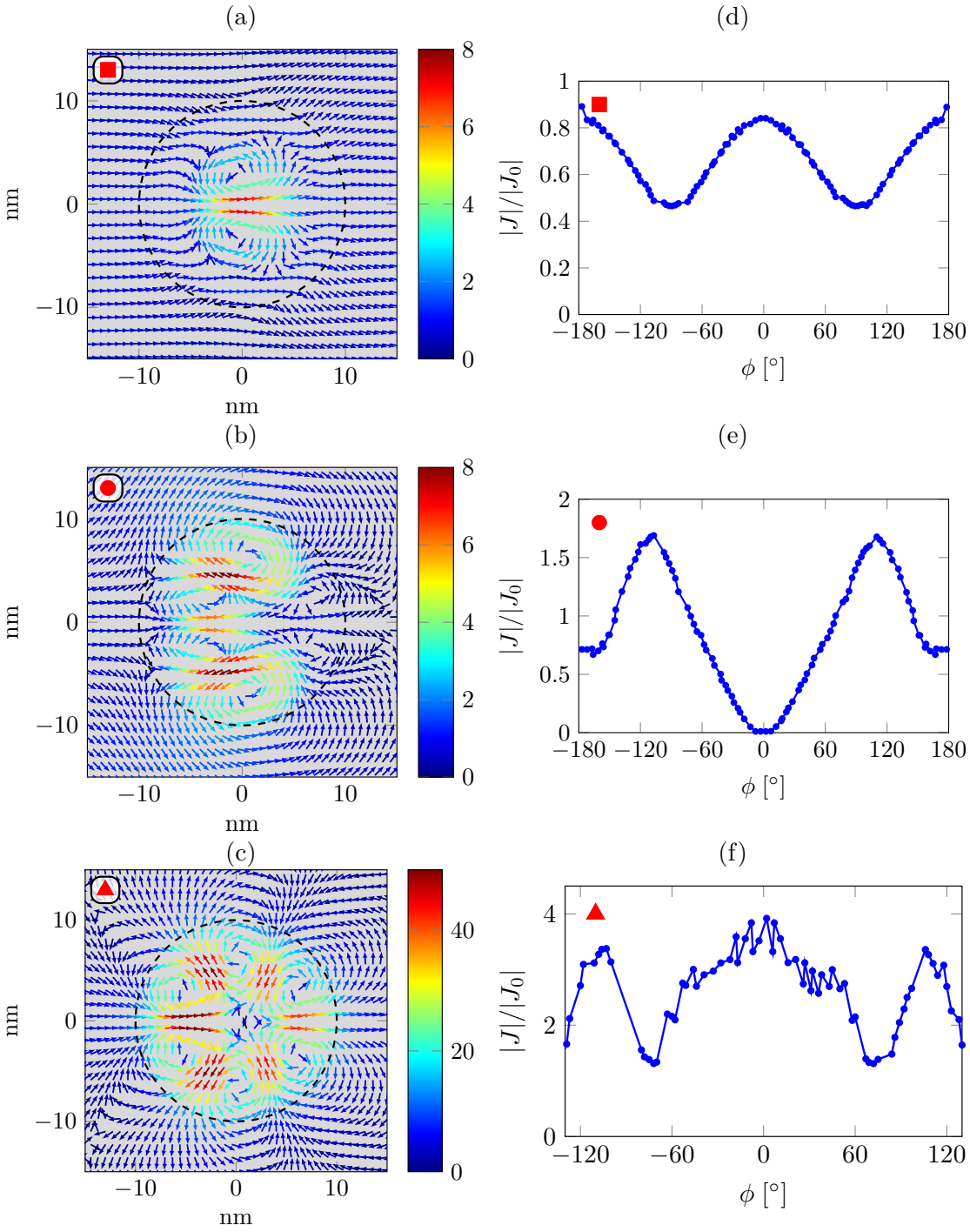

Figure 4.10: (a-c) The bond currents incoming from the left for (a) the $m = 0$ mode ($E = 0.002|t|$), (b) two counterrevolting vortices suppressing the flow through the gated region ($E = 0.01|t|$) and (c) $m = 1$ mode ($E = 0.00125|t|$), see Fig. 4.9. The arrows indicate the direction of the electron flow, whereas the color denotes the magnitude of the current. Each arrow is a sum of all the individual bond currents in a box around the arrow position. (d-f) The size of the bond current relative to the pristine case 5 nm away from the gated region for the cases in (a-c). Here $\phi = 0°$ corresponds to the x-axis. Parameters for the gated region are $R = 10$ nm and $V = 0.1|t|$ and spatial region is indicated by the dashed line.

4.3 Summary

Antidot spectroscopy

A graphene antidot with zigzag edge geometry possesses localized edge states. By studying individual antidots with dimensions of $R \sim 10$ nm within an otherwise infinite graphene sheet, we demonstrate that the interplay between these localized zigzag edge states and the pristine continuum gives rise to Fano-type resonances in the dual probe transmission for probes placed on opposite sides of the antidot.
We show how these resonances are caused by current vortices formed near the zigzag edge segments. The phenomena was found to be strongest for perfect edge geometries but are also visible for even very disordered experimental antidots where the structure are obtained from high resolution TEM images.

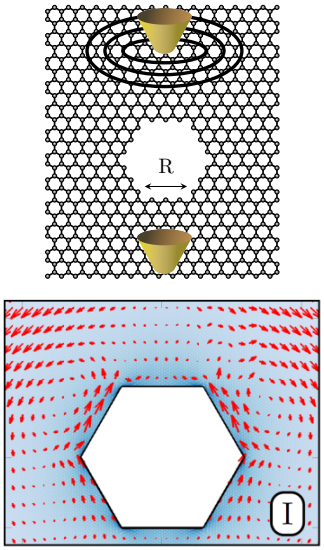

Spectroscopy of locally gated dot

We analyzed the current flow through a locally gated dot and demonstrated the existence of two fundamental modes characterized by the angular quantum number $m = 0$ and $m = 1$. The analytical predictions made from the solution of the Dirac model, where confirmed by numerical tight binding calculations. In this way, we showed the two focusing vortices of the $m = 0$ mode and the six vortices of the $m = 1$ mode. Moreover, we considered the interplay between these two modes giving two counterpropagating vortices, suppressing the current flow and causing a Fano-type resonance in the transmission spectrum.
This opens the possibility of manipulating graphene-based devices by spatially structured electric gating.

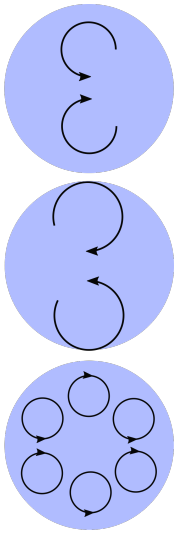

CHAPTER 5

Strain fields with pseudomagnetic effects

Although graphene is only one atom layer thick, it can sustain remarkably large mechanical deformations without breaking. Consequently, graphene offers an outstanding combination of electronic and mechanical properties. The close relation between the structural and electronic properties of graphene opens the possibility of strain engineering as a method to manipulate the electronic, optical and magnetic properties of graphene [28, 29, 86, 147–158]. The application of strain in graphene can lead to effects like bandgap formation [159] or transport gaps [147]. In particular the extraordinary response of graphene to inhomogeneous deformations has received much attention [29, 148, 149]. In fact, the altered tight binding parameters due to the lattice deformation mimics the role of a gauge field in the low energy effective Dirac model of graphene [27, 160]. The formation of a so-called pseudomagnetic field (PMF) suggests the presence of Landau quantization in the absence of external magnetic fields [29] which has been confirmed by STM experiments on bubble-like deformations [151, 161].

Actual strain engineering on the nanoscale would allow for strongly localized PMFs while at the same time enabling continuously varying fields. In addition, the PMF induced by the strain can lead to large field strengths of hundreds of Tesla and enable otherwise unattainable spatial distributions of magnetic fields. These remarkable properties demonstrate the potential of strain engineering to manipulate the electronic and transport properties of graphene.

Following the experiments on bubble-like deformations [151, 161–163], we apply the *patched Green's function method* to various inhomogeneous strain fields giving rise to pseudomagnetic fields ("pseudomagnetic dots"). We first introduce the general method to apply strain through a tight binding model. Afterwards we use this to describe how a triaxial strain induces a constant PMF which in turn results in Landau quantization. Furthermore, we study rotationally symmetric local deformations, investigating the resulting inhomogeneous PMF distributions and the formation of pseudo-Landau quantization in these inhomogeneous fields. The dual probe setup is afterwards used to study the transport properties of single pseudomagnetic dots. Finally, we extend the discussion of single pseudomagnetic dots to arrays of dots and investigate their effect of the transport regimes in the samples.

5.1 Strain using a tight binding approach

We treat graphene through a nearest neighbor tight binding Hamiltonian characterized by the carbon-carbon hopping matrix t which is equal for all couplings. When we displace the atoms relative to each other the bond lengths vary leading to a spatially dependent hopping integral, $t_{ij} = t(\boldsymbol{r}_i, \boldsymbol{r}_j)$. The position of an atom is $\boldsymbol{r}_i = \boldsymbol{r}_i^0 + \boldsymbol{u}$ where $\boldsymbol{r}_i^0$ is the equilibrium position and $\boldsymbol{u} = (u_x(x,y), u_y(x,y), z(x,y))$ is the displacement field. In equilibrium the bond length is $a_0 = 0.142$ nm but after displacement it changes to $d_{ij} = |\boldsymbol{r}_i - \boldsymbol{r}_j|$ and the hoppings are modified according to [28, 152, 158]

$$t_{ij} = t_0 \mathrm{e}^{-\beta\left(d_{ij}/a_0 - 1\right)}, \tag{5.1}$$

where t_0 is the pristine hopping parameter and $\beta = \partial \log(t)/\partial \log(a)|_{a=a_0} \approx 3.37$ [28].

The new bond length is given either directly from the changed positions of the atoms, $\boldsymbol{r}_i$, or from the strain tensor [164]

$$d_{ij} = \frac{1}{a_0}\boldsymbol{r}_{ij} \cdot \boldsymbol{\epsilon} \cdot \boldsymbol{r}_{ij} = \frac{1}{a_0}\left(a_0^2 + \epsilon_{xx}x_{ij}^2 + \epsilon_{yy}y_{ij}^2 + 2\epsilon_{xy}x_{ij}y_{ij}\right), \tag{5.2}$$

where the strain tensor is given from classical continuum mechanics as

$$\epsilon_{ij} = \frac{1}{2}\left(\partial_j u_i + \partial_i u_j + (\partial_i z)(\partial_j z)\right), \quad i,j = x,y, \tag{5.3}$$

where $u_i(x,y) = u_i$ is the in-plane deformation field and $z(x,y) = z$ is the out-of-plane deformation [27].

5.2 Pseudomagnetic field from strain field

We now generalize the low energy effective Dirac Hamiltonian to the situation of deformed graphene. The local modifications of the hopping amplitudes in Eq. (5.1) can be expanded to first order $t_{ij}(\boldsymbol{r}_i, \boldsymbol{r}_j) \approx t_0 + \delta t_{ij}(\boldsymbol{r}_i, \boldsymbol{r}_j)$. The introduction of spatially varying hopping parameters into the tight binding description induces an effective gauge field $\boldsymbol{A}$ into the low energy Dirac Hamiltonian [27, 148]. The components of this vector potential are given by $\boldsymbol{A} = A_x\boldsymbol{e}_x + A_y\boldsymbol{e}_y$ where $\boldsymbol{e}_x$ and $\boldsymbol{e}_y$ are unit vectors in x and y-directions, respectively. Choosing the coordinate system with the x-axis along the zigzag direction, the effective gauge field is given by the change in hopping parameters [156]

$$A_x - \mathrm{i}A_y = -\frac{1}{ev_F}\sum_n \delta t(\boldsymbol{r}, \boldsymbol{r} + \boldsymbol{\delta}_n)\mathrm{e}^{\boldsymbol{K}\cdot\boldsymbol{\delta}_n} \tag{5.4}$$

where $\boldsymbol{\delta}_n$ are the nearest neighbor vectors, and $\boldsymbol{K}$ determines the valley of the first Brillouin zone of graphene. We determine $\delta t(\boldsymbol{r}_i, \boldsymbol{r}_j)$ by expanding Eq. (5.1) and exploiting Eq. (5.2) [27, 28, 160, 165]

$$t_{ij} = t_0\left(1 - \frac{\beta}{a_0}(d_{ij} - a_0)\right) = t_0\left(1 - \frac{\beta}{a_0^2}\boldsymbol{\delta}_n \cdot \boldsymbol{\epsilon} \cdot \boldsymbol{\delta}_{ij}\right) \tag{5.5}$$

We note that this only takes into account the first order corrections. Expanding to higher orders in the deformation leads to Fermi surface anisotropy [157] and spatially dependent Fermi velocity [166–168].

Inserting Eq. (5.5) into Eq. (5.4) while using a general two dimensional strain field, $\epsilon_{ij}(x, y)$, leads to a gauge field of the form [27, 160, 169]

$$\boldsymbol{A} = -\frac{\hbar\beta}{2ea_0}\begin{pmatrix}\epsilon_{xx} - \epsilon_{yy} \\ -2\epsilon_{xy}\end{pmatrix}, \tag{5.6}$$

which gives rise to an effective Dirac Hamiltonian given by [27, 29]

$$H_{\pm\boldsymbol{K}}(\boldsymbol{q}) = v_F\boldsymbol{\sigma} \cdot \Big(\boldsymbol{q} \pm e\boldsymbol{A}\Big), \tag{5.7}$$

where $\boldsymbol{\sigma} = [\sigma_x, \sigma_y]$ with $\sigma_{x/y}$ being Pauli matrices, $\pm\boldsymbol{K}$ denotes the two valleys and v_F is the pristine Fermi velocity. In this way, we see that the gauge field acquires opposite sign in the two valleys and therefore does not break time reversal symmetry.

Similar to a real vector potential, the strain induced vector potential results in a so-called pseudo magnetic field (PMF), B_s, perpendicular to the graphene sheet and given by

$$B_s = \boldsymbol{\nabla} \times \boldsymbol{A} = \partial_x A_y - \partial_y A_x. \tag{5.8}$$

Importantly, the definition of the pseudomagnetic field is inherently connected to a first order expansion of the low energy Dirac model of graphene and we only use the framework of pseudomagnetic fields to provide simple analysis of numerical results. Consequently, all presented calculations are based on a full tight binding model with hopping parameters modified according to Eq. (5.1).

5.3 Constant pseudomagnetic field using triaxial strain

The pseudomagnetic field enters the Dirac Hamiltonian in the same way as a real magnetic field, if we restrict ourselves to a single valley (see Eq. (5.7)). We can therefore compare the constant PMF to a real magnetic field. In the presence of a real magnetic field the electronic spectrum is modified giving rise to Landau quantization [82]. However, as

opposed to the conventional (non-relativistic) Landau levels which have a spectrum linear in the B-field, the Landau levels for the massless Dirac fermions in graphene follow a characteristic $\sqrt{Bn}$-behavior including a zero energy Landau level ($n = 0$). The analogy between real and pseudomagnetic fields therefore suggests the existence of pseudo Landau levels in the presence of a constant pseudomagnetic field [29, 161],

$$E_n = \text{sign}(n)\sqrt{2e\hbar v_F^2 B_s |n|}, \tag{5.9}$$

where E_n is the energy for the Landau level n. The corresponding magnetic length l_B becomes

$$l_B = \sqrt{\frac{\hbar}{eB_s}} = 26\text{nm}/\sqrt{B_s}. \tag{5.10}$$

Guinea *et al.* [29] showed that a triaxial strain leads to a constant PMF according to Eq. (5.6). Below we have collected details about the triaxial strain in the armchair direction. As evident from the analytical derivations, the triaxial strain in the armchair direction gives rise to a constant PMF whose size is determined by the strength of the strain.

Triaxial strain - Armchair direction

$$z(r,\theta) = 0, \tag{5.11a}$$

$$\boldsymbol{u}(r,\theta) = \begin{pmatrix} u_x \\ u_y \end{pmatrix} = \begin{pmatrix} u_0 r^2 \sin(3\theta) \\ u_0 r^2 \cos(3\theta) \end{pmatrix}, \tag{5.11b}$$

$$\boldsymbol{A} = -4u_0 r \frac{\hbar\beta}{2ea_0} \begin{pmatrix} \sin(\theta) \\ -\cos(\theta) \end{pmatrix}, \tag{5.11c}$$

$$B_s = 8u_0 \frac{\hbar\beta}{2ea_0} \tag{5.11d}$$

where u_0 determines the strength of the strain field [29, 153].

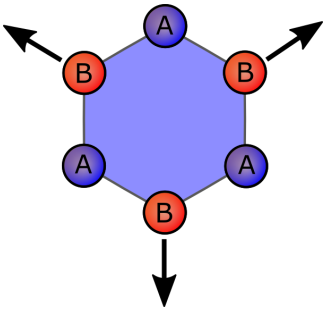

Figure 5.1: Illustration of a triaxial strain along the armchair direction.

5.3.1 Pseudo Landau Levels

Several studies have used classical molecular dynamics to determine the strain field [149, 155]. Neek-Amal *et al.*[154] showed the importance of molecular dynamics when determining the quantitative effect of the PMF on the LDOS. However, Ref. [154] also showed that the qualitative features of a deformation remain after relaxation by molecular dynamics. We therefore use analytic displacement fields as shown in Eq. (5.11) to investigate the formation of Landau levels in the presence of a constant PMF. The strain field is applied in a circular region with radius R. As the strain field in Eq. (5.11) grows with distance from the center, the maximum strain also grows with increasing radius R even for the same strength of the resulting PMF. Consequently, we use the PMF strength B_s as reference parameter below as this relates directly to the features in the electronic structure.

Beyond $r = R$, we apply a smoothing to make the strain field go to zero at the edge of the patch as required by the patched Green's function method. The smoothing is applied using the transformation $\boldsymbol{\epsilon} \to \boldsymbol{\epsilon}\ \mathrm{e}^{-(r-R)^2/2\sigma^2}$ for $r > R$. In the calculations below, we consider a radius of $R = 10$ nm and a smoothing of $\sigma = 3$ nm to ensure a minimal effect of the smoothing region on the interior of the strained region. The finite size effects imposed by such a treatment are discussed at the end of this section.

The resultant PMF distribution caused by such a triaxial strain smoothed after $r > R$ is shown in Fig. 5.2. Here we clearly observe the constant PMF for $r < R$ and the smoothing region with a varying PMF of opposite sign. Note that the opposite sign within the smoothing region arise because we smooth the strain tensor (and not the PMF) causing a *negative* change of the strain for $r > R$. As the constant PMF, $+B_s$, for $r < R$ is caused by a *positive* change in the strain with increasing r, the smoothing gives rise to a PMF of opposite sign while decreasing the strain to zero.

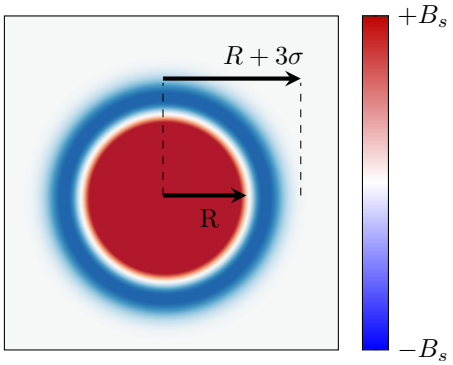

Figure 5.2: The PMF distribution of a triaxial strain (Eq. (5.11)) for $r < R$ which is made finite by an exponential smoothing $\boldsymbol{\epsilon} \to \boldsymbol{\epsilon}\ \mathrm{e}^{-(r-R)^2/2\sigma^2}$ for $r > R$.

Fig. 5.3 shows the average DOS in the center of the constant PMF region with $B_s = 100$ T. Importantly, we note the appearance of peaks in the DOS. These correspond almost perfectly to the Landau levels expected from Eq. (5.9). However, we note one important

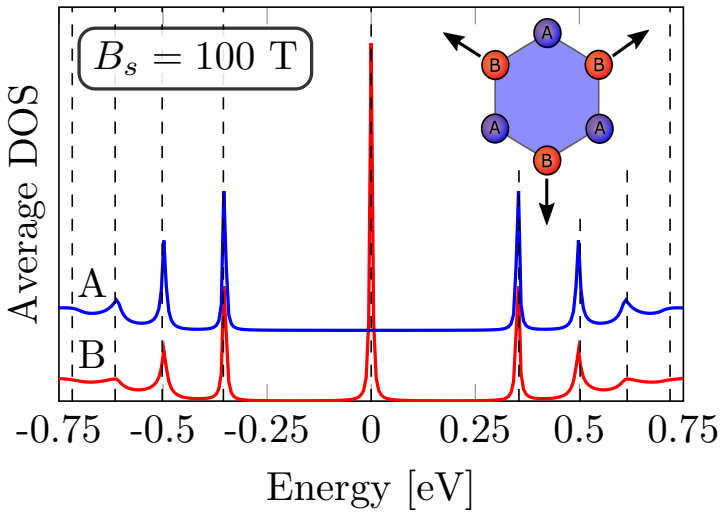

Figure 5.3: Average density of states for both the A and B sublattice at the center of a region with radius of $R = 10$ nm subjected to a triaxial strain corresponding to $B_s = 100$ T. The positions of the Landau levels expected from Eq. (5.9) is indicated by dashed curves. The smoothing region has a width $\sigma = 3$ nm and the curves are translated vertically with respect to each other.

difference between these pseudo Landau levels (pLL's) compared to regular Landau levels: the zeroth pLL only has a finite contribution to the LDOS on one sublattice, as also observed in Refs. [154, 170].

5.3.2 Sublattice splitting of the zeroth pseudo Landau level

We can understand the sublattice splitting of the zeroth pLL by considering the Dirac Hamiltonian Eq. (5.7). The solution to the two dimensional Dirac Hamiltonian around $\boldsymbol{K}$ is a two dimensional spinor $|\Psi_{\boldsymbol{K}}\rangle = (\psi^{\bullet}_{\boldsymbol{K}}, \psi^{\circ}_{\boldsymbol{K}},)$, where $\bullet$ denotes the A sublattice and $\circ$ denotes the B sublattice. The spinor components of valley $\boldsymbol{K}'$ satisfy the same Dirac equation as $\boldsymbol{K}$ with $q_x \to -q_x$ and interchanged sublattice pseudospin. This can be conveniently collected in a four component spinor $|\Psi\rangle$ containing both valleys, [171]

$$|\Psi\rangle = \begin{pmatrix} \psi^{\bullet}_{\boldsymbol{K}} \\ \psi^{\circ}_{\boldsymbol{K}} \\ -\psi^{\circ}_{\boldsymbol{K}'} \\ \psi^{\bullet}_{\boldsymbol{K}'} \end{pmatrix}, \tag{5.12}$$

the minus sign is included following the notation of Ref. [171]. This definition uses the valley isotropic formulation of the four-dimensional Dirac equation with two identical subblocks as adopted earlier in Eq. (5.7). However, we note that other representations

which use two unequal blocks are also common in the literature [82].

$$\begin{pmatrix} v_F\boldsymbol{\sigma}\cdot(\boldsymbol{q}+e\boldsymbol{A}) & \mathbf{0} \\ \mathbf{0} & v_F\boldsymbol{\sigma}\cdot(\boldsymbol{q}-e\boldsymbol{A}) \end{pmatrix} |\Psi\rangle = E|\Psi\rangle, \tag{5.13}$$

First, we conclude from Eqs. (5.12) and (5.13) that interchanging the valley index inverts the role of the two sublattices, *i.e.* $\left(\psi^{\bullet}_{\boldsymbol{K}}, \psi^{\circ}_{\boldsymbol{K}}\right) \to \left(-\psi^{\circ}_{\boldsymbol{K}'}, \psi^{\bullet}_{\boldsymbol{K}'}\right)$. Second, we note that replacing B_s with $-B_s$ corresponds to interchanging the valleys. Generally this follows from the fact that $\boldsymbol{A} \to -\boldsymbol{A}$ interchange to role of the subblocks in Eq. (5.13).

The wavefunction for the different valleys and signs of the B-field can be determined from these symmetries. We can assume a solution to the two dimensional Dirac equation of the form $|\Psi_{\boldsymbol{K}}\rangle = c_1|\bullet\rangle + c_2|\circ\rangle$ for the $\boldsymbol{K}$ valley and positive magnetic field. Here c_1 and c_2 are coefficients determining the size of the A ($|\bullet\rangle$) and B ($|\circ\rangle$) component, respectively. Considering this form of the solution, we use the symmetries to determine the form of the wavefunction (except for a phase factor) for the $\boldsymbol{K}'$ valley, $|\Psi_{\boldsymbol{K}'}\rangle$, and negative B-field.

	B	$-B$
$\lvert\Psi_{\boldsymbol{K}}\rangle$	$c_1\lvert\bullet\rangle + c_2\lvert\circ\rangle$	$c_2\lvert\bullet\rangle + c_1\lvert\circ\rangle$
$\lvert\Psi_{\boldsymbol{K}'}\rangle$	$c_2\lvert\bullet\rangle + c_1\lvert\circ\rangle$	$c_1\lvert\bullet\rangle + c_2\lvert\circ\rangle$

(5.14)

For a pseudomagnetic field the total wavefunction, $|\Psi^{pseudo}\rangle$, contains components from $\boldsymbol{K}$ and $\boldsymbol{K}'$ with opposite sign of the B-field,

$$|\Psi^{pseudo}\rangle = |\Psi_{\boldsymbol{K}}(B)\rangle + |\Psi_{\boldsymbol{K}'}(-B)\rangle. \tag{5.15}$$

On the other hand, the total wavefunction in the presence of a *real* magnetic field, $|\Psi^{real}\rangle$ has the same sign of the B-field in the two valleys,

$$|\Psi^{real}\rangle = |\Psi_{\boldsymbol{K}}(B)\rangle + |\Psi_{\boldsymbol{K}'}(B)\rangle. \tag{5.16}$$

Having defined the wavefunctions by Eqs. (5.15) and (5.16) and the symmetries in Eq. (5.14), we now return to discuss the zeroth Landau level. Below, we first consider the case of a real magnetic field. Afterwards we use this result to discuss the case of a pseudomagnetic field.

Zeroth Landau level in a real magnetic field

We first consider the solution for the zeroth ($n = 0$) Landau level in the $\boldsymbol{K}$ and $\boldsymbol{K}'$ valleys under the influence of a *real* magnetic field according to Ref. [82]

$$|\Psi^{real}_{\boldsymbol{K}}(B)\rangle_{n=0} = \begin{pmatrix} \psi^{\bullet}_{\boldsymbol{K}} \\ \psi^{\circ}_{\boldsymbol{K}} \end{pmatrix} = \begin{pmatrix} 0 \\ |n=0\rangle \end{pmatrix} \tag{5.17a}$$

$$|\Psi^{real}_{\boldsymbol{K}'}(B)\rangle_{n=0} = \begin{pmatrix} \psi^{\circ}_{\boldsymbol{K}'} \\ \psi^{\bullet}_{\boldsymbol{K}'} \end{pmatrix} = \begin{pmatrix} 0 \\ |n=0\rangle \end{pmatrix}. \tag{5.17b}$$

where $|n=0\rangle$ denotes the state belonging to the zeroth Landau level. For a real magnetic field, the zeroth Landau level has a nonzero component corresponding to the B sublattice in the $\boldsymbol{K}$ valley and to the A sublattice in the $\boldsymbol{K}'$ valley. Therefore, the valley and sublattice pseudospin coincide for the zeroth order Landau level in a real magnetic field. Considering the wavefunctions from Eq. (5.14) this corresponds to $c_1 = 0$ and $c_2 \neq 0$. Therefore, we conclude that even though the two sublattices are decoupled both contribute to the total density of states. This can be easily seen by considering the electron density, $\rho = \langle\Psi|\Psi\rangle$, for the two valley with $c_1 = 0$

$$\rho_{\boldsymbol{K}} = \langle\Psi_{\boldsymbol{K}}(B)|\Psi_{\boldsymbol{K}}(B)\rangle = |c_2|^2\langle\circ|\circ\rangle, \tag{5.18a}$$

$$\rho_{\boldsymbol{K}'} = \langle\Psi_{\boldsymbol{K}'}(B)|\Psi_{\boldsymbol{K}'}(B)\rangle = |c_2|^2\langle\bullet|\bullet\rangle. \tag{5.18b}$$

Evidently, Eq. (5.18) means that the sublattices are decoupled at the zeroth Landau level in the presence of a real magnetic field [82].

Zeroth Landau level in a pseudomagnetic field

We now return to the situation of the pseudomagnetic field with the wavefunction Eq. (5.15). For the zero order pseudo Landau level, we have $c_1 = 0$ from the analogy with the real magnetic field. Consequently, the electron density for the two independent parts of the wavefunction ($\boldsymbol{K}$ and $\boldsymbol{K}'$) in the pseudomagnetic case is given by

$$\langle\Psi_{\boldsymbol{K}}(B)|\Psi_{\boldsymbol{K}}(B)\rangle = \langle\Psi_{\boldsymbol{K}'}(-B)|\Psi_{\boldsymbol{K}'}(-B)\rangle = |c_2|^2\langle\circ|\circ\rangle, \tag{5.19}$$

where the expression for $|\Psi_{\boldsymbol{K}}(B)\rangle$ and $|\Psi_{\boldsymbol{K}'}(-B)\rangle$ is given by Eq. (5.14) with $c_1 = 0$. We conclude that the zeroth order pLL only has a finite contribution on one sublattice.

This analysis of the sublattice polarization of the zeroth pLL is confirmed by the numerical calculations in Fig. 5.3. The sublattice with the finite contribution is determined by the direction of the triaxial strain because this determines the sign of the B-field experienced by the $\boldsymbol{K}$ valley. The solution Eq. (5.17) assumes a positive B-field in the $\boldsymbol{K}$ valley yielding $c_1 = 0$. If the $\boldsymbol{K}$ valley experienced a negative B-field, we get a vanishing contribution for the opposite sublattice. The strain direction shown in Fig. 5.1 gives rise to a positive PMF in the $\boldsymbol{K}$ valley resulting in a zeroth pLL with finite contribution on the B sublattice. Rotating this strain field by 60° gives a similar but negative PMF, meaning that the zeroth pLL level would switch to the A sublattice. This special connection between the sublattices, the zero order pLL and the direction of the triaxial strain is investigated in more detail in the next section.

5.3.3 Rotation of triaxial strain

In general a rotation of the triaxial strain by an angle ϕ from the armchair direction as illustrated in Fig. 5.4 leads to a PMF of the form $B_s = B_0\cos(3\phi)$ and we observe a

maximum B-field when the strain is aligned with the armchair direction. On the other hand, a triaxial strain in the zigzag direction does not give rise to a PMF at all. Even if the magnitude of the displacement field is the same but rotated to the zigzag direction, we do not observe any changes in the low energy spectrum.

In Fig. 5.5 we show the average DOS on sublattice B for different rotation angles of the triaxial strain field. First, we observe a decrease in the strength of the PMF as we rotate the strain field away from $\phi = 0°$. The decreasing PMF is evident from the lower energy of the first pLL. Furthermore, we notice the more developed Landau peaks for strain along the armchair directions ($\phi = 0°$ and $\phi = 60°$). Finally, the linear density of states observed at $\phi = 30°$ (zigzag direction) confirms the prediction of zero PMF for zigzag type strain. Clearly, the formation of a PMF is highly dependent on the direction of strain meaning that strain along multiple directions (ex. rotational symmetric strain) becomes a mixture of different peaks, therefore, making the observation of pLLs difficult.

At last, the results in Fig. 5.5 show the existence of a zeroth pLL peak for $\phi = 0°, 10°, 20°$ whereas we do not observe any zero order peak for $\phi = 40°, 50°, 60°$. This confirms the predicted dependence of the zeroth order pLL on the sign of the PMF, because the strain at $\phi = 0°$ to $\phi = 30°$ corresponds to $+B_0$ while the strain at $\phi = 30°$ to $\phi = 60°$ corresponds to $-B_0$. Consequently, the zero order peak exists on the B sublattice for positive PMFs in agreement with the discussion in the previous section.

Triaxial strain - arbitrary direction

$$z(r, \theta) = 0, \tag{5.20a}$$

$$\boldsymbol{u}(r, \theta) = \begin{pmatrix} u_x \\ u_y \end{pmatrix} = \begin{pmatrix} u_0 r^2 \sin(3[\theta + \phi]) \\ u_0 r^2 \cos(3[\theta + \phi]) \end{pmatrix}, \tag{5.20b}$$

$$B_s = 8u_0 \cos(3\phi). \tag{5.20c}$$

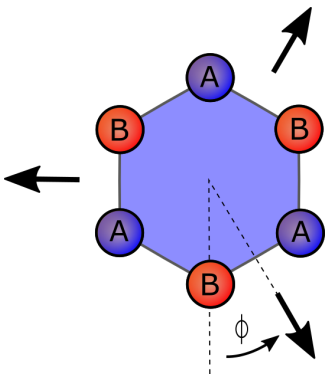

Figure 5.4: Illustration of a triaxial strain rotated an angle ϕ from the armchair direction.

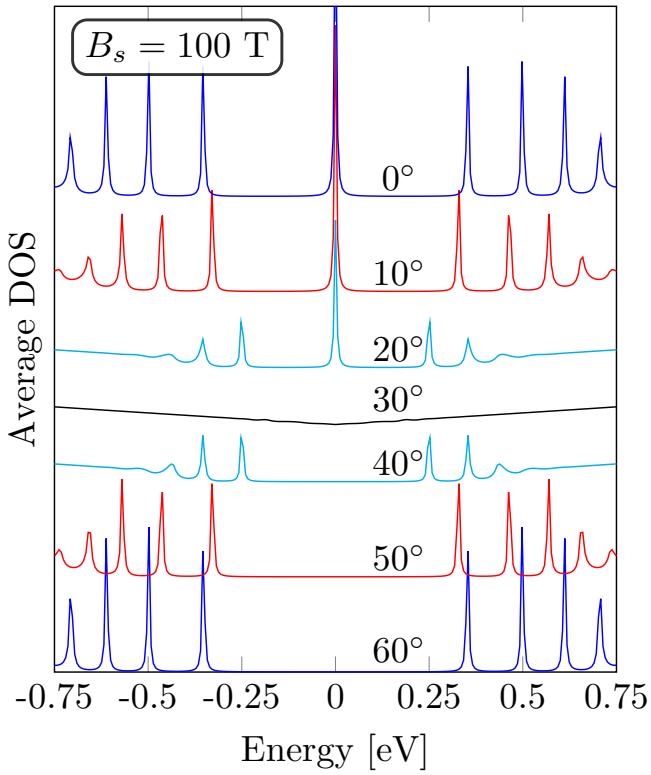

Figure 5.5: The average density of states for sublattice B at the center of a triaxial strain corresponding to $B_s = 100$ T and a radius $R = 15$ nm. The different curves correspond to different rotational angles ϕ as defined in Fig. 5.4.

5.3.4 Finite size effects

We now investigate the influence of the finite size of the strained region. Fig. 5.6 shows the LDOS on the B sublattice for a triaxial strain corresponding to $B_s = 100$ T and with radius $R = 5, 10$ and 15 nm and smoothing $\sigma = 3$ nm. For $B_s = 100$ T we get a magnetic length of $l_B \sim 2.6$ nm from Eq. (5.10). For a radius much larger than l_B, we conclude from Fig. 5.6 that the pLL's are clearly formed. In contrast, the pLLs vanish when l_B is comparable or even smaller than the size of the strained region. This trend is observed for the $R = 5$ nm (black) in Fig. 5.6. Instead, we notice the formation of additional states around $E = 0$ for small R. These are so called quasi bound states and are also observed for small real magnetic dots [172].

In conclusion, regions of constant PMF must be bigger than the corresponding magnetic length for pLLs to be formed, even in the case of the "correct" type of armchair triaxial strain. This important observation is useful when we consider inhomogeneous PMFs in later sections.

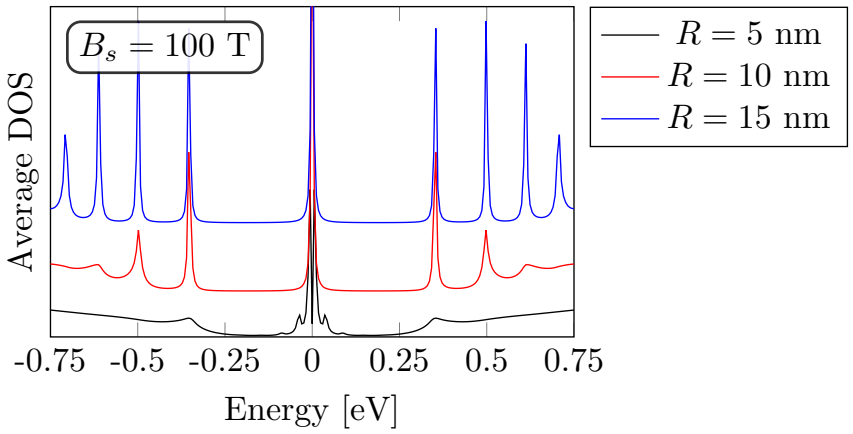

Figure 5.6: Average density of states on sublattice B at the center of a triaxial strain corresponding to $B_s = 100$ T for radius $R = 5, 10$ and 15 nm. Each case has a smoothing region of width $\sigma = 3$ nm and the curves are translated vertically with respect to each other.

5.4 Finite inhomogeneous strain field

Experimentally Levy *et al.*[161] demonstrated that inhomogeneous strain fields in nanobubbles accidentally formed on a platinum (111) surface, showed signatures of pseudo Landau levels in the density of states corresponding to field strengths of up to 300 T. Since these pioneering studies other experiments have tried to control the formation of nanobubbles

[151] or the applied strain via pressure [149, 162], substrate interactions [173] or substrate structuring [163]. Most of these approaches aim at deforming the graphene lattice locally resulting in a spatially concentrated PMF. However, reliable ways to control strain will in general not produce the special triaxial strain as discussed in the last section. Instead, we concentrate on rotationally symmetric displacement fields. We can imagine this class of strain fields to be obtained by experiments modifying the substrate or pressurizing semi-freestanding graphene. We rely on classical continuum mechanics to obtain the displacement fields of local deformations (or nanobubbles). It is expected to provide qualitatively similar results as strain fields obtained using molecular dynamic simulations. The main difference lies in the actual magnitude of the strain as discussed in Refs. [154] and [149].

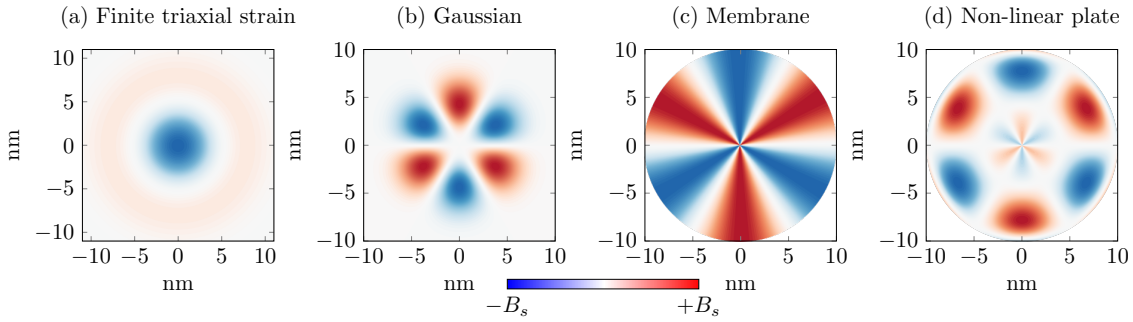

Figure 5.7: Collection of pseudomagnetic field distributions for different strain profiles.

In this section we describe local deformations giving rise to inhomogeneous strain fields and PMFs. We consider four different types of strain fields:

- Finite triaxial strain
- Gaussian height profile
- Membrane bubble model
- Non-linear plate bubble model

The resulting PMF for each strain field is collected in Fig. 5.7 for comparison. In the rest of this chapter, we consider these local deformations (or nanobubbles) and their effect on the electronic properties. For future reference we describe the different models in more detail below.

Finite triaxial strain

We use the triaxial strain considered previously and apply a spherical smoothing modifying the magnitude of the triaxial strain by a Gaussian damping [168],

$$z(r,\theta) = 0, \tag{5.21a}$$

$$\boldsymbol{u}(r,\theta) = \begin{pmatrix} u_x \\ u_y \end{pmatrix} = \begin{pmatrix} u_0 r^2 \sin(3\theta) \\ u_0 r^2 \cos(3\theta) \end{pmatrix} \mathrm{e}^{-\frac{r^2}{2\sigma^2}}, \tag{5.21b}$$

where u_0 is the strength of the strain and σ is the width of the damping.

Using Eqs. (5.3) and (5.6) the PMF becomes

$$B_s = 8u_0 \frac{\hbar\beta}{2ea_0}\left(\frac{r^4}{8\sigma^4} - \frac{r^2}{\sigma^2} + 1\right)\mathrm{e}^{-\frac{r^2}{2\sigma^2}}. \tag{5.21c}$$

The damping decreases the size of the PMF away from the center, creating a spatially varying PMF evident from Fig. 5.8. In consequence, we do not expect pseudo Landau levels unless the Gaussian damping is small, effectively leaving a large part of the triaxial strain profile unchanged to produce a constant PMF.

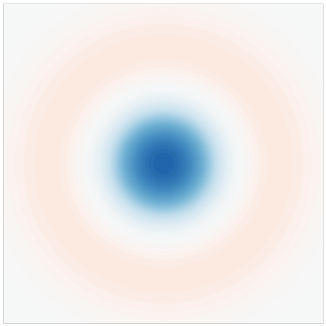

Figure 5.8: The pseudomagnetic field distribution of the finite triaxial strain profile in Eq. (5.21c).

Rotationally symmetric strain fields

The remaining strain profiles for local deformations are rotationally symmetric. We therefore use polar coordinates $\boldsymbol{r} = (r,\theta)$ for the in-plane deformation and $z(r) = z$ for the out-of-plane deformation,

$$\boldsymbol{u} = \begin{pmatrix} u_x \\ u_y \end{pmatrix} = \begin{pmatrix} u_r \cos(\theta) \\ u_r \sin(\theta) \end{pmatrix}. \tag{5.22}$$

We make use of the identities

$$\partial_x = \cos(\theta)\partial_r - \frac{1}{r}\sin(\theta)\partial_\theta, \tag{5.23a}$$

$$\partial_y = \sin(\theta)\partial_r + \frac{1}{r}\cos(\theta)\partial_\theta. \tag{5.23b}$$

Combining Eqs. (5.3) and (5.6) gives the vector potential and corresponding PMF

$$\boldsymbol{A} = -\frac{\hbar\beta}{2ea_0}\begin{pmatrix} A_x \\ A_y \end{pmatrix} = -\frac{\hbar\beta}{2ea_0} g(r) \begin{pmatrix} \cos(2\theta) \\ -\sin(2\theta) \end{pmatrix}, \tag{5.24a}$$

$$B_s = -\frac{\hbar\beta}{2ea_0}\left(\frac{2g(r)}{r} - \partial_r g(r)\right)\sin(3\theta), \tag{5.24b}$$

where we have used the definition

$$g(r) = \partial_r u_r - \frac{u_r}{r} + \frac{1}{2}(\partial_r z)^2. \tag{5.25}$$

We notice from Eq. (5.24b) that the PMF is always 3-fold symmetric for rotationally symmetric displacements. The magnitude, on the other hand, depends on both the in-plane and out-of-plane displacement. This is clearly seen in Fig. 5.7 showing the PMF for a Gaussian height profile, the membrane bubble model and non-linear plate bubble model.

Gaussian height profile

The Gaussian height profile is a simple deflection of the graphene sheet according to a Gaussian profile.

$$z(r,\theta) = h_0 \mathrm{e}^{-\frac{r^2}{2\sigma^2}}, \tag{5.26a}$$

$$\boldsymbol{u}(r,\theta) = \begin{pmatrix} u_x \\ u_y \end{pmatrix} = \begin{pmatrix} 0 \\ 0 \end{pmatrix}, \tag{5.26b}$$

where σ is width and h_0 is the height of the bubble. Using Eq. (5.24b) the PMF becomes

$$B_s = \frac{\hbar\beta}{2ea_0}\frac{r^3 h_0^2}{\sigma^6}\mathrm{e}^{-\frac{r^2}{2\sigma^2}}\sin(3\theta). \tag{5.26c}$$

The Gaussian profile is an example of a rotationally symmetric profile without sharp edge effects. However, as only the out-of-plane component of the position is changed, a rather large height is required to obtain sizable strain fields.

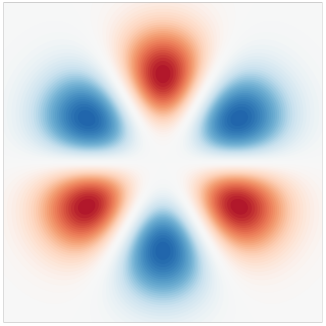

Figure 5.9: The pseudomagnetic field distribution of the gaussian height profile in Eq. (5.26c).

Next, we analyze rotationally symmetric deformations using membrane and non-linear plate theories [174] as derived in Appendix A. This corresponds to the experimental situation of pressurizing a graphene sheet which is free standing for $r < R$ and adhere to the substrate for $r > R$.

Describing the sheet as an elastic plate under a central load p, the central equation governing the deformation is given by Eq. (A.15)

$$\partial_i N_{ij} = 0, \tag{5.27a}$$

$$D\nabla^4 z + N_{ij}\partial_i\partial_j z + p = 0, \tag{5.27b}$$

where $i, j = (x, y)$, D is the bending modulus related to the Young's modus and Poisson's ratio [175], N_{ij} is the tensor of the axial force defined in Appendix A. A general solution to Eq. (5.27) does not exist. Instead, we use two general approximations: The membrane model and the non-linear plate model.

Membrane model ($r < R$)

The membrane bubble model ignores the bending stiffness ($D = 0$) and provides a relatively simple approximate solution to the continuum mechanic problem for a vanishing deflection at $r = R$, see Appendix A.

$$z(r,\theta) = h_0\left(1 - \frac{r^2}{R^2}\right), \tag{5.28a}$$

$$\boldsymbol{u}(r,\theta) = \begin{pmatrix} u_x \\ u_y \end{pmatrix} = \begin{pmatrix} u_0 \frac{r}{R}\left(1 - \frac{r}{R}\right), \\ 0 \end{pmatrix}, \tag{5.28b}$$

$$B_s = \frac{\hbar\beta u_0}{2ea_0R^2}\sin(3\theta). \tag{5.28c}$$

where R is the radius of the bubble, h_0 is the height and u_0 is given by $u_0 = 1.136h_0^2/R$ [174]. The membrane model results in a kink" at the edge which is similar to the clamped nanobubbles studied in Ref. [149] using molecular dynamics.

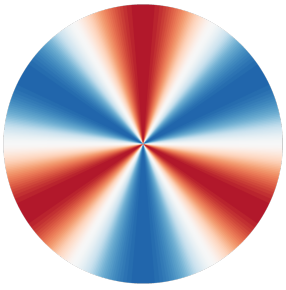

Figure 5.10: The pseudomagnetic field distribution of the membrane model in Eq. (5.28c).

Non-linear plate model ($r < R$)

The non-linear plate bubble model is an extension of the linear plate solution to the elastic plate problem in continuum mechanics, see Appendix A. The non-linear plate model combines the standard out-of-plane solution from the linear plate solution with a non-linear in-plane displacement taking into account a finite in-plane force.

$$z(r,\theta) = h_0\left(1 - \frac{r^2}{R^2}\right)^2 \tag{5.29a}$$

$$\boldsymbol{u}(r,\theta) = \begin{pmatrix} u_r \\ u_\theta \end{pmatrix} = \begin{pmatrix} r(R-r)(c_1 + c_2 r), \\ 0 \end{pmatrix}, \tag{5.29b}$$

$$B_s = \frac{\hbar\beta}{2ea_0}\left[(c_1 - c_2 R) - \frac{32h_0^2 r^3}{R^6}\left(1 - \frac{r^2}{R^2}\right)\right]\sin(3\theta). \tag{5.29c}$$

where R is the radius of the bubble, h_0 is the height and the constants are $c_1 = 1.308h_0^2/R^3$ and $c_1 = -1.931h_0^2/R^4$ [174].

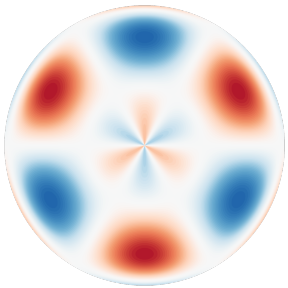

Figure 5.11: The pseudomagnetic field distribution of the non-linear plate model in Eq. (5.29c).

5.5 Local density of states in inhomogeneous strain fields

In this section, we consider the local density of states of the rotationally symmetric bubble models. We focus mainly on the membrane model as this provides a good example of the highly relevant pressurized (or gas-inflated) bubbles. The membrane model has a relatively simple PMF distribution while at the same time showing significant edge effects caused by the sharp edge at $r = R$. Many of the features we discuss below emerge from the strongly clamped nature of this bubble type. The results are published as part of Paper II. The *patched Green's function method* presented in Chapter 2 enables calculations of real space LDOS maps investigating single bubbles in an extended system without applying periodic boundary conditions which may introduce interactions between neighboring bubbles.

Throughout this section we consider a membrane bubble with dimensions $R = 10$ nm and $h_0 = 3$ nm corresponding to a maximum strain of approximately 10 %. The strain profile is given by Eq. (5.28) and gives rise to the PMF distribution shown in Fig. 5.12. First, we analyze real space LDOS maps demonstrating a perfect sublattice polarization caused by the PMF. Secondly, we study the combination of pseudo-Landau levels and Friedel oscillations governing the resonances of the membrane bubble. At last we compare the membrane bubble to a non-linear plate bubble of the same dimensions discussing both the formation of pseudo-Landau levels and Friedel oscillations in the two models.

5.5.1 Sublattice polarization

We first investigate real space LDOS maps of the bubble region where the PMF is threefold symmetric as shown in Fig. 5.12a. The threefold symmetry from the PMF is found to be reproduced in the LDOS maps at all energies. An example is shown in Fig. 5.12b-c where real space LDOS maps for the two sublattices are shown, clearly demonstrating the threefold symmetry of the PMF distribution.

Considering the two LDOS maps in Fig. 5.12b-c belonging to the two sublattices, we also notice the perfect asymmetry or sublattice polarization, as we obtain the LDOS map for the B sublattice by a 60°-rotation of the A sublattice. Earlier studies of Gaussian bubbles [152, 158, 176] also noticed this sublattice polarization and in fact the polarization is present for all the strain models presented in Section 5.4. Below we demonstrate how the polarization is a general consequence of the opposite sign of the PMF in the two valleys.

Following the analysis in Section 5.3, we first consider the generic wavefunction in the $\boldsymbol{K}$-valley, $|\Psi_{\boldsymbol{K}}\rangle = c_1|\bullet\rangle + c_2|\circ\rangle$, where $|\bullet\rangle$ denotes the wavefunction component on the A sublattice and $|\circ\rangle$ denotes component on the B sublattice while the coefficients c_1 and c_2 determine the relative size of the wavefunction components. Using the symmetry

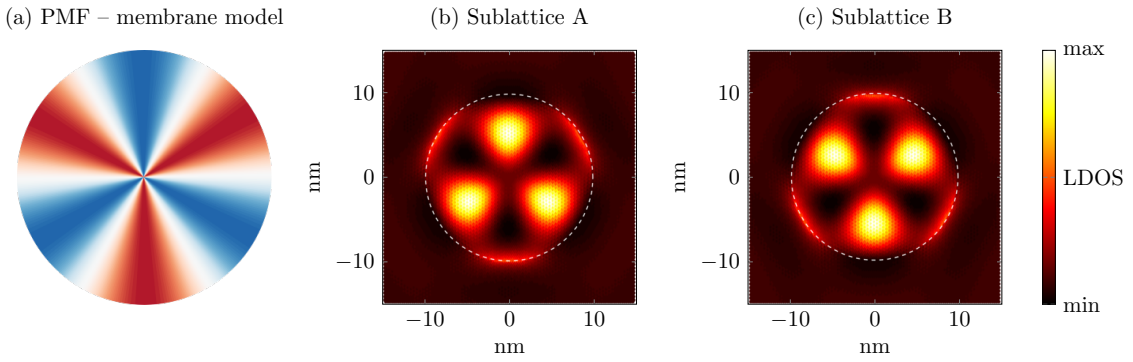

Figure 5.12: (a) The PMF distribution of the membrane model is repeated from Fig. 5.10. (b-c) The real space LDOS map of a resonant state at $E = 0.06|t|$ using the membrane bubble model for (b) sublattice A and (c) sublattice B.

arguments of Section 5.3 this wavefunction behaves differently in the two valleys depending on the sign of the B-field. For reference we repeat the wavefunction analysis from Eq. (5.14)

	B	$-B$
$\|\Psi_{\boldsymbol{K}}\rangle$	$c_1\|\bullet\rangle + c_2\|\circ\rangle$	$c_2\|\bullet\rangle + c_1\|\circ\rangle$
$\|\Psi_{\boldsymbol{K}'}\rangle$	$c_2\|\bullet\rangle + c_1\|\circ\rangle$	$c_1\|\bullet\rangle + c_2\|\circ\rangle$

(5.30)

In case of a PMF the total wavefunction, $|\Psi\rangle$, has contributions from the two valleys with opposite sign of the B-field, $|\Psi\rangle = |\Psi_{\boldsymbol{K}}(B)\rangle + |\Psi_{\boldsymbol{K}'}(-B)\rangle$. Using this we obtain the total electron density $\rho = \langle\Psi|\Psi\rangle$ for the two different parts of the wavefunction,

$$\langle\Psi_{\boldsymbol{K}}(B)|\Psi_{\boldsymbol{K}}(B)\rangle = \langle\Psi_{\boldsymbol{K}'}(-B)|\Psi_{\boldsymbol{K}'}(-B)\rangle = |c_1|^2\langle\bullet|\bullet\rangle + |c_2|^2\langle\circ|\circ\rangle. \tag{5.31}$$

From Eq. (5.31) we conclude that we get the same contribution to the LDOS from the two valleys. Consequently, if the LDOS of the B sublattice follows the PMF in the $\boldsymbol{K}$-valley causing it to increase when the PMF is positive, then Eq. (5.31) concludes that the contribution to the LDOS from the opposite valley is similar. This effectively gives rise to the characteristic sublattice polarization illustrated in Fig. 5.12 and is a generic feature of pseudomagnetic fields causing the two valleys to experience equal but opposite B-fields.

5.5.2 Pseudo Landau levels and Friedel oscillations in clamped bubbles

Above we observed a good correspondence between the real space LDOS maps and the threefold symmetric PMF distribution. However, if we consider the LDOS maps at several energies in Fig. 5.13, we notice additional details. In Fig. 5.14a we therefore calculate the energy dependent LDOS at the positions indicated by symbols (square, circle and triangle) in Fig. 5.13. We first consider the average of the LDOS within the 'slice' containing the

symbols, shown by the bottom (red) curve in Fig. 5.14a. Two distinct oscillation types are observed, and we argue that these can be divided into Friedel-type and PMF-induced features.

At high energies in particular we notice regularly spaced oscillations with an approximate period of $\hbar v_F \pi / 2R$. These are consistent with Friedel-type oscillations related to the size of the structure and emerging from interferences between electrons scattered at opposite sides of the bubble. An exact treatment needs to take into account the renormalized Fermi velocity, v_F, due to the average change in bond length. [177] At lower energies, we observe distinct peaks which are not equally spaced (the first two appear at E_1 and E_2). We will show that these are due to pseudomagnetic effects and we refer to them as pseudo Landau levels.

Besides the Friedel oscillation associated with the bubble radius, we also have similar oscillations associated with the distances to the different edges of the bubble. These features are highly position dependent, and explain the differences between the three single position curves in Fig. 5.14. These position dependent oscillations are washed out, when we consider the average. Accordingly, only the oscillations which dependent on the structure's size are seen in the average (bottom curve in Fig. 5.14). However, at individual positions these oscillations can have a considerable impact. In this way, the individual curves in Fig. 5.14a show that the pLL peak at E_2 is only dominant for the points indicated by the square and triangle. The E_2 peak is suppressed by Friedel-type interference at the circle point, which is also clear from the LDOS map in Fig. 5.13b.

The amplitude of the Friedel-type oscillations is determined by the strength of scattering near the bubble edges. The clamped edge at $r = R$ gives rise to significant strain fields

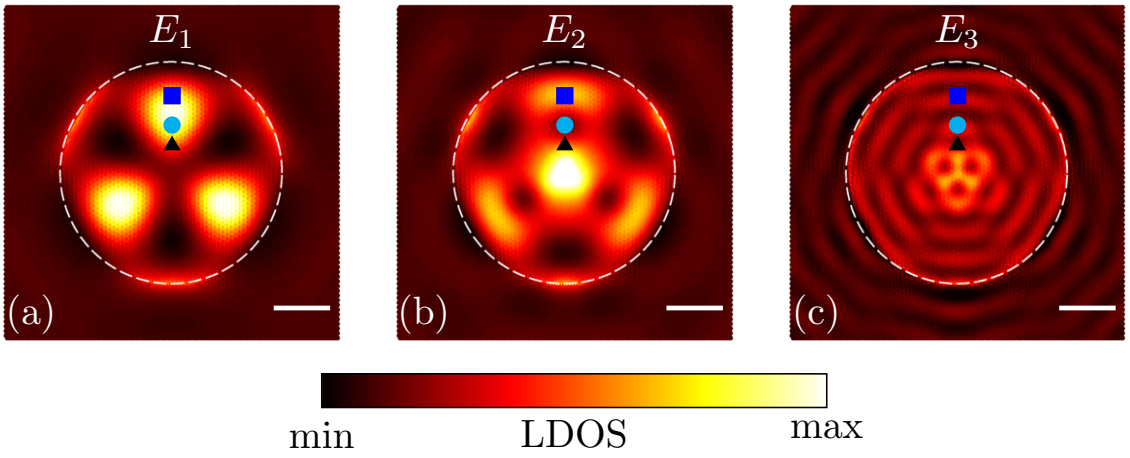

Figure 5.13: (a-c) Real space LDOS maps for the A sublattice taken at the energies $E_1 = 0.06|t|$, $E_2 = 0.089|t|$ and $E_3 = 0.23|t|$, corresponding to energies of the first two pseudo Landau levels and an energy dominated by Friedel type oscillations, respectively. The energies and the symbols correspond the ones used in Fig. 5.14. The scale bar is 5 nm.

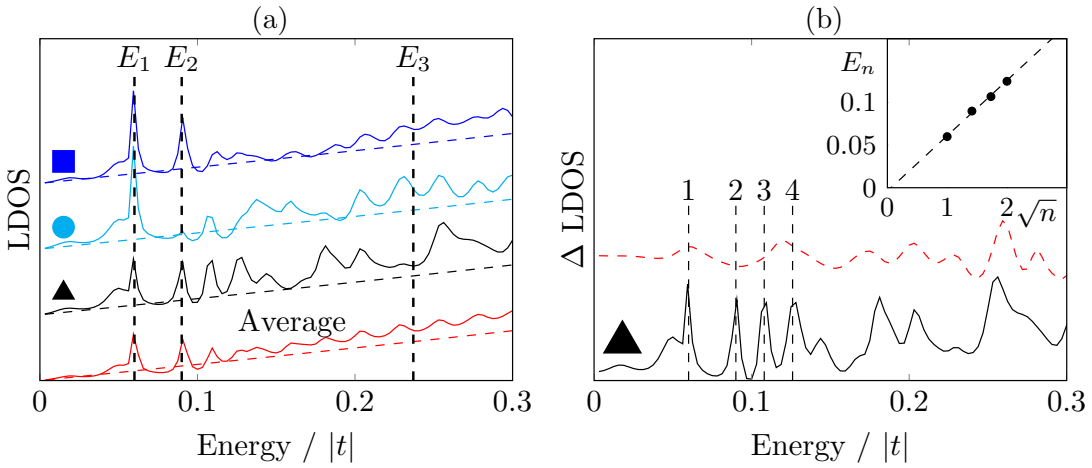

Figure 5.14: (a) The LDOS as a function of energy for the three positions indicated in Fig. 5.13 and for the average of the 'slice' of the bubble region containing the symbols. The dashed lines indicate the LDOS without the bubble. The curves are shifted with respect to each other to increase visibility. (b) The difference in LDOS as a function of energy for the point indicated with a triangle on Fig. 5.13. We show both the full calculation (full line) and an artificial system containing only the perturbation for a small region at the edge of the bubble (dashed line). We adjust the average hopping constant in the calculation of the artificial system to match the full calculation. Inset: The peak energies 1-4 as a function of $\sqrt{n}$, where n is the peak number.

along this edge, leading to a sharp, strong perturbation. More realistic profiles calculated from molecular dynamics also indicate strong perturbations near the edges of clamped bubbles [149]. Our results indicate that edge scattering effects may significantly affect LDOS behavior in clamped bubble systems and even mask PMF-induced features.

To treat the oscillations due to the feature size and edge sharpness in more detail, we calculate the LDOS for an artificial system only taking into account the strain field along a small ring around the edge, see Fig. 5.14b (dashed red line). In this way, only Friedel-type features are expected within the structure. If we compare to the full calculation (full black line in Fig. 5.14b), we notice that the oscillations at higher energies are present in both calculations, whereas the sharp peaks are only present in the full calculation. This confirms the Friedel nature of the higher energy oscillations and suggests the lower energy peaks are due to an alternative mechanism.

To confirm that the alternative mechanism responsible for the sharp peaks are pseudomagnetic effects, we compare the peak positions to the standard form expected for Landau levels in graphene from Eq. (5.9), $E_n = \mathrm{sign}(n)\sqrt{2e\hbar v_F^2 B_s n}$. The peaks labeled 1-4 in Fig. 5.14b display the $\sqrt{n}$ dependence characteristic of Landau levels in graphene, as shown in the inset of Fig. 5.14b. The size of the PMF can furthermore be inferred from the distance between the peaks corresponding to the slope of the inset curve. In this way,

we determine the size of the PMF to be approximately $B_s \sim 30$ T.

To further analyze the two different types of peaks, we compare the full strain profile to the same strain profile only containing the out-of-plane displacement. The membrane out-of-plane displacement is special because it does not produce any PMF according to the effective Dirac description. This can easily be seen by inserting the height profile Eq. (5.28a) into the general expression for the PMF Eq. (5.24b). This is not a general feature of rotationally symmetric bubble models, but is a special feature of the membrane model which we can exploit to study Friedel and pseudo-Landau features separately.

In order to study the real space patterns together with the energy spectrum, we calculate the angle averaged LDOS as a function of the energy and distance from the center of the bubble,

$$\Delta\rho_s(r, E) = \frac{1}{N} \sum_{|\boldsymbol{r}_i|=r} \left[\rho_i(\boldsymbol{r}_i, E) - \rho_i^0(\boldsymbol{r}_i, E)\right], \tag{5.32}$$

where ρ_i and ρ_i^0 is the density of states at site i with and without the bubble, respectively. In Fig. 5.15, we plot the $\Delta\rho_s$ as a function of both E and r for both the full membrane model and "the out-of-plane only" contribution. It is noted that the height is smaller in the out-of-plane only calculation as the in-plane and out-of-plane strain compensate to produce an overall lower strain in the full model. In Fig. 5.15a we therefore choose a maximal height of the out-of-plane only contribution giving roughly the same maximal strain.

Comparing Figs. 5.15a and 5.15b, we notice both have a high DOS at the edge of the bubble ($r \sim 10$ nm) close to zero energy. This peak is related to the sharp edge present in both calculations and are not directly related to pseudomagnetic effects, but due to the artificial nature of the "the out-of-plane only" calculation the peak is larger here.

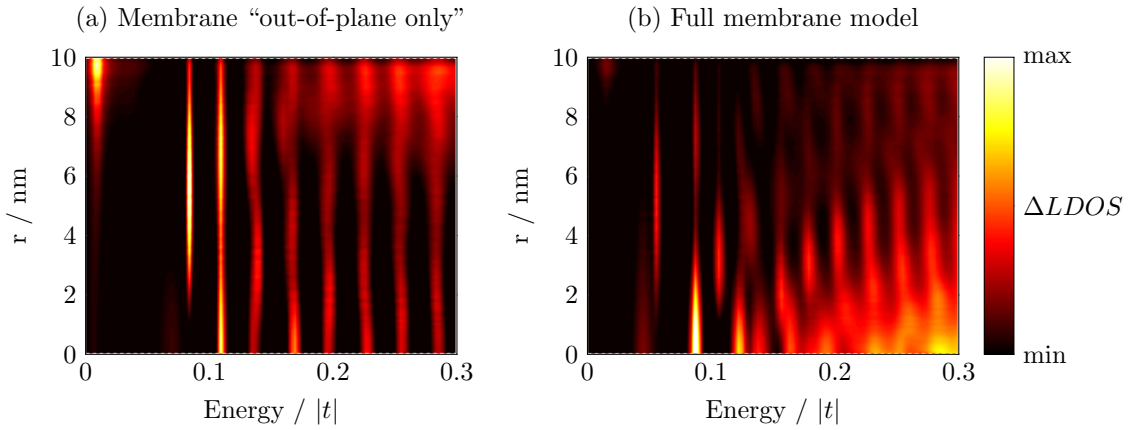

Figure 5.15: A contour showing the average $\Delta LDOS$ for the bubble region ($r < R = 10$ nm), see Eq. (5.32), as a function of energy and position for (a) the out-of-plane contribution to the membrane model and (b) the full membrane model.

If we now consider the rest of the spectrum for the "out-of-plane only" contour in Fig. 5.15a, we immediately notice the regular spaced vertical lines. These lines indicate that the DOS is higher on average in the bubble region at these energies but eventual real space oscillations as a function of r are averaged out when considering all angles. In this way, we consider the regular spaced vertical lines in the (E, r)-contour as a signature of the standing wave pattern characteristic of Friedel oscillations.

If we compare the "out-of-plane only" calculation to the full membrane calculation Fig. 5.15b, we notice similar vertical lines at higher energies comparable to those from the "out-of-plane only" contour. However, the peaks at lower energies are qualitatively different. The vertical lines are no longer uninterrupted in the full calculation and they are no longer regularly spaced as discussed above. This signifies that these peaks have a different origin and are not caused solely by a standing wave resonance. The "out-of-plane only" and the full membrane strain profile both gives rise to resonances, but those not originating from standing wave effects are not present in the case without a PMF and we again conclude that the resonant states at lower energies are related to the existence of a PMF. We must therefore be careful to distinguish between the two type of resonances when investigating the electronic effects of PMFs induced by inhomogeneous strain fields.

5.5.3 Comparison of membrane and non-linear plate models for gas inflated bubbles

In the previous section we considered the membrane model when searching for signatures of PMFs in strained bubbles. We concluded that Landau-like features where superimposed with Friedel-type oscillations caused by the sharp edge features. It is therefore worth to consider a bubble with a softer edge profile than the membrane bubble when considering the formation of pseudo Landau-like states.

Where the membrane model is suitable for very large bubbles when bending stiffness can be neglected, we have also introduced the non-linear plate model which is more appropriate for including bending effects near the edges of smaller bubbles, see Section 5.4. Comparing the height and strain profile of the membrane and non-linear plate model (Fig. 5.16a), we notice that the non-linear plate bubble has much smoother edges than the membrane model. Therefore, we expect the non-linear plate bubble to result in weaker Friedel oscillations.

Considering the average LDOS caused by the two models it is clear that the higher energy oscillations are considerably suppressed in the non-linear plate model compared to the membrane one, see Fig. 5.16b. However, in the non-linear plate model there is also an absence of sharp Landau-level-like peaks following a $\sqrt{n}$ distribution, with the possible exception of the peak denoted by the red circle.

We notice from Fig. 5.16a that the non-linear plate model gives rise to an additional node in the strain profile. This node in turn also produce a radial fluctuation in the sign and strength of the PMF (Fig. 5.17) which is consistent with the lack of pseudo Landau

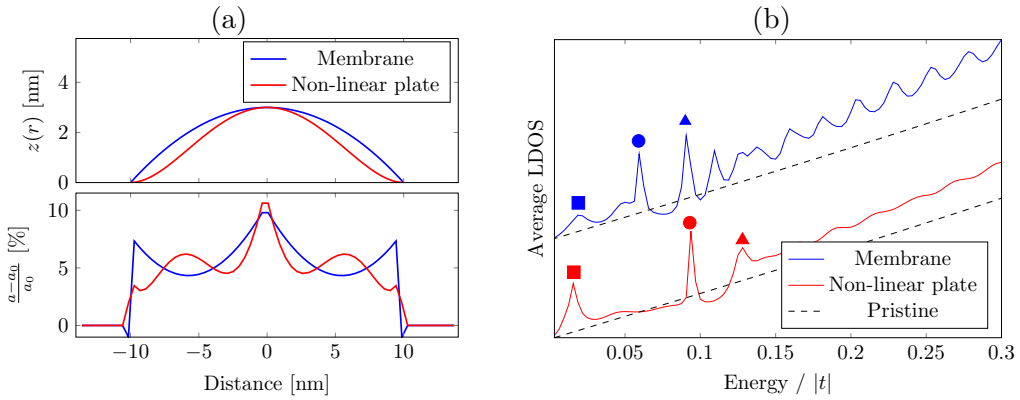

Figure 5.16: (a) The radial height and strain profile for the membrane and non-linear plate model. (b) The average DOS with the two bubble models (membrane and non-linear plate) with $R = 10$ nm and $h_0 = 3$ nm. Important peaks in each are highlighted by symbols and corresponding real space LDOS maps are shown in Fig. 5.17.

level features observed in Fig. 5.16b. In the non-linear plate model, the center of the bubble has a field distribution similar to that of the membrane case, and the central region of the LDOS map in Fig. 5.17 (red, circle) resembles that of the corresponding membrane model peak (blue, circle). The Friedel features for the high energies in Fig. 5.16b (triangle) are more blurred than for the membrane case, as expected for scattering from a less-sharp bubble edge. It seems that bubble shapes which reduce Friedel oscillations also effectively remove pseudomagnetic Landau effects due to the less uniform PMFs induced by their strain profiles.

Finally, we note that the low energy peaks (square symbol) are localized at the edges in both bubble types. It is not directly related to pseudomagnetic effects, but emerges due to the interface between the pristine graphene region outside the bubble and the strained, perturbed region within. The presence of localized states at this boundary acts somewhat like a potential, and induces the scattering which lies behind the Friedel oscillations in these bubbles. We note that these states in the non-linear plate bubble are far less localized than their membrane bubble counterparts, due to an edge which is no longer as sharp. This in turn leads to the smoothening and averaging out of the Friedel oscillations that we observed earlier for the non-linear plate bubbles. Soft-edged bubbles therefore display weaker interference effects, however their shape profiles also resulted in pseudomagnetic field distributions unsuitable for pseudo-Landau level formation. Our results therefore suggest that it will be difficult to obtain reliable Landau level features in such gas inflated systems, unlike bubbles formed on substrates which often display the triaxial-type strain giving rise to a more constant PMF suitable for the formation of Landau levels.

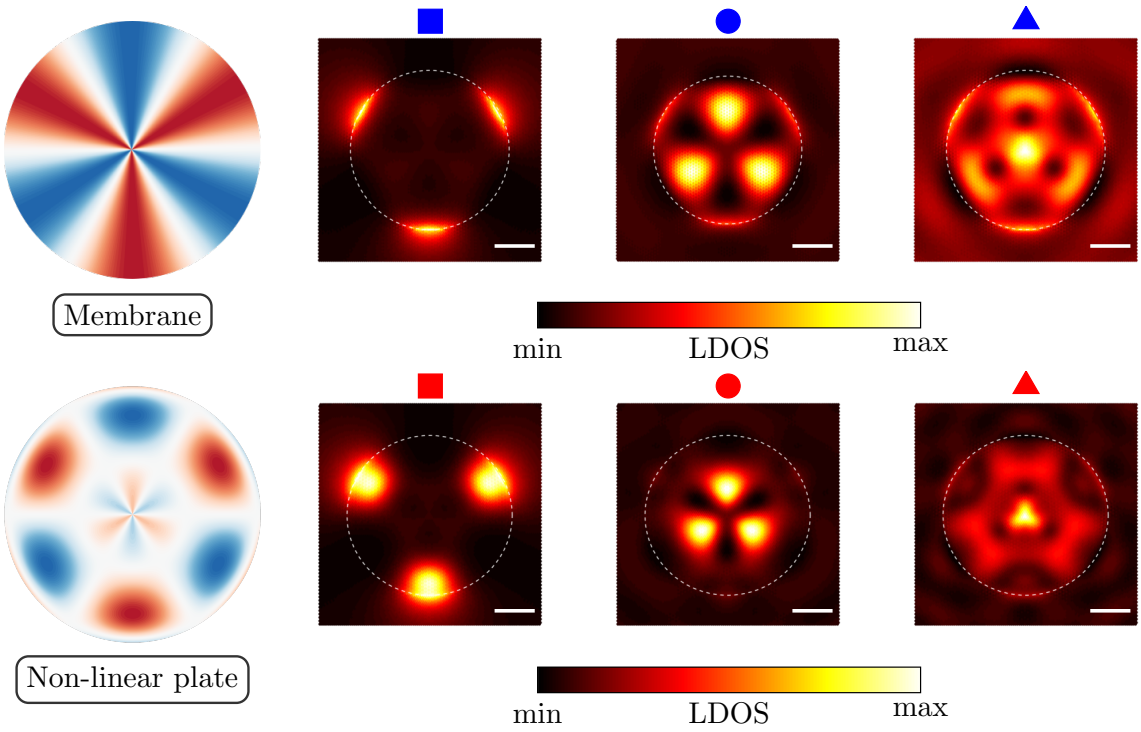

Figure 5.17: The PMF distributions for (top) membrane and (bottom) non-linear plate model. Real space LDOS maps for sublattice A for the peaks highlighted in Fig. 5.16a. The scale bar in all LDOS maps is 5nm.

5.6 Transport through individual pseudomagnetic dots

In the previous sections we have considered features in the density of states. In this section, we now turn to the transport properties of pseudomagnetic dots. Previous studies have considered the transport through nanobubbles in graphene nanoribbons [178] or situations where the whole system is subjected to a constant PMF [179, 180]. The latter is an example of systems containing Landau quantization where the first introduce the strain fields into a nanoribbon making analysis less transparent as the PMF effect competes with the general nanoribbon features. Instead, we embed the local deformations into an infinite sheet by using the *patched Green's function method* derived in Chapter 2. The two probes are placed on opposite sites of the deformation as shown in Fig. 5.18 and we use flat probes coupling to an area of $1-2$ nm^2 to ensure that the setup corresponds to the impinging of a plane wave onto the deformation. We focus on systems which do *not* give rise to ordinary pseudo Landau levels quantization like those discussed in Section 5.3, as these are difficult to obtain for more experimental relevant strain profiles as discussed in Section 5.5.2. In consequence, we consider PMFs giving rise to quasi bound states and discuss the current flow trough these.

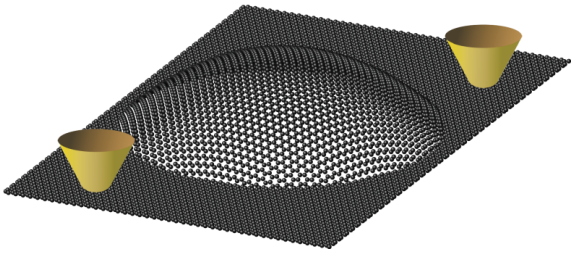

Figure 5.18: Artistic sketch illustrating the dual probe setup around a strained bubble (dot).

5.6.1 Gauss height profile

We start by considering the Gaussian height profile as introduced in Section 5.4. It has a threefold symmetric PMF causing the same sublattice polarization in the LDOS as the membrane bubble. The main difference between this bubble model and the others treated in this thesis, is that the Gaussian height profile does not have sharp edge features. Furthermore, the magnetic type states leading to the form of pseudo Landau levels discussed for the membrane bubble requires very extreme parameter choices. We therefore focus on a situation with moderate strain. Using $h_0 = 3$ nm and $\sigma = 5$ nm gives a maximum strain of approximately $\epsilon \sim 6\%$. In this way, we use the Gaussian height profile as an example of a strain profile without significant Friedel type effects as discussed in the last section for the membrane and non-linear plate model. Consequently, we see no sharp edge features in

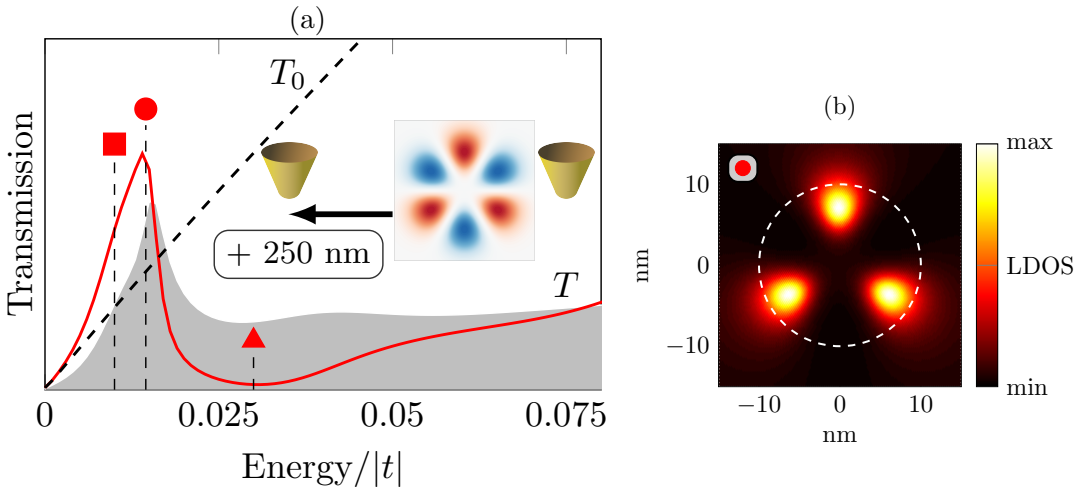

Figure 5.19: (a) Transmission between two probes $\sim$ 300 nm apart with a locally deformed region giving rise to a PMF in between. The setup is schematically shown in the inset. The shaded area corresponds to the average LDOS within the strained region. The marks corresponds to the bond current maps in Fig. 5.20. (b) The real space LDOS map for sublattice B at the energy corresponding to the energy marked by the circle. The white dashed line denotes the $r = 2\sigma$ region.

the LDOS distribution, see Fig. 5.19b. Similar to the membrane model studied in the last section, the Gaussian height profile also gives rise to sublattice polarization. Evidently, the LDOS map in Fig. 5.19b contains only one sublattice and we obtain a similar map for the opposite sublattice by 60°-rotation.

We consider the dual probe setup shown in the inset of Fig. 5.19a and calculate the transmission between the probes. Fig. 5.19a shows both the transmission through strained region and the average LDOS within it. When we discuss the transmission curve it is worth remembering the position of the probes compared to the bubble. The input probe is placed far away from the bubble ensuring a plane wave impinging on the bubble region. The second probe is placed along the same line (x-axis) but much closer to the bubble region. Therefore the transmission reflects the scattered electron flow from an incoming plane wave in the x-direction. If the second probe is moved around the bubble region, the transmission spectrum changes reflecting the electrons scattering in different directions.

From Fig. 5.19a, we first notice that the increased DOS is accompanied by a focusing of the electron flow. The focusing makes the transmission in the presence of the bubble larger than the pristine transmission. Similarly, we observe energies where the transmission is strongly suppressed blocking the electron flow through the bubble.

To study the transmission spectrum in more detail we calculate the bond currents leaving the farthest probe (250 nm from the bubble). The real space bond current maps corresponding to the highlighted energies in Fig. 5.19a are shown in Fig. 5.20a-c. The

current direction is indicated by the arrow and the relative size of the bond current compared to the pristine value, $|J|/|J_0|$, is given by the colormap. In Fig. 5.20a, we associate the initial focusing with a vortex pattern concentrated in the opposite side of the bubble compared to the incoming wave. We show this situation schematically in the inset of Fig. 5.20d. Furthermore, we plot $|J|/|J_0|$ a distance of 5 nm from the bubble region, as a function of the angle ϕ with the x-axis. The angular scattering of Fig. 5.20a is shown in Fig. 5.20d. We note a significant increase in current at $\phi = 0^\circ$ caused by the two vortices at the right side of the bubble. However, the focusing is quite broad with a minimum at $\phi = 90^\circ$

As we increase the energy further, different vortices come into resonance. For the transmission peak highlighted by the circle in Fig. 5.19a we observe a narrower pseudomagnetic focusing effect through the bubble. The electron flow is directed into a narrow flow by six counterrevolting votices as shown in the inset of Fig. 5.20e. Here the angular scattering in Fig. 5.20e reveals that electrons are guided into the region $\phi \approx \pm 30^\circ$. Furthermore, we observe small directional peaks at $\phi \approx \pm 60^\circ$ (zigzag direction) which correspond to the line where two counterpropagating vortices meet. The two small side peaks are therefore an "in-going" current into the bubble region caused by the two vortices.

Finally, we consider the suppression of the transmission highlighted by the triangle in Fig. 5.19. The bond current map in Fig. 5.20c reveals a current in the bubble region. However, the current is guided away from direct transmission along the x-axis. In this way, the angular scattering 5 nm away from the bubble reveals a significant current at $\phi \approx \pm 120^\circ$. Comparing the angular scattering (Fig. 5.20f) with the bond current map (Fig. 5.20c) shows that the peaks at $\phi \approx 120^\circ$ reflect an overall avoidance of the bubble region leaving the transmission suppressed.

Fig. 5.20 demonstrates a pseudomagnetic focusing of the current through a rotationally symmetric bubble. Similarly, we observed an anti-focusing where the current avoids the strained region depleting the current after the bubble. Controlling the strain or the electron energy enables switching between the focusing and anti-focusing regime. However, the Gaussian height profile does not show any pseudomagnetic Landau-like states which we observed in relation to the membrane bubble in the previous section. Furthermore, the Gaussian bump creates a smooth transition into the pristine graphene sheet; therefore no sharp edge effects are observed which we found to be very important in relation to the more realistic gas-inflated bubbles. The effect of both sharp edge features and pseudomagnetic Landau-like states are discussed in the next section treating the bubble using the membrane model.

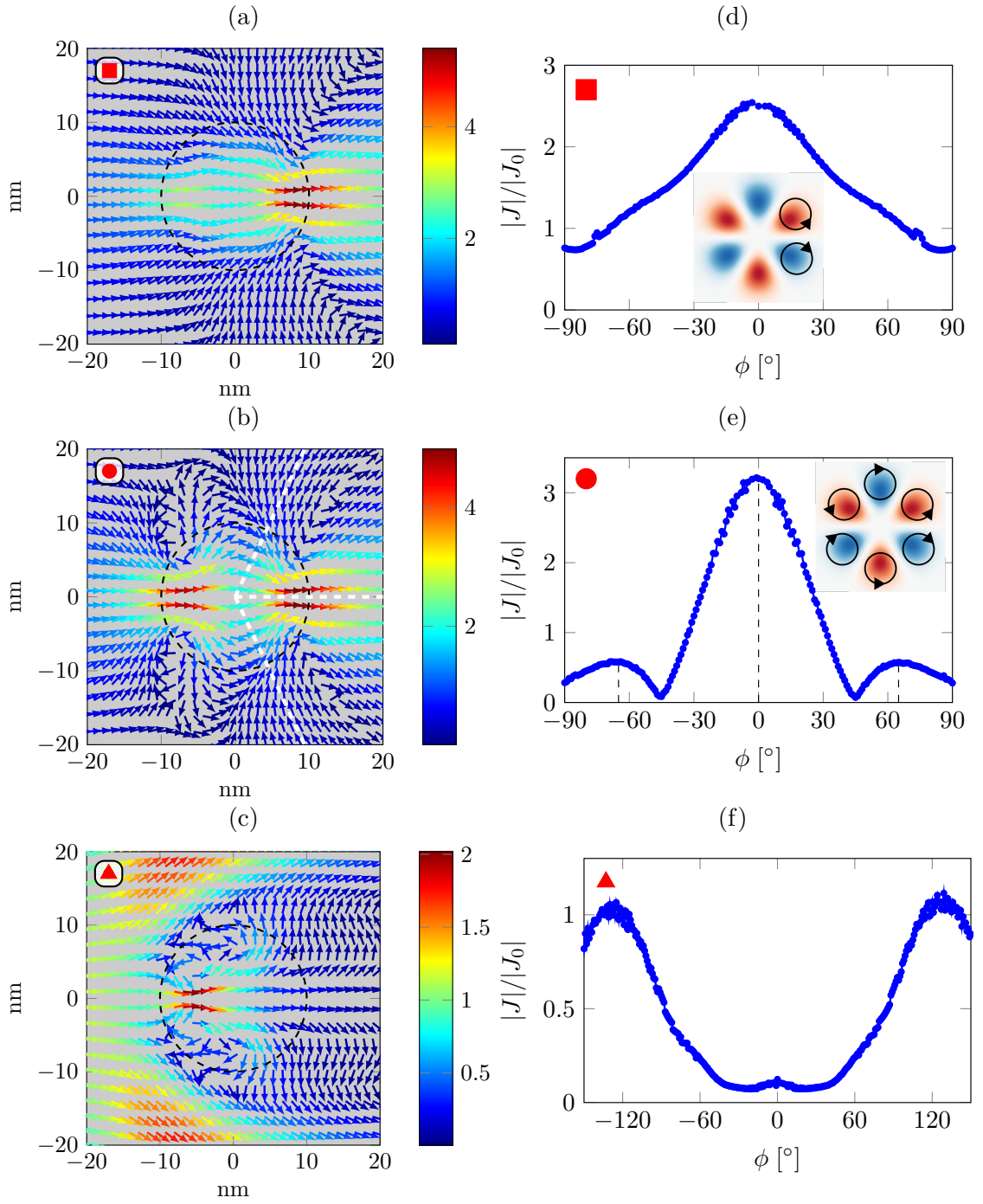

Figure 5.20: (a-c) The bond currents incoming from the left for the marked points in Fig. 5.19. The arrows indicate the direction of the electron flow, whereas the color denotes the magnitude of the current. Each arrow is a sum of the individual bond currents around the position of the arrow. (a) The focusing through the center of the bubble from two vortices. (b) The peak of the transmission (see Fig. 5.19) through the bubble caused by a 6-fold vortex pattern comparable to the PMF distribution. The dashed white lines correspond to the highlighted angles in (e). (c) The suppression of electron flow trough the bubble. (d-f) The size of the bond current relative to the pristine case 5 nm away from the gated region for the cases in (a-c). Here $\phi = 0°$ corresponds to the x-axis. The bubble size is indicated by the dashed line corresponding to $r = 2\sigma$. Parameters for the strain profile are $h_0 = 3$ nm and $\sigma = 5$ nm.

5.6.2 Membrane bubble model

We now turn to the membrane bubble model with the same parameters used previously ($R = 10$ nm and $h_0 = 3$ nm). We consider a similar setup as in the previous section, with the Gaussian strain profile replaced with the membrane, see Fig. 5.21a. The transmission between two probes is given in Fig. 5.21b. At first we notice the similarity with the transmission through the Gaussian strain profile. The initial increase of the DOS within the strained region is accompanied by an increased transmission even surpassing the pristine value. In contrast to the Gaussian strain profile the first transmission peak does not correspond to a LDOS map closely resembling the PMF distribution. For the membrane model the first peak in the DOS is mainly caused by an increased DOS at the edge. Calculating the bond currents and angular scattering for this peak (Figs. 5.22a and 5.22c), we notice that the angular scattering is very similar to the one obtained for the Gaussian profile with a focusing of the current flow through the center of the bubble. This focusing is caused by a very different bond current pattern compared to the Gaussian bump. The membrane model generates two counterpropagating vortices at the edge of the bubble. These two vortices are located where the LDOS is high, see inset of Fig. 5.21b. The focusing effect caused by the vortices at the edges is similar to the one caused by the potential discussed in Chapter 4 and since they are located on the left side of the bubble, the angular scattering becomes quite broad albeit strongest at $\phi = 0°$.

After the first peak, the transmission decreases following the trend seen for the Gaussian bump. However, the membrane model gives rise to several modes in the DOS related to the standing wave patterns in the bubble region. The next peak is therefore associated with the higher order mode where the increased DOS in the bubble region is followed by

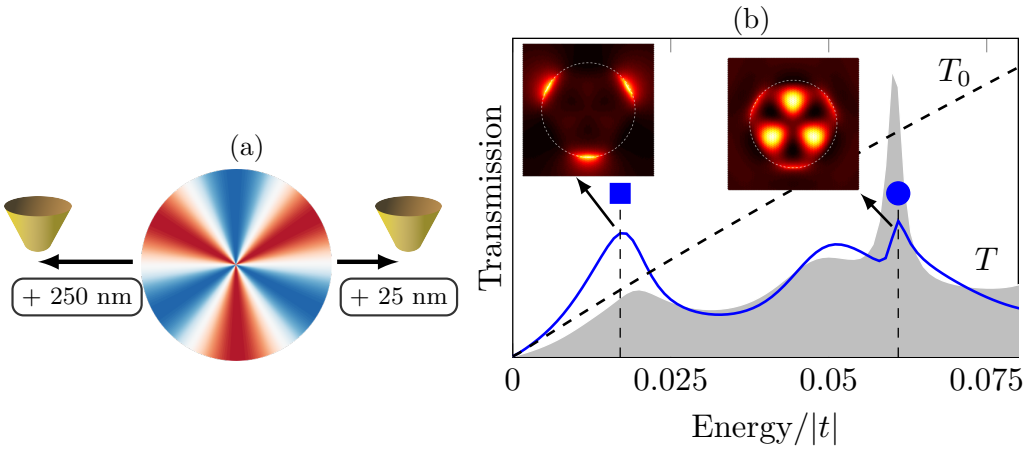

Figure 5.21: (a) Schematic of the dual probe setup with a membrane bubble in between. (b) Transmission spectrum for the dual probe setup in (a) using bubble parameters $R = 10$ nm and $h_0 = 3$ nm. The shaded area indicate the average DOS in the bubble region. The symbols correspond to the bond current maps in Fig. 5.22a-b and the insets show the real space LDOS map for one sublattice at the given energy.

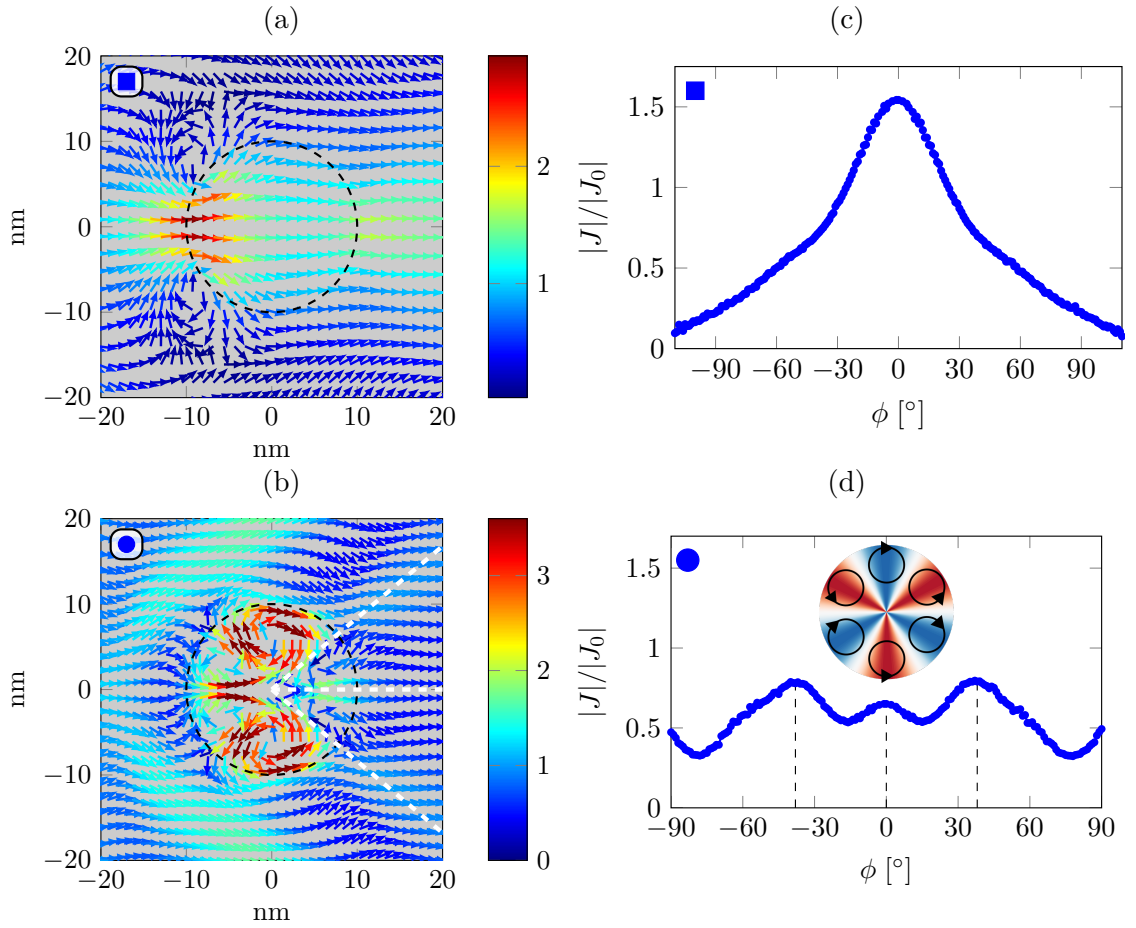

Figure 5.22: (a-b) The bond currents incoming from the left for the marked points in Fig. 5.21. Here the arrows indicate the direction of the electron flow, whereas the color denotes the magnitude of the current. Each arrow is a sum of the individual bond currents around the position of the arrow. (a) The current focusing through the center of the bubble at the first transmission peak caused by a vortex pattern at the bubble edge. (b) The Landau-type state with a six-fold vortex pattern guiding the current. The dashed white lines correspond to the highlighted angles in (d). (c-d) The size of the bond current relative to the pristine value as a function of the angle ϕ with the x-axis 5 nm away from the bubble region for the cases in (a-b). The bubble size is indicated by the dashed line at $r = R$. Parameters for the strain profile are $h_0 = 3$ nm and $R = 10$ nm.

an increased focusing through the pseudomagnetic dot. In addition, we notice a distinct peak at the position of the first pseudo-Landau type state highlighted by the circle. The bond current map at this energy is shown in Fig. 5.22b. Here we identify the six-fold vortex pattern as schematically shown in the inset of Fig. 5.22d. This also shows a very general feature of current paths in pseudomagnetic dots: the current tends to be largest in regions in between the positive and negative fields similar to a snake like current in real magnetic fields. This was also observed in studies of bandgap opening using strain [147]. The distinct vortex pattern gives rise to three preferred scattering directions, see

Fig. 5.22d. Surprisingly these directions do no correspond to transition lines at $\phi = \pm 60°$ between the negative and positive PMF (zigzag direction). Investigating the bond current map we notice that the central vortex is dominating and almost suppresses the rightmost vortices. The current in the central vortex is guided at the bubble edge leaving the bubble region approximately at armchair directions $\phi = 30°$.

Fig. 5.22a demonstrates how the sharp edge features give rise to a focusing of the current similar to the pseudomagnetic focusing seen for the Gaussian height profile in the previous section. Furthermore, Fig. 5.22b considered the Landau-type states of the membrane bubble. This reveals a pseudomagnetic guiding of the current in a clearly formed vortex pattern corresponding to the PMF, but the pseudomagnetic focusing is not as obvious as for the Gaussian bump. However, the vortex patterns responsible for the focusing and guiding effects only correspond to the PMF in one of the valleys. This opens the possibility of manipulating the valley degree of freedom. We discuss this in further detail in the next section.

5.6.3 Pseudomagnetic valley filtering

We have considered both the Gaussian and membrane strain profile and their effect on the current through the resulting PMF. In both cases we find vortex patterns when considering the bond current maps. These vortices are associated with spatial regions experiencing a

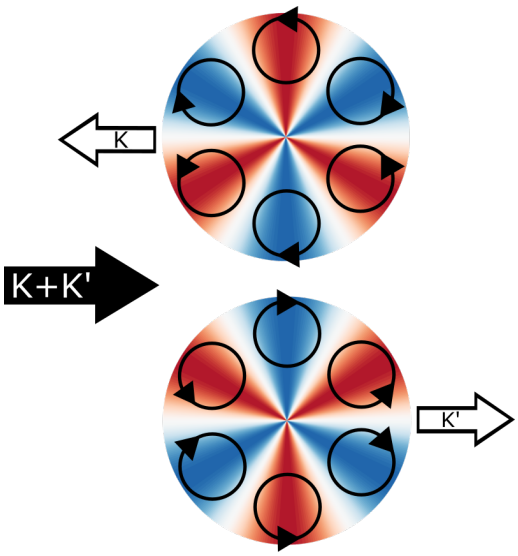

Figure 5.23: Schematic of an the incoming wave containing both valleys impigning on a bubble where each valley experience opposite PMFs. The PMF in the $\boldsymbol{K}$ and $\boldsymbol{K}'$ valleys results in enhanced reflection of the $\boldsymbol{K}$ valley and enhanced transmission of the $\boldsymbol{K}'$ valley.

specific PMF. This can be explained by classical electron trajectories in a magnetic field. Each direction of the PMF can be associated with a vortex (or magnetic orbital) in a given direction. When we change the energy different vortices come into resonance giving rise to the current paths. However, each spatial region experiences both a positive and a negative PMF corresponding to the $\boldsymbol{K}$ and $\boldsymbol{K}'$ valley. Only one of the valleys experiences a PMF matching a transmitting vortex pattern as schematically shown in Fig. 5.23. The valley where the sign of the PMF does not match transmission will preferentially be backscattered. In conclusion, the incoming wave contains both valleys, but since the two valleys experience a different PMF they get scattered differently. Effectively, we conclude that the rotationally symmetric strain fields resulting in three-fold symmetric PMFs should increase the presence of one valley upon transmission – the signature of a valley filter. The manipulation of the valley degree of freedom is commonly referred to as valleytronics [156] and the realization mechanisms creating valley polarized current is a necessary requirement. Valley filters have been suggested by different means such as nanoribbon constrictions [181], strained waveguides [182] or special grain boundaries [183, 184].

5.6.4 Finite triaxial strain

Finally, we turn to the finite triaxial strain introduced in Section 5.4. The dual probe setup is shown in Fig. 5.24a together with the transmission spectrum and average DOS in the strained region (Fig. 5.24b). As mentioned earlier, the Gaussian decay of the triaxial strain causes an inhomogeneous PMF that does not give rise to pseudo-Landau levels unless the strained region is significant larger than a nanobubble. Instead, we focus on a relatively small strained region ($\sigma = 5$ nm) giving rise to quasi bound states as observed from the DOS in Fig. 5.24b. These quasi bound states are roughly regularly spaced and are evidently not equivalent to pseudo-Landau levels.

At first, we consider the transmission peak highlighted by a square in Fig. 5.25b. This peak does not correspond directly to a peak in the DOS. We calculate the bond current map together with the angular scattering at $r = 2\sigma$ (Figs. 5.25a and 5.25d). We clearly notice a focusing through the strained region similar to the one observed for the previous bubble models. However, no vortex pattern is visible and the angular scattering decays smoothly from a maximum at $\phi = 0°$ to $\phi = \pm 90°$.

If we now consider the peaks in the DOS, we notice that these are associated with asymmetric dips or Fano-type resonances in the transmission. This is true for all of the sharp DOS peaks where the lifetime of the quasi bound state is long corresponding to narrow peaks in energy space. For the broad peaks we no longer observe the characteristic asymmetric dip in the transmission after the peak. Instead we experience a regular trans-

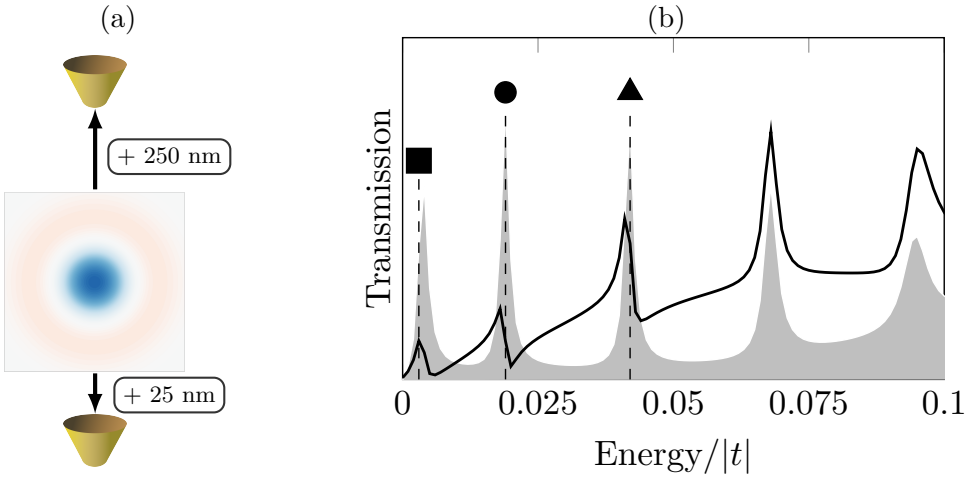

Figure 5.24: (a) Schematic showing the dual probe setup with a finite triaxial strained region in between. (b) Transmission spectrum for the dual probe setup where the shaded area indicate the average DOS in the strained region. The symbols correspond to the bond current maps in Fig. 5.25a-c and the strain profile uses the parameters $\sigma = 5$ nm and $u_0 = 10^{-5}$ nm^{-1} corresponding to a maximum PMF of ~ 300 T in the center of the strained region and a maximum strain of $\epsilon \sim 2.5\%$.

mission peak at the same energy of the peak in the DOS. Now turning to the bond current map for the second peak in the DOS (circle), we observe a different behavior compared to all the previous cases, see Fig. 5.25b. Here transmission dip is caused by a splitting of the current. As a result, we see two preferred scattering directions at $\phi = \pm 90°$. As indicated by the inset in Fig. 5.25e this can be explained by the bending of the trajectory caused by either the positive or negative PMF associated with the two valleys. Following this argument the strain field leads to a "beam splitter" not only separating the current in two, but also separating depending on valley.

At last we consider the third peak in the DOS (triangle), which also gives rise to a transmission dip. Fig. 5.25f reveals multiple preferred scattering directions at $\phi = 0, \pm 60°, \pm 90°, \pm 120°$. From the bond current map in Fig. 5.25c, we see that it is a result of a snake like current running around the strained region. The peaks at $\phi = 0, \pm 60°, \pm 120°$ corresponds to "outgoing" currents whereas the peaks at $\phi = \pm 90°$ are caused by a current flow into the strained region. The snake like current path can be understood as the second order mode corresponding to the beam splitting one. The current is not just bending once, but makes a full period as shown schematically in the inset of Fig. 5.25f giving rise to the multiple scattering directions.

The calculations in Fig. 5.25 demonstrates different transport features for quasi bound states in pseudomagnetic dots. Such quasi bound states have also been discussed for real magnetic dots [172, 185]. Each quasi bound state is associated with an asymmetric transmission peak focusing the current after the dot. However, at resonance the quasi bound states give rise to trajectories connected to the B-field experienced in the different regions of the pseudomagnetic dot. These trajectories give rise to intriguing effects such as snake currents around the dot and beam splitting with suggested valley polarization. This demonstrates the possibilities for pseudomagnetic current guiding in locally strained regions by manipulating both the current trajectories and valley degree of freedom by a single pseudomagnetic dot. However, the interaction between such pseudomagnetic dots is still unexplored together with the average effect of an ensemble of such dots. The latter is the focus of the next section where we go beyond the dual probe investigation of single pseudomagnetic dots and instead consider a full array using an order-N method based on the Kubo-Greenwood formalism.

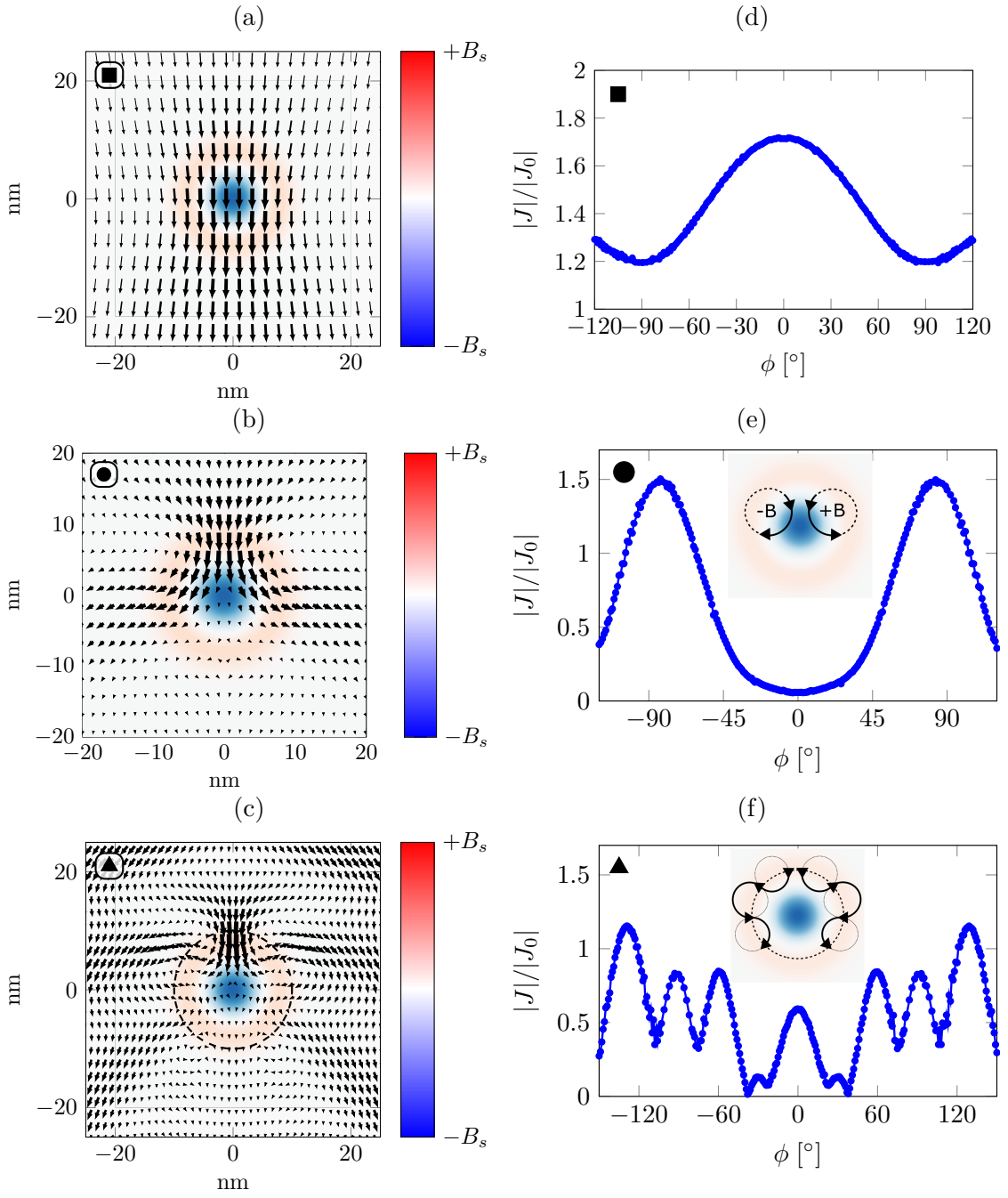

Figure 5.25: (a-b) The bond current maps for a finite strained region at the energies marked in Fig. 5.24. The arrows indicate the direction and the color denotes the magnitude of the current. Each arrow is a sum of the individual bond currents around the position of the arrow. (a) The bubble focusing through the center of the bubble associated with the first transmission peak. (b) The current is split by the PMF at the second peak in the DOS. (c) The third peak in DOS causes a snake like current path around the strained region. The dashed line corresponds to $r = 2\sigma$. (c-d) The size of the bond current relative to the pristine value at $r = 2\sigma$ as a function of the angle ϕ with the y-axis. The strain profile uses the parameters $\sigma = 5$ nm and $u_0 = 10^{-5}$ nm^{-1} corresponding to a maximum PMF of ~ 300 T at the center of the strained region.

5.7 Pseudomagnetic dot arrays

Until now we have considered individual bubble-like deformations using LDOS and bond currents. In this section we briefly consider a periodic array of pseudomagnetic dots supporting pseudo-Landau levels. Such arrays have been proposed experimentally by exploiting substrate interactions [151] or actual substrate nanostructuring [163].

The methods developed for multiple probes in Chapter 2 focused on calculating *local* and nanoscale transport properties, however, this makes them ill suited for studying large periodic features. Instead, we apply the popular Kubo-Greenwood propagation method [15, 186–188]. This approach has been successfully applied to a wide range of graphene systems including polycrystalline samples [189, 190] and samples including chemically doping [116, 191] or other type of defects [192–197]. As opposed to the patched Green's function method, the calculation approach based on the Kubo-Greenwood formula only allows for the calculation of average sample properties. Consequently, the effect of probes or leads is not described by such an approach. Likewise we cannot directly use the Kubo-Greenwood formalism to describe local properties. However, using this approach we can calculate the properties of samples containing millions of atoms effectively treating "lab-sized" systems. Below we briefly outline central concepts of the Kubo-Greenwood propagation method and then apply it to analyze the conductivity of a periodic array of pseudomagnetic dots supporting Landau quantization.

5.7.1 Kubo-Greenwood propagation methods - a quick safari

In linear response theory the Kubo-Greenwood formula for the diagonal DC conductivity, σ_{xx}, reads [15],

$$\sigma_{xx}(\omega) = \frac{2\pi e^2\hbar}{\Omega}\int_{-\infty}^{\infty} \mathrm{d}E \frac{f(E) - f(E-\hbar\omega)}{\hbar\omega} \mathrm{Tr}\Big[v_x\delta(E-\mathcal{H})v_x\delta(E+\hbar\omega-\mathcal{H})\Big], \quad (5.33)$$

where Ω is the area of the sample and v_x is the x component of the velocity operator. The factor of 2 accounts for the spin degeneracy. Limiting ourselves to the case of zero temperature and zero frequency, Eq. (5.33) reduces to

$$\sigma_{xx}(E) = \frac{2\pi e^2\hbar}{\Omega}\mathrm{Tr}\Big[v_x\delta(E-\mathcal{H})v_x\delta(E-\mathcal{H})\Big]. \quad (5.34)$$

We now introduce the mean square spreading of the wavefunction, which is a central quantity for numerical evaluation of Eq. (5.34)

$$\Delta X^2(E,t) = \big\langle (X(t) - X(0))^2 \big\rangle, \quad (5.35)$$

where $X(t) = U^\dagger(t)XU(t)$ is the position operator in the Heisenberg representation and $U(t) = \mathrm{e}^{-\mathrm{i}\mathcal{H}t/\hbar}$ is the time evolution operator. We can show that the conductivity can be expressed using this mean square spreading [15, 198]

$$\sigma_{xx} = \frac{1}{2}e^2\rho(E)\lim_{t\to\infty}\frac{\mathrm{d}}{\mathrm{d}t}\langle\Delta X^2(E,t)\rangle \approx \frac{1}{2}e^2\rho(E)\lim_{t\to\infty}D_x(E,t), \tag{5.36}$$

where the density of states is $\rho(E) = \mathrm{Tr}\big[\delta(E-\mathcal{H})\big]/\Omega$ and we have introduced the diffusion coefficient in the last equation

$$D_x(E,t) = \frac{\langle\Delta X^2(E,t)\rangle}{t}. \tag{5.37}$$

For the isotropic case we usually consider $D(E,t) = D_x(E,t)+D_y(E,t) = 2D_x(E,t)$ when calculating the conductivity.

From Eq. (5.36), we conclude that the central object in the calculation is the mean square spreading of the wavepacket, $\Delta X^2(E,t)$. We can express this quantity conveniently as [15]

$$\begin{aligned}\Delta X^2(E,t) &= \frac{\mathrm{Tr}\Big[\delta(E-\mathcal{H})(X(t)-X(0))^2\Big]}{\mathrm{Tr}\Big[\delta(E-\mathcal{H})\Big]}\\ &= \frac{\mathrm{Tr}\Big[[X,U(t)]^\dagger\delta(E-\mathcal{H})[X,U(t)]\Big]}{\mathrm{Tr}\Big[\delta(E-\mathcal{H})\Big]},\end{aligned} \tag{5.38}$$

where we have used the relation $X(t) - X(0) = U^\dagger(t)[X,U(t)]$ where $[\cdot,\cdot]$ is the commutator.

A computationally effective method to evaluate the traces in Eq. (5.38) is to take advantage of the self-averaging feature in large systems. If we consider a random phase state of the form

$$|\psi_{RP}\rangle = \frac{1}{\sqrt{M}}\sum_{i=1}^{M}\mathrm{e}^{2\mathrm{i}\pi\alpha_i}|i\rangle, \tag{5.39}$$

where α_i is a random number in $[0,1]$ and $|i\rangle$ is the i-th orbital. For sufficiently large systems self-averaging lets the trace of an operator B be approximated by $\mathrm{Tr}[B] \approx \langle\psi_{RP}|B|\psi_{RP}\rangle$. Using this approximation greatly simplifies Eq. (5.38)

$$\Delta X^2(E,t) = \frac{\langle\psi'_{RP}(t)|\delta(E-\mathcal{H})|\psi'_{RP}(t)\rangle}{\langle\psi_{RP}|\delta(E-\mathcal{H})|\psi_{RP}\rangle}, \tag{5.40}$$

where $|\psi'_{RP}(t)\rangle = [X,U(t)]|\psi_{RP}\rangle$. We notice that the numerator and denominator in Eq. (5.40) have the same form and we can use efficient order-N methods like Lanczos

tridiagonalization [199] or Kernel Polynomial methods[200] to evaluate the traces.In order to obtain the states $|\psi'_{RP}(t)\rangle$, we expand the time evolution operator $U(t)$ in Chebyshev polynomials [186] and propagate the initial random phase state in time. For each time step we use $|\psi'_{RP}(t)\rangle$ to calculate the mean square spread from Eq. (5.40) and the diffusion coefficient from Eq. (5.37). The behavior of $D(t)$ reveals the transport mechanism which can generally be divided into three main regimes: ballistic, diffusive and localization, see Fig. 5.26. In the ballistic regime electrons travel through the system without experiencing any scattering and $D(t)$ remains linear with a slope of v_F^2. The diffusive regime, on the other hand, is characterized by a saturation of $D(t)$ for long times. In this regime, we can use the saturation to define quantities such as mean free path l_e and relaxation time τ. At last, in the localization regime where strong disorder causes quantum interference, we observe a decay of the diffusion coefficient following approximately $\sim 1/t$. In this regime, the mean square spreading $\Delta X(E,t)$ reaches a constant value related to the localization length.

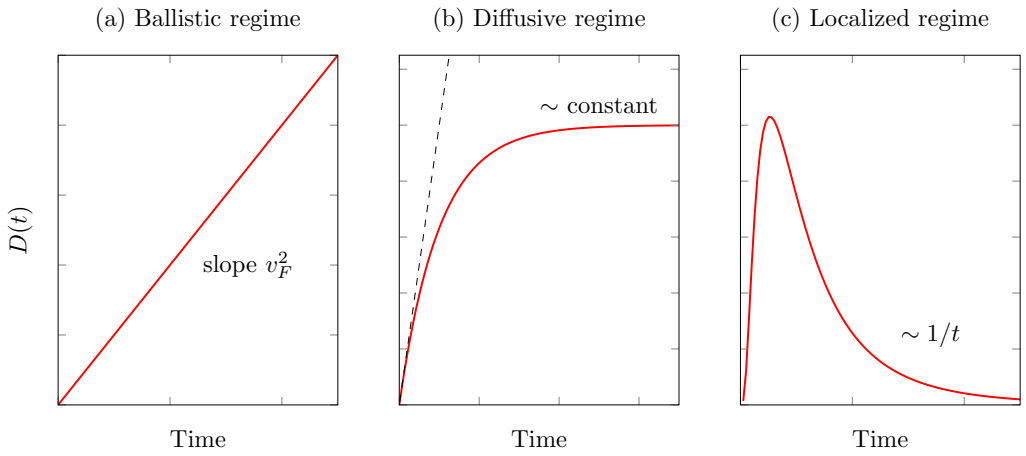

Figure 5.26: Sketch of the typical behavior of the diffusion coefficient for the three characteristic regimes: (a) ballistic, (b) diffusive and (c) localization.

Below we summarize essential quantities and derived quantities like carrier velocity, mean free path and mobility.

Kubo-Greenwood $O(N)$ method

Central quantities for the propagation method calculated at each time step:

$$\text{Mean square spreading:} \quad \Delta X^2(E,t) = \frac{\mathrm{Tr}\Big[\delta(E-\mathcal{H})(X(t)-X(0))^2\Big]}{\mathrm{Tr}\Big[\delta(E-\mathcal{H})\Big]} \tag{5.41a}$$

$$\text{Conductivity:} \quad \sigma_{xx}(E,t) = \frac{1}{2}e^2\rho(E)D_x(E,t) \tag{5.41b}$$

$$\text{Diffusion coefficient:} \quad D_x(E,t) = \frac{\Delta X^2(E,t)}{t} \tag{5.41c}$$

$$\text{Carrier velocity:} \quad v_x(E,t) = \frac{\sqrt{\Delta X^2(E,t)}}{t} \tag{5.41d}$$

$$\text{Propagated length:} \quad L_x(E,t) = 2\sqrt{\Delta X^2(E,t)} \tag{5.41e}$$

Kubo-Greenwood $O(N)$ method - diffusive regime

In the diffusive regime, we assume that $D(E,t) = D_x(E,t) + D_y(E,t)$ saturate at a value $D^{max}(E)$ from which we calculate semi-classical quantities

$$\text{Semi-classical conductivity:} \quad \sigma_{sc}(E) = \frac{1}{4}e^2\rho(E)D^{max}(E) \tag{5.42a}$$

$$\text{Velocity:} \quad v(E) = \lim_{t\to 0}\frac{D(E,t)}{t} \tag{5.42b}$$

$$\text{Mean free path:} \quad l_e(E) = \frac{D^{max}(E)}{2v(E)} \tag{5.42c}$$

$$\text{Relaxation time:} \quad \tau(E) = \frac{v(E)}{l_e(E)} \tag{5.42d}$$

$$\text{Electron mobility:} \quad \mu(E) = \frac{\sigma_{sc}(E)}{e\ n(E)} \tag{5.42e}$$

$$\text{Charge density:} \quad n(E) = \int \rho(E)\mathrm{d}E \tag{5.42f}$$

5.7.2 Superlattice of nanobubbles

In this section we apply the Kubo-Greenwood method presented above to calculate the average sample properties for an array of pseudomagnetic dots. We consider a circular dot with radius R subjected to a triaxial strain profile $\boldsymbol{u} = (u_0 r^2 \sin(3\theta), u_0 r^2 \cos(\theta))$, see Eq. (5.11). Outside this region, we apply a smoothing to the strain tensor making the strain decrease away from the dot. Using a Gaussian decay $\sim \exp\left[-(r-R)^2/2\sigma^2\right]$ for $r > R$ the PMF is effectively zero at $r = R + 3\sigma$ as shown in Fig. 5.27a. As discussed in Section 5.3, the triaxial strain at $r < R$ gives rise to a constant PMF and the smoothing region gives rise to a varying PMF of opposite sign in a ring around the constant region, see Fig. 5.27a. We repeat this pseudomagnetic dot in a periodic array with a lattice constant L as shown in Fig. 5.27b. This system can be considered as an idealized example of the array of self-formed bubble deformations showing pseudo Landau level signatures envisioned experimentally by J. Lu *et al.*[151].

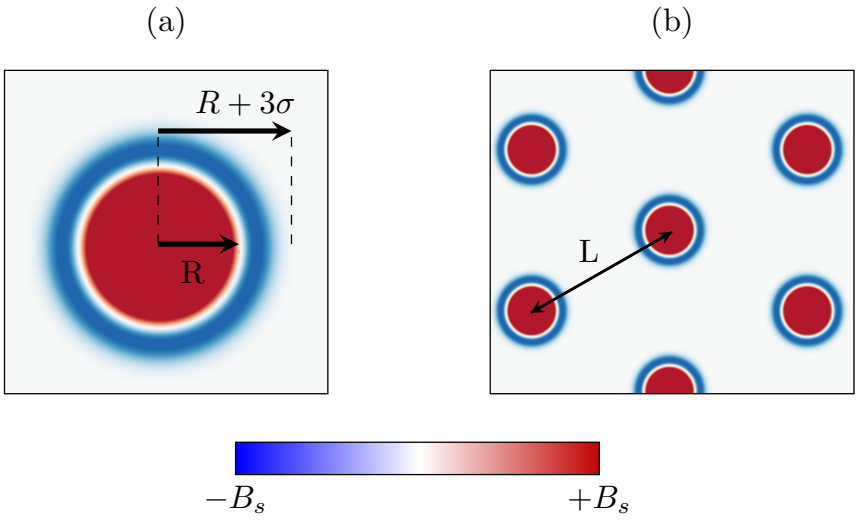

Figure 5.27: (a) A single pseudomagnetic dot showing the region of constant PMF surrounded by a region with PMF of opposite sign. (b) The superlattice of pseudomagnetic dots with a littice constant L..

In the calculations presented below, we use a sample containing 6.4×10^6 atoms corresponding to a sample size of approximately 400 nm $\times$ 350 nm. The state propagation uses time steps of $\Delta t = 10$ fs and a total simulation time $t_{max} = 7.5$ ps. The expansion of the time evolution operator uses Chebyshev polynomials corresponding to coefficients larger than 10^{-12}. Finally, the traces are approximated via the initial phase state and the Lanczos method using 2000 iterations with a broadening included through an imaginary part of $\eta = 5$ meV.

To attain convergence and enforce a saturation of the diffusion coefficient, we furthermore superimpose a random distribution of long range disorder [194, 201]. We consider

impurities with onsite energy $V_n = \sum_i \epsilon_i e^{-|\boldsymbol{r}_n - \boldsymbol{r}_i|^2/(2\xi^2)}$ where $\boldsymbol{r}_i$ is the center of the i-th impurity, the maximum onsite energy is $\epsilon_i \in [-W/2, W/2]$, $W = 2|t_0|$ and $\xi = \sqrt{3}a$ with $a = 0.245$ nm. To ensure that the pseudomagnetic dots are the dominant source of scattering we use a low impurity concentration of $c = 0.01\%, 0.05\%$ and 0.1%.

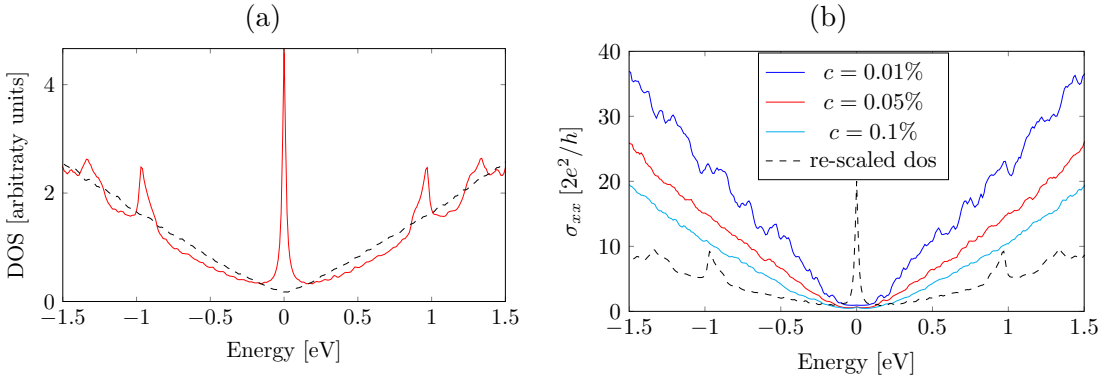

Figure 5.28: (a) Density of states for the strain array with $L = 200a$, $R = 40a$, $\sigma = 10a$ and a strain corresponding to 600 T. The result without the strain array is indicated by the black dashed curve. Both calculations include a 0.05% concentration of long range impurities as explained in the main text. (b) Conductivity, $\sigma_{xx}(E, t_{max})$, for different impurity concentrations. It should be noted that the choice of plotting $\sigma_{xx}(E, t_{max})$ makes the curve dependent on the maximum calculation time. This is mainly important for the low energy regime where localization behavior is observed.

First, we consider the density of states of the pseudomagnetic dot array with $L = 200a$, $R = 40a$ and $\sigma = 10a$ with $a = 0.246$ nm and a strain field corresponding to 600 T (a maximum strain of $\sim 14\%$ for the given dot dimensions), see Fig. 5.28a. With this PMF the characteristic magnetic length is smaller than the dot size and we expect the formation of Landau quantization. Calculating the DOS of the full PMF array (Fig. 5.28a), we clearly see the pseudo-Landau levels and especially the zeroth order peak. The peak features are superimposed with the linear dispersion characteristic of pristine graphene (black, dashed).

To study the transport properties, we first calculate the conductivity, $\sigma_{xx}(E, t_{max})$, for the different impurity concentrations, see Fig. 5.28b. The conductivity decreases with increased impurity concentration for most of the energy spectrum. We immediately notice that the higher order Landau peaks do not translate to special features in the conductivity. To characterize the effect of the pseudo Landau levels at higher energies, we consider the mean free path (Fig. 5.29a) in the diffusive regime as $l_e(E) = D^{max}(E)/2v_F$ where $D(E) = D_x(E) + D_y(E)$ and v_F is taken as the pristine Fermi velocity $v_F = 8.6 \times 10^5$ m/s.

The mean free path with (full) and without (dashed) the pseudomagnetic dot array clearly show features in $l_e(E)$ related to the states in the pseudomagnetic dots. Overall, we observe a decrease of the mean free path, compared to the system without the pseudomagnetic dots, caused by the presence of additional scattering induced by the strain field. Importantly, we furthermore notice significant dips caused by the presence of the pseudo-

magnetic dots corresponding to the pseudo Landau level features. The diffusion coefficient at energies around the first Landau level, shown in Fig. 5.29b, reveals a diffusive transport regime, where the presence of Landau quantization increases the scattering induced on the pristine-like states. The decrease of the diffusion coefficient is, however, compensated by an increase of the DOS, effectively leaving the conductivity unchanged. This reveals that any delocalized Landau states compete with the induced scattering caused by these states upon the pristine behavior and, as evidenced by the dips in the mean free path, the scattering is the most important effect at higher energies.

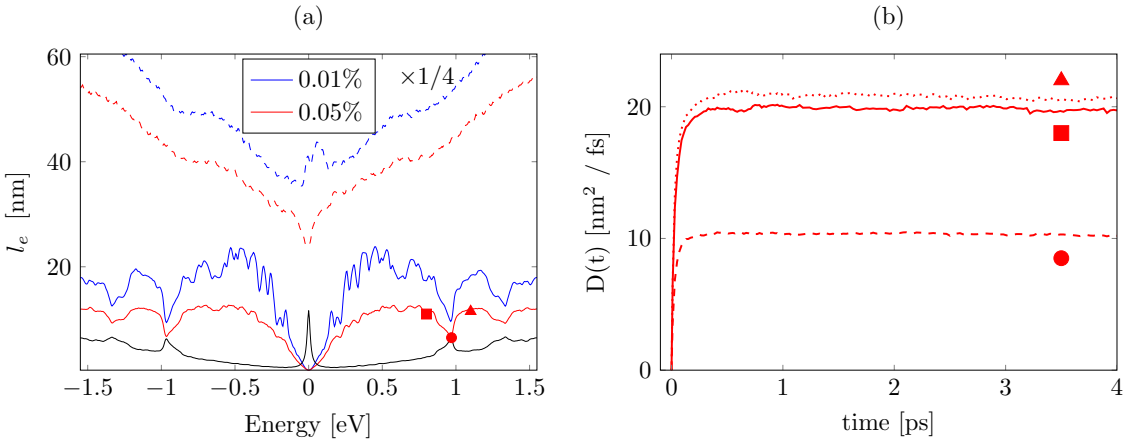

Figure 5.29: (a) The mean free path for impurity concentrations 0.01% (blue) and 0.05% (red). The full lines denote calculations *with* impurities and the dashed curves indicate calculations without. Note that the $c = 0.01\%$ curve is rescaled. The re-scaled DOS is also shown for reference (black curve). (b) The average diffusion coefficient for the energies marked by square, circle and triangle symbols in (a).

Next, we consider the low energy regime around $E = 0$ where the DOS is dominated by the zeroth order pseudo Landau level. This level is special because the pristine DOS vanishes at $E = 0$ and because it exhibits a strong sublattice polarization as discussed in Section 5.3. In Fig. 5.30a-b we show the conductivity and mean free path in the low energy regime for different impurity concentrations. We observe a suppression of the conductivity around $E = 0$ where it even goes below the minimum of the semi-classical value, $\sigma_0 = \frac{4e^2}{\pi h}$ (black dashed). The value of σ_0 has been demonstrated to fix the minimum semi-classical conductivity in disordered graphene systems [196, 202] and separates two different transport regimes. These two regimes can be considered using the time evolution of the diffusion coefficient $D(E,t) = D_x(E,t) + D_y(E,t)$, see Fig. 5.30c-f.

For $\sigma_{xx} > \sigma_0$ the system remains metallic and diffusive which is evident from the diffusion coefficient in Fig. 5.30c (diamond) where all impurity concentrations give rise to diffusive behavior. Decreasing the energy we find energies where the different impurity concentrations give rise to different transport regimes. In this way the energy highlighted by the triangle in Fig. 5.30a exhibits a diffusive regime for the lowest impurity concentration (0.01%) and a weak localization for the higher concentrations (0.05% and 0.1%).

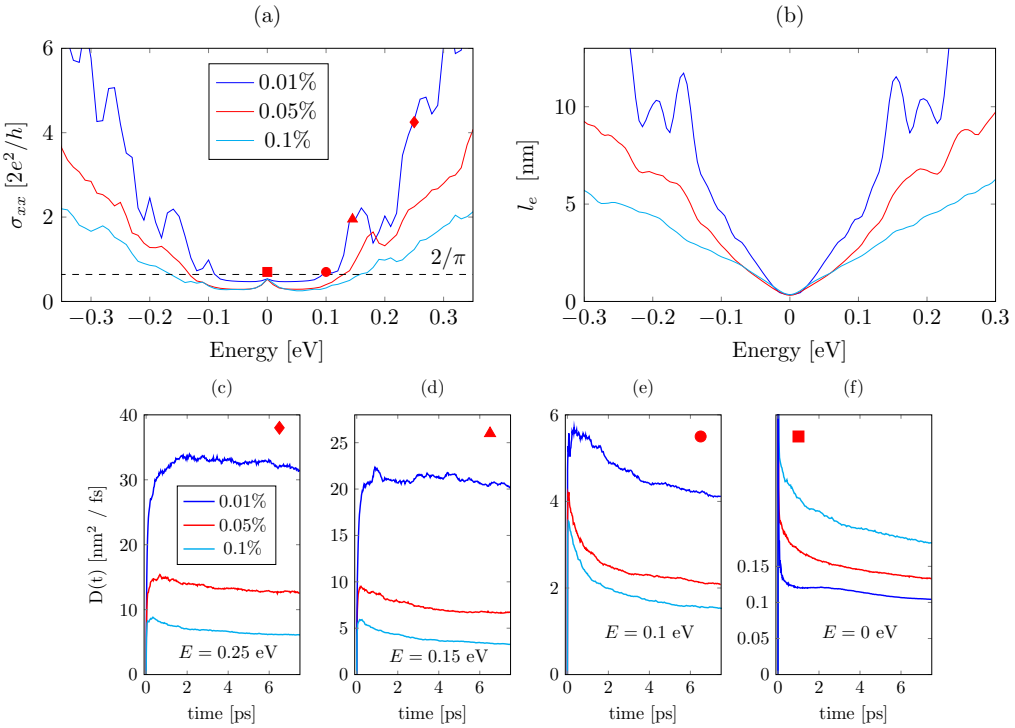

Figure 5.30: (a) A zoom of the conductivities from Fig. 5.28b for different impurity concentrations. The location of the minimum semi-classical conductivity $\sigma_0 = \frac{4e^2}{\pi h}$ is indicated by the horizontal dashed line. (b) A zoom around the Dirac point for the mean free path from Fig. 5.29. (c-f) Time evolution of the diffusion coefficient for different impurity concentration at the energies marked by (c) diamond, (d) triangle, (e) circle and (f) square in (a).

On the other hand, when $\sigma_{xx} < \sigma_0$ on Fig. 5.30a all impurity concentrations give rise to a similar transport regime. We notice that the diffusion coefficient reaches a saturation regime after 1 ps on Fig. 5.30e indicating a diffusive regime. However, at much longer time scales we observe a time-dependent decay of the diffusion coefficient regardless of impurity density, hence, indicating the existence of weak localization effects. Indeed the low energy regime exhibits a transition from diffusive to localization behavior, however, it is unlikely that the pseudo-Landau levels generate an actual metal-to-insulator transition as the localization does not give rise to a specific transition point as seen in relation to the quantized Hall conductance for real magnetic fields. [190, 203, 204].

Finally, we notice the special nature of the Dirac point ($E = 0$). The diffusion coefficient for the Dirac point (Fig. 5.30f) exhibits a qualitatively different behavior compared to the energies around the Dirac point. In Fig. 5.30f, we still observe weak localization behavior but the magnitude of the diffusion coefficients are opposite compared to the other energies shown. At the Dirac point the disorder tends to induce a weak percolation responsible for the larger diffusion coefficient at higher impurity concentrations. This causes

the small peak-like feature at the Dirac point and a similar effect is observed with real magnetic fields in polycrystalline samples [190].

Summarizing we have analyzed the pseudomagnetic dot array supporting pseudo-Landau levels superimposed onto the pristine DOS. The zeroth Landau level at the Dirac point is driving the system towards localization behavior. This suggests the possibility of switching the current at low energy. We could imagine the network of pseudomagnetic dots to be experimentally tuneable by pressure, temperature or similar which would change the mean free path from $\sim$ 160 nm with no strain to the very small values when including strain thus allowing for switching behavior dependent on strain. At higher energies, on the other hand, the Landau states in the pseudomagnetic dots induce significant scattering on the pristine behavior.

5.8 Summary

Triaxial strain and pseudo Landau levels

A triaxial strain along the armchair direction gives rise to a constant pseudomagnetic field which in turn leads to Landau quantization without the presence of a real magnetic field. Using a tight binding approach including the strain through altered hopping parameters, we demonstrated that the pseudomagnetic induced Landau levels followed the usual $\sqrt{Bn}$ behavior of Landau levels for massless Dirac fermions. The zeroth Landau level was shown to only exist on one sublattice depending on the sign of the pseudomagnetic field caused by the strain. Rotation of the triaxial strain with an angle ϕ with respect to the armchair direction resulted in a variation of the pseudomagnetic field, $B_s = B_0 \cos(3\phi)$, causing a transition of the zero order peak to the opposite sublattice for a rotation of $\phi = 60°$.

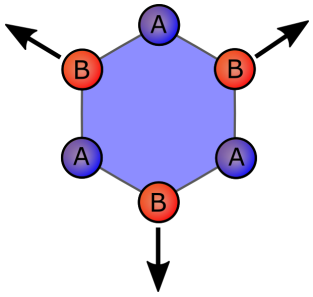

Sublattice polarization and strong edge effects

We studied the local and averaged densities of states in rotationally symmetric graphene bubbles embedded in infinite graphene sheets using the patched Green's function approach. A threefold symmetric pseudomagnetic field was shown to be generic for the rotationally symmetric systems. Furthermore, we demonstrated a distinct sublattice polarization using real space LDOS maps.
We determined that pseudo-Landau level features in sharp-edged bubbles may be hidden by interference effects due to electron scattering at the bubble edges. Softer-edged bubbles were found to display weaker interference effects, however their shape profiles also resulted in pseudomagnetic field distributions unsuitable for pseudo Landau level formation. Our results suggest that it will be difficult to obtain reliable Landau level features in such gas inflated systems.

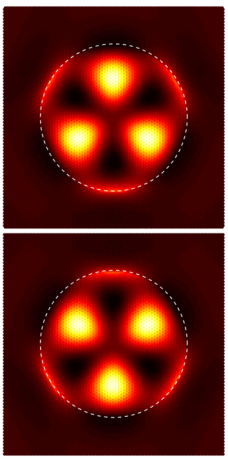

Transport in pseudomagnetic dots

We considered the transport through a rotationally symmetric Gaussian bump and demonstrated pseudomagnetic focusing caused by a vortex pattern corresponding to the PMF distribution. Similarly, we showed an anti-focusing depleting the current after the bubble.

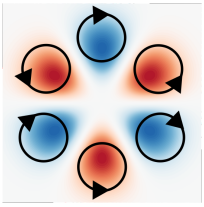

The sharp edge features of the membrane model causing an increased DOS at the bubble edge also exhibited a vortex pattern focusing the current into a broad angle. Besides the edge effects, the membrane bubble showed significant vortex patterns matching the orbitals of the PMF for the pseudo Landau-like states.

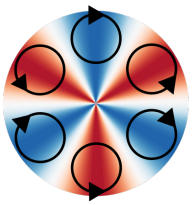

The rotationally symmetric strain field was proposed to act like a valley filter since the two valleys should be scattered differently. The two valleys experience opposite PMFs meaning that only one valley should give rise to trajectories guiding the current through the bubble. In this way, the other valley will be preferentially backscattered.

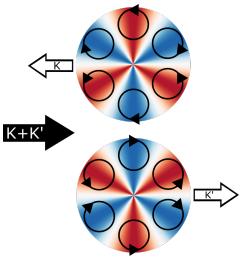

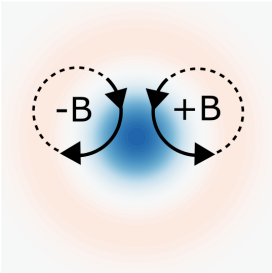

We demonstrated the existence of quasi bound states in a pseudomagnetic dot caused by a finite triaxial strained region. At resonance the quasi bound states give rise to trajectories connected to the spatially varying PMF in the dot. The trajectories showed intriguing effects such as snake current and beam splitting with a suggested valley polarization.

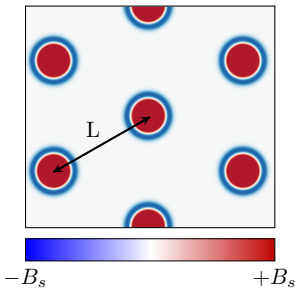

Finally, we considered arrays of pseudomagnetic dots using a Kubo-Greenwood propagation approach which was also briefly summarized. We demonstrated a competition between delocalized pseudo-Landau states and the scattering induced by these states upon the pristine behavior. At higher energies the scattering is the dominant effect decreasing the mean free path at the pseudo-Landau levels whereas the zeroth pseudo-Landau level exhibits localization behavior.

CHAPTER 6

Leaving the phase coherent regime: a mean field approach to disorder

Until now we have only considered the phase coherent regime where the defect or nanostructure is the only source of scattering. The only exception was the Kubo-Greenwood propagation method. However, this method does not allow for inclusion of the probes which is an essential part of the multi-probe setup. Instead we focus on methods which potentially could be combined with the *patched Green's function method*.

Going beyond the coherent regime means that the coherence length becomes comparable or smaller than the characteristic system size, which in our case is the probe separation. In this context, we consider dephasing in the single particle description caused by elastic scattering from defects or impurities other than the main nanostructure. Realistic device materials contain many types of unavoidable and random sources of elastic scattering such as atomistic defects, vacancies, edge roughness etc.

In this chapter we discuss transport in such randomly disordered systems through mean field theory. We introduce the Coherent Potential Approximation (CPA) approach [205] which replaces the disorder average with an effective medium characterized by a self-energy. Extending the CPA theory to transport calculations, we briefly outline the Vertex-Correction (VC) to the transmission through the effective medium. The combined CPA-VC scheme is finally applied to the simple example of substitutional doping in graphene nanoribbons. Here we compare different levels of accuracy within the CPA-VC scheme and their performance while reproducing the results of Ref. [206].

6.1 Mean field theory for disorder

In a randomly disordered system, the device Hamiltonian depends on the configuration of individual defects. Each disorder configuration gives rise to different transport properties and we need to average over many configurations to get the average properties of the

material. Such an average can be carried out by generating many configurations for a given disorder concentration and calculate the transport properties for each individual configuration. However, such brute force analysis is computationally expensive if possible at all. It is therefore desired to obtain the average physical quantities without computing each impurity configuration individually. Aside from only treating systems where the configurational average can be performed with reasonable computational cost, two general approaches exists to deal with this problem.

The first approach is to apply special methods allowing for very large sample sizes in order to take advantage of *self-averaging* features. In this way, the effect of random disorder can be described without having to calculate different realizations. The Kubo-Greenwood method discussed in Section 5.7.1 is such a method, as it scales linearly with the system size allowing for systems containing millions of atoms. However, as mentioned earlier the Kubo-Greenwood approach only allows for calculation of system parameters and does not allow for the inclusion of the geometrical effects from probe positions.

The second approach to avoid the computationally expensive configurational average is to apply mean field theories. Mean field theories replace the randomly disordered material by an effective medium with the same properties. We consider the so-called Coherent Potential Approximation (CPA) which derives a diagonal self-energy describing the effect of statistically independent scatterers. The basic idea behind this technique is to replace the configurational averaged Green's function, $\langle G \rangle$ with an effective Green's function having the properties of the averaged system. The CPA gives an approximation to the average Green's function $\langle G \rangle$, however, properties like transmission are calculated using products of Green's functions such as $\langle \Gamma^R G \Gamma^L G^\dagger \rangle$. In general, $\langle G \rangle \Gamma^L \langle G^\dagger \rangle \neq \langle G \Gamma^L G^\dagger \rangle$ and we apply so-called *vertex corrections* (VC) to determine $\langle G G^\dagger \rangle - \langle G \rangle \langle G^\dagger \rangle$ allowing for calculations of averaged quantities such as transmission.

The derivation of the CPA-VC formalism presented in the following sections uses arguments of the original papers by P. Soven [205] and B. Velicky [207, 208] adapted to the Green's function formalism as presented in the textbook by E. N. Economou [97]. Alternative derivations leading to an equivalent set of equations has been formulated recently by Y. Zhu *et al.*[209]. They employ an elegant approach based on the formalism of contour ordered non-equillibrium Green's functions where the configurational average is carried out on the complex-time contour. This approach is denoted the non-equillibrium coherent potential approximation (NECPA) and we have confirmed numerically that the NECPA result is identical to the CPA-VC approach presented below.

6.2 Green's function in the Coherent Potential Approximation (CPA)

The aim of the CPA approach is to determine an effective GF, $\bar{G}$, which describes the average GF $\langle G \rangle$ obtained by averaging over an ensemble of disorder configurations. We want to construct the effective GF so it differs from the pristine GF only by a self energy Σ^{cpa}. Therefore the central problem is to determine Σ^{cpa} such that

$$\langle G \rangle = \bar{G} = \left(E - \mathcal{H}_0 - \Sigma^{L/R} - \Sigma^{cpa}\right)^{-1}, \tag{6.1}$$

where $\Sigma^{L/R}$ is the self-energy due to the left and right lead where we assume zero disorder, $\langle G \rangle$ is the configuration averaged Green function and $\mathcal{H}_0$ is the pristine Hamiltonian of the device area.

We need to connect $\bar{G}$ to the GF for a specific configuration with the Hamiltonian $\mathcal{H} = \mathcal{H}_0 + V$ where $V = \sum_i (\epsilon_i - \epsilon_{i,0})$ is a random diagonal perturbation. Here $\epsilon_{i,0}$ is the pristine value of the i'th onsite and ϵ_i is a random variable taking on values ϵ_{iq} with the probability x_{iq} where q denotes the type of impurity. It follows that $\sum_q x_{iq} = 1$. The GF for a single configuration then becomes $G = \left(E - \mathcal{H}_0 - \Sigma^{L/R} - V\right)^{-1}$. We can write the Dyson equation for G starting from the effective medium GF $\bar{G}$ and applying the difference between the two systems $V - \Sigma^{cpa}$,

$$G = \bar{G} + \bar{G}(V - \Sigma^{cpa})G. \tag{6.2}$$

Using the t-matrix formalism we can furthermore write

$$G = \bar{G} + \bar{G}T\bar{G}, \tag{6.3}$$

where the t-matrix is given as

$$\begin{aligned} T &= \frac{V - \Sigma^{cpa}}{1 - \bar{G}(V - \Sigma^{cpa})} \\ &= (V - \Sigma^{cpa}) + (V - \Sigma^{cpa})\bar{G}T. \end{aligned} \tag{6.4}$$

Taking the configurational average of the Green function in Eq. (6.2) and using the condition Eq. (6.1), $\langle G \rangle = \bar{G}$ we get the central CPA condition

$$\langle G \rangle = \bar{G} + \bar{G}\langle T \rangle \bar{G} \rightarrow \langle T \rangle = 0, \tag{6.5}$$

where we have used that $\langle \bar{G} \rangle = \bar{G}$ because $\bar{G}$ does not contain any random elements (like V which varies between different configurations making the average different from the individual contributions).

The exact solution to this is complicated. In the CPA the so-called "single-site-approximation" (SSA) is usually applied. The SSA considers the scatterers as statistically independent meaning that we neglect the scattering from clusters of impurities and replace the full t-matrix with a sum of the contributions from single scatterers. In this way the t-matrix becomes a diagonal matrix, where the i-th diagonal element can take the value t_{iq}^{cpa} with a probability of x_{iq} leading to an average given by,

$$\langle t_i \rangle = \sum_q x_{iq} t_{iq}. \tag{6.6}$$

Applying the SSA reduces the CPA condition Eq. (6.5) to

$$\langle t_i \rangle = 0. \tag{6.7}$$

The transfer matrix, t_{iq}, for a given type of onsite value $V_{iq} = \epsilon_{iq} - \epsilon_{i,0}$ can be inferred from the full t-matrix in Eq. (6.4)

$$\begin{aligned} t_{iq}^{cpa} &= (V_{iq} - \Sigma_i^{cpa})\big[1 - \bar{G}_{ii}(V_{iq} - \Sigma_i^{cpa})\big]^{-1} = \big[(V_{iq} - \Sigma_i^{cpa})^{-1} - \bar{G}_{ii}\big]^{-1} \\ &= \bar{G}_{ii}^{-1}\left[\frac{1}{1 - \bar{G}_{ii}(V_{iq} - \Sigma_i^{cpa})} - 1\right], \end{aligned} \tag{6.8a}$$

where $\bar{G}_{ii} = [\bar{G}]_{ii}$. To solve for Σ^{cpa}, we use Eq. (6.8a) and the condition $\langle t_i \rangle = 0$ to obtain

$$\langle t_i \rangle = \sum_q x_{iq} \bar{G}_{ii}^{-1}\left[\frac{1}{1 - \bar{G}_{ii}(V_{iq} - \Sigma_i^{cpa})} - 1\right] = 0, \tag{6.9}$$

which can be recast into the form

$$\Sigma_i^{cpa} = \sum_q x_{iq} \frac{V_{iq}}{1 - \bar{G}_{ii}(V_{iq} - \Sigma_i^{cpa})}. \tag{6.10}$$

This equation can be solved self-consistently. Moreover, the expression simplifies if we only consider a single type of defect, meaning that we have a host site and a disorder site with the concentration c

$$\Sigma_i^{cpa} = \frac{cV_{iq}}{1 - \bar{G}_{ii}(V_{iq} - \Sigma_i^{cpa})}. \tag{6.11}$$

if we furthermore assume that the defect is a vacancy, $\epsilon_q \to \infty$, Eq. (6.11) simplifies to

$$\Sigma_i^{cpa} = -c\bar{G}_{ii}^{-1}. \tag{6.12}$$

However, we can also make further approximations to the general case of Eq. (6.10) to ease the implementation. In the so-called low concentration approximation (LCA), we exploit that both $\bar{G}$ and Σ^{cpa} depend on the concentration of defects. Therefore, if we limit ourselves to first order in the concentrations x_{iq}, we obtain

$$\Sigma_i^{cpa} = \sum_q x_{iq} t_{0,iq} \tag{6.13a}$$

$$t_{0,iq} = V_{iq}\big(1 - G_{0,ii}V_{iq}\big)^{-1} = \Big((\epsilon_{iq} - \epsilon_{i,0})^{-1} - G_{0,ii}\Big)^{-1}. \tag{6.13b}$$

where $G_0 = \big(E - \mathcal{H}_0\big)$ is the pristine GF without disorder and CPA term.

6.3 Transport using vertex corrections (CPA-VC)

We have determined the effective medium GF corresponding to the configurationaly averaged system. We can use this to determine physical quantities related to the GF such as the density of states. However, the transmission contains products of GFs $\mathcal{T} = \mathrm{Tr}\big[\Gamma^R G \Gamma^L G^\dagger\big]$, which results in a configurational average of the form

$$\langle \mathcal{T} \rangle = \mathrm{Tr}\big[\Gamma^R \langle G \Gamma^L G^\dagger \rangle\big], \tag{6.14}$$

where we have used that Γ^R is not a random variable meaning that we can take it outside the averaging. We notice the need for additional treatment since in general $\langle G\Gamma^L G^\dagger\rangle \neq \langle G\rangle \Gamma^L \langle G^\dagger\rangle$ due to multiple scattering by the impurities. Using that $G = \bar{G} + \bar{G}T\bar{G}$ and the condition $\langle T\rangle = 0$ we get

$$\begin{aligned} \langle \mathcal{T} \rangle &= \mathrm{Tr}\big[\Gamma^R \bar{G}\Gamma^L \bar{G}^\dagger\big] + \mathrm{Tr}\big[\Gamma^R \langle \bar{G}T\bar{G}\Gamma^L \bar{G}^\dagger\rangle\big] + \mathrm{Tr}\big[\Gamma^R \langle \bar{G}\Gamma^L \bar{G}^\dagger T^\dagger \bar{G}^\dagger\rangle\big] \qquad (6.15)\\ &\quad + \mathrm{Tr}\big[\Gamma^R \langle \bar{G}T\bar{G}\Gamma^L \bar{G}^\dagger T^\dagger \bar{G}^\dagger\rangle\big] \\ &= \mathrm{Tr}\big[\Gamma^R \bar{G}\Gamma^L \bar{G}^\dagger\big] + \mathrm{Tr}\big[\Gamma^R \bar{G}\Omega\bar{G}^\dagger\big], \qquad (6.16) \end{aligned}$$

where the last equality follows from the fact that neither Γ^L nor $\bar{G}$ are random variables and can be taken outside the averaging *i.e.* $\langle \bar{G}T\bar{G}\Gamma^L\bar{G}^\dagger\rangle = \bar{G}\langle T\rangle \bar{G}\Gamma^L\bar{G}^\dagger = 0$ because $\langle T\rangle = 0$. The quantity Ω is denoted the vertex correction and is given by

$$\Omega = \langle T\bar{G}\Gamma^L\bar{G}^\dagger T^\dagger\rangle \tag{6.17}$$

Eq. (6.16) basically separates the transmission into two parts. The first corresponds to the usual form of the transmission where the pristine GF have been replaced by the GF of the effective medium. This term therefore corresponds to phase coherent transport through the effective medium. The second term describes the diffusive contribution to the transmission. The coherent term corresponds to calculating the transmission from the individual transmission amplitudes a_i as $\mathcal{T} \propto |\sum_i a_i|^2$. The coherent term therefore includes phase information and ultimately leads to quantum interference effects. On the other hand, the second term corresponds to diffusive transport giving the transmission as $\mathcal{T} \propto \sum_i |a_i|^2$ which does not include phase information and therefore does not lead to quantum interference.

To utilize Eq. (6.16) we need to determine the vertex correction Ω. Again, we make the single-site approximation as in the derivation of the CPA self-energy, hence, Ω becomes diagonal ($\Omega_{ij} = \delta_{ij}\Omega_i$). We notice that Ω has the form $\langle B\Gamma^L B^\dagger\rangle$ where B is a non-averaged operator. This is the same form as in Eq. (6.14) therefore giving rise to the same form of solution. Moreover, we take into account that $\langle T\rangle = 0$ and that the different sites are statistically independent meaning $\langle T_m ... T_n^\dagger\rangle = \delta\langle T_n ... T^\dagger\rangle$.

$$\Omega_i = \sum_q x_{iq} t_{iq} \big[\bar{G}\Gamma^L\bar{G}^\dagger\big]_{ii} t_{iq}^\dagger + \sum_{j\neq i}\sum_q x_{iq} t_{iq} \big[\bar{G}_{ij}\Omega_j \bar{G}_{ji}^\dagger\big]_{ii} t_{iq}^\dagger, \tag{6.18}$$

where the single-site scattering matrix is given by Eq. (6.8a)

$$t_{iq} = \frac{V_{iq} - \Sigma^{cpa}}{1 - \bar{G}_{ii}(V_{iq} - \Sigma_i^{cpa})} \tag{6.19}$$

Again we can simplify the implementation by employing the low concentration approximation (LCA) and only keep terms to first order in the concentration x_{iq}

$$\Omega_i = \sum_q x_{iq} t_{0,iq} \left[G_0 \Gamma^L G_0^\dagger \right]_{ii} t_{0,iq}^\dagger, \tag{6.20}$$

where $t_{0,iq}$ is given by Eq. (6.13b).

All results derived in this section have considered finite device regions but the theory can be formulated generally for translational invariant systems in the transverse direction using Bloch's theorem [209, 210]. In this way, the CPA-VC overcomes a major computational challenge offered by disordered systems: the broken translation symmetry precluding the use of the standard Bloch approach.

6.3.1 Summary of CPA-VC Technique

CPA-NVC summary

Using the CPA we replace the Green's function with an effective medium Green's function by applying the self-energy Σ^{cpa}.

$$\bar{G} = \left(E - \mathcal{H}_0 - \Sigma^{L/R} - \Sigma^{cpa}\right)^{-1}, \tag{6.21a}$$

where $\Sigma^{L/R}$ is the self energy for the leads, ϵ_{iq} is the onsite of impurity specie q on site i and x_{iq} is the probability that site i has the onsite energy ϵ_{iq}.

The transmission contains two terms: the ballistic transmission through the effective medium and a term describing the diffusive transport.

$$\langle \mathcal{T} \rangle = \mathrm{Tr}\left[\Gamma^R \bar{G} \Gamma^L \bar{G}^\dagger\right] + \mathrm{Tr}\left[\Gamma^R \bar{G} \Omega \bar{G}^\dagger\right]. \tag{6.21b}$$

where $\Gamma^{L/R} = \mathrm{i}(\Sigma^{L/R} - \Sigma^{L/R\dagger})$ is the broadening. The self-energy, Σ^{cpa}, and vertex correction, Ω, are diagonal within the single site approximation.

$$\Sigma_i^{cpa} = \sum_q x_{iq} \frac{V_{iq}}{1 - \bar{G}_{ii}(V_{iq} - \Sigma_i^{cpa})}, \tag{6.21c}$$

$$\Omega_i = \sum_q x_{iq} t_{iq} \left[\bar{G} \Gamma^L \bar{G}^\dagger\right]_{ii} t_{iq}^\dagger + \sum_{j \neq i} \sum_q x_{iq} t_{iq} \bar{G}_{ij} \Omega_j \bar{G}_{ji}^\dagger t_{iq}^\dagger ., \tag{6.21d}$$

$$t_{iq} = \frac{V_{iq} - \Sigma^{cpa}}{1 - \bar{G}_{ii}(V_{iq} - \Sigma_i^{cpa})}, \tag{6.21e}$$

$$V_{iq} = \epsilon_{iq} - \epsilon_{i,0}. \tag{6.21f}$$

Low concentration approximation

The low concentration approximation (LCA) is valid for low concentrations of defects

$$\Sigma_i^{cpa} = \sum_{q>0} x_{iq} \frac{V_{iq}}{1 - \bar{G}_{0,ii} V_{iq}}, \tag{6.22a}$$

$$\Omega_i = \sum_{q>0} x_{iq} t_{0,iq} \left[G_0 \Gamma^L G_0^\dagger\right]_{ii} t_{0,iq}^\dagger, \tag{6.22b}$$

$$t_{0,iq} = V_{iq}\left(1 - G_{0,ii} V_{iq}\right)^{-1}, \tag{6.22c}$$

$$V_{iq} = \epsilon_{iq} - \epsilon_{i,0}. \tag{6.22d}$$

We note that summation $\sum_{q>0}$ denotes all defect types *i.e.* not the host site which is taken to have onsite ϵ_0.

6.4 Graphene nanoribbon with nitrogen doping

In this section we study the effect of intentional chemical doping by nitrogen in graphene nanoribbons (GNRs). This provides a simple case where the CPA and CPA-VC frameworks are straightforwardly applied and studied as suggested by Refs. [211] and [212].

Chemical doping provides a natural way to alter the performance of graphene-based devices. Efficient doping of graphene can be achieved by incorporating nitrogen (or boron) into the pristine graphene sheet as these species can substitute for carbon atoms without distorting the lattice significantly. Using chemical vapor deposition (CVD) doping concentrations of up to 10% substitution of carbon atoms with the doping atoms can be fabricated. Early theoretical studies of the electronic properties of such samples found that a periodic arrangement of nitrogen (or boron) dopants, forming a dopant superlattice, would open a band gap. However, a random distribution of dopants among lattice sites yields no band gap [213]. A recent study [206] has examined transmission for different distributions of nitrogen doping. We consider a similar setup as Ref. [206] using the framework of CPA-VC. First, we consider *symmetrical* doping where the dopants have equal probability to occupy both sublattice. Afterwards, we investigate the case of *asymmetrical* doping where the dopants only reside on one sublattice.

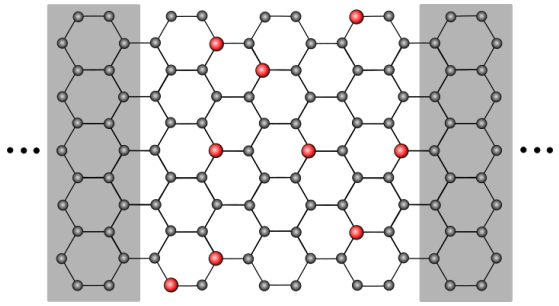

Figure 6.1: Schematic showing an armchair graphene nanoribbon with substitutional doping (red atoms).

6.4.1 Symmetric nitrogen doping

We consider substitutional nitrogen doping symmetrically distributed between the two sublattices. We treat GNRs with both armchair and zigzag edge terminations as the edge geometry has proven to be essential for the electronic structure and transport properties [214]. We model a nitrogen atom by an onsite change $\epsilon_{iq} - \epsilon_0 = t$ and use the CPA-VC scheme, Eq. (6.21), to calculate the average density of states in the GNR as well as

the transmission through the GNR. To analyze the accuracy of the CPA-VC scheme, we compare to quantities calculated using configurational average over 300 individual disorder configurations. The result for both armchair (AGNR) and zigzag (ZGNR) ribbons are shown in Fig. 6.2 for a 5% concentration of nitrogen dopants.

First, we compare the CPA-VC scheme with the brute force configurational average. We notice the very good agreement between the CPA and the configurational average for the DOS, see Fig. 6.2a-b . It is worth noticing that the configurational average does not constitute the "exact" result and are also subject to statistical error. The transmission shown in Fig. 6.2c-d also exhibit good agreement between the CPA-VC and the

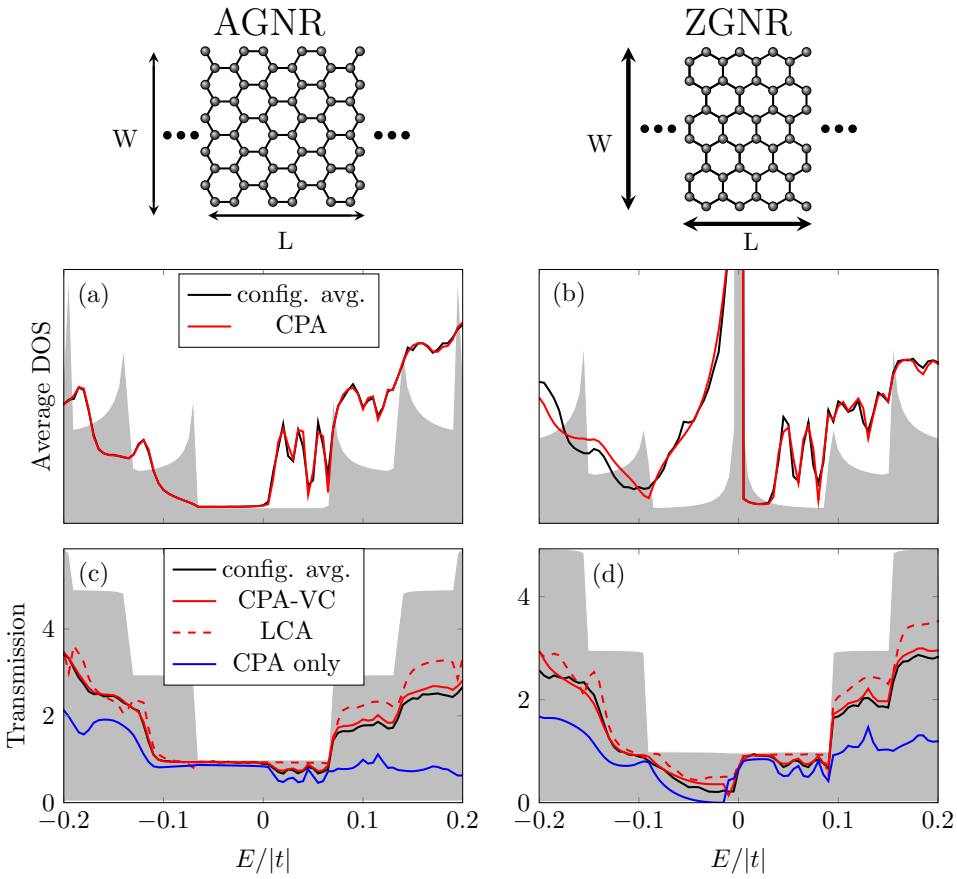

Figure 6.2: (Top) Schematic of AGNR and ZGNR. The shown AGNR has dimensions $W = 7\sqrt{3}a_0$ and $L = 5D_{ac}$ where $D_{ac} = 3a_0$ with $a_0 = 0.142$ nm. The shown ZGNR has dimensions $W = 4D_{ac}$ and $L = 8\sqrt{3}a_0$. (a-b) Average DOS calculated using CPA self-energy and a configurational average over 300 individual distributions. The shaded area corresponds to the pristine DOS for the system. (c-d) The transmission through the GNR calculated from a configurational average (black), the full CPA-VC scheme (red), the LCA (dashed red) and only including the CPA term thus neglecting the vertex corrections (blue). The dopant concentration is 5%. AGNR parameters: $W = 40\sqrt{3}a_0 \approx 9.8$ nm and $L = 40D_{ac} \approx 17$ nm. ZGNR parameters: $W = 25D_{ac} \approx 10.6$ nm and $L = 50\sqrt{3}a_0 \approx 12.3$ nm.

configurational average. Moreover, we conclude that even at 5%, the low concentration approximation (LCA) gives a good agreement with the more accurate calculations. This is especially true in the low energy regime. On the other hand, a calculation which includes only the CPA term of Eq. (6.16) ("CPA only" in Fig. 6.2c-d), $\mathcal{T}^{cpa} = \mathrm{Tr}\big[\Gamma^R \bar{G} \Gamma^L \bar{G}^\dagger\big]$, shows significant discrepancies. This underlines the importance of the vertex correction.

Returning to the average DOS in Fig. 6.2a-b we notice a distinct electron-hole asymmetry for both AGNR and ZGNR. For the AGNR, we observe a nearly unchanged DOS for holes ($E < 0$), see Fig. 6.2a. However, we modify both electron and hole spectra for energies beyond the first mode, characterized by the onset of the van-Hove singularities characteristic of the pristine DOS. The transmission, on the other hand, does not exhibit the same level of electron-hole asymmetry and we see that the first plateau persists in the presence of dopants.

Turning to the ZGNR results, we also observe a significant electron-hole asymmetry in the DOS, see Fig. 6.2b. The sharp peak at $E = 0$ is associated with localized edge states which in first nearest neighbor tight binding do not show up in the transmission spectrum. On the electron side the DOS is not significantly changed signifying that scattering effects are less important in this regime. This is also apparent in the transmission curve in Fig. 6.2d where the doping only introduces minor changes in the transmission. On the hole side, however, scattering plays a dominant role smearing the plateaus of the pristine transmission. Furthermore, we observe a suppression of the transmission through the ZGNR on the hole side ($E < 0$), even though we note a significant DOS in this region.

6.4.2 Asymmetric nitrogen doping

In this section, we consider asymmetric nitrogen doping as motivated by recent experiments where CVD growth demonstrated the possibility for samples with large domains of nitrogen atoms primarily occupying a single sublattice [215–218]. We therefore consider the same devices as in the previous section following the analysis of Ref. [206] with the dopants distributed on one sublattice.

In pristine graphene, the equivalence of the two sublattices leads the characteristic gapless band structure. Breaking the symmetry by applying a sublattice dependent potential is predicted to be similar to introducing a mass term. Consequently, a perfect sublattice asymmetric nitrogen doping are predicted to exhibit transport gaps as well as a electron-hole asymmetric conductivity [206, 219–222]

Using the CPA-VC approach only adding the effective self-energy term to one sublattice yields both DOS and transmission through the asymmetrically doped system. Practically this means that $x_{iq} = 0$ in Eq. (6.10) for all sites belonging to one sublattice corresponding to zero chance that a dopant atom occupies this sublattice. We again use a concentration of 5% and the same model for nitrogen as in the previous section. The results for both the AGNR and ZGNR are shown in Fig. 6.3.

First we consider the AGNR where the DOS exhibits electron-hole asymmetry for both

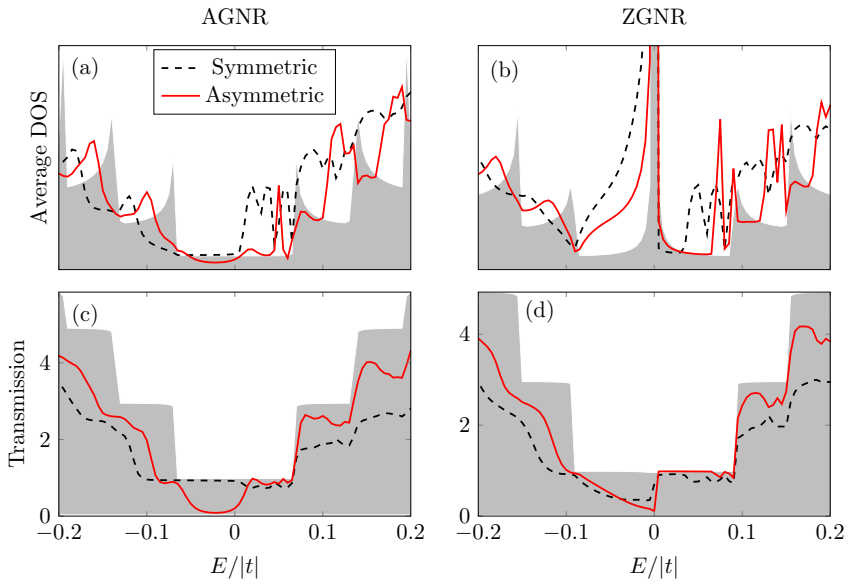

Figure 6.3: (a-b) Average DOS and (c-d) transmission, calculated using the CPA-VC scheme for a 5% nitrogen doping either sublattice symmetric (black,dashed) or sublattice asymmetric (red). The parameters system sizes are the same as in Fig. 6.2.

the symmetric and asymmetric doping, see Fig. 6.3a. In the asymmetric case, however, we notice a bandgap emerging for $E < 0$ caused by the effective mass term originating from the sublattice dependent potential. We see that the DOS has not entirely vanished which might be due to the small sample size where edge effects become increasingly important. In larger calculations based on configurational average [206] and in Kubo-Greenwood calculations of 2D graphene sheets [220] the bandgap was observed. The diminishing DOS leads to a strong suppression of the transmission in the AGNR for $E < 0$, see Fig. 6.3c. This constitutes a significant difference compared to the symmetric doping (dashed line), where the transmission is almost unchanged. On the other hand, the electron side is not modified significantly at low energies by the introduction of the asymmetric doping showing that the nitrogen impurities do not contribute significant scattering at these energies.

When considering the ZGNR in Fig. 6.3b and 6.3d, the predicted bandgab for asymmetric sublattice doping is seen to be sensitive to the presence of zigzag edges [206]. The DOS is decreasing on the hole side leading to a more pronounced peak at $E = 0$ but qualitatively the effect of the asymmetric doping is a lot less dramatic for the ZGNR. This leads to the conclusion that the effective mass term created by the asymmetric doping which created a bandgap for the AGNR is not the dominant effect. Instead the finite DOS which lead to propagation within the expected bandgap can be associated with sites near the ribbon edge corresponding to the doped sublattice as discussed in Ref. [206].

Overall the results for the symmetric and asymmetric doping agree well with the results of Ref. [206], demonstrating the ability of the CPA-VC approach to accurately describe the effect of nitrogen doping in graphene.

6.4.3 Computational cost

We consider the scaling of the computational cost. In Fig. 6.4a, we compare the CPU time of calculations using the CPA-VC, LCA and configurational average approach. The most computational costly operation in all the approaches is the matrix inversion. The computational cost of a matrix inversion is N^3, where N is the total system size. The implementation used in this chapter relies on such a full inversion both for the configurational average and the CPA-VC/LCA calculation. However, we note that both methods can be greatly improved using recursive schemes [209] going from a N^3 scaling to a $N_{cell} \times M^3$ scaling in a recursive implementation, where N_{cell} is the number of recursive cells and M is the number of sites in each cell. We therefore expect similar performance increases for all methods using a recursive approach.

From Fig. 6.4a it is clear that the CPA-VC and LCA is more computationally effective than the configurational average approach. For a system containing 6500 atoms the CPA-VC is ~ 4 faster than the configurational average. Moreover, the difference increases with system size making the CPA-VC/LCA much more effective for large systems. Furthermore, the LCA approach is more effective than the full CPA-VC as it does not require the full self-consistent calculation of the CPA self-energy in Eq. (6.10).

The above considerations disregard any so-called "self-averaging" effects obtained for large disordered samples which tend to decrease the number of individual realizations needed within a configurational average approach. However, the CPA-VC approach being

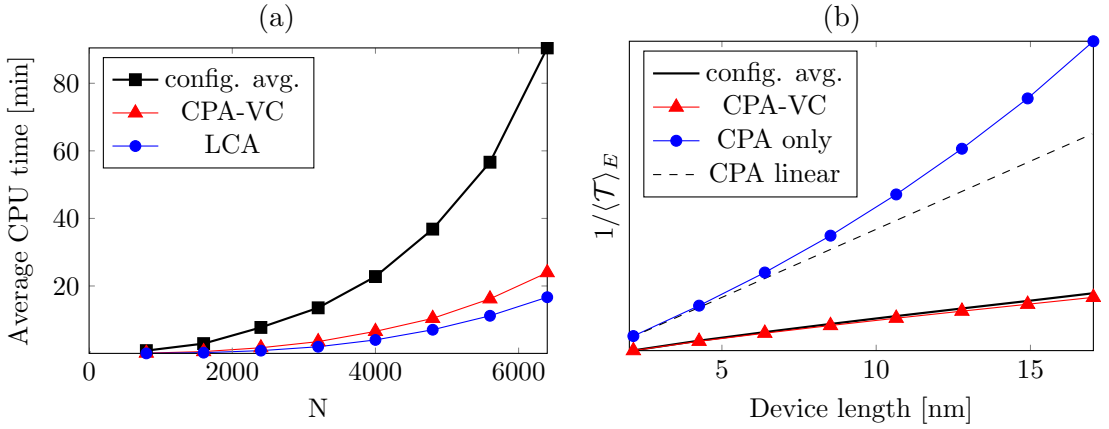

Figure 6.4: (a) The average CPU time for the calculation using the three different approaches as a function of the system size N, where N is the number of atoms in the system. (b) Average resistance of $W = 9.8$ nm wide AGNR as a function of the device length for symmetric nitrogen doping with a 5% concentration similar to the one used in Fig. 6.2. The configurational average (black) uses 300 individual distributions. The "CPA+VC" curve (red, triangle) uses both the phase coherent and the diffusive term in Eq. (6.16) whereas "CPA only" curve (blue, circle) uses only the phase coherent term. The dashed curve is a linear extrapolation of the blue curve showing that the "CPA only" term increases exponentially.

an effective medium theory restores the translation symmetry required by a Bloch scheme theorem or by self-energy approaches similar to the one used extensively throughout this thesis.

6.4.4 Scaling behavior of resistance

At last, we consider the scaling behavior using the CPA-VC. From ballistic scattering theory it follows that a phase coherent average of transmission modes in a 1D system scales exponentially with the device length. In a single mode conductor this can be determined analytically as [72]

$$\frac{1}{\mathcal{T}(L)} = R(L) \propto \frac{1}{2}\big(\mathrm{e}^{\frac{2L}{L_0}} - 1\big), \tag{6.23}$$

where L is the device length and L_0 is a length comparable to the elastic mean free path. Evidently this is not the classical Ohmic behavior where the resistance scales linearly with L. If we include the incoherent contribution the resistance instead becomes [72]

$$\frac{1}{\mathcal{T}(L)} = R(L) \propto L, \tag{6.24}$$

giving rise to the usual form of Ohm's law. These two different scalings arise due to either coherent (Eq. (6.23)) or diffusive mechanism (Eq. (6.24)). The inclusion of dephasing reaching the diffusive regime is at the core of the CPA-VC approach.

These two regimes are confirmed for the CPA-VC approach by calculating the average resistance (or $1/\langle\mathcal{T}\rangle_E$) for all energies as a function of the device length using symmetric disorder of 5%, see Fig. 6.4b. We clearly notice that the CPA-VC approach including the diffusive term gives rise to a linear scaling $1/\langle\mathcal{T}\rangle_E \propto L$ as appropriate when comparing to the configurational average. On the other hand, if we only include the CPA term in Eq. (6.16) we get a nonlinear increase of the resistance characteristic of phase coherent transport. In conclusion the CPA-VC approach allows us to obtain the correct scaling characteristic of diffusive transport.

The above conclusion is highly relevant in connection to the multi-probe setup, as most experimental analyses of multi-probe systems are based on classical Ohmic behavior. On the other hand, the theoretical framework developed in this thesis is applied in the phase coherent regime where ballistic and quantum interference effects are important. Increasing the probe separation and/or the amount of disorder would cause a transition from the quantum regime towards the diffusive semi-classical regime. Here the CPA-VC could be a valuable tool to allow an investigation of this transition and bridge the two regimes.

6.5 Summary

Nitrogen doping of graphene nanoribbons

We introduced the CPA-VC approach to treat averaged quantities of disordered systems. The CPA-VC calculation scheme was applied to the case of nitrogen doping in graphene nanoribbons using both the full and the LCA scheme. The LCA was found to agree reasonably with the more accurate calculations even for the 5 % disorder concentration. In addition, we demonstrated that the CPA-VC reproduced the expected $R \propto L$ regime of diffusive Ohmic conductors.
We furthermore investigated both the case of symmetric and asymmetric doping. For symmetric doping where both sublattices are occupied by a dopant atom with the same probability we do not observe any bandgap formation. However, for the asymmetric doping we demonstrate the formation of a bandgap in armchair nanoribbons. The gap opening, however, is not observed for zigzag nanoribbons where the dopants are shown simply to act as additional scatterers.

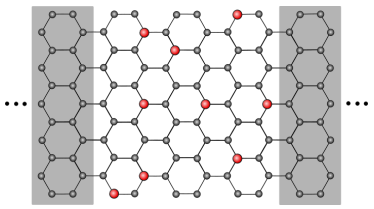

CHAPTER 7

Summary & Outlook

This thesis has developed theoretical and computational methods to treat multi-probe systems within the phase coherent regime where quantum interference effects are significant. The central development in this thesis has been the *patched Green's function method* using an adaptive recursive scheme combined with a specially constructed self-energy term to treat the extended part of the system. We can use this method to calculate the conductance between local probes and treat the local electronic and transport properties of finite "patches" embedded within extended two-dimensional systems.

The developed calculation methods are applied to a broad range of phenomena related to nanostructured graphene. In Chapter 3 we introduced the two main operation modes of a dual-STM setup: *scanning* and *spectroscopy*. Using these two modes, we considered quantum interference effects in the transmission between the two probes in the presence of simple defects and showed how this can be applied to study scattering processes. In Chapters 4 and 5 we extended the dual probe analysis to more complex nanostructures such as antidots, locally gated dots and pseudomagnetic dots caused by inhomogeneous strain fields. This demonstrated the ability of the dual probe setup to investigate nanoscale transport phenomena where effects like current guiding, focusing, depletion or similar are observed around nanostructures in graphene. In this final chapter we summarize the main findings of the thesis and finally we discuss the status and possible future investigations starting from the presented systems or methods.

Thesis summary

In Chapter 2 we developed two approaches to calculate the transport in multi-probe setups. The *integral Green's function method* allows efficient treatment of systems with small perturbations using a combination of analytical and numerical integration techniques. On the other hand, the *patched Green's function method* exploits a specially constructed self-energy term together with an adapted recursive scheme to calculate the local electronic and transport properties for spatially separated "patches" within extended systems.

Dual probe setup

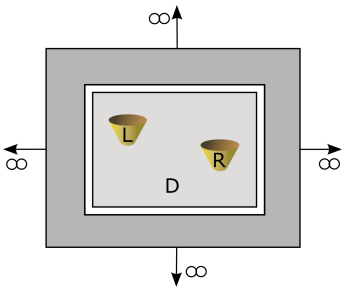

Scanning mode

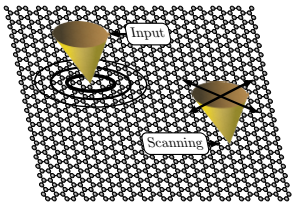

The dual-STM setup in *scanning mode* uses one stationary probe and one movable probe. We calculate the conductance between the probes as the second probe scans across the sample producing real space conductance maps. These maps can be used to study directional behavior and quantum interference effects around defects and crystalline edges. Furthermore, the Fourier transform of the real space maps can be used to extract information about scattering processes.

Spectroscopy mode

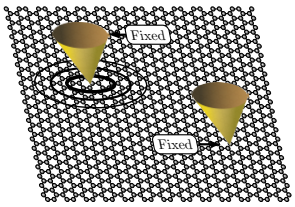

In the *spectroscopy mode* we keep both probes fixed and vary the energy of the electrons. The spectroscopy reveals fingerprints which can be used to characterize directional effects or resonances originating from adatoms or interference effects.

In Chapter 4 we considered antidots and locally gated dots in graphene. We demonstrated how single states (antidot) or modes (gated dot) and their interplay gives rise to resonances in the dual probe transmission. Using bond current mapping for electron waves leaving a probe far from the nanostructure, we conclude that the asymmetric transmission peaks are caused by vortex patterns either guiding or suppressing the current.

Antidot

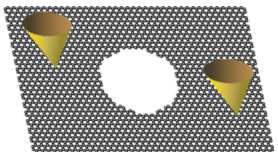

Locally gated dot

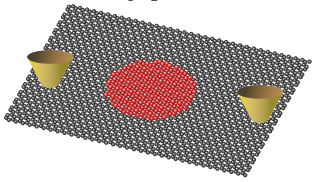

Local strain fields

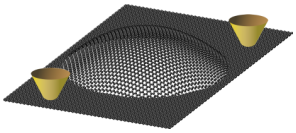

In Chapter 5 we first demonstrated pseudo-Landau quantization in pseudomagnetic dots and discussed sublattice polarization, finite size effects and the importance of the strain direction in relation to the pseudomagnetic field. The analysis was extended to various rotationally symmetric strain fields giving rise to three-fold symmetrically pseudomagnetic fields. The existence of pseudo-Landau levels was considered in relation to gas-inflated bubbles with clamped edges. Here the sharp edges caused Friedel oscillations to be superimposed with any pseudo-Landau peaks making a clear distinction between the two effects difficult.

Vortex patterns in pseudomagnetic fields

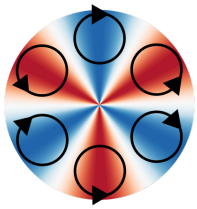

Using the dual probe setup, we demonstrated pseudomagnetic current focusing caused by a vortex pattern corresponding to the pseudomagnetic field distribution in the dot. Similarly, we showed the possibility of switching from the focusing regime to an anti-focusing regime depleting the current after the dot. Since the two valleys experience a different pseudomagnetic field they scatter the two valleys differently. We therefore suggested the possibility for valley filtering phenomena.

Array of pseudomagnetic dots

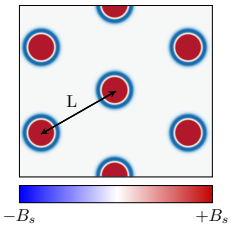

At last we considered an array of pseudomagnetic dots supporting pseudo-Landau levels. The Kubo-Greenwood method revealed a transport determined by the competition between delocalized Landau states and the induced scattering caused by these states on the pristine behavior. At higher energies the induced scattering is the dominant effect whereas localization effects is seen around the zeroth pseudo-Landau level.

Finally in Chapter 6 we introduced the CPA-VC scheme to treat averaged quantities of disordered systems. We first demonstrated that the CPA-VC scheme correctly described the case of substitutional doping in graphene nanoribbons where it captured both the bandgab formation for asymmetrically doping and the corresponding absence of a bandgab in the symmetric case.
We furthermore showed how the CPA-VC approach correctly reproduced scaling laws for 1D diffusive conductors. Potentially an extension of the *patched Green's function method* using the CPA-VC approach could therefore allow studies of the transition for a multi-probe system between the classical Ohmic regime and the quantum regime.

Substitutional doping

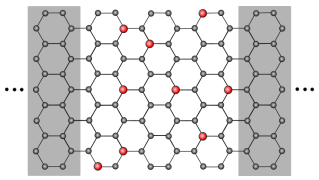

Outlook

Besides the development of a novel calculation method, the thesis work has covered numerous aspects of nanostructured graphene within a relatively short time scale. This of course has the disadvantage that several questions remain unanswered and many studies presented in this thesis represent the initial step towards more elaborate investigations. Therefore, we finish the thesis by reviewing possible future investigations and extensions.

Electron optics

The intriguing subject of electron optics within graphene has only been briefly discussed during this thesis in relation to the single circularly gated region. As suggested in Ref. [22] taking advantage of the "optic-like" electron dynamics holds the promise of a variety of analogies with optical devices, where some have already been realized experimentally [22, 25]. Here, the *patched Green's function method* allows for a tight binding description of the individual gate profiles. We can investigate the detailed response to an incoming wave mimicking the optical situation without needing to introduce the structure into a finite nanoribbon. Combining the study of individual gating profiles with large scale simulations using the Kubo-Greenwood approach opens a variety of possible routes to investigate electron optics phenomena at different length-scales.

Strain engineering

The effect of inhomogeneous strain on various transport phenomena still contains novel routes of investigation where dot-dot interactions, different relative geometrical placement of pseudomagnetic dot or the interplay between inhomogeneous pseudo-fields and real magnetic fields could be interesting systems to study. Furthermore, we can use strain to manipulate the valley degree of freedom as pointed out by Ref. [180] in relation to real magnetic fields which exactly cancel the pseudomagnetic field in one of the valleys. The results in Chapter 5 suggest a valley polarizing effect of the pseudomagnetic dots as well as current guiding phenomena which potentially could be used to design the current through the system based on the applied strain.

Another interesting proposal in this direction is to investigate the pseudomagnetic field in the context of the Quantum Hall Effect. The results presented in this thesis suggest that this would require large strained regions beyond the regime of nanobubbles. To study such effects, we need to calculate the Hall conductivity. The Kubo-Greenwood propagation method applied in this thesis has been extended to compute the Hall conductivity [204]. However, this approach is computationally expensive. Instead, we could apply the related

Kernel Polynomial method [200] which allows for the calculation of Hall conductivity while retaining the desirable order-N scaling.

Model development/extension

We can also consider extensions of the *patched Green's function* framework. Here we could imagine generalizing the calculation of the boundary self-energy to treat arbitrary two-dimensional systems. Furthermore, we can imagine other areas where an atomistic description of a finite perturbation within an extended system is useful. This could for example be in the field of plasmonics where light couples to the graphene sheet in a finite region.

At last, we turn to the overall topic of this thesis: multi-probe setups. The current state of the theoretical understanding is still limited to the coherent regime where ballistic effects and quantum interference play a significant role. Most experimental analyses are still based on classical Ohmic behavior. In this regime the resistance between two probes scales as $R \sim \ln(D)$ where D is the distance between the probes [53]. However, the current quantum mechanical treatment predicts $R \sim D$, see Chapter 2. Consequently, it is still an open question when and how this transition would happen. Several aspects could be included in the present framework to investigate this important transition. Most important is the role of disorder as the classical Ohmic regime assumes a fixed material conductivity of a disordered material. Here the CPA-VC approach presented in Chapter 6 could prove useful, as we demonstrated that it recovers the correct diffusive scaling for 1D conductors. Secondly, the potential field caused by the probes could be included at different levels of accuracy to capture the effect of a finite bias. A more complex understanding of the multi-probe setup going from the classical description to the quantum description developed in this thesis, would pave the way for a fundamentally important investigation of the current flow in graphene and other two dimensional materials using these very promising multi-probe tools.

> *"There is no real ending. Its just the place where you stop the story."*
>
> — Frank Herbert, Dune Cronicles

APPENDIX A

Plate theory

In this appendix we consider classical theory of elasticity and treat graphene as a thin plate or membrane. We introduce central concepts in order to show the origin of the displacement fields used for the graphene bubbles in Chapter 5. A thorough derivation of the framework of elasticity is beyond the scope of this discussion. Instead we refer to standard textbooks on elasticity [164, 223] and its specific application to thin plates [175, 224].

Definitions of bending and axial force

We use the standard definition of cylindrical coordinates for the displacement field, such that u_x and u_y denotes the in-plane displacements and z is the lateral deflection. In this way, indices i and j denotes in-plane coordinates and the corresponding in-plane strain tensor ϵ_{ij} and curvature κ_{ij} becomes,

$$\epsilon_{ij} = \frac{1}{2}\Big(\partial_j u_i + \partial_i u_j + \partial_i z \partial_j z\Big) \tag{A.1a}$$

$$\kappa_{ij} = \partial_i \partial_j z \tag{A.1b}$$

We use the general Einstein summation convention with δ_{ij} being the Kronecker delta to write Hook's law relating strain ϵ_{ij} and stress σ_{ij} as,

$$\sigma_{ij} = \frac{E}{1-\nu^2}\Big[(1-\nu)\epsilon_{ij} + \nu\epsilon_{kk}\delta_{ij}\Big], \tag{A.2}$$

where E is Young's modulus and ν is Poisson's ratio.

In terms of individual xy-components we get

$$\sigma_{xx} = \frac{E}{1-\nu^2}\big(\epsilon_{xx} + \nu\epsilon_{yy}\big), \tag{A.3a}$$

$$\sigma_{yy} = \frac{E}{1-\nu^2}\big(\epsilon_{yy} + \nu\epsilon_{xx}\big), \tag{A.3b}$$

$$\sigma_{xy} = \frac{E}{1+\nu}\epsilon_{xy}. \tag{A.3c}$$

We use the general form of the strain tensor including curvature by making the replacement,

$$\epsilon_{ij} \to \epsilon_{ij} + z\kappa_{ij}. \tag{A.4}$$

with ϵ_{ij} and κ_{ij} given by Eq. (A.1).

We now divide the forces related to in-plane forces (setting $\epsilon_{ij} = 0$) or curvature forces (setting $\kappa_{ij} = 0$). The former can be expressed conveniently using the tensor of axial force (membrane force), N_{ij}. For $\kappa_{ij} = 0$ we therefore obtain

$$N_{ij} = \int_{-d/2}^{d/2} \sigma_{ij} \mathrm{d}z = \int_{-d/2}^{d/2} \sigma_{ij} \mathrm{d}z, \tag{A.5a}$$

$$= \frac{E}{1-\nu^2}\Big[(1-\nu)\epsilon_{ij} + \nu\epsilon_{kk}\delta_{ij})\Big] \int_{-d/2}^{d/2} \mathrm{d}z, \tag{A.5b}$$

$$= C\Big[(1-\nu)\epsilon_{ij} + \nu\epsilon_{kk}\delta_{ij}\Big], \tag{A.5c}$$

where we have defined the constant

$$C = \frac{Ed}{1-\nu^2}. \tag{A.6}$$

Likewise, we define the bending moments for $\epsilon_{ij} = 0$ related to the curvature forces,

$$M_{ij} = \int_{-d/2}^{d/2} \sigma_{ij} z \mathrm{d}z = \frac{E}{1-\nu^2} \int_{-d/2}^{d/2} \Big[(1-\nu)\epsilon_{ij} + \nu\epsilon_{kk}\delta_{ij})\Big] z \mathrm{d}z, \tag{A.7a}$$

$$= \frac{E}{1-\nu^2}\Big[(1-\nu)\kappa_{ij} + \nu\kappa_{kk}\delta_{ij})\Big] \int_{-d/2}^{d/2} z^2 \mathrm{d}z, \tag{A.7b}$$

$$= D\Big[(1-\nu)\kappa_{ij} + \nu\kappa_{kk}\delta_{ij}\Big], \tag{A.7c}$$

where we have defined the bending modulus D.

$$D = \frac{Ed^3}{12(1-\nu^2)}. \tag{A.8}$$

Strain energy

The potential energy associated with the elastic strain due to the in-plane strain is given by the integral of the membrane energy density over the area of the plate S,

$$U_\epsilon = \int_S \frac{1}{2}\epsilon_{ij} N_{ij} \mathrm{d}^2\boldsymbol{r}. \tag{A.9}$$

Likewise, the potential energy associated with the bending (curvature) can be expressed using the bending moment

$$U_\kappa = \int_S \frac{1}{2}\kappa_{ij} M_{ij} \mathrm{d}^2\boldsymbol{r}. \tag{A.10}$$

The strain energy density becomes,

$$U = U_\epsilon + U_\kappa = \int_S \left(\frac{1}{2}\epsilon_{ij} N_{ij} + \frac{1}{2}\kappa_{ij} M_{ij}\right) \mathrm{d}^2\boldsymbol{r} \tag{A.11}$$

In addition to the potential strain energy we can have energies related external forces. Although external forces can come from many different sources, we focus on lateral (transverse) load p which does work on the transverse deflection

$$U_{ext} = \int_S pz \ \mathrm{d}^2\boldsymbol{r}. \tag{A.12}$$

Summing all contributions to the energy finally gives

$$V = U_\epsilon + U_\kappa + U_{ext} = \int_S \left(\frac{1}{2}\epsilon_{ij} N_{ij} + \frac{1}{2}\kappa_{ij} M_{ij} + pz\ \right) \mathrm{d}^2\boldsymbol{r} \tag{A.13}$$

General governing equation

The final form of the plate is determined by minimizing the total energy $V = U + U_{ext}$. Using variation calculus, $\delta V = \delta\big(U + U_{ext}\big)$, we obtain the following equations determining the shape of the plate under hydrostatic pressure p

$$\partial_i N_{ij} = 0, \tag{A.14a}$$

$$\partial_i \partial_j M_{ij} + \partial_i (N_{ij} \partial_j z) + p = 0, \tag{A.14b}$$

Inserting Eq. (A.7c) into Eq. (A.14b) and using the in-plane equilibrium, $\partial_i N_{ij} = 0$, we obtain a more convenient form of the governing equations usually called the von Karman equation for the deflection z

$$D\nabla^4 z + N_{ij}\partial_i\partial_j z + p = 0, \tag{A.15}$$

Rotation symmetry

We now restrict the general equations to the rotational symmetric case subjected to axisymmetric loading. We express the displacement in polar coordinates for the in-plane $(u_r, u_\theta) = (u(r), 0)$ and out-of-plane $z(r) = z$ contributions, where $r = \sqrt{x^2 + y^2}$.

To express the equations in cylindrical coordinates for the rotational symmetric case, we write the operators

$$\boldsymbol{\nabla} \cdot \boldsymbol{A} = \partial_i A_i = \frac{1}{r}\partial_r(rA_r) + \frac{1}{r}\partial_r A_\theta + \partial_z A_z \to \partial_r A_r + \frac{A_r}{r}, \tag{A.16a}$$

$$\nabla^2 f = \partial_i^2 f = \frac{1}{r}\partial_r(r\partial_r f) + \frac{1}{r^2}\partial_\theta^2 f + \partial_r^2 f \to \partial_r^2 f + \frac{1}{r}\partial_r f. \tag{A.16b}$$

Using Eq. (A.16) in Eq. (A.1a) we can write the in-plane strain components

$$\epsilon_{rr} = \partial_r u + \frac{1}{2}(\partial_r z)^2, \tag{A.17a}$$

$$\epsilon_{\theta\theta} = \frac{u}{r}, \tag{A.17b}$$

$$\epsilon_{r\theta} = \epsilon_{\theta r} = 0. \tag{A.17c}$$

Likewise, the curvature becomes

$$\kappa_{rr} = \partial_r^2 z, \tag{A.18a}$$

$$\kappa_{\theta\theta} = \frac{1}{r}\partial_r z, \tag{A.18b}$$

$$\kappa_{r\theta} = \kappa_{\theta r} = 0. \tag{A.18c}$$

From Eq. (A.5c), the radial and tangential components of the membrane force are

$$N_{rr} = C\Big(\epsilon_{rr} + \nu\epsilon_{\theta\theta}\Big) = C\Big(\partial_r u + \nu\frac{u}{r} + \frac{1}{2}(\partial_r z)^2\Big), \tag{A.19a}$$

$$N_{\theta\theta} = C\Big(\epsilon_{\theta\theta} + \nu\epsilon_{rr}\Big) = C\Big(\nu\partial_r u + \frac{u}{r} + \frac{\nu}{2}(\partial_r z)^2\Big). \tag{A.19b}$$

From Eq. (A.7c), the bending moments for the rotational symmetric case become

$$M_{rr} = D\Big(\kappa_{rr} + \nu\kappa_{\theta\theta}\Big) = D\Big[\partial_r^2 z + \frac{\nu}{r}\partial_r z\Big], \tag{A.20a}$$

$$M_{\theta\theta} = D\Big(\kappa_{\theta\theta} + \nu\kappa_{rr}\Big) = D\Big[\nu\partial_r^2 z + \frac{1}{r}\partial_r z\Big], \tag{A.20b}$$

$$\tag{A.20c}$$

Linear plate solution

In the linear plate approximation we consider pure bending and neglect the in-plane strain force $N_{ij} = 0$. In this regime Eq. (A.15) reduces to

$$D\nabla^4 z = D\frac{1}{r}\partial_r\Big[r\partial_r\Big(\frac{1}{r}\partial_r\big[r\partial_r z\big]\Big)\Big] + p = 0. \tag{A.21}$$

Integrating four times yields the general solution for the deflection $z(r)$

$$z(r) = -\frac{pr^4}{64D} + C_1 \ln r + C_2 r^2 \ln r + C_3 r^2 + C_4, \tag{A.22}$$

where C_i with $i = (1, 2, 3, 4)$ are arbitrary integration constants to be determined by the boundary conditions.

We take the origin of the coordinate system at the center of the plate. As the deflection must be finite at $r = 0$ why we conclude that $C_1 = C_2 = 0$,

$$\partial_r z = -\frac{pr^3}{16D} + 2C_3 r, \qquad z = -\frac{pr^4}{64D} + C_3 r^2 + C_4, \tag{A.23}$$

To determine C_3 and C_4 we consider the clamped boundary condition requiring that the deflection and its derivative must be zero at the edge of the plate, $z = \partial_r z = 0$ at $r = R$.

$$C_3 = -\frac{pR^2}{32D}, \qquad C_4 = \frac{pR^4}{64D}, \tag{A.24}$$

Inserting Eq. (A.24) into the general solution Eq. (A.23) we obtain the deflection

$$z(r) = h_0 \left(1 - \frac{r^2}{R^2}\right)^2, \tag{A.25}$$

where $h_0 = pR^4/64D$ is the height of the deflection.

Non linear plate approximation

The linear plate solution assumed a vanishing in-plane strain forces. To relief this condition we generally need to solve the coupled equations Eqs. (A.14a) and (A.15)

$$\partial_r N_{rr} + \frac{N_{rr} - N_{\theta\theta}}{r} = 0, \tag{A.26}$$

$$D\nabla^4 z + \frac{1}{r}\partial_r \left[N_{rr} r \partial_r z\right] + p = 0. \tag{A.27}$$

This set of coupled nonlinear equations are in general not analytical solvable. Instead we will use an approximate solution. The deflection is assumed to be equal to the linear plate solution

$$z(r) = h_0 \left(1 - \frac{r^2}{R^2}\right)^2. \tag{A.28}$$

The in-plane displacement needs to fulfill the boundary conditions $u(r = 0) = 0$ and $u(r = R) = 0$. The first condition implies that $u(r) \propto r$ whereas the second suggests

solutions on the type $u(r) \propto (1 - r/R)$. We combine these two conditions and assume a polynomial form of the rest of the displacement field

$$u(r) = \frac{r}{R}\left(1 - \frac{r}{R}\right)\big(c_1 - c_2 r\big), \tag{A.29}$$

where the constants c_1 and c_2 must be determine by energy optimization.

Inserting Eqs. (A.28) and (A.29) into the strain energy Eq. (A.13) and minimizing yields [174]

$$c_1 = \frac{179 - 89\nu}{126}\frac{h_0^2}{R^3} = 1.308\frac{h_0^2}{R^3}, \tag{A.30}$$

$$c_2 = \frac{13\nu - 79}{42}\frac{h_0^2}{R^4} = -1.831\frac{h_0^2}{R^4}, \tag{A.31}$$

$$\tag{A.32}$$

where the last quality in each line uses $\nu = 0.16$.

Membrane approximation

Finally, we make the membrane assumption of vanishing bending stiffness $M_{ij} = 0$. In this regime the governing equations become

$$\partial_r N_{rr} + \frac{N_{rr} - N_{\theta\theta}}{r} = 0, \tag{A.33}$$

$$\frac{1}{r}\partial_r\big[N_{rr} r \partial_r z\big] + p = 0. \tag{A.34}$$

Integrating the last equation yields

$$N_{rr}\partial_r z = -\frac{pr}{2}. \tag{A.35}$$

In general the membrane force is given by Eq. (A.19) as $N_{rr} = C\big(\epsilon_{rr} + \nu\epsilon_{\theta\theta}\big)$, but to determine the form of the approximate solution we can treat N_{rr} as a constant and solve for $z(r)$

$$z(r) = -\frac{pr^2}{4N_{rr}} + c_1, \tag{A.36}$$

where c_1 is an integration constant determined by the boundary condition $z(r = R) = 0$

$$c_1 = \frac{pR^2}{4N_{rr}}. \tag{A.37}$$

Inserting and rearranging gives the final form of the deflection

$$z(r) = h_0\left(1 - \frac{r^2}{R^2}\right), \tag{A.38}$$

where $h_0 = \frac{pR^2}{4N_{rr}}$. In general we use the form of Eq. (A.38), but the maximal deflection h_0 is determined generally by minimizing the energy in Eq. (A.13) using this form of the deflection.

The form of the in-plane displacement is determined similar to the non linear plate approximation above but now we only include the zeroth order term in the polynomial

$$u(r) = u_0\frac{r}{R}\left(1 - \frac{r}{R}\right), \tag{A.39}$$

where u_0 is a constant to be determined by energy minimization. Using Eqs. (A.38) and (A.39) and minimizing the total potential energy we obtain the relation between the constant u_0 and the height h_0 as $u_0 = 1.136h_0^2/R$ using $\nu = 0.16$ [174].

Paper I

Mikkel Settnes, Stephen R. Power, Dirch H. Petersen and Antti-Pekka Jauho

Theoretical analysis of a dual-probe scanning tunneling microscope setup on graphene

Phys. Rev. Lett. **112**, 096801 (2014)

arXiv:1401.8156v2 [cond-mat.mes-hall] 18 Jul 2014

Theoretical analysis of a dual-probe scanning tunneling microscope setup on graphene

Mikkel Settnes,* Stephen R. Power, Dirch H. Petersen, and Antti-Pekka Jauho
Center for Nanostructured Graphene (CNG), Department of Micro- and Nanotechnology Engineering, Technical University of Denmark, DK-2800 Kgs. Lyngby, Denmark
(Dated: July 21, 2014)

Experimental advances allow for the inclusion of multiple probes to measure the transport properties of a sample surface. We develop a theory of dual-probe scanning tunnelling microscopy using a Green's Function formalism, and apply it to graphene. Sampling the local conduction properties at finite length scales yields real space conductance maps which show anisotropy for pristine graphene systems and quantum interference effects in the presence of isolated impurities. The spectral signatures of the Fourier transform of real space conductance maps include characteristics that can be related to different scattering processes. We compute the conductance maps of graphene systems with different edge geometries or height fluctuations to determine the effects of non-ideal graphene samples on dual-probe measurements.

Local scattering centers such as impurities, defects and substrate inhomogeneities limit the theoretically high mobility of graphene [1–3]. Improved sample preparation and specialized substrates have improved the quality of graphene electronics [4] such that even a single scatterer can influence the whole device and perhaps render it useful for, e.g. sensing applications [5, 6]. A detailed understanding of the influence of such defects on electronic properties is necessary in order to exploit or avoid their influence [7, 8].

Information about single scatterers can be obtained via scanning tunnelling microscopy (STM), yielding direct information about the local density of states (LDOS). Previously the LDOS of graphene has been studied, both experimentally and theoretically, in the presence of defects [9–16], edges [17–21], constrictions [22] and charge puddle formation caused by trapped molecules [23, 24].

However, in many contexts one is interested in how the local electronic transport properties, and not just the LDOS, vary along the sample. To this aim multi-probe STM has been used to characterize a wide range of systems, including carbon nanotubes [25], Si-nanowires [26, 27], two-dimensional thin films [28] and graphene [27, 29, 30]. This technique analyzes nanoscale features on surfaces without the need to fabricate invasive contacts into the sample [29–32]. Graphene is especially interesting as it is intrinsically two-dimensional and we thus probe the material properties by measuring the surface. Furthermore graphene has a long inelastic mean free path [33–37], enabling the possibility of placing two STM tips within a length scale at which interference effects are not washed out by dephasing [25, 37–39].

In this Letter we consider such quantum interferences as we present a theoretical analysis of the dual-probe STM setup as sketched in Fig. 1. The methodology and analysis is described for pristine graphene sheets and vacancies, but is completely general and can be easily extended to other systems. Applications to graphene systems with edges or height fluctuations are presented as examples.

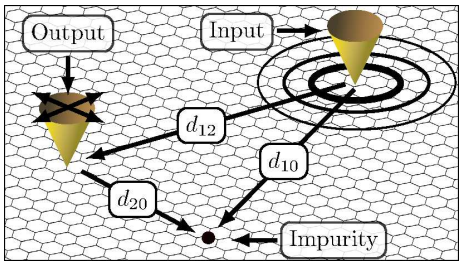

FIG. 1. Schematic overview of a dual-probe STM setup. Current input/output probes and an impurity on site 0 are indicated together with their relative separations.

Methods. – In nonequilibrium Green's function formalism (NEGF) semi-infinite leads are coupled to a finite device region [40, 41]. We instead consider an *infinite* two-dimensional device connected to one fixed and one scanning STM probe as in Fig. 1 so that conventional recursive methods are not directly applicable, and an alternative approach must be used. Although we consider graphene in this work, the method is applicable to other surfaces by using the relevant Green's Function (GF) in the following derivations. For pristine graphene in the nearest neighbour tight-binding model, the real-space single-particle equilibrium GF is given by [42]

$$g^0_{ij}(z) = \frac{1}{\Omega_{BZ}} \int \mathrm{d}^2\boldsymbol{k} \frac{\mathrm{e}^{\mathrm{i}\boldsymbol{k}\cdot(\boldsymbol{r}_j-\boldsymbol{r}_i)}}{z^2 - t^2|f(\boldsymbol{k})|^2} \begin{pmatrix} z & tf(\boldsymbol{k}) \\ tf^*(\boldsymbol{k}) & z \end{pmatrix}, \tag{1}$$

where $z = E + \mathrm{i}0^+$ is the energy, Ω_{BZ} is the area of the first Brillouin zone, $\boldsymbol{r}_i = m_i\boldsymbol{a}_1 + n_i\boldsymbol{a}_2$ (with m_i and n_i integers) is the position of site i, $\boldsymbol{a}_1$ and $\boldsymbol{a}_2$ are the graphene lattice vectors, and $f(\boldsymbol{k}) = 1 + \mathrm{e}^{\mathrm{i}\boldsymbol{k}\cdot\boldsymbol{a}_1} + \mathrm{e}^{\mathrm{i}\boldsymbol{k}\cdot\boldsymbol{a}_2}$. The carbon-carbon hopping integral is $t \approx -2.7$ eV [43].

The zero-temperature conductance is given by the Landauer formula $\frac{2e^2}{h}\mathcal{T}_{12}$ [40], where the transmission coefficient between the two probes is

$$\mathcal{T}_{12}(E) = \mathrm{Tr}\big[G(E)\Gamma_2(E)G^\dagger(E)\Gamma_1(E)\big], \tag{2}$$

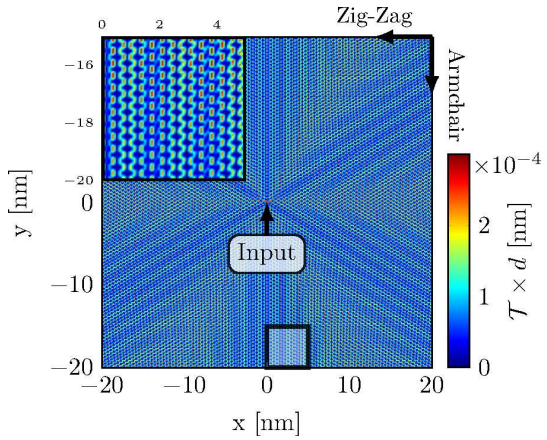

FIG. 2. The conductance map for pristine graphene with $E_F = 0.5|t|$. The fixed input probe is at the origin, and the map represents the conductance between the probes as a function of scanning probe position. The conductance has been multiplied by the inter-probe distance d_{12} to compensate for a geometric decay, see Eq. (3). The inset is a magnification of the boxed area.

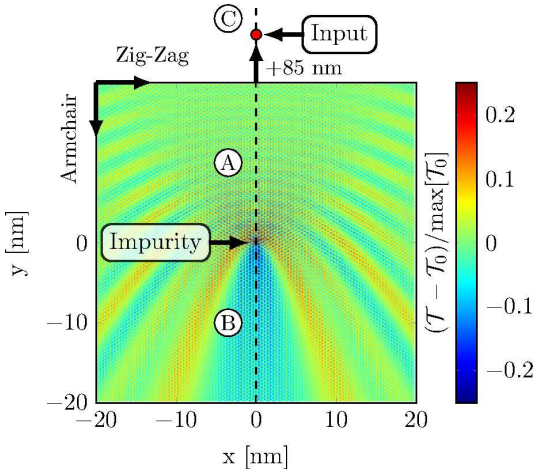

FIG. 3. Relative conductance map for $E_F = 0.25|t|$ around a vacancy at $(0, 0)$. The fixed probe (outside the scan area) at $(0, 106)$ nm is separated from the impurity along the armchair direction.

$\Gamma_i(E)$ $(i = 1, 2)$ is the coupling to the probes and $G/G^\dagger$ is the retarded/advanced Green's function of the sample including probe effects.

Experimental STM tips have finite radii of curvature, limiting the resolution due to couplings with multiple lattice sites. We employ the Tersoff-Hamann approach [44–46] to describe a structureless tip with only the end orbital of a linear atomic chain coupled to the sample. The DOS of the chain is constant in the considered energy range. The coupling between the tip and a nearby lattice site i is angle dependent and decays exponentially with separation [47]. The results presented below are in broad agreement with test calculations performed for more realistic tips, where a predictable smearing of the shorter range features occurs.

Pristine Graphene. – The transmission $\mathcal{T}_{12}$ is obtained from Eq. (2) using a numerical evaluation of Eq. (1). The resulting map is shown in Fig. 2 for $E_F = 0.5|t|$. Other Fermi energies show similar qualitative behaviour, but lower E_F values require a larger scan area to obtain the same number of oscillation periods. In armchair directions a constant $\mathcal{T}_{12} \times d_{12}$ transmission is observed, while oscillations occur for zigzag directions. The results are not very sensitive to the exact position of the stationary probe, with the exponential coupling generally ensuring that the probe primarily couples to a single site.

To qualitatively understand the different behaviour for the two high symmetry directions, we exploit the fact that Eq. (1) can be approximated analytically for separations above a few lattice spacings using the stationary phase approximation (SPA)[42]. The GF can thus be written for the armchair and zigzag directions, respectively, as

$$g_{ij}^{0,ac} = \frac{\mathcal{A}(E)\mathrm{e}^{\mathrm{i}\mathcal{Q}(E)d_{ij}}}{\sqrt{d_{ij}}}, \quad g_{ij}^{0,zz} = \sum_{\eta=\pm} \frac{\mathcal{A}^\eta(E)\mathrm{e}^{\mathrm{i}\mathcal{Q}^\eta(E)d_{ij}}}{\sqrt{d_{ij}}}, \tag{3}$$

where $\mathcal{A}(E)$ is an energy-dependent amplitude and $\mathcal{Q}(E)$ is identified with the Fermi wavevector in the direction of separation between the probes.

Assuming that each probe couples only to a single site, we find, from Eq. (2), that $\mathcal{T}_{12} \propto |g_{12}^0|^2$. The transmission decays monotonically as $1/d_{12}$. Correcting for this geometrical decay yields the constant $\mathcal{T} \times d$ transmission observed in Fig. 2 for armchair directions. The zigzag direction exhibits interference between the $\mathcal{Q}^+$ and $\mathcal{Q}^-$ terms entering in Eq. (3). As seen in the inset of Fig. 2 this leads to both long and short range oscillations. The long range oscillations depend on the Fermi wavelength. The short range oscillation on the other hand has a period of three graphene unit cells and is inherent to quantities measured along the zigzag direction and is independent of E_F. This oscillation varies on the atomic scale and tends to get cancelled for probes coupling to many sites with different phases. However, the long range oscillations are more robust, particularly for small E_F, as the phase is constant over a wider range of sites and should thus be observable even for tips with a larger radius of curvature. The expressions in Eq. (3) can also be used to determine the energy-dependent oscillations arising for fixed probes when a gate is applied. Thus the method described here can be easily extended for a spectroscopic mode of a dual-probe system.

Single Vacancy. The GF for a graphene system with a

perturbation can be calculated using the Dyson equation,

$$G_{ij} = g^0_{ij} + \sum_{nm} g^0_{in} V_{nm} G_{mj}, \tag{4}$$

where V_{nm} is the perturbation matrix element between site n and m. In principle any local perturbation can be included using this technique, and accurate parameterization for defects can be determined by comparison with density functional theory calculations [48, 49]. The same approach is used throughout to include hopping terms between the probes and device region.

Fig. 3 shows the relative change in transmission from the pristine lattice case when a single vacancy is introduced at the origin. The vacancy and fixed probe are separated along the armchair direction and the scanning probe measures conductance fluctuations in the region around the vacancy. Quantum interference effects are clearly visible in Fig. 3. The map for a zigzag separation of fixed probe and vacancy (not shown) looks qualitatively similar. To describe the oscillations we again turn to the SPA expression for the GF. The solution of the Dyson equation for a vacancy is $G_{ij} = g^0_{ij} + g^0_{i0} t_{00} g^0_{0j}$, where $t_{00} = -1/g^0_{00}$ is the t-matrix element of site 0 when $V_{00} \to \infty$. Analytic solutions can be found for the scanning probe path shown by the dashed line in Fig. 3. We observe oscillations in region A, where the scanning probe is between the fixed probe and vacancy such that $d_{12} = d_{10} - d_{20}$ (see Fig. 1). From Eq. (3) we find $\Delta\mathcal{T} \propto \mathcal{R}e\left[\mathcal{A} t_{00} \exp\left(2\mathrm{i}\mathcal{Q} d_{20}\right)/\sqrt{d_{10} d_{20} d_{12}}\right]$, which exhibits $2\mathcal{Q}$ oscillations. When the scanning probe is not between the fixed probe and vacancy no oscillations occur. In region B the transmission is decreased due to scattering, whereas in region C the transmission is either enhanced or decreased depending on the phase difference between the emitted and backscattered waves.

This simple analytical picture allows us to interpret the oscillations as interferences between an incoming plane wave and the backscattered wave, analogous to optical interference effects. To analyze the pattern we consider the Fourier transform (FT) of the conductance map. This approach is generally applicable to scanning images and is not limited to the graphene example. Similar procedures are often employed in the analysis of conventional STM measurements [12, 13, 23]. Fig. 4 shows the FTs of $\Delta\mathcal{T}$ for the single vacancy at different energies and positions of the fixed probe relative to a vacancy at the origin, with Panel (a) corresponding to Fig. 3.

For the incoming wave along the $-y$ (armchair) direction the double-ring patterns in Fig. 4 are the result of scattering from the top and bottom of the Fermi surface where the k vectors are along the y direction (indicated by red dots in Figs. 4f and 4g), to all other points (indicated with arrows) on either the same Fermi surface (intravalley, Fig. 4f) or that of the opposite valley (intervalley, Fig. 4g). The intravalley scattering produces the short wavevector features present at the center of the

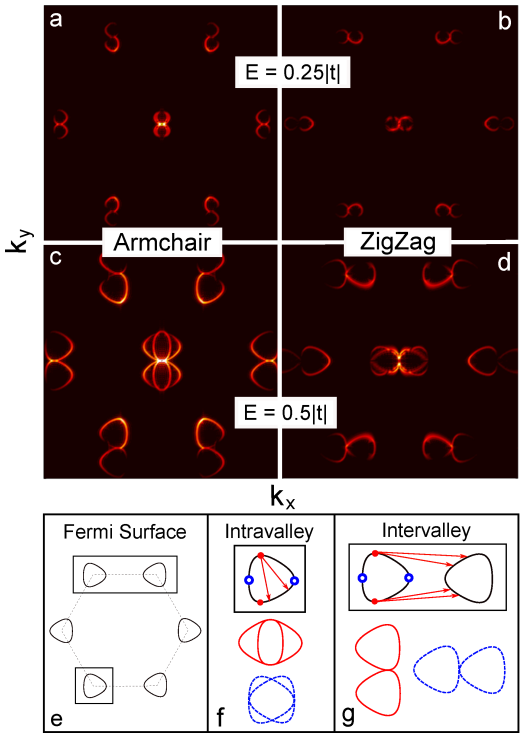

FIG. 4. Fourier transform of the real-space map of $\Delta\mathcal{T}$ for a single vacancy separated from the fixed probe along the armchair ((a) and (c)), and zigzag ((b) and (d)) directions. Energy is in the linear regime ($E = 0.25|t|$) in (a) and (b), and beyond the linear regime ($E = 0.5|t|$) in (c) and (d). (e) The Fermi surface of graphene beyond the linear regime. (f)-(g) Scattering diagrams for intra- and intervalley scattering.

FT (and at all reciprocal lattice vectors), while the intervalley scattering yields the larger wavevector features at the K and K'-points. Figs. 4a and 4b correspond to an energy in the linear dispersion regime whereas 4c and 4d show an energy with trigonal warping, thus leading to the FT signatures sketched by the diagrams of Fig. 4f-g.

Additional fine structure is seen in Fig. 4 due to deviations from the ideal picture of a plane incoming wave. Allowing a broader range of incoming k-vectors increases the part of the Fermi surface which can act as an initial state. This effect is more pronounced for incoming waves along the zigzag direction where even a small broadening of the incoming k-vector allows a larger part of the Fermi surface to act as an initial state. Similar calculations performed for a Gaussian shaped charge distribution, modelling a trapped charge, find that the FT scattering fingerprint is qualitatively similar to that of

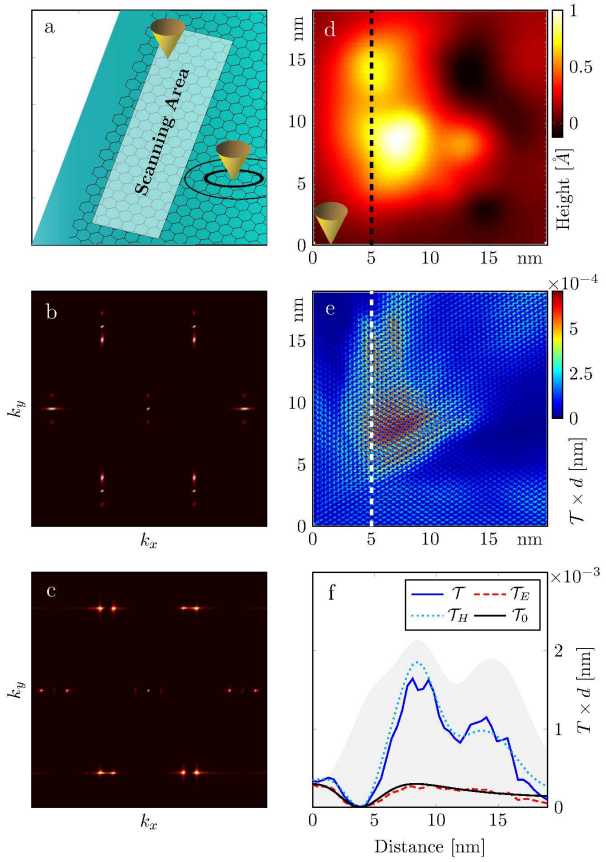

FIG. 5. (a) Dual-probe calculation on an edged graphene system. (b)-(c) Fourier transform of the conductance map near a zigzag edge (b) and an armchair edge (c) for $E_F = 0.25|t|$. (d) Height profile of a non-planar graphene sheet. (e) Conductance map for the non-planar surface from (d) with the stationary probe at (0,0). (f) Transmissions along the dashed line in (b),(e). See main text for further description.

the single vacancy. This is in contrast to single-probe LDOS measurements, where the intervalley scattering fingerprint vanishes for extended defects[22, 50].

Other Geometries. – We now consider two examples of more complicated defects: (i) A graphene sheet with an edge (Fig 5a), and (ii) a non-planar sheet with an irregular height profile (Fig 5d).

In Fig. 5a, we consider a semi-infinite graphene sheet with a pristine zigzag or armchair edge[51]. The incoming wave for the armchair edge is along the zigzag direction, and vice versa. The conductance maps (not shown) reveal oscillations away from the edge arising from the interference between incoming and backscattered waves. In contrast to the single vacancy case, not all scattering angles are available and the double-ring features in the FTs reduce to points indicating the direction of propagation (zigzag for armchair edge and vice versa) as shown in Figs. 5b and 5c. The only qualitative difference is the direction of the incoming wave and hence the direction of the scattering fingerprint in the FT. This is in sharp contrast to single-probe STM measurements, where the zigzag edge does not show an intervalley signal[52]. The dual-probe setup thus opens the possibility of characterizing an edge by its interference pattern as both edges are equally visible with different signatures.

A non-planar height profile, as in Fig. 5d, affects the dual-probe measurement in two ways[53]. The underlying electronic properties of the system are altered by the varying bond lengths throughout the sample and secondly, the tip-sample coupling is affected by their now spatially-varying separation. The conductance map in Fig. 5e takes both of these effects into account. The signal enhancement for regions where the tip and sample are nearest suggest that it is the tip-sample separation dependent contribution which dominates. This is confirmed in Fig. 5f where we calculate the full transmission (blue) along the cross section shown by the white dashed line in Fig. 5e, with the shaded region showing the height profile along this path. In addition, we show the transmissions including the electronic contribution only, $\mathcal{T}_E$, (dashed red, calculated by mapping the changed electronic structure onto a flat surface) and the height contribution only, $\mathcal{T}_H$ (dotted green, calculated by varying the tip-sample separation but leaving the sample electronic structure unchanged). We note that $\mathcal{T}_H$ is a good match to the full calculation, whereas $\mathcal{T}_E$ only slightly deviates from the pristine T_0 (black) curve. However, the height fluctuations considered here are not large enough to give rise to pseudomagnetic field effects like the ones considered in Ref. [54]. In such cases the behaviour of $\mathcal{T}_E$ may provide an ideal framework to determine the effects of pseudomagnetic fields on the transport properties.

Conclusion. – The dual-probe setup offers new flexibility to study directional transport effects in nanosystems beyond the reach for a single STM probe experiment. Using graphene as a case study, anisotropic effects in the pristine material and quantum interferences around defects have been treated. The methodology developed is general and easily applicable to other materials. While the focus of this work has been on the scanning mode to reveal topographic details of the sample, an extension to the case of fixed probes and a variable gate gathering spectroscopic data is straightforward. This may be particularly useful when examining non-planar systems, where the variations due to tip-sample separation may outweigh contributions arising from the actual electronic properties of the system.

Acknowledgements The Center for Nanostructured Graphene (CNG) is sponsored by the Danish Research Foundation, Project DNRF58.

* mikse@nanotech.dtu.dk

[1] A. H. Castro Neto, N. M. R. Peres, K. S. Novoselov, and A. K. Geim, Reviews of Modern Physics **81**, 109 (2009).

[2] J.-H. Chen, C. Jang, S. Xiao, M. Ishigami, and M. S. Fuhrer, Nature nanotechnology **3**, 206 (2008).

[3] E. H. Hwang, S. Adam, and S. Das Sarma, Physical Review Letters **98**, 186806 (2007).

[4] C. R. Dean, A. F. Young, I. Meric, C. Lee, L. Wang, S. Sorgenfrei, K. Watanabe, T. Taniguchi, P. Kim, K. L. Shepard, and J. Hone, Nature Nanotechnology **5**, 722 (2010).

[5] F. Schedin, A. K. Geim, S. V. Morozov, E. W. Hill, P. Blake, M. I. Katsnelson, and K. S. Novoselov, Nature Materials **6**, 652 (2007).

[6] V. W. Brar, R. Decker, H.-M. Solowan, Y. Wang, L. Maserati, K. T. Chan, H. Lee, c. O. Girit, A. Zettl, S. G. Louie, M. L. Cohen, and M. F. Crommie, Nature Physics **7**, 43 (2010).

[7] N. M. R. Peres, F. Guinea, and A. H. Castro Neto, Physical Review B **73**, 125411 (2006).

[8] N. M. R. Peres, Reviews of Modern Physics **82**, 2673 (2010).

[9] C. Bena, Physical Review Letters **100**, 076601 (2008).

[10] L. Simon, C. Bena, F. Vonau, D. Aubel, H. Nasrallah, M. Habar, and J. C. Peruchetti, The European Physical Journal B **69**, 351 (2009).

[11] H. Amara, S. Latil, V. Meunier, P. Lambin, and J.-C. Charlier, Physical Review B **76**, 115423 (2007).

[12] P. Mallet, F. Varchon, C. Naud, L. Magaud, C. Berger, and J.-Y. Veuillen, Physical Review B **76**, 041403 (2007).

[13] G. M. Rutter, J. N. Crain, N. P. Guisinger, T. Li, P. N. First, and J. A. Stroscio, Science **317**, 219 (2007).

[14] N. M. R. Peres, L. Yang, and S.-W. Tsai, New Journal of Physics **11**, 095007 (2009).

[15] V. V. Cheianov and V. I. Fal'ko, Physical Review Letters **97**, 226801 (2006).

[16] A. Bácsi and A. Virosztek, Physical Review B **82**, 193405 (2010).

[17] J. Xue, J. Sanchez-Yamagishi, K. Watanabe, T. Taniguchi, P. Jarillo-Herrero, and B. J. LeRoy, Physical Review Letters **108**, 016801 (2012).

[18] H. Yang, A. J. Mayne, M. Boucherit, G. Comtet, G. Dujardin, and Y. Kuk, Nano Letters **10**, 943 (2010).

[19] C. Park, H. Yang, A. J. Mayne, G. Dujardin, S. Seo, Y. Kuk, J. Ihm, and G. Kim, Proceedings of the National Academy of Sciences **108**, 18622 (2011).

[20] V. Barone, O. Hod, and G. E. Scuseria, Nano Letters **6**, 2748 (2006).

[21] D. J. Mason, M. F. Borunda, and E. J. Heller, Physical Review B **88**, 165421 (2013).

[22] A. Bergvall and T. Löfwander, Physical Review B **87**, 205431 (2013).

[23] A. Deshpande, W. Bao, F. Miao, C. N. Lau, and B. J. LeRoy, Physical Review B **79**, 205411 (2009).

[24] Y. Zhang, V. W. Brar, C. Girit, A. Zettl, and M. F. Crommie, Nature Physics **5**, 722 (2009).

[25] T. Nakayama, O. Kubo, Y. Shingaya, S. Higuchi, T. Hasegawa, C.-S. Jiang, T. Okuda, Y. Kuwahara, K. Takami, and M. Aono, Advanced materials **24**, 1675 (2012).

[26] S. Qin, T.-H. Kim, Z. Wang, and A.-P. Li, Review of Scientific Instruments **83**, 063704 (2012).

[27] V. Cherepanov, E. Zubkov, H. Junker, S. Korte, M. Blab, P. Coenen, and B. Voigtländer, Review of scientific instruments **83**, 033707 (2012).

[28] A. Bannani, C. A. Bobisch, and R. Moller, Review of scientific instruments **79**, 083704 (2008).

[29] S.-H. Ji, J. B. Hannon, R. M. Tromp, V. Perebeinos, J. Tersoff, and F. M. Ross, Nature materials **11**, 114 (2012).

[30] P. W. Sutter, J.-I. Flege, and E. A. Sutter, Nature Materials **7**, 406 (2008).

[31] W. Wang and M. R. Beasley, Applied Physics Letters **102**, 131605 (2013).

[32] J. D. Buron, D. H. Petersen, P. Bøggild, D. G. Cooke, M. Hilke, J. Sun, E. Whiteway, P. F. Nielsen, O. Hansen, A. Yurgens, and P. U. Jepsen, Nano Letters **12**, 5074 (2012).

[33] M. F. Borunda, H. Hennig, and E. J. Heller, Physical Review B **88**, 125415 (2013).

[34] A. S. Mayorov, R. V. Gorbachev, S. V. Morozov, L. Britnell, R. Jalil, L. A. Ponomarenko, P. Blake, K. S. Novoselov, K. Watanabe, T. Taniguchi, and A. K. Geim, Nano Letters **11**, 2396 (2011).

[35] C. Berger, Z. Song, X. Li, X. Wu, N. Brown, C. Naud, D. Mayou, T. Li, J. Hass, A. N. Marchenkov, E. H. Conrad, P. N. First, and W. A. de Heer, Science **312**, 1191 (2006).

[36] K. Bolotin, K. Sikes, Z. Jiang, M. Klima, G. Fudenberg, J. Hone, P. Kim, and H. Stormer, Solid State Communications **146**, 351 (2008).

[37] P. Rickhaus, R. Maurand, M.-H. Liu, M. Weiss, K. Richter, and C. Schönenberger, Nature communications **4**, 2342 (2013).

[38] J. Baringhaus, F. Edler, and C. Tegenkamp, Journal of Physics: Condensed Matter **25**, 392001 (2013).

[39] F. R. Eder, J. Kotakoski, K. Holzweber, C. Mangler, V. Skakalova, and J. C. Meyer, Nano Letters **13**, 1934 (2013).

[40] S. Datta, *Electronic Transport in Mesoscopic Systems* (Cambridge University Press, 1997).

[41] H. Haug and A.-P. Jauho, *Quantum kinetics in transport and optics of semiconductors* (Springer, 2008).

[42] S. R. Power and M. S. Ferreira, Physical Review B **83**, 155432 (2011).

[43] S. Reich, J. Maultzsch, C. Thomsen, and P. Ordejón, Physical Review B **66**, 035412 (2002).

[44] V. Meunier and P. Lambin, Physical Review Letters **81**, 5588 (1998).

[45] T. Fukuda, H. Oymak, and J. Hong, Physical Review B **75**, 195428 (2007).

[46] T. Nakanishi and T. Ando, Physica E: Low-dimensional Systems and Nanostructures **42**, 726 (2010).

[47] The coupling is calculated using[11, 44], $t_i = t_0 w_i \mathrm{e}^{-d_i/\lambda} \cos\left(\theta_i\right)$ where $w_i = \mathrm{e}^{-a d_i^2} / \sum_j \mathrm{e}^{-a d_j^2}$, θ_i is the angle between the tip apex and site i, $\lambda = 0.85\mathring{A}$, $a = 0.6\mathring{A}^{-2}$. t_0 is a scaling factor which we set to $t_0 = 10t$.

[48] R. M. Ribeiro, V. M. Pereira, N. M. R. Peres, P. R. Briddon, and A. H. Castro Neto, New Journal of Physics **11**, 115002 (2009).

[49] S. M.-M. Dubois, A. Lopez-Bezanilla, A. Cresti, F. Triozon, B. Biel, J.-C. Charlier, and S. Roche, ACS nano **4**, 1971 (2010).

[50] K. Wakabayashi, Y. Takane, and M. Sigrist, Physical

Paper II

Mikkel Settnes, Stephen R. Power, Dirch H. Petersen and Antti-Pekka Jauho

Dual-probe spectroscopic fingerprints of defects in graphene

Phys. Rev. B **90**, 035440 (2014)

arXiv:1405.0385v1 [cond-mat.mes-hall] 2 May 2014

Dual-probe spectroscopic fingerprints of defects in graphene

Mikkel Settnes,[1,*] Stephen R. Power,[1] Dirch H. Petersen,[1] and Antti-Pekka Jauho[1]

[1] *Center for Nanostructured Graphene (CNG), Department of Micro and Nanotechnology, DTU Nanotech, Technical University of Denmark, DK-2800 Kongens Lyngby, Denmark*

(Dated: May 5, 2014)

Recent advances in experimental techniques emphasize the usefulness of multiple scanning probe techniques when analyzing nanoscale samples. Here, we analyze theoretically dual-probe setups with probe separations in the nanometer range, *i.e.*, in a regime where quantum coherence effects can be observed at low temperatures. In a dual-probe setup the electrons are injected at one probe and collected at the other. The measured conductance reflects the local *transport properties* on the nanoscale, thereby yielding information complementary to that obtained with a standard one-probe setup (the local density-of-states). In this work we develop a real space Green's function method to compute the conductance. This requires an extension of the standard calculation schemes, which typically address a finite sample between the probes. In contrast, the developed method makes no assumption on the sample size (*e.g.*, an extended graphene sheet). Applying this method, we study the transport anisotropies in pristine graphene sheets, and analyze the spectroscopic fingerprints arising from quantum interference around single-site defects, such as vacancies and adatoms. Furthermore, we demonstrate that the dual-probe setup is a useful tool for characterizing the electronic transport properties of extended defects or designed nanostructures. In particular, we show that nanoscale perforations, or antidots, in a graphene sheet display Fano-type resonances with a strong dependence on the edge geometry of the perforation.

I. INTRODUCTION

A key step towards developing novel applications for graphene and other two-dimensional materials[1–3] is to obtain a detailed understanding of their electron transport properties on the nanoscale.[4] At these length scales structural details play a crucial role due to the restricted dimensionality. Thus, studying spatially resolved electron transport becomes important, especially near defects and boundaries, which dramatically affect the conductance of a device.[5,6]

Scanning Tunnelling Microscopy (STM)[7,8] is an important non-invasive method for studying the electronic structure of surfaces. Nanometer scale STM measurements, yielding both local density of states (LDOS) and topographic details, are extensively used both theoretically[9–16] and experimentally[17–22] in the study of graphene. On the other hand, transport properties are most commonly measured by using invasive macroscopic contacts. Such contacts represent only a minor perturbation in large systems, but can be the main source of scattering in nanoscale devices. Here we evaluate the conductance between two STM-like tips, *i.e.*, a situation where nanoscale transport properties can be extracted with noninvasive probes. The considered regime is thus between the single STM setup and the fixed macroscopic contacts.

The envisaged technique requires independently positioned point probes to act as input and output. Such setups have been achieved experimentally[23–28] and the recent progress is reviewed in detail in Refs. 29 and 30. State-of-the-art experimental techniques[24,31] allow for tip separations down to 50-100 nm. Multi-probe measurements have been used to characterize several systems: anisotropic transport;[32] nanowires;[24,33] carbon nanotubes;[34] graphene nanoribbons;[31] grain boundaries both in graphene[35,36] and other materials;[37] and monolayer and bilayer graphene.[38–40]

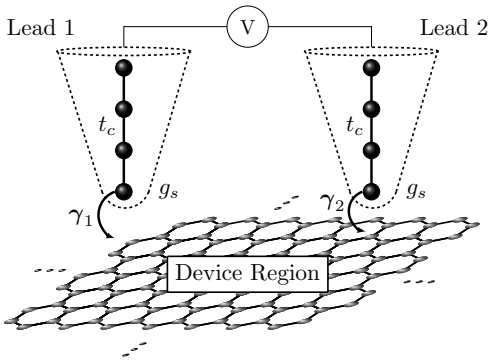

FIG. 1. Setup sketch including the leads modelled as one dimensional chains with a hopping t_c between the sites. The surface Green's functions g_s are indicated together with the coupling $\boldsymbol{\gamma}^{1/2}$ between the lead and the graphene sample.

Graphene-based materials are particularly interesting because the mean free path in high quality samples is comparable to or perhaps even longer than the probe separation.[31] As a result, the dual-STM setup is effectively in the phase coherent regime at low temperatures. In this regime, structural details, such as single-site scattering centers, edges, or grain boundaries, limit the conductance, such that quantum interference phenomena become visible in the transmission between the probes.

In a recent work,[41] the present authors proposed a dual-probe setup on graphene with one fixed probe while the other probe operating in the scanning mode. We used real-space conductance maps to explore quantum interference effects near defects and edges in graphene.

Fourier transforms of the real-space conductance maps allowed us to extract further details, and in particular they revealed information about intra and intervalley scattering due to these defects. In the present work, we extend the theoretical investigation to the spectroscopic mode of the dual-probe system, where two fixed probes operate in the presence of an applied gate, which allows the Fermi energy to be varied. While we focus on graphene as an illustrative example, particularly suited for the observation of quantum interference phenomena, the methodology is general and applicable to other surfaces or two-dimensional materials. We use a combination of numerical calculations and analytic expressions to explain the spectroscopic fingerprints observed both in pristine graphene and in the presence of vacancies and adatoms. Finally, we extend the framework to nanostructures such as perforations.

The paper is organized as follows: Section II introduces the real space Green's function (GF) method and highlights the conceptual differences compared to standard recursive GF techniques. Section III considers dual-probe spectroscopy of pristine graphene based on both analytical approximations of the GF and numerical calculations. Section IV introduces defects where both single vacancies and adatoms are considered in the high symmetry directions, but also randomly placed in the sample. Finally, Section V considers perforations of the graphene lattice with different edge geometries.

II. METHOD

A. Transport calculations using point probes

The transport setup consists of a device region and two leads as illustrated on Fig. 1. We describe the leads by the surface GF, g_S, which couples to the device region that is described by the retarded/advanced GF $\boldsymbol{G}/\boldsymbol{G}^\dagger$. We view g_S as a known quantity (a simple analytic model is used below, but more elaborate models are readily incorporated in the formalism), and solve $\boldsymbol{G}/\boldsymbol{G}^\dagger$ from the appropriate Dyson equation, see below. The main difference between the setup sketched in Fig. 1 and the standard Landauer setup[42], where left and right lead couple to the edge of a finite device region, is that the device region is now *infinite*. Standard recursive methods, treating infinite systems, use periodic boundary conditions. However, imposing periodic boundary conditions for the two-point probe setup would lead to a spurious repetition of the probes. As a consequence we require a real space formalism ensuring that the probes only appear locally.

B. Real space graphene Green's function

The basic building block of our method is the real space representation of the GF for an infinite pristine graphene sheet, $\boldsymbol{G}^0$. This object is computed using a nearest neighbour tight-binding model, and the GF element connecting sites i and j is given by

$$G^0_{ij}(z) = \frac{1}{\Omega_{BZ}} \int \mathrm{d}^2\boldsymbol{k} \frac{N_{ij}(z)\mathrm{e}^{\mathrm{i}\boldsymbol{k}\cdot(\boldsymbol{r}_j-\boldsymbol{r}_i)}}{z^2-\gamma_{cc}^2|f(\boldsymbol{k})|^2} \qquad (1)$$

where $z = E + \mathrm{i}0^+$ is the energy, Ω_{BZ} is the area of the first Brillouin zone and the carbon-carbon hopping integral is $\gamma_{cc} \approx -2.7$ eV.[43] The position of site i is denoted by $\boldsymbol{r}_i = m_i\boldsymbol{a}_1 + n_i\boldsymbol{a}_2$ in units of the lattice vectors $\boldsymbol{a}_1$ and $\boldsymbol{a}_2$ with m_i and n_i being integers. We introduced the definition $N_{ij}(z) = z$, when i and j are on the same sublattice and $N_{ij}(z) = \gamma_{cc}f(\boldsymbol{k})$ if i and j are on opposite sublattices ($N_{ji} = N^*_{ij}$). Finally, we use the definition $f(\boldsymbol{k}) = 1 + \mathrm{e}^{\mathrm{i}\boldsymbol{k}\cdot\boldsymbol{a}_1} + \mathrm{e}^{\mathrm{i}\boldsymbol{k}\cdot\boldsymbol{a}_2}$.

The two dimensional integral Eq. (1) can be converted to a single integration using complex contour techniques.[44] The remaining integration can be treated using standard numerical integration. This approach is valid regardless of the separation between the points i and j; even long distance terms are easily obtained with only a minor complications arising in the convergence of Eq. (1) due to the rapidly oscillating phase.

C. Including defects

To include modifications to the pristine lattice, we use the Dyson equation:

$$\boldsymbol{G} = \boldsymbol{G}^0 + \boldsymbol{G}^0\boldsymbol{V}\boldsymbol{G} = \left(\boldsymbol{1} - \boldsymbol{G}^0\boldsymbol{V}\right)^{-1}\boldsymbol{G}^0, \qquad (2)$$

where $\boldsymbol{G}^0$ is the pristine GF matrix and $\boldsymbol{V}$ is the perturbation. Any local perturbation (*e.g.*, adatoms, vacancies, coupling to leads) can be included using this technique. Accurate parametrizations for many of these perturbations can be obtained using density functional theory.[45,46]

We note that the dimension of the $\boldsymbol{V}$-matrix is determined by the number of the modified sites. Thus, for N modified sites one needs to solve a $N \times N$ system, and the computational cost thus follows the number of defect and contact sites, rather than the sample size which is usual for recursive GF methods.

All perturbations to the pristine lattice are added in real space using Eqs. (1) and (2), as opposed to describing them with additional terms in the reciprocal space Hamiltonians. This ensures that modifications are added locally and not repeated via periodic boundary conditions. The approach is well suited to situations where the majority of the sample is pristine, as unmodified graphene is computationally "free".

D. Transmission

The transmission coefficient between the two probes, $\mathcal{T}_{12}$, yields the zero temperature conductance as $\mathcal{G}_{12} =$

$\frac{2e^2}{h}\mathcal{T}_{12}$ (here we treat the spin degenerate case). The transmission is given by[42,47]

$$\mathcal{T}_{12}(E) = \mathrm{Tr}\big[\boldsymbol{G}(E)\boldsymbol{\Gamma}_1(E)\boldsymbol{G}^\dagger(E)\boldsymbol{\Gamma}_2(E)\big], \qquad (3)$$

where E is the energy, $\boldsymbol{G}$ is the full Green function Eq. (2) (including the sites coupling to the leads) and $\boldsymbol{\Gamma}_{1/2}$ is the coupling to the leads given as $\boldsymbol{\Gamma}_{1/2}(E) = \mathrm{i}\big(\boldsymbol{\Sigma}_{1/2} - \boldsymbol{\Sigma}_{1/2}^\dagger\big)$. The self-energies $\boldsymbol{\Sigma}_{1/2}$ of the leads are calculated from the coupling matrix between the lead and the sample $\boldsymbol{\gamma}_{1/2}$ and the surface GF of the lead g_s, *i.e.* $\boldsymbol{\Sigma}_{1/2} = \boldsymbol{\gamma}_{1/2}{}^\dagger g_s \boldsymbol{\gamma}_{1/2}$. We use a linear atomic chain model for the leads where the surface GF is known exactly:[48] $g_S = \frac{E \pm \sqrt{E^2 - 4\gamma_l^2}}{2\gamma_l^2}$, where γ_l is the coupling between the sites in the linear chain (here $\gamma_l = \gamma_{cc}$ is used). The parameters are chosen to ensure a constant DOS in the leads in the considered energy interval.

The coupling between the graphene and the tip of the probes is calculated using the Tersoff-Hamann approach[49,50]

$$\gamma_j = \gamma_0 w_j \mathrm{e}^{-d_j/\lambda}\cos\big(\theta_j\big), \qquad (4)$$

where θ_j and d_j are the angle and the distance, respectively, between the tip apex and site j, $w_j = \mathrm{e}^{-ad_j^2}/\sum_m \mathrm{e}^{-ad_m^2}$, $\lambda = 0.85$Å and $a = 0.6\text{Å}^{-2}$ are constants chosen in accordance to Refs. 50 and 51. γ_0 is a scaling factor, which in practical calculations is set to $\gamma_0 = 10\gamma_{cc}$.

When considering a probe coupling to a single site, the transmission in Eq. (3) reduces to the following simple form:

$$\mathcal{T}_{12}(E) = \big(2\pi\gamma_1\gamma_2\rho_{lead}\big)^2\,|G_{12}(E)|^2, \qquad (5)$$

where $\rho_{lead} = -\mathrm{Im}(g_s)/\pi$ is the constant density of states of the last atom of lead. Hence the only energy dependence originates from the GF term.

From Eq. (5) we notice that the transmission scales with the DOS of the leads. The transmission also scales with the coupling to the probes as $\sim \gamma_1^2\gamma_2^2$. As $\gamma_{1/2}$ depend exponentially on the distance between the tip and the sample, this means that decreasing the distance between sample and tip by ~ 1 Å increases the coupling which in turn increases the transmission by a factor of ~ 100.

In what follows, we consider STM-like probes (*i.e.* probes which couple only to a very limited number of sites in the sample) in order to obtain transparent results giving insight into the processes which dominate the transport between the point probes. More realistic or larger probes may be included within the presented framework by increasing the number of graphene lattice sites that couple to the probes or by substituting the semi-infinite mono-atomic chain by other surface GF's.

Finally, it is noted that we consider the low temperature and low bias regime and therefore ignore inelastic effects such as phonon scattering.[52] Here we also neglect the possible non-planarity of the graphene sheet, either due to the intrinsic ripples[53] or caused by one of the probes.[38] However, we previously discussed the effect of ripples on dual-probe scanning mode calculations in Ref. 41.

III. PRISTINE GRAPHENE

We first consider the case of pristine graphene without defects. In this case we can gain a transparent understanding by the so called stationary phase approximation (SPA)[44] to the GF in Eq. (1). The SPA is valid for the high symmetry directions (armchair or zigzag) and for separations between the i and j sites exceeding a few lattice spacings. Using the SPA, the graphene GF in Eq. (1) can be expressed as

$$G^{0,ac}_{ij,\mathrm{SPA}} = \frac{\mathcal{A}(E)\mathrm{e}^{\mathrm{i}\mathcal{Q}(E)d_{ij}}}{\sqrt{d_{ij}}}, \qquad (6a)$$

$$G^{0,zz}_{ij,\mathrm{SPA}} = \sum_{\eta=\pm}\frac{\mathcal{A}^\eta(E)\mathrm{e}^{\mathrm{i}\mathcal{Q}^\eta(E)d_{ij}}}{\sqrt{d_{ij}}}, \qquad (6b)$$

where $\mathcal{A}(E)$ is an energy dependent amplitude and $\mathcal{Q}(E)$ is the Fermi wavevector in the armchair and zigzag directions. The coefficients are given in Appendix A and derived in Ref. 44.

Inserting Eq. (6) into Eq. (5) gives the distance dependence of the transmission, $\mathcal{T}_{12} \propto 1/d_{12}$. Consequently the resistance scales linearly with probe separation, $R \propto d_{12}$.

Consider now the case when the separation between the two probes is in the armchair direction. Using Eq. (6a), we find that the transmission coefficient increases linearly with energy. The linear increase of $\mathcal{T}^{(ac)} \propto |\mathcal{A}|^2/d_{12}$ originates from the fact that $|\mathcal{A}|^2$ grows linearly with energy for low energies, see Appendix A.

The zigzag direction is more complicated because of the two terms in Eq. (6b), caused by the two non-identical sides of the Fermi surface along the zigzag direction:

$$\begin{aligned}\mathcal{T}^{(zz)}_{12}\times d_{12} &\propto \Big|\sum_{\eta=\pm}\mathcal{A}^\eta\mathrm{e}^{\mathrm{i}\mathcal{Q}^\eta d_{12}}\Big|^2\\ &= |\mathcal{A}^+|^2 + |\mathcal{A}^-|^2\\ &\quad + |\mathcal{A}^+||\mathcal{A}^-|\cos\left(\Big[\mathcal{Q}^+ - \mathcal{Q}^-\Big]d_{12}\right). \end{aligned} \qquad (7)$$

In addition to the linear increase (the first two terms), we also find an oscillating term. The oscillation period decreases with increasing energy due to the energy dependence of $\mathcal{Q}^+ - \mathcal{Q}^-$. We therefore expect a more rapid oscillation for higher values of the Fermi energy.

In Fig. 2b-c we plot the energy dependent transmission for d_{ij} parallel to either armchair (b) and zigzag (c) for probe separation ~ 50 nm. The transmissions are calculated using both Eq. (6) (dots) and using a numerical evaluation of Eq. (1) (line). We note an almost perfect

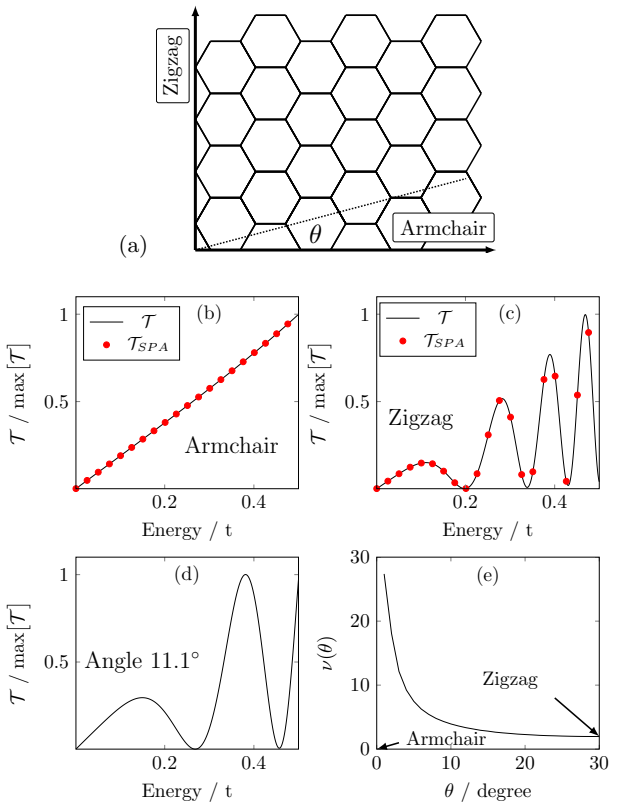

FIG. 2. (a) Sketch showing the pristine sample and the rotation angle θ from the armchair direction. (b-d) The transmission as a function of energy between the two leads separated by 50 nm along (b) armchair, (c) zigzag and (d) rotated $\theta = 11.1^\circ$ from the armchair direction. In (b) and (c) the transmission calculated using the SPA is indicated (red dots). (e) The oscillation period $\nu(\theta)$ (see main text for definition) is plotted against rotation angle θ as defined in (a). The curve is constructed by averaging over many individual calculations with distances ranging from 20 to 100 nm.

match for all energies, which confirms the validity of the SPA approach.

In Fig. 2d we consider a direction rotated $\theta \approx 11^\circ$ relative to the armchair direction. Consequently the oscillation period depends on the rotation angle θ, as defined on Fig. 2a. The oscillation is a consequence of the asymmetry of the Fermi surface in the given direction and is therefore a fingerprint of the crystalline direction between the probes.

The GFs for all other separations (except armchair) have the same form as Eq. (6b).[44] So the transmission generally takes a form equivalent to Eq. (7) but with different expressions for $\mathcal{Q}^+$ and $\mathcal{Q}^-$, which depend on the direction of separation. In the limit of low energies we can expand the coefficients as $|\mathcal{A}|^2 \propto E$ and $(\mathcal{Q}^+ - \mathcal{Q}^-) \propto E^2/\nu(\theta)$. Here $\nu(\theta)$ is an oscillation period that depends on the angle θ (defined in Fig. 2a). Accordingly $\theta = 0$ denotes armchair separation and $\theta = 30^\circ$ denotes zigzag separation between the probes. The energy dependence of the transmission in Eq. (7) now becomes

$$\mathcal{T}_{12} \propto E \cos\left(E^2 d_{12}/\nu(\theta) + \phi_{ph}\right), \tag{8}$$

where ϕ_{ph} is a phase factor, which is independent of the direction but depends on the distance and the exact atoms coupling to the probes. If we plot $\mathcal{T}_{12}/E$ as a function of $d_{12}E^2$ we can determine the period $\nu(\theta)$ as the lowest full period of oscillation in the $\mathcal{T}_{12}/E$ vs $d_{12}E^2$ plot for the corresponding angle θ. In Fig. 2e, we plot $\nu(\theta)$ as a function of angle. Fig. 2e is the average of many individual calculations of $\nu(\theta)$ for separations ranging from 20 to 100 nm.

From Fig. 2e we conclude that $\nu(\theta)$ provides a fingerprint of the probe separation direction. Furthermore $\nu(\theta)$ enables us to determine the crystalline direction with a simple spectroscopic measurement provided we know the distance between the probes and that the gate is kept sufficiently small.

IV. SIMPLE DEFECTS

Next we consider defects like vacancies and adatoms. To obtain an analytical treatment in this case let the defects be coupled to a group of sites denoted 0 and the probes coupled to sites denoted 1 and 2. We restate the Dyson equation (Eq. (2)) using the t-matrix formalism

$$\boldsymbol{G}_{12} = \boldsymbol{G}^0_{12} + \boldsymbol{G}^0_{10}\mathbf{t}_{00}\boldsymbol{G}^0_{02}, \tag{9}$$

where

$$\mathbf{t}_{00} = \left(\mathbf{1} - \boldsymbol{V}_{00}\boldsymbol{G}^0_{00}\right)^{-1}\boldsymbol{V}_{00}. \tag{10}$$

Inserting this into Eq. (3) we obtain

$$\begin{aligned}\mathcal{T}_{12} &\propto \mathrm{Tr}\left[\left(\boldsymbol{G}_{12} + \boldsymbol{G}_{10}\mathbf{t}_{00}\boldsymbol{G}_{02}\right)\left(\boldsymbol{G}^\dagger_{12} + \boldsymbol{G}^\dagger_{02}\mathbf{t}^\dagger_{00}\boldsymbol{G}^\dagger_{10}\right)\right] \\ &= \mathrm{Tr}\Big[\boldsymbol{G}_{12}\boldsymbol{G}^\dagger_{12} + \left(\boldsymbol{G}_{10}\mathbf{t}_{00}\boldsymbol{G}_{02}\right)\left(\boldsymbol{G}_{10}\mathbf{t}_{00}\boldsymbol{G}_{02}\right)^\dagger \\ &\quad + 2\mathrm{Re}\Big\{\left(\boldsymbol{G}_{10}\mathbf{t}_{00}\boldsymbol{G}_{02}\right)\boldsymbol{G}^\dagger_{12}\Big\}\Big].\end{aligned} \tag{11}$$

Eq. (11) is generally applicable. If the probes and the defect couple to single sites all matrices reduce to scalar quantities and enable simple analytic expressions. For example, we use the SPA expression Eq. (6a) when both probes and defects are along the armchair direction

$$\begin{aligned}\Delta\mathcal{T}_{12} = \mathcal{T}_{12} - \mathcal{T}^0_{12} &\propto \frac{|\mathcal{A}|^4}{d_{10}d_{20}}|t_{00}|^2 \\ &\quad - \frac{|\mathcal{A}|^3}{\sqrt{d_{10}d_{20}d_{12}}}\mathrm{Re}\Big\{(1+\mathrm{i})t_{00}\mathrm{e}^{\mathrm{i}\mathcal{Q}(d_{10}+d_{20}-d_{12})}\Big\},\end{aligned} \tag{12}$$

where $\mathcal{T}^0_{12}$ is the pristine transmission, d_{12} denotes the distance between the two probes, and d_{10} and d_{20} denote

the distance between the defect site and probe 1 and 2, respectively.

Assuming the defect lies between the probes, *i.e.* $d_{12} = d_{10} + d_{20}$, we get from Eq. (12)

$$\Delta\mathcal{T}_{12} \propto \frac{|\mathcal{A}|^4}{d_{10}d_{20}}|t_{00}|^2 - \frac{|\mathcal{A}|^3}{\sqrt{d_{10}d_{20}d_{12}}}\mathrm{Re}\Big\{(1+\mathrm{i})t_{00}\Big\}. \tag{13}$$

Thus, a change in transmission occurs due to the backscattering at the defect. This was also observed in Ref. 41 where one probe scanned around the defect position to obtain a real space image of the transmission change. The size and form of $\Delta\mathcal{T}_{12}$ depend on the type of defect through t_{00}.

For the defect on either side of the probes, *i.e.* $d_{10} = d_{12} + d_{20}$, Eq. (12) becomes

$$\Delta\mathcal{T}_{12} \propto \frac{|\mathcal{A}|^4}{d_{10}d_{20}}|t_{00}|^2 - \frac{|\mathcal{A}|^3}{\sqrt{d_{10}d_{20}d_{12}}}\mathrm{Re}\Big\{(1+\mathrm{i})t_{00}\mathrm{e}^{2\mathrm{i}\mathcal{Q}d_{20}}\Big\}. \tag{14}$$

The result for the impurity on the other side of the probes ($d_{20} = d_{12} + d_{10}$) is obtained by interchanging 1 and 2. The case in Eq. (14) gives rise to oscillations as we change the energy (by changing $\mathcal{Q}$). The oscillations are a consequence of quantum interference between the outgoing wave from the output probe and the scattered wave. Similar expressions as Eqs. (13) and (14) can be derived for the zigzag separation, but the simple form is complicated by the two interfering terms in Eq. (6b).

Eqs. (13) and (14) show that the effect of the impurity enters through the t-matrix, which depends on the type of impurity. In this section we consider two specific defects: vacancies and adatoms. Vacancies are modelled as a change of the on-site energy, $V_{00} \to \infty$. On the other hand, adatoms are modelled with an energy dependent self energy Σ^α, describing a resonant level with energy ϵ_α, coupled to the graphene sample with coupling constant γ_α, *i.e.* $V_{00} = \Sigma^\alpha_{00} = |\gamma_\alpha|^2/(E + \mathrm{i}0^+ - \epsilon_\alpha)$. The t-matrices become,[54,55]

$$\text{Vacancy}: \; t_{00} = \frac{V_{00}}{1 - V_{00}G^0_{00}} \to -\frac{1}{G^0_{00}}. \tag{15a}$$

$$\begin{aligned}\text{Adatom}: \; t_{00} &= \frac{\Sigma^\alpha_{00}}{1 - \Sigma^\alpha_{00}G^0_{00}} = \left(\Sigma^{\alpha\,-1}_{00} - G^0_{00}\right)^{-1} \\ &= \frac{|t_\alpha|^2}{E - \epsilon_\alpha - |t_\alpha|^2 G^0_{00}}.\end{aligned} \tag{15b}$$

The adatom gives rise to a resonant level whose position is determined by both ϵ_α and γ_α. We choose parameters from Ref. 56 as $\epsilon_\alpha = -0.185|t|$ and $t_\alpha = 0.37|t|$. This gives a resonant level within the energy interval of consideration.

Fig. 3 shows the numerical result compared to the analytical expression Eq. (13) for both a vacancy and an adatom. The impurities are located equidistant ($d_{10} = d_{20} = d_{12}/2$) from the two probes. Again, we observe an almost perfect match between the analytic (symbols) and numerical (lines) results. The vacancy gives rise to an overall reduction in transmission due to scattering, while the adatom leads to a smaller reduction of transmission, except at the resonance. Especially at resonance the level of the adatom interacts strongly with the continuum of the graphene states giving rise to the asymmetric Fano type resonance[57] observed at approximately -0.15 eV in Fig. 3. Similar results are obtained for the zigzag direction, but superimposed onto the characteristic zigzag oscillation discussed in Section III.

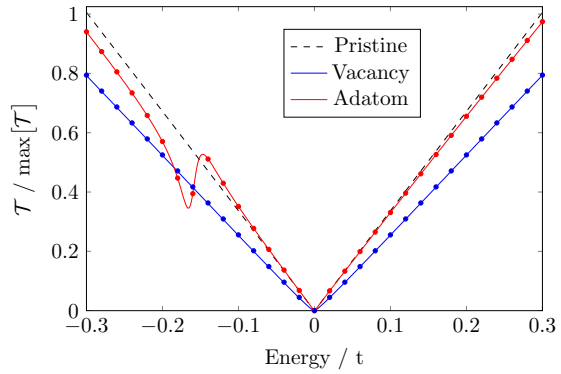

FIG. 3. The transmission as a function of energy for pristine graphene (dashed), vacancy (red) and adatom (blue). The impurity is in between probes, which are separated by ~ 50 nm along the armchair direction. The dots denote a similar calculation using the SPA expression Eq. (13). The paramters for the adatom are chosen as in Ref. 56 as $\epsilon_\alpha = -0.185|t|$ and $t_\alpha = 0.37|t|$.

Impurity positions

To investigate the influence of adatom position on the resonance, we now move the adatom away from the high symmetry point between the probes. First, the adatom is moved along the line connecting the probes such that it is no longer equidistant from the probes. These positions are shown by the red and green squares in Fig. 4a. The corresponding dual-probe transmissions are shown in Fig. 4b and the change relative to the pristine graphene sheet is shown in Fig. 4c. Furthermore, both panels include the transmission for the equidistant impurity (blue curve) for comparison. Likewise Figs. 4d and 4e show the corresponding transmissions as the adatom is moved perpendicular to the line separating the probes while keeping the impurity equidistant to the probes.

First, we consider the parallel case. Here the adatom is either in-between the probes, yet closer to one of them, or to the far side of one of the probes (*i.e.* green and red square on Fig. 4). The Fano-type resonance persists as the adatom is moved. Only the form of the resonance changes. However, we notice a distinct difference between the two cases. When the impurity does not lie

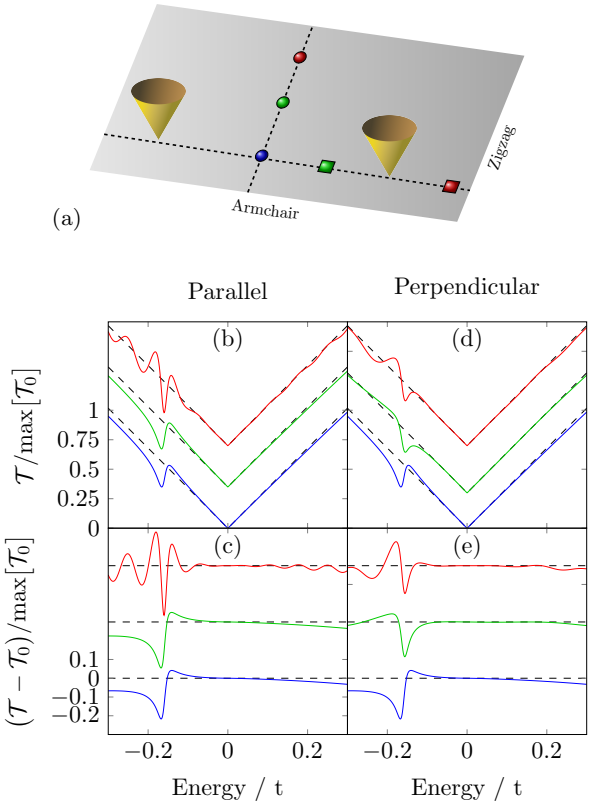

FIG. 4. (a) Sketch illustrating the two probes separated along the armchair direction by ~ 50 nm. The marks refers to impurity positions. Blue is along the line of separation and equidistant of the probes. The green and red squares are moved relative to the blue site along the armchair direction (parallel) by 12.8 nm and 34 nm, respectively. The transmission for the parallel translation are shown in (b) and (c). The green and red circles are equidistant of the probes but moved along the zigzag direction (perpendicular) to 7.4 nm and 17.2 nm, respectively. The transmission function for impurities in these positions are shown in (d) and (e). The zero point for the curves has been translated for better distinction between curves.

between the probes (red square), additional oscillations arise. This can be understood by comparing Eqs. (13) and (14) where the difference is the term, $\exp\left[2i\mathcal{Q}d_{20}\right]$. This term gives rise to oscillations through the energy dependence of $\mathcal{Q}$. The oscillations have the same origin as these investigated in real space in Ref. 41, while scanning one probe around the impurity. We notice the same effect for vacancy positions everywhere outside the high symmetry positions.

The same type of oscillations are present for the perpendicular direction. In this case we have to consider the interference between the emitted wave and the scattered wave returning from the impurity in the direction of the second probe.

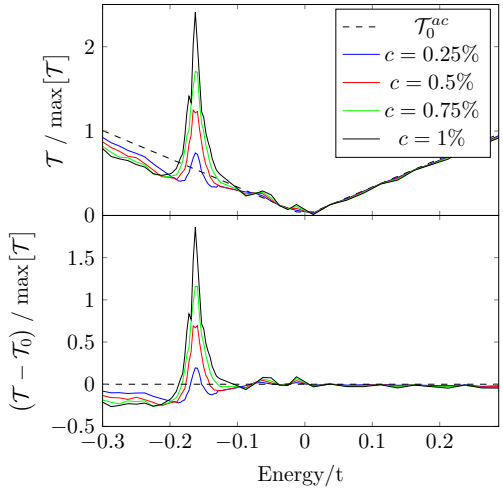

FIG. 5. (a) Configuration averaged transmission as a function of energy. (b) The difference between the averaged transmission and the pristine transmission. We place impurities in a 50×85 nm square around the probes The unequal sides are chosen to take into account the probe separation direction. The curves are made from averaging $2 \cdot 10^4$ configurations.

Configurational average

In an experimental setup, however, individual defects or adatoms can be difficult to locate. This makes investigations of many randomly scattered defects important. We fix the two probes with an armchair separation of 50 nm and place adatoms randomly with varying concentration. The averaged transmissions are shown in Fig. 5. The transmission is almost unchanged at energies away from the resonance, despite the oscillations caused by individual impurity positions shown in Fig. 4. This shows that the oscillations, induced by interference between incoming and scattered waves, tend to average out for many defects. However, the resonance feature persists through configurational averaging as is evident from Fig. 5. The signal is enhanced on resonance and an overall Fano type resonance is present in Fig. 5b with a height that scales with impurity concentration. This suggests that the dual-probe setup can detect the type (position of resonant level) and concentration (peak height) of adatoms on the surface of a graphene sample. This is in line with the suggested applications of graphene as a gas sensor.[58,59] In the case of random vacancies we see an overall decrease in the transmission following the impurity concentration. In this case a zero energy peak is present due to localisation effects around vacancies. This feature has been described in several works addressing the LDOS[5,11,15].

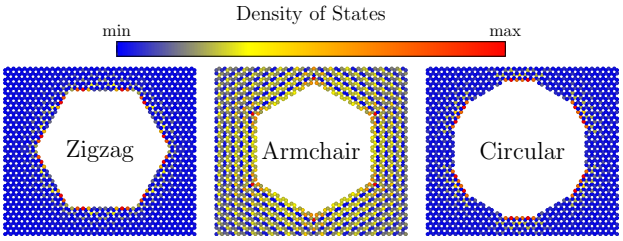

FIG. 6. The density of states for $E = 0.028|t|$ around antidots with different edge structures as indicated. The maps are individually scaled.

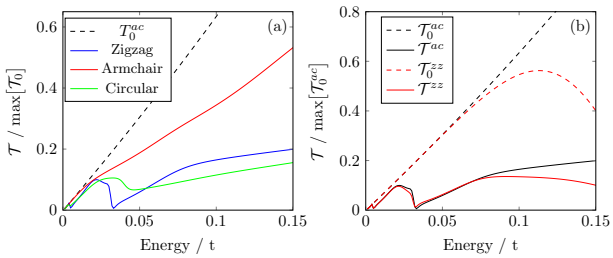

FIG. 7. (a) The transmission for probes separated along the armchair direction (~ 50 nm) for zigzag, armchair and circular antidots, respectively. The antidot structures are shown in Fig. 6. (b) The transmission for the same zig-zag antidot as (a), with probe separations (~ 50 nm) along armchair and zig-zag direction, respectively.

V. PERFORATED GRAPHENE

Many applications require deliberate nanostructuring of the graphene in order to engineer its electronic structure. Therefore tools to investigate the transport properties of individual nanostructures are important in order to confirm the fabricated structure and its influence on nanoscale electron transport.

In this section we consider perforations in the pristine graphene sheet – so called antidots (see Fig. 6).[60] Several studies[61–63] show that arrays of antidots can induce a bandgap in graphene. The effect of antidots on the electronic properties of graphene strongly depends on the exact edge geometries of the antidots. Therefore it is important to study the formation of single antidots and determine their edge configuration.

The perforations are modelled by removing the hopping matrix elements between sites around the edge of the hole, effectively disconnecting the sites from the rest of the graphene lattice.

We consider three possible edge geometries for antidots: zigzag, armchair or circular, the last contains an alternating sequence of armchair and zigzag edges (Fig. 6). We calculate the transmission for each antidot type placed between probes separated in the armchair direction. The result is shown in Fig. 7. As expected the transmission is generally lowered by introduction of the perforation. A notable difference between the antidot types is a transmission dip present for the circular and especially zigzag type antidots. This dip resembles the Fano type resonance observed for single adatoms, Fig. 3. Fig. 7a suggests that the resonant feature is connected to the zigzag edges, as the circular antidot consists of a mixture of zigzag and armchair edges. We therefore map the local density of states on sites around the antidot at the energy of the transmission dip (*cf.* Fig. 6). The DOS is localised around the zigzag edges as discussed in Ref. 63. These localised zigzag edge states being essentially dispersionless resemble a single level and therefore create a Fano type resonance in the transmission for antidots possessing zigzag edges. In addition, we notice the difference between the resonance of the circular and zigzag antidot on Fig. 7a. The resonance of the pure zigzag edge has a sharper feature than the mixed edge (circular antidot). This leads to the conclusion that the resonance features can be related to the amount of zigzag edge present. This in turn can be used as a fingerprint to determine the edge profile of antidots and other nanostructures.

A necessary condition for the dual-probe setup to be a useful tool for characterization of larger nanostructures, such as antidots, is that the exact direction between the probes should not have a great impact on the spectroscopic fingerprints of the nanostructure. Therefore we compare the transmission for both zigzag and armchair probe separations in Fig. 7b and note very similar behaviour at low energies. This shows that especially the Fano-type resonance is not particularly sensitive to the orientation of the probes, and that the two-probe setup indeed can be a useful characterization tool for the electrical properties of individual nanstructures.

VI. CONCLUSION

A dual-probe setup with probe separation distances in the nanometer range, makes it possible to obtain local transport properties on the nanoscale. We have presented a theoretical treatment of such a setup based on a real space Green's function method. This allows calculation of the transmission between two point probes on an infinite graphene sheet, without requiring periodicity of either probe or sample, while keeping the computational size proportional to the number of modified sites, as opposed to proportional to the total system size.

Directional transport effects, not directly attainable using macroscopic contacts, are explored together with the spectroscopic fingerprints of local perturbations such as vacancies and adatoms. Additionally we show the capability of the dual-probe system to characterize nanostructures. In particular, we observe Fano-type resonances arising from resonant states in adatoms or near edges witha zigzag geometry.

The demonstrated features of the dual-probe setup, like conductance mapping[41] and spectroscopic analysis, suggest that it has a high potential for applications in

the exploration of transport properties on the nanometer-scale.

Acknowledgements The Center for Nanostructured Graphene (CNG) is sponsored by the Danish Research Foundation, Project DNRF58.

Appendix A: Coefficients for the SPA

Below are given the coefficients for the SPA expressions Eq. (6) as derived in 44

$$\mathcal{Q}(E) = \pm\cos^{-1}\left(-\sqrt{1-\tfrac{E^2}{t^2}}\right) \tag{A1a}$$

$$\mathcal{A}(E) = -\frac{1+\mathrm{i}}{\sqrt{\pi}}\frac{\sqrt{E}}{\sqrt{(E^2+3t^2)\sqrt{t^2-E^2}}} \tag{A1b}$$

$$\mathcal{Q}^{+}(E) = \pm\cos^{-1}\left(\frac{-t-E}{2t}\right) \tag{A1c}$$

$$\mathcal{Q}^{-}(E) = \pm\cos^{-1}\left(\frac{-t+E}{2t}\right) \tag{A1d}$$

$$\mathcal{A}^{+}(E) = -\frac{1+1i}{\sqrt{4\pi}}\sqrt{\frac{E}{|t|(t+E)}}\frac{1}{\left((3t+E)(t-E)\right)^{1/4}} \tag{A1e}$$

$$\mathcal{A}^{-}(E) = -\frac{1+1i}{\sqrt{4\pi}}\sqrt{\frac{E}{|t|(t-E)}}\frac{1}{\left((3t-E)(t+E)\right)^{1/4}} \tag{A1f}$$

* mikse@nanotech.dtu.dk

[1] K. S. Novoselov, D. Jiang, F. Schedin, T. J. Booth, V. V. Khotkevich, S. V. Morozov, and a. K. Geim, Proceedings of the National Academy of Sciences of the United States of America **102**, 10451 (2005).

[2] C. R. Dean, A. F. Young, I. Meric, C. Lee, L. Wang, S. Sorgenfrei, K. Watanabe, T. Taniguchi, P. Kim, K. L. Shepard, and J. Hone, Nature Nanotechnology **5**, 722 (2010).

[3] Q. H. Wang, K. Kalantar-Zadeh, A. Kis, J. N. Coleman, and M. S. Strano, Nature nanotechnology **7**, 699 (2012).

[4] A. H. Castro Neto, N. M. R. Peres, K. S. Novoselov, and A. K. Geim, Reviews of Modern Physics **81**, 109 (2009).

[5] N. M. R. Peres, F. Guinea, and A. H. Castro Neto, Physical Review B **73**, 125411 (2006).

[6] J.-H. Chen, C. Jang, S. Xiao, M. Ishigami, and M. S. Fuhrer, Nature nanotechnology **3**, 206 (2008).

[7] G. Binnig, H. Rohrer, C. Gerber, and E. Weibel, Phys. Rev. Lett. **49**, 57 (1982).

[8] A. Deshpande and B. J. LeRoy, Physica E: Low-dimensional Systems and Nanostructures **44**, 743 (2012).

[9] V. V. Cheianov and V. I. Fal'ko, Physical Review Letters **97**, 226801 (2006).

[10] C. Bena, Physical Review Letters **100**, 076601 (2008).

[11] F. M. D. Pellegrino, G. G. N. Angilella, and R. Pucci, Physical Review B **80**, 094203 (2009).

[12] N. M. R. Peres, L. Yang, and S.-W. Tsai, New Journal of Physics **11**, 095007 (2009).

[13] G. I. Márk, P. Vancsó, C. Hwang, P. Lambin, and L. P. Biró, Physical Review B **85**, 125443 (2012).

[14] A. Bergvall and T. Löfwander, Physical Review B **87**, 205431 (2013).

[15] J. A. Lawlor, S. R. Power, and M. S. Ferreira, Physical Review B **88**, 205416 (2013).

[16] S. Lounis, (2014), arXiv:1404.0961.

[17] G. M. Rutter, J. N. Crain, N. P. Guisinger, T. Li, P. N. First, and J. A. Stroscio, Science **317**, 219 (2007).

[18] P. Mallet, F. Varchon, C. Naud, L. Magaud, C. Berger, and J.-Y. Veuillen, Physical Review B **76**, 041403 (2007).

[19] H. Yang, A. J. Mayne, M. Boucherit, G. Comtet, G. Dujardin, and Y. Kuk, Nano Letters **10**, 943 (2010).

[20] L. Tapaszto, P. Nemes-Incze, G. Dobrik, K. Jae Yoo, C. Hwang, and L. P. Biro, Applied Physics Letters **100**, 053114 (2012).

[21] J. Xue, J. Sanchez-Yamagishi, K. Watanabe, T. Taniguchi, P. Jarillo-Herrero, and B. J. LeRoy, Physical Review Letters **108**, 016801 (2012).

[22] J. C. Koepke, J. D. Wood, D. Estrada, Z.-Y. Ong, K. T. He, E. Pop, and J. W. Lyding, ACS Nano **7**, 75 (2013).

[23] S. Hasegawa, I. Shiraki, T. Tanikawa, C. L. Petersen, T. M. Hansen, P. Bøggild, and F. Grey, Journal of Physics: Con-

densed Matter **14**, 8379 (2002).
[24] O. Kubo, Y. Shingaya, M. Nakaya, M. Aono, and T. Nakayama, Applied Physics Letters **88**, 254101 (2006).
[25] P. Jaschinsky, P. Coenen, G. Pirug, and B. Voigtlander, Review of Scientific Instruments **77**, 093701 (2006).
[26] T.-H. Kim, Z. Wang, J. F. Wendelken, H. H. Weitering, W. Li, and A.-P. Li, The Review of scientific instruments **78**, 123701 (2007).
[27] J. Baringhaus, F. Edler, C. Neumann, C. Stampfer, S. Forti, U. Starke, and C. Tegenkamp, Applied Physics Letters **103**, 111604 (2013).
[28] A. Roychowdhury, M. A. Gubrud, R. Dana, C. J. Lobb, F. C. Wellstood, and M. Dreyer, (2014), arXiv:1311.1855v2.
[29] T. Nakayama, O. Kubo, Y. Shingaya, S. Higuchi, T. Hasegawa, C.-S. Jiang, T. Okuda, Y. Kuwahara, K. Takami, and M. Aono, Advanced materials **24**, 1675 (2012).
[30] A.-P. Li, K. W. Clark, X.-G. Zhang, and A. P. Baddorf, Advanced Functional Materials **23**, 2509 (2013).
[31] J. Baringhaus, M. Ruan, F. Edler, A. Tejeda, M. Sicot, A.-P. Li, Z. Jiang, E. H. Conrad, C. Berger, C. Tegenkamp, and W. A. de Heer, Nature **506**, 349 (2014).
[32] T. Kanagawa, R. Hobara, I. Matsuda, T. Tanikawa, A. Natori, and S. Hasegawa, Phys. Rev. Lett. **91**, 036805 (2003).
[33] V. Cherepanov, E. Zubkov, H. Junker, S. Korte, M. Blab, P. Coenen, and B. Voigtländer, Review of scientific instruments **83**, 033707 (2012).
[34] H. Watanabe, C. Manabe, T. Shigematsu, and M. Shimizu, Applied Physics Letters **78** (2001).
[35] K. W. Clark, X.-G. Zhang, I. V. Vlassiouk, G. He, R. M. Feenstra, and A.-P. Li, ACS nano **7**, 7956 (2013).
[36] K. W. Clark, X.-G. Zhang, G. Gu, J. Park, G. He, R. M. Feenstra, and A.-P. Li, Physical Review X **4**, 011021 (2014).
[37] T.-H. Kim, X.-G. Zhang, D. M. Nicholson, B. M. Evans, N. S. Kulkarni, B. Radhakrishnan, E. A. Kenik, and A.-P. Li, Nano Letters **10**, 3096 (2010).
[38] F. R. Eder, J. Kotakoski, K. Holzweber, C. Mangler, V. Skakalova, and J. C. Meyer, Nano Letters **13**, 1934 (2013).
[39] S.-H. Ji, J. B. Hannon, R. M. Tromp, V. Perebeinos, J. Tersoff, and F. M. Ross, Nature materials **11**, 114 (2012).
[40] P. W. Sutter, J.-I. Flege, and E. A. Sutter, Nature Materials **7**, 406 (2008).
[41] M. Settnes, S. R. Power, D. H. Petersen, and A.-P. Jauho, Phys. Rev. Lett. **112**, 096801 (2014).
[42] S. Datta, *Electronic Transport in Mesoscopic Systems* (Cambridge University Press, 1997).
[43] S. Reich, J. Maultzsch, C. Thomsen, and P. Ordejón, Physical Review B **66**, 035412 (2002).
[44] S. R. Power and M. S. Ferreira, Physical Review B **83**, 155432 (2011).
[45] A. Lherbier, S. M. M. Dubois, X. Declerck, Y.-M. Niquet, S. Roche, and J.-C. Charlier, Physical Review B **86**, 075402 (2012).
[46] L. E. F. F. Torres, S. Roche, and J.-C. Charlier, *Introduction to Graphene-Based Nanomaterials* (Cambridge University Press, 2014).
[47] H. Haug and A.-P. Jauho, *Quantum kinetics in transport and optics of semiconductors* (Springer, 2008).
[48] E. N. Economou, *Green's functions in quantum physics* (Springer, 2005).
[49] J. Tersoff and D. R. Hamann, Physical Review Letters **50**, 1998 (1983).
[50] V. Meunier and P. Lambin, Physical Review Letters **81**, 5588 (1998).
[51] H. Amara, S. Latil, V. Meunier, P. Lambin, and J.-C. Charlier, Physical Review B **76**, 115423 (2007).
[52] Y. Zhang, V. W. Brar, F. Wang, C. Girit, Y. Yayon, M. Panlasigui, A. Zettl, and M. F. Crommie, Nature Physics **4**, 627 (2008).
[53] A. Fasolino, J. H. Los, and M. I. Katsnelson, Nature Materials **6**, 858 (2007).
[54] J. P. Robinson, H. Schomerus, L. Oroszlány, and V. I. Fal'ko, Phys. Rev. Lett. **101**, 196803 (2008).
[55] T. O. Wehling, S. Yuan, A. I. Lichtenstein, A. K. Geim, and M. I. Katsnelson, Phys. Rev. Lett. **105**, 056802 (2010).
[56] B. Uchoa, L. Yang, S. W. Tsai, N. M. R. Peres, and A. H. Castro Neto, Physical Review Letters **103**, 206804 (2009).
[57] U. Fano, Phys. Rev. **124**, 1866 (1961).
[58] F. Schedin, A. K. Geim, S. V. Morozov, E. W. Hill, P. Blake, M. I. Katsnelson, and K. S. Novoselov, Nature Materials **6**, 652 (2007).
[59] A. Cagliani, D. Mackenzie, L. K. Tschammer, F. Pizzocchero, K. Almdal, and P. Bøggild, (2014), arXiv:1403.4791.
[60] J. A. Fürst, J. G. Pedersen, C. Flindt, N. A. Mortensen, M. Brandbyge, T. G. Pedersen, and A. P. Jauho, New Journal of Physics **11**, 095020 (2009).
[61] T. G. Pedersen, C. Flindt, J. G. Pedersen, N. A. Mortensen, A.-P. Jauho, and K. Pedersen, Physical Review Letters **100**, 136804 (2008).
[62] J. G. Pedersen, T. Gunst, T. Markussen, and T. G. Pedersen, Phys. Rev. B **86**, 245410 (2012).
[63] T. Gunst, T. Markussen, A.-P. Jauho, and M. Brandbyge, Phys. Rev. B **84**, 155449 (2011).

Paper III

Mikkel Settnes, Stephen R. Power,Jun Lin, Dirch H. Petersen and Antti-Pekka Jauho

Patched Green's function techniques for two-dimensional systems: Electronic behavior of bubbles and perforations in graphene

Phys. Rev. B **91**, 125408 (2015)

arXiv:1501.06036v1 [cond-mat.mes-hall] 24 Jan 2015

Patched Green's function techniques for two dimensional systems: Electronic behaviour of bubbles and perforations in graphene

Mikkel Settnes,[1,*] Stephen R. Power,[1] Jun Lin,[1] Dirch H. Petersen,[1] and Antti-Pekka Jauho[1]

[1] *Center for Nanostructured Graphene (CNG), DTU Nanotech, Technical University of Denmark, DK-2800 Kongens Lyngby, Denmark*

(Dated: January 27, 2015)

We present a numerically efficient technique to evaluate the Green's function for extended two dimensional systems without relying on periodic boundary conditions. Different regions of interest, or 'patches', are connected using self energy terms which encode the information of the extended parts of the system. The calculation scheme uses a combination of analytic expressions for the Green's function of infinite pristine systems and an adaptive recursive Green's function technique for the patches. The method allows for an efficient calculation of both local electronic and transport properties, as well as the inclusion of multiple probes in arbitrary geometries embedded in extended samples. We apply the Patched Green's function method to evaluate the local densities of states and transmission properties of graphene systems with two kinds of deviations from the pristine structure: bubbles and perforations with characteristic dimensions of the order of 10-25 nm, *i.e.* including hundreds of thousands of atoms. The strain field induced by a bubble is treated beyond an effective Dirac model, and we demonstrate the existence of both Friedel-type oscillations arising from the edges of the bubble, as well as pseudo-Landau levels related to the pseudomagnetic field induced by the nonuniform strain. Secondly, we compute the transport properties of a large perforation with atomic positions extracted from a TEM image, and show that current vortices may form near the zigzag segments of the perforation.

I. INTRODUCTION

Following the isolation of graphene a general class of two dimensional materials with widely diverse and unique electrical, mechanical and optical properties has been realized.[1,2] Two dimensional materials are almost entirely surface and are therefore very susceptible to external influences like direct patterning[3], adsorbate atoms[4], strain[5], *etc.* This variety of ways to alter and control the material properties opens a huge range of engineering possibilities.[6] In this context, it becomes important to investigate large scale disorder or patterning in relation to the electronic properties of graphene and related two dimensional materials. From a theoretical perspective several methods are available.[7] Typically, the electronic structure of the system is described with a tight-binding type Hamiltonian and a popular approach is then to construct the entire system in a piece-wise manner using recursive Green's functions (RGFs).[8] In this way, we can extract the necessary terms for calculating physical quantities of interest. The RGF method is best-suited for systems which are either finite or periodic in one dimension. It is frequently used for modeling transport, where self energies calculated using recursive techniques are used to attach semi-infinite pristine leads to either side of a finite device region.[9] Alternatively, an efficient approach to large disordered systems is the real space Kubo-Greenwood approach.[10] However, this method cannot include open boundary conditions and can only obtain average system quantities, as opposed to local electronic and transport properties.

In the most common formulation, the RGF method treats (quasi) one dimensional systems with only two leads. Although variants of the method can be used for arbitrary geometries and multiple leads,[11,12] the method remains limited to finite-width or periodic systems. Consequently, it cannot describe local and non-periodic perturbations, or point-like probes similar to those considered experimentally.[13,14] An extension of recursive techniques, to allow efficient treatment of local properties in systems without periodicity or finite sizes, would allow for easier theoretical investigation of systems which are computationally very expensive, or completely out of reach, using existing methods.

In this paper, we develop a Green's function (GF) method which is able to efficiently treat large and finite sized 'patches' embedded in an extended system, as shown in Fig. 1. The method combines an analytical formulation of the Green's functions describing a pristine system[15,16] with an adaptive recursive Green's function method to described the patches. It allows for calculation of both local electronic and transport properties and for the inclusion of multiple leads and arbitrary geometries embedded within an extended sample.

This patched Green's function method exploits an efficient calculation of the GF for an infinite pristine system using complex contour techniques. Using this GF, an open boundary self energy term can be included in the device Hamiltonian to describe its connection to an extended sample. The device region itself, containing nanostructures and/or leads, is then treated with an adaptive recursive method. We demonstrate the formulation using graphene, but it is generally applicable to all (quasi) 2D structures where the Green's function for the infinite pristine system can be determined. Consequently, the patched Green's function method is a versatile tool for efficient investigation of non-periodic nanostructures in extended two dimensional systems.

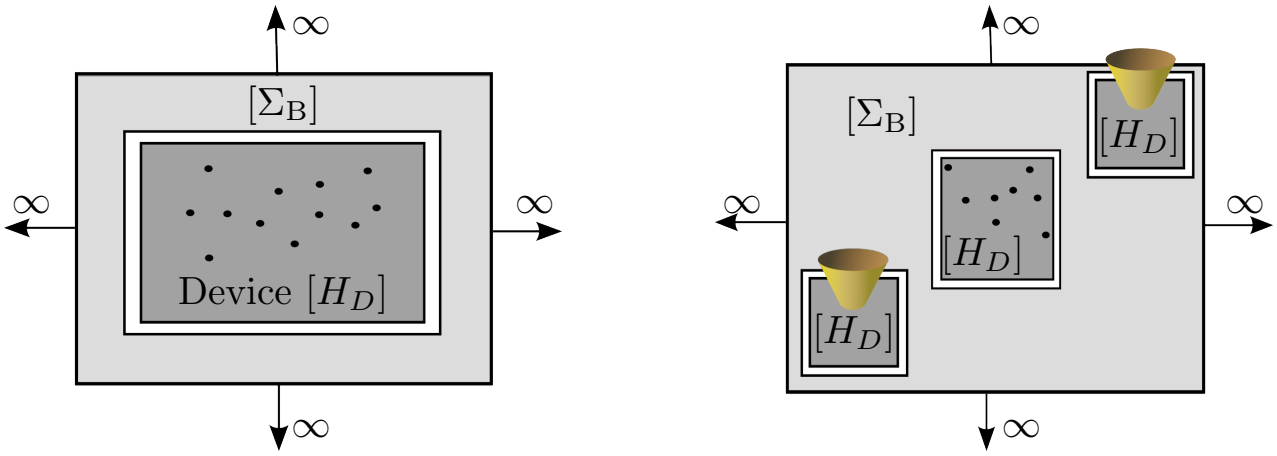

FIG. 1. The left panel shows a schematic of a computational setup containing a finite device 'patch' , described by $\boldsymbol{H}_D$, embedded within an extended system described by the self energy $\boldsymbol{\Sigma}_B$. The right panel shows a computational setup containing several device 'patches' of interest.

The rest of the paper is outlined as follows: the general formalism is developed in Section II A by calculating the open boundary self energy from the pristine GF. In Section II B we use graphene as an example to show the calculation of the pristine GF, while Section II C discusses the adaptive recursive method used to treat the device when including the boundary self energy. In Section III we use the developed method to study the local density of states of a graphene sample under the influence of a local strain field. As a result, we can compare local density of state (LDOS) maps with pseudomagnetic field distributions. In this way, we show the existence of Friedel-type oscillations along with pseudomagnetic field effects in the LDOS. Finally, in Section IV, we use the patched Green's function technique to demonstrate the existence of vortex like current patterns in the presence of a perforation within an extended graphene sheet.

II. METHOD

We consider the computational setup schematically shown in the left panel of Fig. 1, where a device region is embedded within an extended two dimensional system. This setup ensures that we are not including edge effects due to the finite-size of the simulation domain.[17] The device region is described by a Hamiltonian, $\boldsymbol{H}$, which may include disorder, deformations, mean field terms or leads *etc.* This device region is embedded into an extended system by applying a self energy term, Σ_B. To consider the setup in Fig. 1, we need two things: first, we need to construct Σ_B to describe the extended part of the system and secondly, we need an efficient way to describe the device region while taking Σ_B into account. Furthermore, the treatment of the device should be able to consider arbitrary geometries, including mutually disconnected patches within the extended system, as shown in the right panel of Fig. 1.

We describe the method in three steps:

A: Derivation of the boundary self energy term, Σ_B, in terms of the pristine lattice GFs.

B: Calculation of the real-space GF needed in the self energy calculation. We use graphene as an example.

C: Implementation of an adaptive RGF method to build the device region(s) efficiently while including the self energy term(s) Σ_B.

A. Boundary self energy

To construct the boundary self energy describing the extended region in Fig. 1, we consider the simple graphene example in Fig. 2a. Here a central device region, indicated by the dashed square, is embedded into an extended sheet. In this example both the extended area and the device region are assumed to be graphene-based, but the following arguments are general to any two dimensional material. We consider a division of the system into two parts: sites in the device (D) or sites in the extended sheet region. Furthermore, we subdivide the extended sheet into boundary sites (B) which are indicated by blue in Fig. 2 and have a non-zero Hamiltonian element coupling them to the device region, or 'sheet' sites which do not couple to the device region. Within a nearest-neighbour tight-binding Hamiltonian, the boundary sites in Fig. 2a are shown by blue symbols and have non-zero couplings to the device sites indicated by red symbols. We can now write the Hamiltonian for

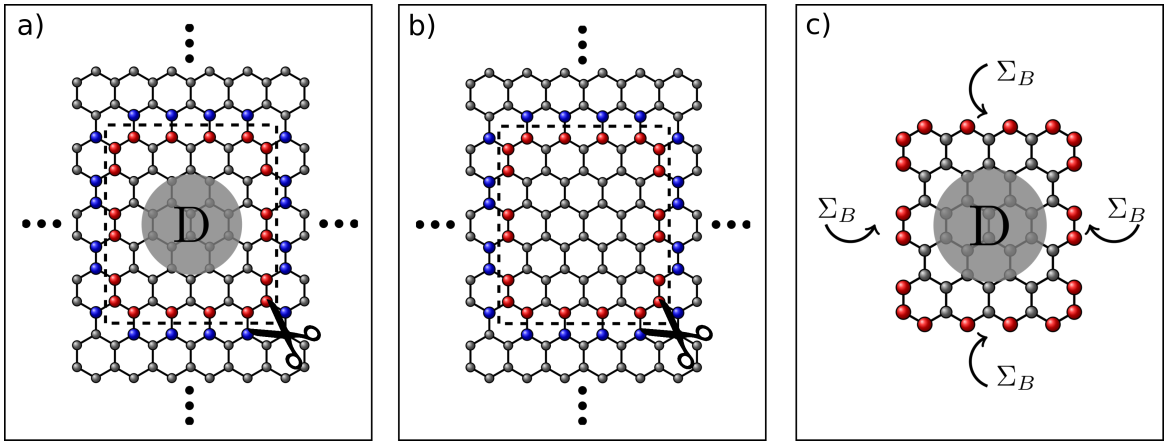

FIG. 2. a) Shows the desired device region, indicated by the dashed square, embedded within an extended system. Red symbols are the edge of the device and blue symbols indicate sites in the surrounding sheet that couples to the device. We obtain the disconnected system discussed in the text by removing the couplings that cross the dashed line. b) Shows the corresponding pristine system. Again the disconnected system is obtained by removing couplings along the dashed line. c) Illustrates how the effect of the extended sheet on the device region is taken into account by the self energy, see Eq. (4).

the entire system, in block matrix form, as

$$\boldsymbol{H} = \begin{pmatrix} \boldsymbol{H}_{D,D} & \boldsymbol{V}_{D,B} & 0 \\ \boldsymbol{V}_{B,D} & \boldsymbol{H}_{B,B} & \boldsymbol{V}_{B,\text{sheet}} \\ 0 & \boldsymbol{V}_{\text{sheet},B} & \boldsymbol{H}_{\text{sheet}} \end{pmatrix}, \tag{1}$$

where the light shaded part of Eq. (1) represent an infinite Hamiltonian. The connections between device and sheet, (i.e. between the red and blue symbol sites) are contained in the off-diagonal blocks $\boldsymbol{V}_{D,B}$ and $\boldsymbol{V}_{B,D}$.

We aim to replace the infinite Hamiltonian $\boldsymbol{H}$ with a finite effective Hamiltonian, $\boldsymbol{H}_{\text{eff}} = \boldsymbol{H}_{D,D} + \boldsymbol{\Sigma}_B$, which takes into account the extended sheet using a self energy term $\boldsymbol{\Sigma}_B$. To do this, we consider the *connected* system in panel a) of Fig. 2, and a disconnected system formed by removing the Hamiltonian elements $\boldsymbol{V}_{D,B}$ and $\boldsymbol{V}_{B,D}$, corresponding to removing couplings crossing the dashed line in Fig. 2a. The GFs of the connected ($\boldsymbol{G}^{(\text{con})}$) and disconnected ($\boldsymbol{G}^{(\text{dis})}$) systems can be related via the Dyson equation, and in particular we can write the GF of the connected device region as

$$\boldsymbol{G}^{(\text{con})}_{D,D} = \boldsymbol{G}^{(\text{dis})}_{D,D} + \boldsymbol{G}^{(\text{dis})}_{D,D}\boldsymbol{V}_{D,B}\boldsymbol{G}^{(\text{con})}_{B,D}. \tag{2}$$

Applying the Dyson equation again to obtain $\boldsymbol{G}^{(\text{con})}_{B,D}$ and inserting this into Eq. (2) allows us to simplify,

$$\boldsymbol{G}^{(\text{con})}_{D,D} = \left(E\mathbf{1} - \boldsymbol{H}_{D,D} - \boldsymbol{\Sigma}_B\right)^{-1}, \tag{3}$$

where the self energy term is given by

$$\boldsymbol{\Sigma}_B = \boldsymbol{V}_{D,B}\boldsymbol{G}^{(\text{dis})}_{B,B}\boldsymbol{V}_{B,D}. \tag{4}$$

We note that the self energy in Eq. (4) is independent of the considered device and depends only on GF matrix elements connecting sites in the pristine surrounding 'frame' that remains when the device is removed from the full system. We take advantage of this to temporarily replace the device with a corresponding pristine region of the same size, as shown in panel b) of Fig. 2. The self-energy required to incorporate the finite pristine region into an infinite, pristine sheet is the same self energy, $\boldsymbol{\Sigma}_B$, that is required in Eq. (3). We can therefore write the required GF matrix, $\boldsymbol{G}^{(\text{dis})}_{B,B}$, in terms of the GF of the infinite pristine sheet, $\boldsymbol{G}^{(0)}$. These are related using the Dyson equation with a perturbation $-\boldsymbol{V}_{D,B}$,

$$\boldsymbol{G}^{(\text{dis})}_{B,B} = \left(\mathbf{1} + \boldsymbol{G}^{(0)}_{B,D}\boldsymbol{V}_{D,B}\right)^{-1}\boldsymbol{G}^{(0)}_{B,B}. \tag{5}$$

The advantage of writing the self-energy in terms of the pristine sheet GFs, $\boldsymbol{G}^{(0)}_{B,B}$ and $\boldsymbol{G}^{(0)}_{B,D}$, becomes clear in the next section, where we demonstrate an efficient method to calculate these two terms. It is worth noting that $\boldsymbol{G}^{(0)}_{B,D}$ only needs to be calculated for the sites in D which connect to sites in B. These sites are indicated by red in Fig. 2 and are where the self-energy terms need to be added, as shown in panel c). In this way, the computations only involve matrices corresponding to the edge of the device and not the size of the full device region as straight forward inversion would require.

The calculation scheme can be summarized as follows:

1: Calculate $\boldsymbol{G}^{(0)}_{B,B}$ and $\boldsymbol{G}^{(0)}_{B,D}$ using the methods outlined in Section II B.

2: Calculate $\boldsymbol{\Sigma}_B$ from Eq. (4) and Eq. (5).

3: The finite GF for the device region, $\boldsymbol{G}^{(\text{con})}_{D,D}$, is given by Eq. (3) and can be treated using an adaptive RGF method, see Section II C.

We note that this approach does not require a specific geometric shape of the device, nor does the device region need to be contiguous. We can treat different non-connected patches in an extended system, as shown in the right panel of Fig. 1, by extending the set D to include sites inside each patch and similarly expanding B to include sites at the boundary of each patch. The method presented in this section is applicable to any system where the connected, pristine GFs are easily obtainable as demonstrated in the next section using a tight-binding description of graphene as an example.

B. Real space graphene Green's function

We now turn to the calculation of the real space GF of the pristine system, which is needed to calculate the self energy, Σ_B, in Eq. (4) and Eq. (5). The approach required to calculate this quantity is demonstrated below for the case of a graphene sheet described with a nearest-neighbor tight-binding Hamiltonian, but is easily generalized for other cases.

This Hamiltonian is given by

$$\boldsymbol{H} = \sum_{<i,j>} t\hat{c}_i^\dagger \hat{c}_j, \tag{6}$$

where the sum $< i, j >$ runs over all nearest neighbour pairs and the carbon-carbon hopping integral is $t \approx -2.7$ eV. The graphene hexagonal lattice can be split into two triangular sublattices, which we denote A and B, and neighbouring sites reside on opposite sublattices to each other. Using Bloch functions, the Hamiltonian can be rewritten in reciprocal space as[7]

$$\boldsymbol{H_k} = t\begin{pmatrix} 0 & f(\boldsymbol{k}) \\ f^*(\boldsymbol{k}) & 0 \end{pmatrix}, \tag{7}$$

where the matrix form arises from sublattice indexing within a 2 atom unit cell and we have used the definition $f(\boldsymbol{k}) = 1 + \mathrm{e}^{\mathrm{i}\boldsymbol{k}\cdot\boldsymbol{a}_1} + \mathrm{e}^{\mathrm{i}\boldsymbol{k}\cdot\boldsymbol{a}_2}$, with the lattice vectors $\boldsymbol{a}_1 = a_0(\sqrt{3}, 3)/2$ and $\boldsymbol{a}_2 = a_0(-\sqrt{3}, 3)/2$ and a_0 the carbon-carbon distance. With this definition of the unit vectors we have the armchair direction along the y-axis (and zigzag along the x-axis).

The eigenenergies and eigenstates of the system are easily obtained from this form of the Hamiltonian, and transforming back to real space allows us to write the desired Green's function between sites i and j as[16,18]

$$G^0_{ij}(z) = \frac{1}{\Omega_{BZ}} \int \mathrm{d}^2\boldsymbol{k} \frac{N_{ij}(z, \boldsymbol{k})\mathrm{e}^{\mathrm{i}\boldsymbol{k}\cdot(\boldsymbol{r}_j - \boldsymbol{r}_i)}}{z^2 - t^2|f(\boldsymbol{k})|^2}, \tag{8}$$

where $z = E + \mathrm{i}0^+$ is the energy, Ω_{BZ} is the area of the first Brillouin zone. The position of the unit cell containing site i is denoted by $\boldsymbol{r}_i = m_i\boldsymbol{a}_1 + n_i\boldsymbol{a}_2$ with m_i and n_i being integers. Finally we use the definition $N_{ij}(z, \boldsymbol{k}) = z$, when i and j are on the same sublattice and $N_{ij}(z, \boldsymbol{k}) = tf(\boldsymbol{k})$ if i is on the A sublattice and j is on the B sublattice and $N_{ij}(z, \boldsymbol{k}) = tf^*(\boldsymbol{k})$ when i is on B and j on A.

To simplify the notation we introduce the dimensionless k-vectors $k_A = 3k_y a_0/2$ and $k_Z = \sqrt{3}k_x a_0/2$ such that $f(k_A, k_Z) = 1 + 2\cos\left(k_Z\right)\mathrm{e}^{\mathrm{i}k_A}$, and write the separation vector in terms of the lattice vectors $\boldsymbol{r} = \boldsymbol{r}_j - \boldsymbol{r}_i = m\boldsymbol{a}_1 + n\boldsymbol{a}_2$. Inserting this into Eq. (8) gives

$$G^0(z, \boldsymbol{r}) = \frac{1}{2\pi^2}\int \mathrm{d}k_A \int \mathrm{d}k_Z N_{ij}(z, k_A, k_Z) \times \frac{\mathrm{e}^{\mathrm{i}k_A(m+n)+\mathrm{i}k_Z(m-n)}}{z^2 - t^2\left(1 + 4\cos^2(k_Z) + 4\cos(k_A)\cos(k_Z)\right)}. \tag{9}$$

Eq. (9) can be solved using a two-dimensional numerical integration, but as we require Eq. (9) for each Green's function element individually, we wish to increase the performance by doing one integration analytically using complex contour techniques.

Following the approach of Ref. 16, we use k_A as complex variable and consider the poles, q, of the denominator

$$q = \cos^{-1}\left[\frac{\frac{z^2}{t^2} - 1 - 4\cos^2\left(k_Z\right)}{4\cos\left(k_Z\right)}\right]. \tag{10}$$

The sign of the pole must be selected carefully to ensure that it lies within the integration contour, *i.e.* $\mathrm{Im}(q) > 0$, for contours in the positive half plane corresponding to the situation $m + n \geq 0$. Care must also be taken with the additional phase terms that arise for opposite sublattice GFs.

Using the residue theorem and integrating over a rectangular Brillouin zone, $k_A \in [-\pi; \pi]$ and $k_Z \in [-\pi/2; \pi/2]$, we finally reduce Eq. (9) to

$$G^0(z, \boldsymbol{r}) = \frac{\mathrm{i}}{4\pi t^2}\int_{-\frac{\pi}{2}}^{\frac{\pi}{2}} \mathrm{d}k_Z \frac{N_{ij}(z, q, k_Z)\mathrm{e}^{\mathrm{i}q(m+n)+\mathrm{i}k_Z(m-n)}}{\cos\left(k_Z\right)\sin\left(q\right)}, \tag{11}$$

with q given by Eq. (10). A similar expression to Eq. (11) can be derived when using k_Z as first integration variable.[16] The above derivation is based upon a nearest neighbour model, but can be generalised to also include, for example, second nearest neighbour terms[19] or uniaxial strains.[20]

We can now use Eq. (11) to calculate the elements of the required GFs, $\boldsymbol{G}^{(0)}_{B,B}$ and $\boldsymbol{G}^{(0)}_{B,D}$, defined in Section II A. In this way, Eq. (11) can be used to fill up the elements of the desired matrices one at a time. Since we need GF matrices of size $N_B \times N_B$ and $N_B \times N_D$, where N_D and N_B are the number of sites at the edge of the device region and in the region B, respectively, it could seem very ineffective to calculate one element at a time. However, the total number of GF elements to be calculated is greatly reduced by the symmetries of the pristine graphene lattice. The lattice itself is six-fold symmetric

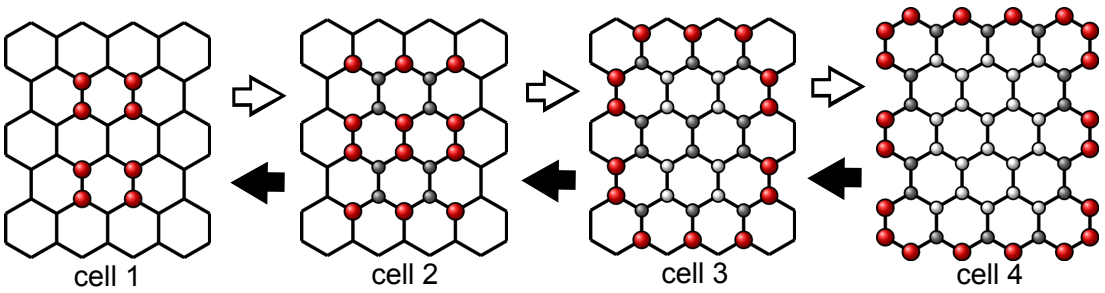

FIG. 3. The partitioning of a small graphene sample where all sites of interest are located in cell 1. Cell 2 contains all the sites coupling to cell 1 but which are not themselves part of cell 1. Likewise cell 3 is the sites coupling to cell 2 and so on. The red sites are assigned to the current cell and the lines indicate the sites still to be assigned. The previous cell and all sites already added are indicated by gray and white, respectively. The recursive sweep starting at the final cell and ending in cell 1, indicated by filled arrows, gives the GFs connecting all sites of interest. We can also employ a second recursive sweep, as indicated by the white arrows, to obtain local properties everywhere within the device region.

and each of these six identical wedges is in turn mirror symmetric, resulting in a 12-fold degeneracy of the GFs indexed by site separation vectors. Additionally, many of the required elements in $\boldsymbol{G}^{(0)}_{B,B}$ and $\boldsymbol{G}^{(0)}_{B,D}$ are identical. For instance, the onsite and nearest neighbour GF element appear many times, but only need to be calculated once. Taking the device region in Fig. 2 as example we have $N_D = N_B = 20$, yielding 400 individual elements for a brute force calculation. Instead, using symmetries and duplicates, we only need to calculate 38 and 42 elements when determining $\boldsymbol{G}^{(\mathrm{con})}_{B,B}$ and $\boldsymbol{G}^{(\mathrm{con})}_{B,D}$, respectively. The reduction becomes more significant for larger systems, as we generally only need to add the GF elements corresponding to the longest couplings. Consequently, only a small percentage of the GF elements need to be calculated individually and their values for frequently used separations and energies can be stored or reused to enable extremely fast calculation of the required self energies.

C. Adaptive recursion for device region

In this section we consider the device region where the boundary self energy can be added at the edge. The full GF of the device region is given by $\boldsymbol{G}_D = \left(E\mathbf{1} - \boldsymbol{H}_D - \boldsymbol{\Sigma}_B\right)^{-1}$, where we have simplified the notation from Eq. (3). From this GF both transport and local properties can be obtained. However, for most purposes we do not require every element of the Green's function matrix element in the device region, and so to avoid a time consuming full matrix inversion, recursive methods are often applied[8,17,21–26].

This section outlines an adaptive recursion method which efficiently includes the boundary self energy as well as an arbitrary device region shape and configuration (and number) of leads. Alternative approaches have been developed to treat arbitrary shaped regions with multiple leads[11,12,26]. These so-called knitting-algorithms add single sites at a time. They rely on a complicated categorizing of sites into different intermediate updating blocks making the theory and implementation cumbersome. Hence, we use an approach similar to the ones in Refs. 21–23, and employ an adaptive partitioning of the Hamiltonian matrix in order to bring it into the desired tridiagonal form suitable for recursive methods.

Calculating physical properties generally requires certain GFs connecting a specific set of sites in the device region. These sites of interest, for example, could be sites where we want to introduce defects, or couple to probes for transport calculations, or measure properties like the local density of states. We focus first on the general partitioning process, and then demonstrate how it can be quickly modified to account for the edge self-energy terms. We begin by placing all these sites of interest into recursive cell 1, as shown by the red sites in Fig. 3. We emphasize that the cells in this process are not of a fixed size and may consist of arbitrary sites which are not necessarily connected. Cell 2 is determined by selecting all the remaining unpartitioned sites which couple directly to sites in cell 1 via a non-zero Hamiltonian matrix element. In the example in Fig. 3, this consists of nearest neighbor sites of those in cell 1, which are not themselves in cell 1. This process is repeated until all sites in the device region have been allocated a cell, and is demonstrated schematically in the panels of Fig. 3 where red sites indicate the current cell, and dark gray or white sites indicate sites added to the previous cell, or to earlier cells, respectively.

With the resultant block tridiagonal Hamiltonian, we can now employ the usual recursive algorithm, starting from cell $n = N$, so that the final step yields the required GF sites in cell $n = 1$. These terms can then be used to calculate observable quantities like transmission, LDOS, *etc.* Afterwards a reverse recursive sweep from $n = 1$ to $n = N$ can be implemented to efficiently map local quantities like bond currents or LDOS everywhere within the device region[8]. For completeness the full recursive method is summarized in Appendix A including the reverse sweep. We emphasize that the presented method

is not unique to graphene systems, but can be employed to arbitrary tight-binding-like models.

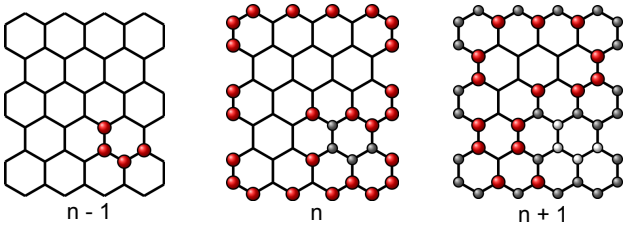

FIG. 4. An example of the partitioning when the cell $n-1$ is connected to the edge, and we need to include the boundary self-energy, $\mathbf{\Sigma}_B$. In this case, all edge sites and self energy terms are included in cell n. The symbols are similar to Fig. 3.

Including the boundary self-energy

We now return to the specific case at hand where the recursive method outlined above needs to be adapted carefully to take account of the boundary self energy. In general $\mathbf{\Sigma}_B$ is a non-hermitian dense matrix connecting all edge sites of the device region. Therefore it is essential to assign all edge sites to the same cell. This principle is shown in Fig. 4. If cell $n-1$ contains sites which connect to an edge site, then cell n must contain not only the edge sites directly connecting to cell $n-1$, but also all other edge sites, as these are connected to each other via $\mathbf{\Sigma}_B$. In this way, the cell, $n+1$, must then contain all the sites connecting to cell n, *i.e.* also connecting to the edge, but not included in cell n. The full cell partitioning algorithm, including this step, is given in Appendix A.

III. INHOMOGENEOUS STRAIN FIELDS IN GRAPHENE BUBBLES

In this section, we employ the patched Green's function method to a locally strained graphene system, demonstrating how it can prove a useful tool in investigating local properties of non-periodic nanostructures in extended two dimensional systems.

Strain engineering has been proposed as a method to manipulate the electronic, optical and magnetic properties of graphene.[20,27–40] It is based on the close relation between the structural and electronic properties of graphene. The application of strain can lead to effects like bandgap formation[41], transport gaps[27] and pseudo-magnetic fields (PMFs).[28–30]

Uniaxial or isotropic strain will not produce PMFs, although it has been shown to shift the Dirac cone of graphene and induce additional features in the Raman signal.[42] On the other hand, inhomogeneous strain fields can introduce PMFs. In this case, the altered tight binding hoppings mimic the role of a gauge field in the low energy effective Dirac model of graphene.[43,44]

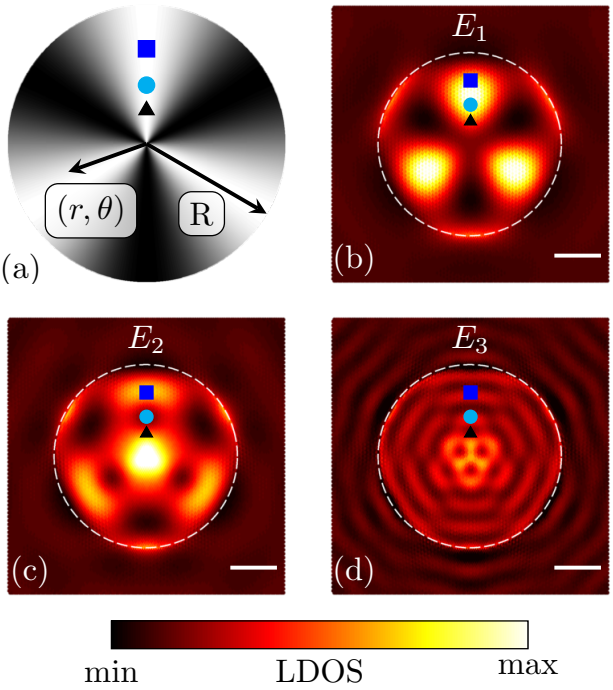

FIG. 5. (a) The PMF distribution calculated using the strain distribution in Eq. (13), dark being negative field and light being positive. (b-d) Real space LDOS maps for the A sublattice taken at the energies $E_1 = 0.06|t|$, $E_2 = 0.089|t|$ and $E_3 = 0.23|t|$, corresponding to energies of the first two pseudo Landau levels and an energy dominated by Friedel type oscillations, respectively. The energies and the symbols correspond the ones used in Fig. 6. Sublattice B is similar and is obtained by rotating 60°. The scale bar is 5 nm.

For example Guinea *et al.* [28] demonstrated that nearly homogeneous PMFs can be generated by applying triaxial strain. One of the most striking consequences of homogeneous PMFs is the appearance of a Landau-like quantization.[28,35] Scanning tunnelling spectroscopy on bubble-like deformations see this quantization, where the observed pseudo-Landau levels corresponds to PMFs stronger than 300 T.[32,45]

Deformations can be induced in graphene samples by different techniques like pressurizing suspended graphene[30,46] or by exploiting the thermal expansion coefficients of different substrates.[32] As a result, introducing nonuniform strain distributions at the nanoscale is a promising way of realizing strain engineering. The standard theoretical approach to treat strain effects employs continuum mechanics to obtain the strain field. Several studies improve the accuracy by replacing the continuum mechanics by classical molecular dynamics simulations.[5,30,31] The strain field can then be coupled to an effective Dirac model of graphene to study the generation of PMFs in various geometries. In most studies, only the PMF distribution is considered as opposed to experimentally observable quantities like local density of states.

The framework presented in Section II enables us to treat the effect of strain on the LDOS directly from a tight-binding Hamiltonian. Consequently, we are now able to describe a single bubble in an extended system without applying periodic boundary conditions which may introduce interactions between neighboring bubbles. The dual recursive sweep then allows for efficient calculation of local properties everywhere in the device region surrounding a bubble, enabling us to investigate spatial variations in real space LDOS maps. In this section we only treat one nanostructure, but the patched Green's function technique efficiently handles several spatially separated nanostructures, as the separation is added very efficiently through the self energy term.

To account for strain within a tight binding approach we modify the hopping parameters.[33,37,40] The nearest neighbour hopping in Eq. (6) between site i and j is given by the new distance, d_{ij}, between the sites,

$$t_{ij} = t\mathrm{e}^{-\beta\left(\frac{d_{ij}}{a_0}-1\right)}, \tag{12}$$

where the coefficient $\beta = -\partial \ln t/\partial \ln a_0 \approx 3.37$.[37] We treat the deformation problem by applying an analytical displacement profile $(u(x,y), z(x,y))$ matched against experimental data for pressurized suspended graphene.[47] Here $u(x,y)$ and $z(x,y)$ are the in-plane and vertical displacements, respectively, which are induced by the applied strain. For a rotationally symmetric aperture with radius R, these are given, in spherical coordinates (r,θ), as

$$z(r,\theta) = h_0\left(1-\frac{r^2}{R^2}\right), \tag{13a}$$

$$u(r,\theta) = u_0\frac{r}{R}\left(1-\frac{r}{R}\right), \tag{13b}$$

for $r < R$. Here h_0 is the maximal height of the bubble and $u_0 = 1.136h_0^2/R$ is a constant relating the out-of-plane and in-plane deformations.[47] We note that this profile gives rise to a sharp edge at $r = R$, and many of the features we discuss below emerge from the strongly clamped nature of this bubble type.

As shown in Appendix B, rotationally symmetric strain profiles give rise to threefold symmetric PMFs in the effective Dirac model. This is shown in Fig. 5a for the strain profile considered in Eq. (13). As discussed in earlier studies,[33,40] we get an asymmetric sublattice occupancy such that the LDOS of each sublattice has a threefold symmetric distribution following the PMF while rotated 60° compared to the opposite sublattice. In all calculations below, we therefore show only one sublattice, as the result for the opposite sublattice can be obtained by a 60° rotation and the total pattern is a superposition of both.[29,34]

Comparing the PMF distribution in Fig. 5a with the calculated LDOS maps at different energies in Fig. 5b-d for a bubble of radius $R = 10$ nm and height $h_0 = 3$ nm, we immediately notice that the threefold symmetry is also present in the LDOS maps. However, the spatial LDOS maps have significant additional details compared to the PMF distribution.

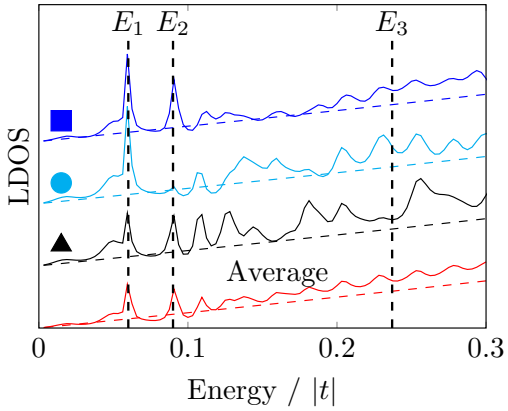

FIG. 6. The LDOS as a function of energy for the three positions indicated in Fig. 5 and for the average of the 'slice' of the bubble region containing the symbols. The dashed lines indicate the LDOS without the bubble. The curves are shifted with respect to each other to increase visibility.

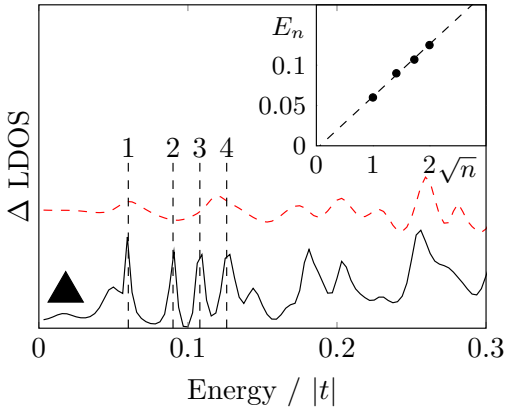

FIG. 7. The difference in LDOS as a function of energy for the point indicated with a triangle on Fig. 5. We show both the full calculation (full line) and an artificial system containing only the perturbation for a small region at the edge of the bubble (dashed line). We adjust the average hopping constant in the calculation of the artificial system to match the full calculation. Inset: The peak energies 1-4 as a function of $\sqrt{n}$, where n is the peak number.

In Fig. 6 we calculate the energy dependent LDOS at the positions indicated by symbols (square, circle and triangle) in Fig. 5. We first consider the average of the LDOS within the 'slice' containing the symbols, shown by the bottom (red) curve in Fig. 6. Two distinct oscillation types are observed, and we argue that these can be divided into Friedel-type and PMF-induced features. At high energies in particular we notice regularly space oscillations with an approximate period of $\hbar v_F\pi/2R$. These are consistent with Friedel-type oscillations related to the

size of the structure and emerging from interferences between electrons scattered at opposite sides of the bubble. An exact treatment needs to take into account the renormalized Fermi velocity, v_F, due to the average change in bond length.[48] At lower energies we observe distinct peaks which are not equally spaced (the first two appear at E_1 and E_2). We will show that these are due to pseudomagnetic effects and we refer to them as pseudo Landau levels.

Besides the Friedel oscillation associated with the bubble radius, we also have similar oscillations associated with the distances to different edges of the bubble. These features are highly position dependent, and explain the differences between the three single position curves in Fig. 6. When considering the average, these position dependent oscillations are washed out (bottom curve in Fig. 6), leaving only the oscillation dependent on the structure size. However, at individual positions these oscillations can have a considerable impact. Returning to the individual position STS curves in Fig. 6, we note that the peak at E_2 is only dominant for the points indicated by the square and triangle. It is suppressed by Friedel-type interferences at the circle point, which is also clear from the LDOS map in Fig. 5c.

The amplitude of the Friedel-type oscillations is determined by the strength of scattering near the bubble edges. The clamped edge implied by the strength profile in Eq. (13) gives rise to significant strain fields along this edge, leading to a sharp, strong perturbation. More realistic profiles calculated from molecular dynamics also indicate strong perturbations near the edges of clamped bubbles.[30] Our results indicate that edge scattering effects may significantly affect LDOS behavior in clamped bubble systems and even mask PMF-induced features.

To treat the oscillations due to the feature size and edge sharpness in more detail, we calculate the LDOS for an artificial system only taking into account the strain field along a small ring around the edge, see Fig. 7 (dashed red line). In this way, only Friedel-type features are expected within the structure. If we compare to the full calculation (full black line in Fig. 7), we notice that the oscillations at higher energies are present in both calculations, whereas the sharp peaks are only present in the full calculation. This confirms the Friedel nature of the higher energy oscillations and suggests the lower energy peaks are due to an alternative mechanism. To confirm that the sharp peaks are due to pseudomagnetic effects, we compare the peak positions to the standard form expected for Landau levels in graphene $E_n = \mathrm{sign}(n)\sqrt{2e_0\hbar v_F^2 B_s n}$, where e_0 is the electron charge, B_s is the magnetic field and n is the peak number.[7] The peaks labelled 1-4 in Fig. 7 display the $\sqrt{n}$ dependence characteristic of Landau levels in graphene, as shown in the inset of Fig. 7. The size of the PMF can furthermore be inferred to be $B_s \sim 30$ T from the inset.

To conclude, we discussed how the features in the LDOS spectra of clamped graphene bubbles can be explained by a combination of size-dependent scattering and PMF-induced effects like pseudo Landau quantization. Significant strain fields near the edge of the structure give rise to strong Friedel-type oscillations in the LDOS and these oscillations envelope the effect of a PMF. We must therefore be careful to distinguish between the two type of oscillations when investigating the electronic effects of PMFs induced by inhomogeneous strain fields.

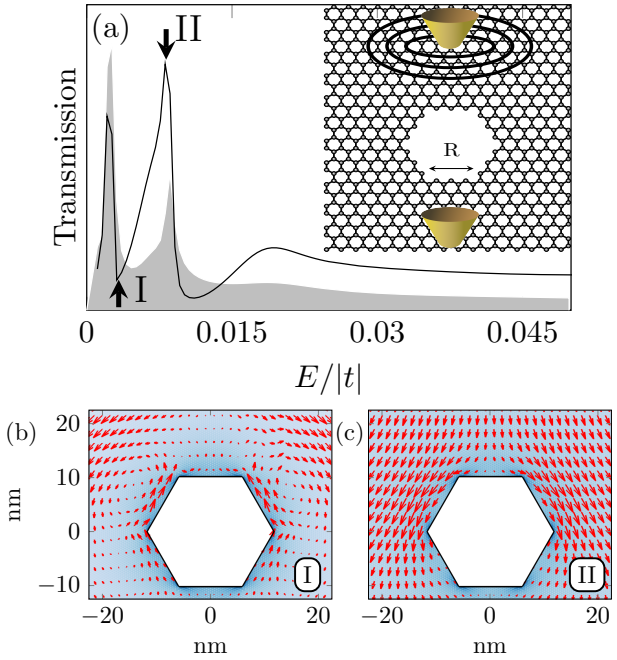

FIG. 8. (a) The transmission as a function of energy for a dual probe setup with an antidot in between the probes as schematically shown in the inset. The distance between the probes are 200 nm and the antidot with purely zigzag edges has side length $R = 48a_0 \sim 6.8$ nm. The shaded area corresponds to the LDOS around the edge of the antidot. antidot

IV. VORTEX CURRENTS NEAR PERFORATIONS

In this section we investigate local transport properties near antidots (*i.e.* perforations) in a graphene sheet. Periodic arrays of antidots have been studied as a way to open a bandgap in graphene[49–51] or to obtain waveguiding effects.[52,53] Furthermore, a single perforation in a graphene sheet has been considered as a nanopore for DNA sensing.[54,55]

Several studies show that the electronic structure of antidots is closely related to the exact edge geometry.[49,53,56] Experimental fabrication techniques like block copolymer[3,57,58] or electron beam lithography,[59–61] inevitably lead to disorder and imperfect edges. However, it may be possible to control the edge geometry of the antidot by heat treatment[60,62], or

selective etching.[61,63]

Motivated by the interest in how current flows in antidot systems, we apply the patched GF method to a single perforation in a graphene sheet. The method allows us to study the perforation with no influence from periodic repetition or finite sample size. Additionally, the combination of recursive methods and a boundary self-energy allows for investigation of antidot sizes realizable experimentally.[3,55,64] In fact we consider both an example antidot with perfect edges and an exact structure found from high resolution transmission electron microscope (TEM) images using pattern recognition.[65,66]

To investigate current on the nanoscale, recent experiments have realized multiple STM-systems.[13,14,67,68] These allow for individual manipulation of several STM-tips in order to make electrical contact to the sample near the considered nanostructure. Theoretically, we previously considered multiple STM setups allowing for both fixed and scanning probes.[15,56] The method presented here allows for not only transmission calculations but also calculation of local electronic and transport properties in the presence of multiple point probes. At the same time large separations between the different probes and/or nanostructures are easily included as additional separation is achieved in a very computationally efficient manner through the self energy term connecting multiple patches. The combination of large spatial separation between features, while still enabling calculation of local electronic and transport properties, can prove a useful tool in investigating extended two dimensional systems where we take special interest in a particular region of the extended sample.

In order to consider transmissions and current patterns, we add leads to the system through inclusion of a lead self-energy term, $\Sigma^L_{ij} = V^L_{is} g^s(\boldsymbol{r}_i - \boldsymbol{r}_j) V^L_{sj}$, where V^L_{is} is the coupling element between the device site i and the lead. To model the structureless lead, we use the surface GF of a single atomic chain, as this has a constant DOS in the considered energy range. The distance dependence in $g^s(\boldsymbol{r}_i - \boldsymbol{r}_j)$ is necessary to avoid an unphysical coupling between different lattice sites via the lead. We therefore add a $1/|\boldsymbol{r}_i - \boldsymbol{r}_j|$-dependence for the off-diagonal terms[69] where $\boldsymbol{r}_i \neq \boldsymbol{r}_j$, as appropriate for a structureless three-dimensional free electron gas.[70]

First, we consider a zigzag-edged antidot with side length $R = 48a \sim 12$ nm, where a is the length of the graphene unit cell and $a = \sqrt{3}a_0 = 2.46$ Å. This is comparable to experimental sizes where sub-20-nm feature sizes have been reported.[3,55,57,58] The antidot is between two probes placed 200 nm apart, as shown schematically in the inset of Fig. 8a. The main panel of Fig. 8a shows the transmission as a function of energy for this dual point probe setup. We note the distinct transmission peaks. As explained in Ref. 56, these peaks are related to localized states along the zigzag edges. As a consequence, we notice the correspondence between the peaks in the transmission and the peaks in the LDOS around the edge, see shaded area in Fig. 8a.

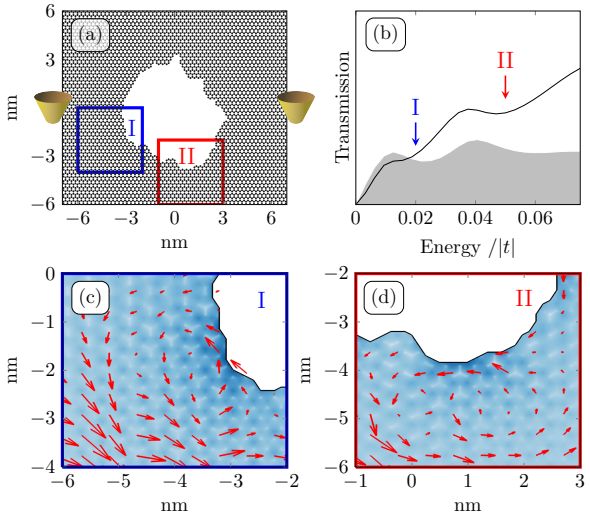

FIG. 9. An actual perforation is obtained from high resolution TEM images through pattern recognition and we consider the vortex like current paths forming around the perforation as certain energies. (a) Shows the structure of the perforation as well as an indication of the probe position (in the actual calculations the probes are 200 nm apart). The indicated areas corresponds to the zooms in (c) and (d). (b) The transmission for the dual probe setup. The shaded area indicate the average LDOS around the edge of the antidot. Furthermore, the energies I and II corresponding to the energies used on (c) and (d), respectively. (c-d) Bond current maps taken at the energies I and II, respectively, and shown at the positions indicated on (a).

Next, we calculate the bond currents from the top lead. The bond current between site i and j from lead L are calculated, as explained in Appendix A, by $J^L_{ij} = -H_{ij}\mathrm{Im}\left[\boldsymbol{G}^a \boldsymbol{\Gamma}^L \boldsymbol{G}^r\right]_{ij}/\hbar$, where H_{ij} is the Hamiltonian matrix element connecting site i and j. The bond currents around the zigzag antidot for the energies indicated in Fig. 8a are shown in Figs. 8b and 8c. In this way, we see that the transmission dips are related to vortex like current paths. These vortex paths create a larger 'effective size' for the antidot at this energy, characterized by a region around the antidot avoided by the current paths. On the other hand, at the transmission peaks the current passes near to the antidot edge.

The antidot considered in Fig. 8, although of realistic size, is an idealization, as experimental perforations will inevitably contain imperfections. To consider a more realistic case, we turn to a perforation observed in experimental TEM images. Using pattern recognition[65,66] the positions of the individual carbon atoms are obtained from high resolution TEM images (see Fig. 9 of Ref. 66). Pristine graphene is added around the experimentally obtained perforation to obtain the system shown in Fig. 9a. From the transmission (see Fig. 9b), we notice that peaks are still present, but broadened by the disorder. Considering the two energies I and II in Fig. 9b and

comparing their spatial current maps, we find that certain positions around the antidot are responsible for the additional backscattering causing the transmission dips. Dip I corresponds to a vortex pattern at the left side of the antidot (see Fig. 9c), whereas the dip at II is caused by a vortex pattern at the bottom of the antidot (see Fig. 9d). This result suggests that electrons at different energies see a different effective perforation size and shape and are scattered accordingly.

V. CONCLUSION

We have expanded the standard recursive Green's function method to calculate local and transport properties enabling calculations in extended non-periodic systems. We exploit an efficient calculation of the pristine two-dimensional GF using complex contour methods. Once calculated, the pristine GFs are used to determine a boundary self energy term describing the extended system. In this way, we can treat a finite device region embedded within an extended sample.

We first demonstrated how this approach is able to efficiently treat the electronic properties of strained bubbles in an extended graphene sheet. Considering a clamped bubble, we have shown that the finite size gives rise to Friedel-type oscillations in the density of states. This effect mixes with any pseudomagnetic effects arising from the strain field. We show that the edge effects can cloud pseudomagnetic signatures in the LDOS by adding additional structure which is not directly related to pseudomagnetic effects.

Secondly, we showed how finite leads can be added to a patched device region to efficiently calculate transport properties for spatially separated features, while still being able to map local properties in various parts of the system. In particular, we investigated the current flow around perforations of a graphene lattice. Both idealized geometries and experimental geometries obtained from high resolution TEM images were considered. The transmissions show distinct dips caused by localized states along zigzag segments of the perforations. The transmission dips were associated with vortex-like current paths formed near the perforation edges.

We have demonstrated the versatility of this novel approach to the popular recursive GF method. The method allows for calculation of the same local and transport properties as standard methods, but adds the ability to treat large non-periodic structures embedded in extended samples. We can extend the present method beyond nearest neighbor and to relevant alloys like hBN or transition metal dichalcogenides. We therefore predict that the patched Green's function method will prove a valuable tool in the investigation of nanostructures in two dimensional materials.

Acknowledgements We thank B.K. Nikolic for enlightening discussions of recursive methods applied to arbitrary geometries. We also thank J. Kling for providing the experimental TEM data used in modelling current paths around realistic perforations. The work was supported by the Villum Foundation, Project No. VKR023117. The Center for Nanostructured Graphene (CNG) is sponsored by the Danish Research Foundation, Project DNRF58.

Appendix A: Recursive Algorithm

To obtain a tridiagonal Hamiltonian we let cell $n = 1$ contain all sites of interest. Then following the algorithm outlined below we assign all sites into cells.

1: Let $\{n\}$ denote all sites in cell n and $\{"unassigned"\}$ denote all sites not yet assigned to a cell.

2: Find all sites j for which $H_{nj} \neq 0$ where $n \in \{n\}$ and $j \in \{"unassigned"\}$. Denote these sites $\{n+1\}$.

2a: If $\{n+1\}$ contains an edge site, then all remaining edge sites are added to $\{n+1\}$.

3: Sites in $\{n+1\}$ are removed from $\{"unassigned"\}$

4: Repeat 1-3 until all sites are assigned to a cell.

Step 2a is included if we require an edge self energy term Σ_B as described in Section II.

Assuming the block tridiagonal partitioning obtained from the algorithm above, we make an update sweep starting from cell $n = N$, as shown schematically in Fig. 10. The steps are calculated using the recursive relations[8]

$$\boldsymbol{g}_{N,N} = \big(E - \boldsymbol{H}_{N,N}\big)^{-1}, \tag{A1a}$$

$$\boldsymbol{g}_{n,n} = \big(E - \boldsymbol{H}_{n,n} - \boldsymbol{V}_{n,n+1}\boldsymbol{g}_{n+1,n+1}\boldsymbol{V}_{n+1,n}\big)^{-1}, \tag{A1b}$$

$$\boldsymbol{g}_{1,1} = \big(E - \boldsymbol{H}_{1,1} - \boldsymbol{V}_{1,2}\boldsymbol{g}_{2,2}\boldsymbol{V}_{2,1} - \sum_{m=1}^{M}\Sigma^{m}_{lead}\big)^{-1}, \tag{A1c}$$

where one of the $\boldsymbol{H}_{n,n}$ terms includes the self energy and Σ^{m}_{lead} terms are included if we calculate transmission. After the sweep is complete, the fully connected GF of cell $n = 1$ is obtained as $\boldsymbol{G}_{1,1} = \boldsymbol{g}_{1,1}$. As all sites of interest are placed in this cell, we can now calculate observables involving these sites. For example we calculate transmission, $\mathcal{T}_{L,L'}$, between lead L and L' using these GFs.

$$\mathcal{T}_{L,L'}(E) = \mathrm{Tr}\big[\boldsymbol{G}_{L',L}\boldsymbol{\Gamma}^{L}_{L,L}\boldsymbol{G}^{\dagger}_{L,L'}\boldsymbol{\Gamma}^{L'}_{L',L'}\big], \tag{A2}$$

where $\Gamma^{L} = \mathrm{i}(\Sigma^{L} - \Sigma^{L\dagger})$ and $\boldsymbol{G}_{L,L'}$ ($\boldsymbol{G}^{\dagger}_{L,L'}$) is the retarded (advanced) GF connecting the two leads L and L'.

In order to obtain other blocks of the full GF matrix, we need to store the GF matrix, $\boldsymbol{g}_{n,n}$, for each cell as

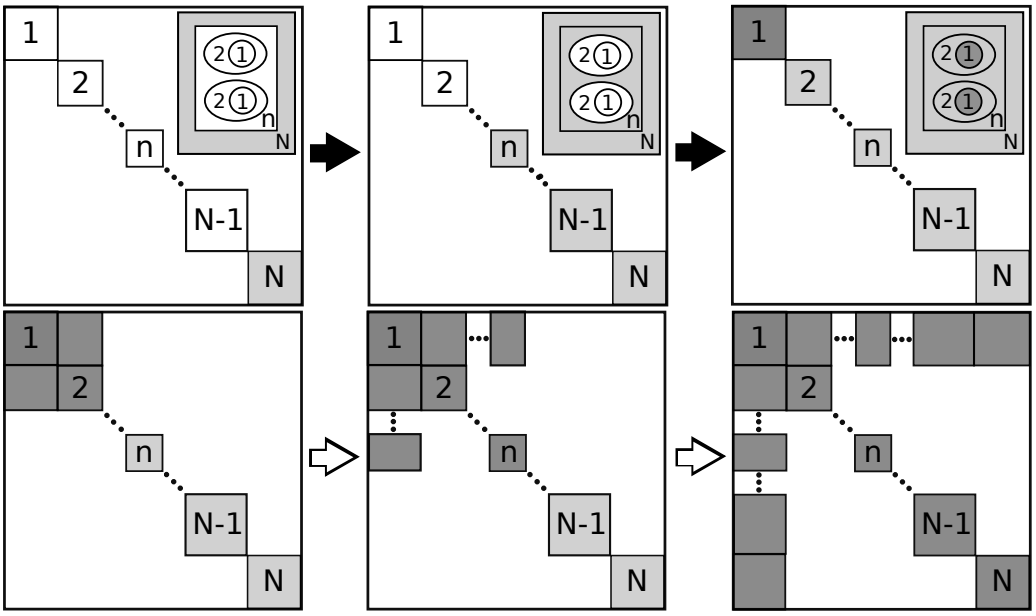

FIG. 10. Top row: recursive sweep going from cell $n = N$ to $n = 1$. Light gray indicate blocks that are stored for the reversed sweep and dark gray indicate blocks of the full GF. The inset shows an illustration of how the different blocks correspond to neighboring cells in the device region. Bottom row: reversed recursive sweep going from $n = 1$ 1 to $n = N$ showing how this sweep can obtain both diagonal and off-diagonal blocks.

we sweep from $n = N$ to $n = 1$. The stored blocks are shown in light gray on Fig. 10.

To obtain the LDOS at site i, $\rho_{ii} = -\mathrm{Im}\big(G_{ii}\big)/\pi$, we need the diagonal of the GF matrix. We calculate the block diagonal from a reversed sweep from $n = 1$ to $n = N$, see Fig. 10. The reversed sweep uses the block diagonals, $\boldsymbol{g}_{n,n}$, from the first sweep to calculate the full diagonal GF, $\boldsymbol{G}$,

$$\boldsymbol{G}_{n,n} = \boldsymbol{g}_{n,n} + \boldsymbol{g}_{n,n}\boldsymbol{V}_{n,n-1}\boldsymbol{G}_{n-1,n-1}\boldsymbol{V}_{n-1,n}\boldsymbol{g}_{n,n}. \quad \text{(A3)}$$

Finally, we want to obtain bond currents for the state leaving a lead L. This can be calculated by $J^L_{ij} = -H_{ij}\mathrm{Im}\big[\boldsymbol{G}_{i,1}\boldsymbol{\Gamma}^L_{1,1}\boldsymbol{G}^\dagger_{1,j}\big]/\hbar$. Remembering that the leads are assigned to cell $n = 1$, we need the off-diagonal blocks, $\boldsymbol{G}_{1,n}$ and $\boldsymbol{G}_{n,1}$, in order to obtain bond currents. Using the stored GFs from the first sweep we can calculate the needed off-diagonals,

$$\boldsymbol{G}_{1,n} = \boldsymbol{G}_{1,n-1}\boldsymbol{V}_{n-1,n}\boldsymbol{g}_{n,n}, \quad \text{(A4a)}$$
$$\boldsymbol{G}_{n,1} = \boldsymbol{g}_{n,n}\boldsymbol{V}_{n,n-1}\boldsymbol{G}_{n-1,n}. \quad \text{(A4b)}$$

Appendix B: Pseudomagnetic field for rotational symmetric strain field

The strain tensor is generally given as

$$\epsilon_{ij} = \frac{1}{2}\Big(\partial_j u_i + \partial_i u_j + (\partial_i z)(\partial_j z)\Big), \quad i,j = x,y, \quad \text{(B1)}$$

where $\boldsymbol{u}(x,y)$ is the in-plane deformation field and $z(x,y)$ is the out-of-plane deformation.[44]

A general two dimensional strain field, $\epsilon_{ij}(x,y)$, leads to a gauge field in the effective Dirac Hamiltonian of graphene[43,44]

$$\boldsymbol{A} = -\frac{\hbar\beta}{2ea_0}\begin{pmatrix}\epsilon_{xx} - \epsilon_{yy}\\ -2\epsilon_{xy}\end{pmatrix}, \quad \text{(B2)}$$

which in turn gives a PMF

$$B_s = \boldsymbol{\nabla}\times\boldsymbol{A} = \partial_x A_y - \partial_y A_x. \quad \text{(B3)}$$

Eqs. (B2) and (B3) imply that the x-axis is chosen along the zigzag direction of the graphene lattice.

Now restricting ourselves to rotationally symmetric deformations, $u(r) = u_r$ and $z(r) = z$, while using polar coordinates (r,θ) yields

$$B_s = -\frac{\hbar\beta}{2ea_0}\left(2\frac{g(r)}{r} - \partial_r g(r)\right)\sin(3\theta), \quad \text{(B4)}$$

with $g(r) = \partial_r u_r - u_r/r + \frac{1}{2}\big(\partial_r z\big)^2$. We notice from Eq. (B4) that the PMF for a rotationally symmetric displacement field is always 6-fold symmetric. On the other hand, the magnitude depends on both the in-plane and out-of-plane displacement.

Considering the displacement field in Eq. (13) we now obtain a PMF of the form,

$$B_s = -\frac{\hbar\beta u_0}{2ea_0R^2}\sin(3\theta). \quad \text{(B5)}$$

Taking into account the scaling $u_0 \propto h_0^2/R$, we obtain a final scaling of the PMF with the size of the bubble, $B_s \propto h_0^2/R^3$.

* mikse@nanotech.dtu.dk

[1] A. K. Geim and I. V. Grigorieva, Nature **499**, 419 (2013).
[2] G. Fiori, F. Bonaccorso, G. Iannaccone, T. Palacios, D. Neumaier, A. Seabaugh, S. K. Banerjee, and L. Colombo, Nature Nanotechnology **9**, 768 (2014).
[3] J. Bai, X. Zhong, S. Jiang, Y. Huang, and X. Duan, Nature nanotechnology **5**, 190 (2010).
[4] F. Schedin, A. K. Geim, S. V. Morozov, E. W. Hill, P. Blake, M. I. Katsnelson, and K. S. Novoselov, Nature Materials **6**, 652 (2007).
[5] Z. Qi, D. A. Bahamon, V. M. Pereira, H. S. Park, D. K. Campbell, and A. H. C. Neto, Nano letters **13**, 2692 (2013).
[6] K. S. Novoselov and A. H. Castro Neto, Physica Scripta **T146**, 014006 (2012).
[7] A. H. Castro Neto, N. M. R. Peres, K. S. Novoselov, and A. K. Geim, Reviews of Modern Physics **81**, 109 (2009).
[8] C. Lewenkopf and E. Mucciolo, Journal of Computational Electronics **12**, 203 (2013).
[9] S. Datta, *Electronic Transport in Mesoscopic Systems* (Cambridge University Press, 1997).
[10] L. E. F. Foa Torres, S. Roche, and J.-C. Charlier, *Introduction to Graphene-Based Nanomaterials* (Cambridge University Press, 2014).
[11] K. Kazymyrenko and X. Waintal, Physical Review B **77**, 115119 (2008).
[12] M. Wimmer and K. Richter, Journal of Computational Physics **228**, 8548 (2009).
[13] J. Baringhaus, M. Ruan, F. Edler, A. Tejeda, M. Sicot, A.-P. Li, Z. Jiang, E. H. Conrad, C. Berger, C. Tegenkamp, and W. A. de Heer, Nature **506**, 349 (2014).
[14] P. W. Sutter, J.-I. Flege, and E. A. Sutter, Nature Materials **7**, 406 (2008).
[15] M. Settnes, S. R. Power, D. H. Petersen, and A.-P. Jauho, Phys. Rev. Lett. **112**, 096801 (2014).
[16] S. R. Power and M. S. Ferreira, Physical Review B **83**, 155432 (2011).
[17] R. N. Sajjad, C. A. Polanco, and A. W. Ghosh, Journal of Computational Electronics **12**, 232 (2013).
[18] C. Bena, Physical Review B **79**, 125427 (2009).
[19] J. A. Lawlor and M. S. Ferreira, ArXiv e-prints (2014), arXiv:1411.6240.
[20] S. R. Power, P. D. Gorman, J. M. Duffy, and M. S. Ferreira, Phys. Rev. B **86**, 195423 (2012).
[21] D. A. Areshkin and B. K. Nikolić, Physical Review B **81**, 155450 (2010).
[22] M. Yang, X.-J. Ran, Y. Cui, and R.-Q. Wang, Chinese Physics B **20**, 097201 (2011).
[23] G. Thorgilsson, G. Viktorsson, and S. Erlingsson, Journal of Computational Physics **261**, 256 (2014).
[24] G. Metalidis and P. Bruno, Physical Review B **72**, 235304 (2005).
[25] A. Cresti, R. Farchioni, G. Grosso, and G. P. Parravicini, Physical Review B **68**, 075306 (2003).
[26] E. Costa Girão and V. Meunier, Journal of Computational Electronics **12**, 123 (2013).
[27] T. Low, F. Guinea, and M. I. Katsnelson, Physical Review B **83**, 195436 (2011).
[28] F. Guinea, M. I. Katsnelson, and A. K. Geim, Nature Physics **6**, 30 (2009).
[29] G. W. Jones and V. M. Pereira, New Journal of Physics **16**, 093044 (2014).
[30] Z. Qi, A. L. Kitt, H. S. Park, V. M. Pereira, D. K. Campbell, and A. H. Castro Neto, Phys. Rev. B **90**, 125419 (2014).
[31] M. Neek-Amal and F. M. Peeters, Phys. Rev. B **85**, 195445 (2012).
[32] J. Lu, A. H. Castro Neto, and K. P. Loh, Nature communications **3**, 823 (2012).
[33] R. Carrillo-Bastos, D. Faria, A. Latgé, F. Mireles, and N. Sandler, Physical Review B **90**, 041411 (2014).
[34] F. D. Juan, A. Cortijo, M. A. H. Vozmediano, and A. Cano, Nature Physics **7**, 810 (2011).
[35] M. Neek-Amal, L. Covaci, K. Shakouri, and F. M. Peeters, Physical Review B **88**, 115428 (2013).
[36] M. Neek-Amal and F. M. Peeters, Physical Review B **85**, 195446 (2012).
[37] V. M. Pereira, A. H. Castro Neto, and N. M. R. Peres, Physical Review B **80**, 045401 (2009).
[38] V. M. Pereira and A. H. Castro Neto, Phys. Rev. Lett. **103**, 046801 (2009).
[39] V. M. Pereira, R. M. Ribeiro, N. M. R. Peres, and A. H. Castro Neto, EPL (Europhysics Letters) **92**, 67001 (2010).
[40] D. Moldovan, M. Ramezani Masir, and F. M. Peeters, Physical Review B **88**, 035446 (2013).
[41] F. M. D. Pellegrino, G. G. N. Angilella, and R. Pucci, Physical Review B **81**, 035411 (2010).
[42] Z. H. Ni, T. Yu, Y. H. Lu, Y. Y. Wang, Y. P. Feng, and Z. X. Shen, ACS Nano **2**, 2301 (2008).
[43] H. Suzuura and T. Ando, Phys. Rev. B **65**, 235412 (2002).
[44] M. Vozmediano, M. Katsnelson, and F. Guinea, Physics Reports **496**, 109 (2010).
[45] N. Levy, S. A. Burke, K. L. Meaker, M. Panlasigui, A. Zettl, F. Guinea, A. H. Castro Neto, and M. F. Crommie, Science **329**, 544 (2010).
[46] J. S. Bunch, S. S. Verbridge, J. S. Alden, A. M. van der Zande, J. M. Parpia, H. G. Craighead, and P. L. McEuen, Nano Letters **8**, 2458 (2008).
[47] K. Yue, W. Gao, R. Huang, and K. M. Liechti, Journal of Applied Physics **112**, 083512 (2012).
[48] F. M. D. Pellegrino, G. G. N. Angilella, and R. Pucci, Phys. Rev. B **84**, 195404 (2011).
[49] T. G. Pedersen, C. Flindt, J. G. Pedersen, N. A. Mortensen, A.-P. Jauho, and K. Pedersen, Physical Review Letters **100**, 136804 (2008).
[50] T. Gunst, T. Markussen, A.-P. Jauho, and M. Brandbyge, Phys. Rev. B **84**, 155449 (2011).
[51] J. A. Fürst, J. G. Pedersen, C. Flindt, N. A. Mortensen, M. Brandbyge, T. G. Pedersen, and A. P. Jauho, New Journal of Physics **11**, 095020 (2009).
[52] J. G. Pedersen, T. Gunst, T. Markussen, and T. G. Pedersen, Phys. Rev. B **86**, 245410 (2012).
[53] S. R. Power and A.-P. Jauho, Phys. Rev. B **90**, 115408 (2014).

Paper IV

Mikkel Settnes, Stephen R. Power, Jun Lin, Dirch H. Petersen and Antti-Pekka Jauho

Bubbles in graphene - a computational study

Journal of Physics: Conference Series (JPCS) (2015), submitted

arXiv:1506.06509v1 [cond-mat.mes-hall] 22 Jun 2015

Bubbles in graphene - a computational study

Mikkel Settnes, Stephen R. Power, Jun Lin, Dirch H. Petersen and Antti-Pekka Jauho

Center for Nanostructured Graphene (CNG),
DTU Nanotech, Technical University of Denmark, DK-2800 Kgs. Lyngby, Denmark

E-mail: Antti-Pekka.Jauho@nanotech.dtu.dk

Abstract. Strain-induced deformations in graphene are predicted to give rise to large pseudomagnetic fields. We examine theoretically the case of gas-inflated bubbles to determine whether signatures of such fields are present in the local density of states. Sharp-edged bubbles are found to induce Friedel-type oscillations which can envelope pseudo-Landau level features in certain regions of the bubble. However, bubbles which minimise interference effects are also unsuitable for pseudo-Landau level formation due to more spatially varying field profiles.

1. Introduction

Strain engineering has been proposed as a method to manipulate the electronic, optical and magnetic properties of graphene [1–10].It is based on the close relation between the structural and electronic properties of graphene. An inhomogeneous strain field can introduce pseudomagnetic fields (PMFs), [1, 4, 5] where the altered tight binding hoppings mimic the role of a gauge field in the low energy effective Dirac model of graphene [11, 12]. Guinea *et al* [1] demonstrated that nearly homogeneous PMFs can be generated by applying triaxial strain. One of the most striking consequences of homogeneous PMFs is the appearance of a Landau-like quantization. [1, 8] Scanning tunnelling spectroscopy on bubble-like deformations has observed pseudo-Landau levels corresponding to PMFs stronger than 300 T [2, 3].

Deformations can be induced in graphene samples by different techniques like pressurizing suspended graphene [5, 13] or by exploiting the thermal expansion coefficients of different substrates [3]. As a result, introducing nonuniform strain distributions at the nanoscale is a promising route towards strain engineering. The standard theoretical approach to treat strain effects employs continuum mechanics to obtain the strain field. The strain field can then be coupled to an effective Dirac model of graphene to study the generation of PMFs in various geometries. In most studies, only the PMF distribution is considered as opposed to experimentally observable quantities like local density of states (LDOS). This study calculates the LDOS of such systems without applying periodicity, which can introduce spurious interactions between neighboring bubbles.

2. Model

2.1. Patched Green's function approach

The patched Green's function approach, developed in Ref [14], treats device 'patches' embedded within an extended two dimensional system described by a tight-binding Hamiltonian. This approach allows us to insert a single bubble into an otherwise pristine infinite graphene sheet,

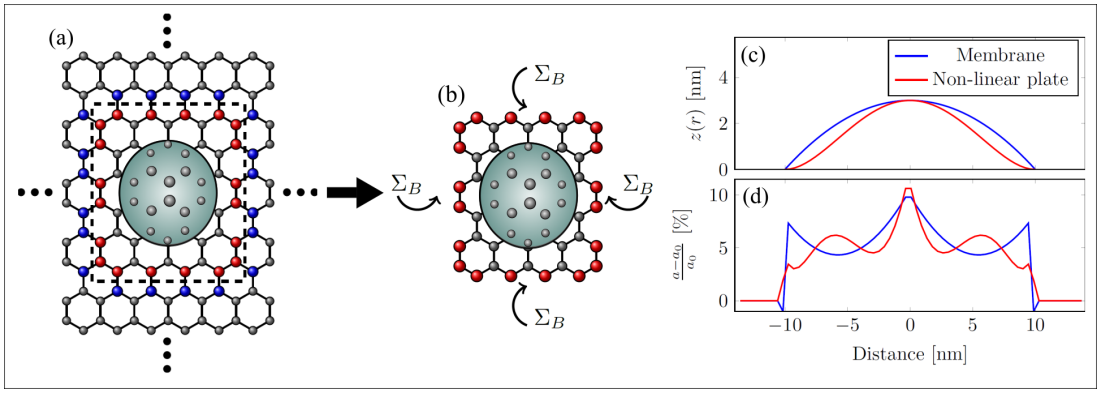

Figure 1. The patched GF method describes the extended graphene sheet away from the bubble device region (a) with a self energy term $\mathbf{\Sigma}_B$ (b). We consider membrane and non-linear plate type bubbles with radially dependent (c) height and (d)strain profiles.

and avoids issues such as interferences between a bubble and its periodic images or system edges. The extended part of the system is treated through a self-energy Σ_B entering the device area.

$$\boldsymbol{G}_{D,D} = \left(E\mathbf{1} - \boldsymbol{H}_{D,D} - \mathbf{\Sigma}_B\right)^{-1}, \tag{1}$$

The self-energy is written in terms of Green's functions (GFs) of an infinite, pristine sheet so that it can be calculated using methods taking advantage of periodicity and analytic integrability [15]. The Hamiltonian for the device region can be tridiagonalized allowing the GF of the device region, $\boldsymbol{G}_{D,D}$, to be treated using an adaptive recursive method. A dual recursive sweep allows for efficient calculation of local properties everywhere in the device region surrounding a bubble, enabling us to investigate spatial variations of the LDOS.

2.2. Strain model

In this work we consider two possibilities for the shape of a gas inflated bubble, namely the *membrane* and *non-linear plate* models. [16] The membrane model is suitable for very large bubbles where bending stiffness can be neglected, whereas the non-linear plate model is more appropriate for including bending effects near the edges of smaller bubbles. Membrane bubbles therefore have very sharp edges, whereas the edges are smoother in the non-linear plate bubbles. While these continuum models have been found to agree well with experimental shape profiles, more accurate modeling of bubble shapes and strain distributions can be achieved using molecular dynamics simulations. [5, 17, 18]

Using the deformation field $\boldsymbol{u} = (u_r, u_\theta, z)$ the position of the atom i initially at $\boldsymbol{R}_i^0$ becomes $\boldsymbol{R}_i = \boldsymbol{R}_i^0 + \boldsymbol{u}$. The new bond lengths are afterwards determined as $d_{ij} = |\boldsymbol{R}_i - \boldsymbol{R}_j|$. Hoppings are modified according to $t_{ij} = t_0 \mathrm{e}^{-\beta\left(d_{ij}/a_0 - 1\right)}$, where $t_0 \approx 2.7$ eV is the pristine coupling, $a_0 = 1.42$Å is the carbon-carbon distance and $\beta \approx \partial \log(t)/\partial \log(a)|_{a=a_0} \approx 3.37$ [7]. The strain tensor created by the strain field, $\epsilon_{ij} = \frac{1}{2}\left(\partial_j u_i + \partial_i u_j + \partial_i z \partial_j z\right)$, gives rise to a gauge field [11],

$$\boldsymbol{A} = -\frac{\hbar\beta}{2ea_0}\begin{pmatrix}\epsilon_{xx} - \epsilon_{yy} \\ 2\epsilon_{xy}\end{pmatrix}, \tag{2}$$

with the resulting PMF given by $\mathbf{B_s} = \nabla \times \mathbf{A}$. Table 1 shows the height profile, in-plane displacements and PMFs for the two types of bubbles considered here.

Model type	$z(r,\theta)$	$\boldsymbol{u}(r,\theta) = \begin{pmatrix} u_r \\ u_\theta \end{pmatrix}$	$B_s(r,\theta)$
Membrane	$h_0\left(1-\frac{r^2}{R^2}\right)$	$\begin{pmatrix} u_0\frac{r}{R}\left(1-\frac{r}{R}\right) \\ 0 \end{pmatrix}$	$\frac{\hbar\beta u_0}{2ea_0R^2}\sin(3\theta)$
Non-linear plate	$h_0\left(1-\frac{r^2}{R^2}\right)^2$	$\begin{pmatrix} r(R-r)(c_1+c_2r) \\ 0 \end{pmatrix}$	$\frac{\hbar\beta}{2ea_0}\left[(c_1-c_2R) - \frac{32h_0^2r^3}{R^6}\left(1-\frac{r^2}{R^2}\right)\right]\sin(3\theta)$

Table 1. Height profile $z(r,\theta)$, in-plane displacements $\boldsymbol{u}(r,\theta)$ and PMF distributions $B_s(r,\theta)$ for the membrane and non-linear plate bubbles, where R and h_0 are the bubble radius and height respectively, and $u_0 = 1.136h_0^2/R$, $c_1 = 1.308h_0^2/R^3$ and $c_1 = -1.931h_0^2/R^4$. [16]

3. Results

New hopping parameters, calculated from atomic coordinates generated by the continuum model displacements, give a tight-binding description of the bubble region which can be used within the patched GF approach. From this, the LDOS at every site in the bubble, as well as the average DOS, can be quickly calculated. Fig. 2a shows the averaged DOS for membrane (blue) and non-linear plate (red) model bubbles. For the membrane model, we have previously distinguished between two different type of oscillations [14]. A series of sharp peaks, such as those highlighted by the blue circle and triangle, were found to have an energy dependence, $E_n \sim \sqrt{n}$, consistent with Landau-like levels arising due to the PMF. In addition, the periodic oscillations visible at higher energies are identified as Friedel-type oscillations arising due to scattering of electrons induced by the sharp edges of the membrane-model bubble.

Before discussing the interplay between different oscillation types, we note that both features vary independently with position throughout the bubble region. The position dependence of the pseudo-Landau level features arises due to the non-uniform PMF distribution within the bubble, which is plotted in Fig. 2d. This takes maximum amplitudes along the armchair directions which occur every 60°, but is only three-fold symmetric due to a sign change between two consecutive amplitude maxima. Unlike real magnetic fields, PMFs conserve time-reveral symmetry by taking opposite signs in the K and K' valleys of graphene. One manifestation of this is a strong sublattice polarisation [14, 19, 20], which is clearly visible for the sublattice-split LDOS maps shown in Fig. 2b-c, where the circle LDOS peak from Fig. 2a is localized in different regions for different sublattices. Comparison to panel 1 confirm that these correspond to a change in the sign of the PMF. We note that this, the first "pseudomagnetic peak", is localized along armchair directions where the PMFs are largest and reasonably constant. The position dependence of the Friedel oscillations meanwhile emerges from interference between electrons scattered at different sides of the bubble. The interplay of both oscillation types in membrane bubbles leads to the Friedel type acting as an envelope and quenching the LDOS signature of pseudo-Landau peaks in certain regions of the bubble, as is clear for the dark spots in the LDOS map for the higher energy in Fig. 2h. STS measurements taken at such a spot would completely omit this peak due to the enveloping effects of the edge-induced Friedel oscillations.

When searching for signatures of PMFs in gas-inflated bubbles, it may thus be worth considering bubbles with a softer edge profile, such as the non-linear plate model, which should give riser to weaker Friedel oscillations. This is clear from the averaged LDOS curve in Fig. 2a, where the higher energy oscillations are considerably suppressed compared to the membrane case. However, in this case there is also an absence of sharp Landau-level-like peaks following a $\sqrt{n}$ distribution, with the possible exception of the peak denoted by the red circle. This lack

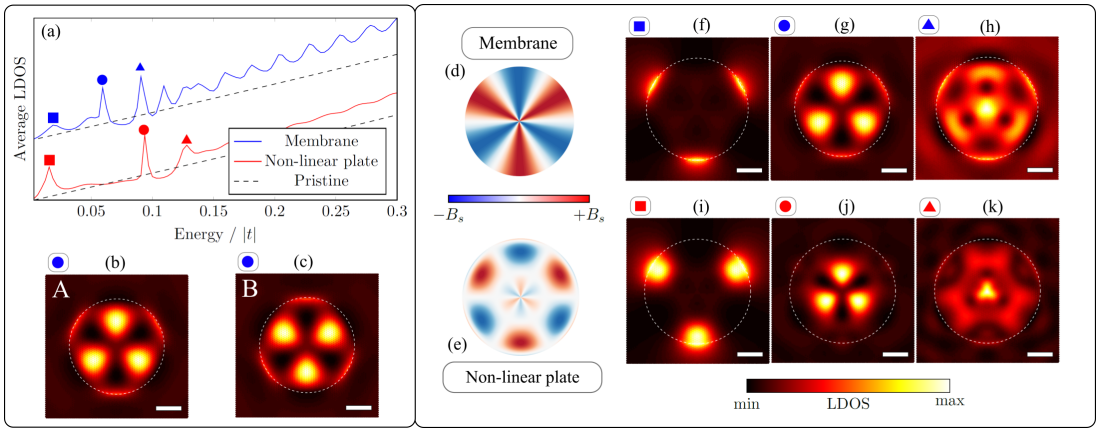

Figure 2. a) shows the averaged DOS with each bubble model with $R = 10$nm and $h_0 = 10$nm. Important peaks in each are highlighted by symbols. b,c) The LDOS for the membrane model at the circle energy is mapped for the A and B sublattices separately. d,e) show the PMF distributions for each bubble type and f-k) show A sublattice LDOS maps for the peaks highlighted in a). The scale bar in all LDOS maps is 5nm.

of pseudo-Landau features is consistent with the PMF distribution for this bubble type, plotted in Fig. 2e. We note that this bubble, with less sharp edges, also has a radial fluctuation in the sign and strength of the PMF. The center of the bubble has a field distribution similar to that of the membrane case, and the central region of the LDOS map in Fig 2j resembles that of the corresponding membrane model peak (Fig 2g). We note also that the Friedel features for the higher (triangle) energy in Fig. 2k (which does not fit the $\sqrt{n}$ distribution) are more blurred than for the membrane case, as expected for scattering from a less-sharp bubble edge. Thus it seems that bubble shapes which reduce Friedel oscillations also effectively remove pseudomagnetic Landau effects due to the less uniform PMFs induced by their strain profiles.

Finally, we note that the square symbol energy peak at low energies in both bubble types is a state localized near the bubble edge and plotted in Figs. 2f and 2i. It is not directly related to pseudomagnetic effects, but emerges due to the interface between the pristine graphene region outside the bubble and the strained, perturbed region within. The presence of localized states at this boundary acts somewhat like a potential, and induces the scattering which lies behind the Friedel oscillations in these bubbles. We note that these states in the non-linear plate bubble are far less localized than their membrane bubble counterparts, due to an edge which is no longer as sharp. This in turn leads to the smoothening and averaging out of the Friedel oscillations that we observed earlier for the non-linear plate bubbles.

4. Conclusions

We studied theoretically the local and averaged densities of states in gas-inflated graphene bubbles embedded in infinite graphene sheets by making use of the patched Green's function approach. We determined that pseudo-Landau level features in sharp-edged bubbles may be hidden by interference effects due to electron scattering at the bubble edges. Softer-edged bubbles were found to display weaker interference effects, however their shape profiles also resulted in pseudomagnetic field distributions unsuitable for pseudo-Landau level formation. Our results suggest that it will be difficult to obtain reliable Landau level features in such gas inflated systems, unlike bubbles formed on substrates which often display the triaxial-type strain which is predicted to give a more appropriate pseudomagnetic field for Landau level formation.

Bibliography

[1] R. P. Feynman. There's plenty of room at the bottom. *Engineering and Science*, page 2236, 1960.

[2] A. K. Geim and I. V. Grigorieva. Van der Waals heterostructures. *Nature*, 499(7459):419–25, July 2013.

[3] M. Scarselli, P. Castrucci, and M. De Crescenzi. Electronic and optoelectronic nano-devices based on carbon nanotubes. *Journal of Physics: Condensed Matter*, 24(31):313202, 2012.

[4] K. S. Novoselov, V. I. Fal'ko, L. Colombo, P. R. Gellert, M. G. Schwab, and K. Kim. A roadmap for graphene. *Nature*, 490(7419):192–200, October 2012.

[5] A. K. Geim. Graphene: status and prospects. *Science (New York, N.Y.)*, 324(5934):1530–4, June 2009.

[6] P. R. Wallace. The band theory of graphite. *Phys. Rev.*, 71:622–634, May 1947.

[7] J. C. Slonczewski and P. R. Weiss. Band structure of graphite. *Phys. Rev.*, 109:272–279, Jan 1958.

[8] K. S. Novoselov, A. K. Geim, S. V. Morozov, D. Jiang, Y. Zhang, S. V. Dubonos, I. V. Grigorieva, and A. A. Firsov. Electric field effect in atomically thin carbon films. *Science (New York, N.Y.)*, 306(5696):666–9, October 2004.

[9] Y. Zhang, Y.-W. Tan, H. L. Stormer, and P. Kim. Experimental observation of the quantum Hall effect and Berry's phase in graphene. *Nature*, 438(7065):201–4, November 2005.

[10] K. S. Novoselov, A. K. Geim, S. V. Morozov, D. Jiang, M. I. Katsnelson, I. V. Grigorieva, S. V. Dubonos, and A. A. Firsov. Two-dimensional gas of massless Dirac fermions in graphene. *Nature*, 438(7065):197–200, November 2005.

[11] M. I. Katsnelson, K. S. Novoselov, and A. K. Geim. Chiral tunnelling and the Klein paradox ingraphene. *Nature Physics*, 2(9):620–625, August 2006.

[12] A. H. Castro Neto, F. Guinea, N. M. R. Peres, K. S. Novoselov, and A. K. Geim. The electronic properties of graphene. *Rev. Mod. Phys.*, 81:109–162, Jan 2009.

[13] A. K. Geim and K. S. Novoselov. The rise of graphene. *Nature materials*, 6(3):183–91, March 2007.

[14] A. C. Ferrari. Science and technology roadmap for graphene, related two-dimensional crystals, and hybrid systems. *Nanoscale*, 7(11):4598–4810, September 2014.

[15] L. E. F. Foa Torres, S. Roche, and J.-C. Charlier. *Introduction to Graphene-Based Nanomaterials*. Cambridge University Press, 2014.

[16] M. I. Katsnelson. *Graphene – Carbon in Two Dimensions*. Cambridge University Press, 2012.

[17] M. F. Borunda, H. Hennig, and E. J. Heller. Ballistic versus diffusive transport in graphene. *Physical Review B*, 88(12):125415, September 2013.

[18] A. S. Mayorov, R. V. Gorbachev, S. V. Morozov, L. Britnell, R. Jalil, L. A. Ponomarenko, P. Blake, K. S. Novoselov, K. Watanabe, T. Taniguchi, and A. K. Geim. Micrometer-scale ballistic transport in encapsulated graphene at room temperature. *Nano Letters*, 11(6):2396–9, June 2011.

[19] C. Berger, Z. Song, X. Li, X. Wu, N. Brown, C. Naud, D. Mayou, T. Li, J. Hass, A. N. Marchenkov, E. H. Conrad, P. N. First, and W. A. de Heer. Electronic confinement and coherence in patterned epitaxial graphene. *Science*, 312(5777):1191–6, May 2006.

[20] K. Bolotin, K. Sikes, Z. Jiang, M. Klima, G. Fudenberg, J. Hone, P. Kim, and H. Stormer. Ultrahigh electron mobility in suspended graphene. *Solid State Communications*, 146(9):351–355, 2008.

[21] V. V. Cheianov, V. Fal'ko, and B. L. Altshuler. The focusing of electron flow and a veselago lens in graphene p-n junctions. *Science*, 315(5816):1252–1255, 2007.

[22] P. Rickhaus, R. Maurand, M.-H. Liu, M. Weiss, K. Richter, and C. Schönenberger. Ballistic interferences in suspended graphene. *Nature communications*, 4:2342, January 2013.

[23] J. A. Fürst, J. G. Pedersen, C. Flindt, N. A. Mortensen, M. Brandbyge, T. G. Pedersen, and A. P. Jauho. Electronic properties of graphene antidot lattices. *New Journal of Physics*, 11(9):095020, September 2009.

[24] J. G. Pedersen, T. Gunst, T. Markussen, and T. G. Pedersen. Graphene antidot lattice waveguides. *Phys. Rev. B*, 86:245410, Dec 2012.

[25] J. R. Williams, T. Low, M. S. Lundstrom, and C. M. Marcus. Gate-controlled guiding of electrons in graphene. *Nature nanotechnology*, 6(4):222–5, April 2011.

[26] Y. Zhao, J. Wyrick, F. D. Natterer, J. F. Rodriguez-Nieva, C. Lewandowski, K. Watanabe, T. Taniguchi, L. S. Levitov, N. B. Zhitenev, and J. A. Stroscio. Creating and probing electron whispering-gallery modes in graphene. *Science*, 348(6235):672–675, 2015.

[27] M. Vozmediano, M. Katsnelson, and F. Guinea. Gauge fields in graphene. *Physics Reports*, 496(4):109–148, 2010.

[28] V. M. Pereira, A. H. Castro Neto, and N. M. R. Peres. Tight-binding approach to uniaxial strain in graphene. *Physical Review B*, 80(4):045401, July 2009.

[29] F. Guinea, M. I. Katsnelson, and A. K. Geim. Energy gaps and a zero-field quantum Hall effect in graphene by strain engineering. *Nature Physics*, 6(1):30–33, September 2009.

[30] K. S. Novoselov, Z. Jiang, Y. Zhang, S. V. Morozov, H. L. Stormer, U. Zeitler, J. C. Maan, G. S. Boebinger, P. Kim, and A. K. Geim. Room-temperature quantum Hall effect in graphene. *Science (New York, N.Y.)*, 315(5817):1379, March 2007.

[31] S. Z. Butler, S. M. Hollen, L. Cao, Y. Cui, J. A. Gupta, H. R. Gutiérrez, T. F. Heinz, S. S. Hong, J. Huang, A. F. Ismach, E. Johnston-Halperin, M. Kuno, V. V. Plashnitsa, R. D. Robinson, R. S. Ruoff, S. Salahuddin, J. Shan, L. Shi, M. G. Spencer, M. Terrones, W. Windl, and J. E. Goldberger. Progress, challenges, and opportunities in two-dimensional materials beyond graphene. *ACS nano*, 7(4):2898–926, April 2013.

[32] F. Schwierz, J. Pezoldt, and R. Granzner. Two-dimensional materials and their prospects in transistor electronics. *Nanoscale*, 7(18):8261–83, April 2015.

[33] A. H. Castro Neto and K. Novoselov. Two-Dimensional Crystals: Beyond Graphene. *Materials Express*, 1(1):10–17, March 2011.

[34] X. Cui, G.-H. Lee, Y. D. Kim, G. Arefe, P. Y. Huang, C.-H. Lee, D. A. Chenet, X. Zhang, L. Wang, F. Ye, F. Pizzocchero, B. S. Jessen, K. Watanabe, T. Taniguchi, D. A. Muller, T. Low, P. Kim, and J. Hone. Multi-terminal transport measurements of MoS2 using a van der Waals heterostructure device platform. *Nature Nanotechnology*, 10(6):534–540, April 2015.

[35] A.-P. Li, K. W. Clark, X.-G. Zhang, and A. P. Baddorf. Electron Transport at the Nanometer-Scale Spatially Revealed by Four-Probe Scanning Tunneling Microscopy. *Advanced Functional Materials*, 23(20):2509–2524, May 2013.

[36] G. Binnig, H. Rohrer, C. Gerber, and E. Weibel. Surface studies by scanning tunneling microscopy. *Phys. Rev. Lett.*, 49:57–61, Jul 1982.

[37] A. Deshpande and B. J. LeRoy. Scanning probe microscopy of graphene. *Physica E: Low-dimensional Systems and Nanostructures*, 44(4):743 – 759, 2012.

[38] V. V. Cheianov and V. I. Fal'ko. Selective transmission of Dirac electrons and ballistic magnetoresistance of n-p junctions in graphene. *Physical Review B - Condensed Matter and Materials Physics*, 74(4):1–4, 2006.

[39] C. Bena. Effect of a Single Localized Impurity on the Local Density of States in Monolayer and Bilayer Graphene. *Physical Review Letters*, 100(7):076601, February 2008.

[40] F. M. D. Pellegrino, G. G. N. Angilella, and R. Pucci. Effect of impurities in high-symmetry lattice positions on the local density of states and conductivity of graphene. *Physical Review B*, 80(9):094203, September 2009.

[41] N. M. R. Peres, L. Yang, and S.-W. Tsai. Local density of states and scanning tunneling currents in graphene. *New Journal of Physics*, 11(9):095007, September 2009.

[42] G. I. Márk, P. Vancsó, C. Hwang, P. Lambin, and L. P. Biró. Anisotropic dynamics of charge carriers in graphene. *Physical Review B*, 85(12):125443, March 2012.

[43] A. Bergvall and T. Löfwander. Spectral footprints of impurity scattering in graphene nanoribbons. *Physical Review B*, 87(20):205431, May 2013.

[44] J. A. Lawlor, S. R. Power, and M. S. Ferreira. Friedel oscillations in graphene: Sublattice asymmetry in doping. *Physical Review B*, 88(20):205416, November 2013.

[45] S. Lounis. Theory of Scanning Tunneling Microscopy. 2014.

[46] Y. Dedkov, E. Voloshina, and M. Fonin. Scanning probe microscopy and spectroscopy of graphene on metals (phys. status solidi b 3/2015). *physica status solidi (b)*, 252(3):n/a–n/a, 2015.

[47] G. M. Rutter, J. N. Crain, N. P. Guisinger, T. Li, P. N. First, and J. A. Stroscio. Scattering and interference in epitaxial graphene. *Science*, 317(5835):219–22, July 2007.

[48] P. Mallet, F. Varchon, C. Naud, L. Magaud, C. Berger, and J.-Y. Veuillen. Electron states of mono- and bilayer graphene on SiC probed by scanning-tunneling microscopy. *Physical Review B*, 76(4):041403, July 2007.

[49] H. Yang, A. J. Mayne, M. Boucherit, G. Comtet, G. Dujardin, and Y. Kuk. Quantum interference channeling at graphene edges. *Nano Letters*, 10(3):943–7, March 2010.

[50] L. Tapaszto, P. Nemes-Incze, G. Dobrik, K. Jae Yoo, C. Hwang, and L. P. Biro. Mapping the electronic properties of individual graphene grain boundaries. *Applied Physics Letters*, 100(5):053114, February 2012.

[51] J. Xue, J. Sanchez-Yamagishi, K. Watanabe, T. Taniguchi, P. Jarillo-Herrero, and B. J. LeRoy. Long-Wavelength Local Density of States Oscillations Near Graphene Step Edges. *Physical Review Letters*, 108(1):016801, January 2012.

[52] J. C. Koepke, J. D. Wood, D. Estrada, Z.-Y. Ong, K. T. He, E. Pop, and J. W. Lyding. Atomic-scale evidence for potential barriers and strong carrier scattering at graphene grain boundaries: A scanning tunneling microscopy study. *ACS Nano*, 7(1):75–86, 2013.

[53] T. Nakayama, O. Kubo, Y. Shingaya, S. Higuchi, T. Hasegawa, C.-S. Jiang, T. Okuda, Y. Kuwahara, K. Takami, and M. Aono. Development and application of multiple-probe scanning probe microscopes. *Advanced materials*, 24(13):1675–92, April 2012.

[54] S. Hasegawa, I. Shiraki, T. Tanikawa, C. L. Petersen, T. M. Hansen, P. Bøggild, and F. Grey. Direct measurement of surface-state conductance by microscopic four-point probe method. *Journal of Physics: Condensed Matter*, 14(35):8379, 2002.

[55] D. H. Petersen, O. Hansen, T. M. Hansen, P. Boggild, R. Lin, D. Kjæ r, P. F. Nielsen, T. Clarysse, W. Vandervorst, E. Rosseel, N. S. Bennett, and N. E. B. Cowern. Review of electrical characterization of ultra-shallow junctions with micro four-point probes. *Journal of Vacuum Science & Technology B: Microelectronics and Nanometer Structures*, 28(1):C1C27, 2010.

[56] I. Miccoli, F. Edler, H. Pfnür, and C. Tegenkamp. The 100th anniversary of the four-point probe technique: the role of probe geometries in isotropic and anisotropic systems. *Journal of Physics: Condensed Matter*, 27(22):223201, 2015.

[57] T. Kanagawa, R. Hobara, I. Matsuda, T. Tanikawa, A. Natori, and S. Hasegawa. Anisotropy in conductance of a quasi-one-dimensional metallic surface state measured by a square micro-four-point probe method. *Phys. Rev. Lett.*, 91:036805, Jul 2003.

[58] V. Cherepanov, E. Zubkov, H. Junker, S. Korte, M. Blab, P. Coenen, and B. Voigtländer. Ultra compact multitip scanning tunneling microscope with a diameter of 50 mm. *Review of scientific instruments*, 83(3):033707, March 2012.

[59] O. Kubo, Y. Shingaya, M. Nakaya, M. Aono, and T. Nakayama. Epitaxially grown wox nanorod probes for sub-100nm multiple-scanning-probe measurement. *Applied Physics Letters*, 88(25):–, 2006.

[60] H. Watanabe, C. Manabe, T. Shigematsu, and M. Shimizu. Dual-probe scanning tunneling microscope: Measuring a carbon nanotube ring transistor. *Applied Physics Letters*, 78(19), 2001.

[61] J. Baringhaus, M. Ruan, F. Edler, A. Tejeda, M. Sicot, A.-P. Li, Z. Jiang, E. H. Conrad, C. Berger, C. Tegenkamp, and W. A. de Heer. Exceptional ballistic transport in epitaxial graphene nanoribbons. *Nature*, 506(7488):349–354, February 2014.

[62] K. W. Clark, X.-G. Zhang, I. V. Vlassiouk, G. He, R. M. Feenstra, and A.-P. Li. Spatially resolved mapping of electrical conductivity across individual domain (grain) boundaries in graphene. *ACS nano*, 7(9):7956–66, September 2013.

[63] K. W. Clark, X.-G. Zhang, G. Gu, J. Park, G. He, R. M. Feenstra, and A.-P. Li. Energy Gap Induced by Friedel Oscillations Manifested as Transport Asymmetry at Monolayer-Bilayer Graphene Boundaries. *Physical Review X*, 4(1):011021, February 2014.

[64] M. Kim, N. S. Safron, E. Han, M. S. Arnold, and P. Gopalan. Fabrication and characterization of large-area, semiconducting nanoperforated graphene materials. *Nano letters*, 10(4):1125–31, April 2010.

[65] F. R. Eder, J. Kotakoski, K. Holzweber, C. Mangler, V. Skakalova, and J. C. Meyer. Probing from both sides: reshaping the graphene landscape via face-to-face dual-probe microscopy. *Nano Letters*, 13(5):1934–40, May 2013.

[66] S.-H. Ji, J. B. Hannon, R. M. Tromp, V. Perebeinos, J. Tersoff, and F. M. Ross. Atomic-scale transport in epitaxial graphene. *Nature materials*, 11(2):114–9, February 2012.

[67] P. W. Sutter, J.-I. Flege, and E. A. Sutter. Epitaxial graphene on ruthenium. *Nature Materials*, 7(5):406–11, May 2008.

[68] J. D. Buron, D. H. Petersen, P. Bøggild, D. G. Cooke, M. Hilke, J. Sun, E. Whiteway, P. F. Nielsen, O. Hansen, A. Yurgens, and P. U. Jepsen. Graphene conductance uniformity mapping. *Nano Letters*, 12(10):5074–81, October 2012.

[69] J. D. Buron, F. Pizzocchero, B. S. Jessen, T. J. Booth, P. F. Nielsen, O. Hansen, M. Hilke, E. Whiteway, P. U. Jepsen, P. Bggild, and D. H. Petersen. Electrically continuous graphene from single crystal copper verified by terahertz conductance spectroscopy and micro four-point probe. *Nano Letters*, 14(11):6348–6355, 2014.

[70] J. Baringhaus, F. Edler, C. Neumann, C. Stampfer, S. Forti, U. Starke, and C. Tegenkamp. Local transport measurements on epitaxial graphene. *Applied Physics Letters*, 103(11):–, 2013.

[71] D. H. Petersen, O. Hansen, R. Lin, and P. F. Nielsen. Micro-four-point probe Hall effect measurement method. *Journal of Applied Physics*, 104(1):013710, 2008.

[72] S. Datta. *Electronic Transport in Mesoscopic Systems*. Cambridge University Press, 1997.

[73] H. Haug and A.-P. Jauho. *Quantum kinetics in transport and optics of semiconductors*. Springer, 2008.

[74] M. Paulsson. Non Equilibrium Green's Functions for Dummies: Introduction to the One Particle NEGF equations. *arXiv*, 2002.

[75] M. Brandbyge, J.-L. Mozos, P. Ordejón, J. Taylor, and K. Stokbro. Density-functional method for nonequilibrium electron transport. *Physical Review B*, 65(16):165401, March 2002.

[76] M. P. L. Sancho, J. M. L. Sancho, and J. Rubio. Quick iterative scheme for the calculation of transfer matrices: application to mo (100). *Journal of Physics F: Metal Physics*, 14(5):1205, 1984.

[77] C. H. Lewenkopf and E. Mucciolo. The recursive greens function method for graphene. *Journal of Computational Electronics*, 12(2):203–231, 2013.

[78] K. Kazymyrenko and X. Waintal. Knitting algorithm for calculating Green functions in quantum systems. *Physical Review B*, 77(11):115119, March 2008.

[79] M. Wimmer and K. Richter. Optimal block-tridiagonalization of matrices for coherent charge transport. *Journal of Computational Physics*, 228(23):8548–8565, December 2009.

[80] C. W. Groth, M. Wimmer, A. R. Akhmerov, and X. Waintal. Kwant: a software package for quantum transport. *New Journal of Physics*, 16(6):063065, 2014.

[81] A. Lherbier, S. M. M. Dubois, X. Declerck, Y.-M. Niquet, S. Roche, and J.-C. Charlier. Transport properties of graphene containing structural defects. *Physical Review B*, 86(7):075402, August 2012.

[82] M. O. Goerbig. Electronic properties of graphene in a strong magnetic field. *Rev. Mod. Phys.*, 83:1193–1243, Nov 2011.

[83] C. Bena. Greens functions and impurity scattering in graphene. *Physical Review B*, 79(12):125427, March 2009.

[84] S. R. Power and M. S. Ferreira. Electronic structure of graphene beyond the linear dispersion regime. *Physical Review B*, 83(15):155432, April 2011.

[85] J. A. Lawlor and M. S. Ferreira. Green functions of graphene: An analytic approach. *Physica B: Condensed Matter*, 463(0):48 – 53, 2015.

[86] S. R. Power, P. D. Gorman, J. M. Duffy, and M. S. Ferreira. Strain-induced modulation of magnetic interactions in graphene. *Phys. Rev. B*, 86:195423, Nov 2012.

[87] M. Settnes, S. R. Power, J. Lin, D. H. Petersen, and A.-P. Jauho. Patched Green's function techniques for two-dimensional systems: Electronic behavior of bubbles and perforations in graphene. *Physical Review B*, 91(12):125408, March 2015.

[88] D. A. Areshkin and B. K. Nikolić. Electron density and transport in top-gated graphene nanoribbon devices: First-principles Green function algorithms for systems containing a large number of atoms. *Physical Review B*, 81(15):155450, April 2010.

[89] M. Yang, X.-J. Ran, Y. Cui, and R.-Q. Wang. An easy and efficient way to treat Green's function for nano-devices with arbitrary shapes and multi-terminal configurations. *Chinese Physics B*, 20(9):097201, September 2011.

[90] G. Thorgilsson, G. Viktorsson, and S. Erlingsson. Recursive Greens function method for multi-terminal nanostructures. *Journal of Computational Physics*, 261:256–266, March 2014.

[91] G. Metalidis and P. Bruno. Greens function technique for studying electron flow in two-dimensional mesoscopic samples. *Physical Review B*, 72(23):235304, December 2005.

[92] A. Cresti, R. Farchioni, G. Grosso, and G. P. Parravicini. Keldysh-Green function formalism for current profiles in mesoscopic systems. *Physical Review B*, 68(7):075306, August 2003.

[93] R. N. Sajjad, C. A. Polanco, and A. W. Ghosh. Atomistic deconstruction of current flow in graphene based hetero-junctions. *Journal of Computational Electronics*, 12(2):232–247, May 2013.

[94] E. Costa Girão and V. Meunier. Patchwork algorithm for the parallel computation of the Greens function in open systems. *Journal of Computational Electronics*, 12(2):123–133, March 2013.

[95] F. Libisch, S. Rotter, and J. Burgdörfer. Coherent transport through graphene nanoribbons in the presence of edge disorder. *New Journal of Physics*, 14(12):123006, 2012.

[96] P. Drouvelis, P. Schmelcher, and P. Bastian. Parallel implementation of the recursive Greens function method. *Journal of Computational Physics*, 215(2):741–756, July 2006.

[97] E. N. Economou. *Green's functions in quantum physics*. Springer, 2005.

[98] J. Tersoff and D. R. Hamann. Theory and Application for the Scanning Tunneling Microscope. *Physical Review Letters*, 50(25):1998–2001, June 1983.

[99] V. Meunier and P. Lambin. Tight-Binding Computation of the STM Image of Carbon Nanotubes. *Physical Review Letters*, 81(25):5588–5591, December 1998.

[100] T. Fukuda, H. Oymak, and J. Hong. Electron transport from a one- to a two-dimensional system: Scanning tunneling microscopy of an adatom on a metal surface. *Physical Review B*, 75(19):195428, May 2007.

[101] T. Nakanishi and T. Ando. Conductance images between two STM probes in graphene. *Physica E: Low-dimensional Systems and Nanostructures*, 42(4):726–728, 2010.

[102] H. Amara, S. Latil, V. Meunier, P. Lambin, and J.-C. Charlier. Scanning tunneling microscopy fingerprints of point defects in graphene: A theoretical prediction. *Physical Review B*, 76(11):115423, September 2007.

[103] M. Settnes, S. R. Power, D. H. Petersen, and A.-P. Jauho. Theoretical analysis of a dual-probe scanning tunneling microscope setup on graphene. *Phys. Rev. Lett.*, 112:096801, Mar 2014.

[104] V. Barone, O. Hod, and G. E. Scuseria. Electronic structure and stability of semiconducting graphene nanoribbons. *Nano Letters*, 6(12):2748–54, December 2006.

[105] A. Deshpande, W. Bao, F. Miao, C. N. Lau, and B. J. LeRoy. Spatially resolved spectroscopy of monolayer graphene on SiO2. *Physical Review B*, 79(20):205411, May 2009.

[106] I. Brihuega, P. Mallet, C. Bena, S. Bose, C. Michaelis, L. Vitali, F. Varchon, L. Magaud, K. Kern, and J. Veuillen. Quasiparticle Chirality in Epitaxial Graphene Probed at the Nanometer Scale. *Physical Review Letters*, 101(20):206802, November 2008.

[107] T. O. Wehling, A. V. Balatsky, M. I. Katsnelson, A. I. Lichtenstein, K. Scharnberg, and R. Wiesendanger. Local electronic signatures of impurity states in graphene. *Phys. Rev. B*, 75:125425, Mar 2007.

[108] V. M. Pereira, F. Guinea, J. M. B. Lopes dos Santos, N. M. R. Peres, and A. H. Castro Neto. Disorder induced localized states in graphene. *Phys. Rev. Lett.*, 96:036801, Jan 2006.

[109] A. Bácsi and A. Virosztek. Local density of states and Friedel oscillations in graphene. *Physical Review B*, 82(19):193405, November 2010.

[110] K. Wakabayashi, Y. Takane, and M. Sigrist. Perfectly Conducting Channel and Universality Crossover in Disordered Graphene Nanoribbons. *Physical Review Letters*, 99(3):036601, July 2007.

[111] J. M. Duffy, P. D. Gorman, S. R. Power, and M. S. Ferreira. Variable range of the rkky interaction in edged graphene. *Journal of Physics: Condensed Matter*, 26(5):055007, 2014.

[112] C. Casiraghi, A. Hartschuh, H. Qian, S. Piscanec, C. Georgi, A. Fasoli, K. S. Novoselov, D. M. Basko, and A. C. Ferrari. Raman spectroscopy of graphene edges. *Nano Letters*, 9(4):1433–41, April 2009.

[113] Y. Kobayashi, K.-i. Fukui, T. Enoki, K. Kusakabe, and Y. Kaburagi. Observation of zigzag and armchair edges of graphite using scanning tunneling microscopy and spectroscopy. *Phys. Rev. B*, 71:193406, May 2005.

[114] M. Settnes, S. R. Power, D. H. Petersen, and A.-P. Jauho. Dual-probe spectroscopic fingerprints of defects in graphene. *Phys. Rev. B*, 90:035440, Jul 2014.

[115] J. P. Robinson, H. Schomerus, L. Oroszlány, and V. I. Fal'ko. Adsorbate-limited conductivity of graphene. *Phys. Rev. Lett.*, 101:196803, Nov 2008.

[116] T. O. Wehling, S. Yuan, A. I. Lichtenstein, A. K. Geim, and M. I. Katsnelson. Resonant scattering by realistic impurities in graphene. *Phys. Rev. Lett.*, 105:056802, Jul 2010.

[117] B. Uchoa, L. Yang, S. W. Tsai, N. M. R. Peres, and A. H. Castro Neto. Theory of Scanning Tunneling Spectroscopy of Magnetic Adatoms in Graphene. *Physical Review Letters*, 103(20):206804, November 2009.

[118] U. Fano. Effects of configuration interaction on intensities and phase shifts. *Phys. Rev.*, 124:1866–1878, Dec 1961.

[119] F. Schedin, A. K. Geim, S. V. Morozov, E. W. Hill, P. Blake, M. I. Katsnelson, and K. S. Novoselov. Detection of individual gas molecules adsorbed on graphene. *Nature Materials*, 6(9):652–5, September 2007.

[120] A. Cagliani, D. Mackenzie, L. Tschammer, F. Pizzocchero, K. Almdal, and P. Bøggild. Large-area nanopatterned graphene for ultrasensitive gas sensing. *Nano Research*, 7(5):743–754, 2014.

[121] N. M. R. Peres, F. Guinea, and A. H. Castro Neto. Electronic properties of disordered two-dimensional carbon. *Physical Review B*, 73(12):125411, March 2006.

[122] T. G. Pedersen, C. Flindt, J. G. Pedersen, N. A. Mortensen, A.-P. Jauho, and K. Pedersen. Graphene Antidot Lattices: Designed Defects and Spin Qubits. *Physical Review Letters*, 100(13):136804, April 2008.

[123] T. Gunst, T. Markussen, A.-P. Jauho, and M. Brandbyge. Thermoelectric properties of finite graphene antidot lattices. *Phys. Rev. B*, 84:155449, Oct 2011.

[124] S. S. Gregersen, J. G. Pedersen, S. R. Power, and A.-P. Jauho. Graphene on graphene antidot lattices: Electronic and transport properties. *Phys. Rev. B*, 91:115424, Mar 2015.

[125] S. R. Power and A.-P. Jauho. Electronic transport in disordered graphene antidot lattice devices. *Phys. Rev. B*, 90:115408, Sep 2014.

[126] J. Bai, X. Zhong, S. Jiang, Y. Huang, and X. Duan. Graphene nanomesh. *Nature nanotechnology*, 5(3):190–4, March 2010.

[127] M. Kim, N. S. Safron, E. Han, M. S. Arnold, and P. Gopalan. Electronic transport and raman scattering in size-controlled nanoperforated graphene. *ACS Nano*, 6(11):9846–9854, 2012.

[128] J. Eroms and D. Weiss. Weak localization and transport gap in graphene antidot lattices. *New Journal of Physics*, 11(9):095021, September 2009.

[129] Q. Xu, M.-Y. Wu, G. F. Schneider, L. Houben, S. K. Malladi, C. Dekker, E. Yucelen, R. E. Dunin-Borkowski, and H. W. Zandbergen. Controllable atomic scale patterning of freestanding monolayer graphene at elevated temperature. *ACS Nano*, 7(2):1566–1572, 2013.

[130] F. Oberhuber, S. Blien, S. Heydrich, F. Yaghobian, T. Korn, C. Schüller, C. Strunk, D. Weiss, and J. Eroms. Weak localization and Raman study of anisotropically etched graphene antidots. *Applied Physics Letters*, 103(14):143111, 2013.

[131] X. Jia, M. Hofmann, V. Meunier, B. G. Sumpter, J. Campos-Delgado, J. M. Romo-Herrera, H. Son, Y.-P. Hsieh, A. Reina, J. Kong, M. Terrones, and M. S. Dresselhaus. Controlled formation of sharp zigzag and armchair edges in graphitic nanoribbons. *Science*, 323(5922):1701–1705, 2009.

[132] F. Pizzocchero, M. Vanin, J. Kling, T. W. Hansen, K. W. Jacobsen, P. Bøggild, and T. J. Booth. Graphene Edges Dictate the Morphology of Nanoparticles during Catalytic Channeling. *The Journal of Physical Chemistry C*, 118(8):4296–4302, 2014.

[133] G. F. Schneider, S. W. Kowalczyk, V. E. Calado, G. Pandraud, H. W. Zandbergen, L. M. K. Vandersypen, and C. Dekker. DNA translocation through graphene nanopores. *Nano letters*, 10(8):3163–7, August 2010.

[134] C. A. Merchant, K. Healy, M. Wanunu, V. Ray, N. Peterman, J. Bartel, M. D. Fischbein, K. Venta, Z. Luo, A. T. C. Johnson, and M. Drndić. DNA translocation through graphene nanopores. *Nano letters*, 10(8):2915–21, August 2010.

[135] Y. I. Latyshev, a. P. Orlov, V. a. Volkov, V. V. Enaldiev, I. V. Zagorodnev, O. F. Vyvenko, Y. V. Petrov, and P. Monceau. Transport of Massless Dirac Fermions in Non-topological Type Edge States. *Scientific reports*, 4:7578, January 2014.

[136] J. Kling, J. S. Vestergaard, A. B. Dahl, N. Stenger, T. J. Booth, P. Bøoggild, R. Larsen, J. B. Wagner, and T. W. Hansen. Pattern recognition approach to quantify the atomic structure of graphene. *Carbon*, 74(0):363 – 366, 2014.

[137] J. S. Vestergaard, J. Kling, A. B. Dahl, T. W. Hansen, J. B. Wagner, and R. Larsen. Structure identification in high-resolution transmission electron microscopic images: An example on graphene. *Microscopy and Microanalysis*, 20:1772–1781, 12 2014.

[138] T. Low and J. Appenzeller. Electronic transport properties of a tilted graphene *p-n* junction. *Phys. Rev. B*, 80:155406, Oct 2009.

[139] R. R. Hartmann, N. J. Robinson, and M. E. Portnoi. Smooth electron waveguides in graphene. *Phys. Rev. B*, 81:245431, Jun 2010.

[140] C. E. P. Villegas and M. R. S. Tavares. Comment on "guided modes in graphene waveguides" [Appl. Phys. Lett. 94, 212105 (2009)]. *Applied Physics Letters*, 96(18):2009–2011, 2010.

[141] P. Rickhaus, P. Makk, M.-H. Liu, E. Tóvári, M. Weiss, R. Maurand, K. Richter, and C. Schönenberger. Snake trajectories in ultraclean graphene pn junctions. *Nature Communications*, 6:6470, 2015.

[142] J. Cserti, A. Pályi, and C. Péterfalvi. Caustics due to a negative refractive index in circular graphene *p-n* junctions. *Phys. Rev. Lett.*, 99:246801, Dec 2007.

[143] A. Matulis and F. M. Peeters. Quasibound states of quantum dots in single and bilayer graphene. *Phys. Rev. B*, 77:115423, Mar 2008.

[144] R. L. Heinisch, F. X. Bronold, and H. Fehske. Mie scattering analog in graphene: Lensing, particle confinement, and depletion of klein tunneling. *Phys. Rev. B*, 87:155409, Apr 2013.

[145] A. Pieper, R. L. Heinisch, G. Wellein, and H. Fehske. Dot-bound and dispersive states in graphene quantum dot superlattices. *Phys. Rev. B*, 89:165121, Apr 2014.

[146] A. Pieper, R. L. Heinisch, and H. Fehske. Electron dynamics in graphene with gate-defined quantum dots. *EPL (Europhysics Letters)*, 104(4):47010, 2013.

[147] T. Low, F. Guinea, and M. I. Katsnelson. Gaps tunable by electrostatic gates in strained graphene. *Physical Review B*, 83(19):195436, May 2011.

[148] G. W. Jones and V. M. Pereira. Designing electronic properties of two-dimensional crystals through optimization of deformations. *New Journal of Physics*, 16(9):093044, September 2014.

[149] Z. Qi, A. L. Kitt, H. S. Park, V. M. Pereira, D. K. Campbell, and A. H. Castro Neto. Pseudomagnetic fields in graphene nanobubbles of constrained geometry: A molecular dynamics study. *Phys. Rev. B*, 90:125419, Sep 2014.

[150] M. Neek-Amal and F. M. Peeters. Strain-engineered graphene through a nanostructured substrate. i. deformations. *Phys. Rev. B*, 85:195445, May 2012.

[151] J. Lu, A. H. Castro Neto, and K. P. Loh. Transforming Moiré blisters into geometric graphene nano-bubbles. *Nature communications*, 3(may):823, January 2012.

[152] R. Carrillo-Bastos, D. Faria, A. Latgé, F. Mireles, and N. Sandler. Gaussian deformations in graphene ribbons: Flowers and confinement. *Physical Review B*, 90(4):041411, July 2014.

[153] F. D. Juan, A. Cortijo, M. A. H. Vozmediano, and A. Cano. deformations in graphene. *Nature Physics*, 7(10):810–815, 2011.

[154] M. Neek-Amal, L. Covaci, K. Shakouri, and F. M. Peeters. Electronic structure of a hexagonal graphene flake subjected to triaxial stress. *Physical Review B*, 88(11):115428, September 2013.

[155] M. Neek-Amal and F. M. Peeters. Strain-engineered graphene through a nanostructured substrate. II. Pseudomagnetic fields. *Physical Review B*, 85(19):195446, May 2012.

[156] V. M. Pereira and A. H. Castro Neto. Strain engineering of graphene's electronic structure. *Phys. Rev. Lett.*, 103:046801, Jul 2009.

[157] V. M. Pereira, R. M. Ribeiro, N. M. R. Peres, and A. H. Castro Neto. Optical properties of strained graphene. *EPL (Europhysics Letters)*, 92(6):67001, 2010.

[158] D. Moldovan, M. Ramezani Masir, and F. M. Peeters. Electronic states in a graphene flake strained by a Gaussian bump. *Physical Review B*, 88(3):035446, July 2013.

[159] F. M. D. Pellegrino, G. G. N. Angilella, and R. Pucci. Strain effect on the optical conductivity of graphene. *Physical Review B*, 81(3):035411, January 2010.

[160] H. Suzuura and T. Ando. Phonons and electron-phonon scattering in carbon nanotubes. *Phys. Rev. B*, 65:235412, May 2002.

[161] N. Levy, S. A. Burke, K. L. Meaker, M. Panlasigui, A. Zettl, F. Guinea, A. H. Castro Neto, and M. F. Crommie. Strain-induced pseudo-magnetic fields greater than 300 tesla in graphene nanobubbles. *Science*, 329(5991):544–7, July 2010.

[162] J. S. Bunch, S. S. Verbridge, J. S. Alden, A. M. van der Zande, J. M. Parpia, H. G. Craighead, and P. L. McEuen. Impermeable atomic membranes from graphene sheets. *Nano Letters*, 8(8):2458–2462, 2008.

[163] A. Reserbat-Plantey, D. Kalita, Z. Han, L. Ferlazzo, S. Autier-Laurent, K. Komatsu, C. Li, R. Weil, A. Ralko, L. Marty, S. Guron, N. Bendiab, H. Bouchiat, and V. Bouchiat. Strain superlattices and macroscale suspension of graphene induced by corrugated substrates. *Nano Letters*, 14(9):5044–5051, 2014. PMID: 25119792.

[164] L. D. Landau and E. M. Lifshitz. *Theory of elasticity, third edition: volune 7 (course of theoretical physics)*. Springer, 1986.

[165] A. L. Kitt, V. M. Pereira, A. K. Swan, and B. B. Goldberg. Lattice-corrected strain-induced vector potentials in graphene. *Phys. Rev. B*, 85:115432, Mar 2012.

[166] J. L. Mañes, F. de Juan, M. Sturla, and M. A. H. Vozmediano. Generalized effective hamiltonian for graphene under nonuniform strain. *Phys. Rev. B*, 88:155405, Oct 2013.

[167] M. R. Masir, D. Moldovan, and F. Peeters. Pseudo magnetic field in strained graphene: Revisited. *Solid State Communications*, 175176(0):76 – 82, 2013. Special Issue: Graphene V: Recent Advances in Studies of Graphene and Graphene analogues.

[168] F. de Juan, J. L. Mañes, and M. A. H. Vozmediano. Gauge fields from strain in graphene. *Phys. Rev. B*, 87:165131, Apr 2013.

[169] D. Faria, A. Latgé, S. E. Ulloa, and N. Sandler. Currents and pseudomagnetic fields in strained graphene rings. *Physical Review B*, 87(24):241403, June 2013.

[170] C. Poli, J. Arkinstall, and H. Schomerus. Degeneracy doubling and sublattice polarization in strain-induced pseudo-landau levels. *Phys. Rev. B*, 90:155418, Oct 2014.

[171] C. W. J. Beenakker. *Colloquium* : Andreev reflection and klein tunneling in graphene. *Rev. Mod. Phys.*, 80:1337–1354, Oct 2008.

[172] M. Ramezani Masir, P. Vasilopoulos, and F. M. Peeters. Graphene in inhomogeneous magnetic fields: bound, quasi-bound and scattering states. *Journal of physics. Condensed matter : an Institute of Physics journal*, 23(31):315301, August 2011.

[173] S. T. Gill, J. H. Hinnefeld, S. Zhu, W. T. Swanson, T. Li, and N. Mason. Mechanical control of graphene on engineered pyramidal strain arrays. *ACS Nano*, 0(ja):null, 0.

[174] K. Yue, W. Gao, R. Huang, and K. M. Liechti. Analytical methods for the mechanics of graphene bubbles. *Journal of Applied Physics*, 112(8):083512, 2012.

[175] S. Timoshenko and S. Woinowsky-Krieger. *Theory of plates and shells*. Mcgraw-Hill, 1989.

[176] M. Schneider, D. Faria, S. Viola Kusminskiy, and N. Sandler. Local sublattice symmetry breaking for graphene with a centrosymmetric deformation. *Phys. Rev. B*, 91:161407, Apr 2015.

[177] F. M. D. Pellegrino, G. G. N. Angilella, and R. Pucci. Transport properties of graphene across strain-induced nonuniform velocity profiles. *Phys. Rev. B*, 84:195404, Nov 2011.

[178] D. A. Bahamon, Z. Qi, H. S. Park, V. M. Pereira, and D. K. Campbell. Conductance signatures of electron confinement induced by strained nanobubbles in graphene. *arXiv:1503.08488v1*, (i):1–13, 2015.

[179] T. Low and F. Guinea. Strain-induced pseudomagnetic field for novel graphene electronics. *Nano letters*, 10(9):3551–4, September 2010.

[180] Z. Qi, D. A. Bahamon, V. M. Pereira, H. S. Park, D. K. Campbell, and A. H. Castro Neto. Resonant tunneling in graphene pseudomagnetic quantum dots. *Nano letters*, 13(6):2692–7, June 2013.

[181] A. Rycerz, J. Tworzydo, and C. W. J. Beenakker. Valley filter and valley valve in graphene. *Nature Physics*, 3(3):172–175, February 2007.

[182] Z. Wu, F. Zhai, F. M. Peeters, H. Q. Xu, and K. Chang. Valley-dependent brewster angles and goos-hänchen effect in strained graphene. *Phys. Rev. Lett.*, 106:176802, Apr 2011.

[183] L. Jiang, X. Lv, and Y. Zheng. Valley polarized electronic transport through a line defect in graphene: An analytical approach based on tight-binding model. *Physics Letters A*, 376(2):136 – 141, 2011.

[184] D. Gunlycke and C. T. White. Graphene valley filter using a line defect. *Phys. Rev. Lett.*, 106:136806, Mar 2011.

[185] M. Ramezani Masir, a. Matulis, and F. Peeters. Quasibound states of Schrödinger and Dirac electrons in a magnetic quantum dot. *Physical Review B*, 79(15):155451, April 2009.

[186] S. Roche and D. Mayou. Conductivity of quasiperiodic systems: A numerical study. *Phys. Rev. Lett.*, 79:2518–2521, Sep 1997.

[187] T. Markussen, R. Rurali, M. Brandbyge, and A. P. Jauho. Electronic transport through Si nanowires: Role of bulk and surface disorder. *Physical Review B - Condensed Matter and Materials Physics*, 74(24):1–11, 2006.

[188] Z. Fan, A. Uppstu, T. Siro, and A. Harju. Efficient linear-scaling quantum transport calculations on graphics processing units and applications on electron transport in graphene. *Computer Physics Communications*, 185(1):28 – 39, 2014.

[189] D. Van Tuan, J. Kotakoski, T. Louvet, F. Ortmann, J. C. Meyer, and S. Roche. Scaling properties of charge transport in polycrystalline graphene. *Nano Letters*, 13(4):1730–1735, April 2013.

[190] A. W. Cummings, A. Cresti, and S. Roche. Quantum hall effect in polycrystalline graphene: The role of grain boundaries. *Phys. Rev. B*, 90:161401, Oct 2014.

[191] N. Leconte, A. Lherbier, F. Varchon, P. Ordejon, S. Roche, and J.-C. Charlier. Quantum transport in chemically modified two-dimensional graphene: From minimal conductivity to anderson localization. *Phys. Rev. B*, 84:235420, Dec 2011.

[192] T. M. Radchenko, A. A. Shylau, and I. V. Zozoulenko. Influence of correlated impurities on conductivity of graphene sheets: Time-dependent real-space Kubo approach. *Physical Review B - Condensed Matter and Materials Physics*, 86(3):1–13, 2012.

[193] S. Yuan, H. De Raedt, and M. I. Katsnelson. Modeling electronic structure and transport properties of graphene with resonant scattering centers. *Physical Review B*, 82(11):115448, September 2010.

[194] F. Ortmann, A. Cresti, G. Montambaux, and S. Roche. Magnetoresistance in disordered graphene: The role of pseudospin and dimensionality effects unraveled. *EPL (Europhysics Letters)*, 94(4):47006, 2011.

[195] A. Lherbier, B. Biel, Y.-M. Niquet, and S. Roche. Transport length scales in disordered graphene-based materials: Strong localization regimes and dimensionality effects. *Phys. Rev. Lett.*, 100:036803, Jan 2008.

[196] A. Lherbier, S. M.-M. Dubois, X. Declerck, S. Roche, Y.-M. Niquet, and J.-C. Charlier. Two-dimensional graphene with structural defects: Elastic mean free path, minimum conductivity, and anderson transition. *Phys. Rev. Lett.*, 106:046803, Jan 2011.

[197] J. G. Pedersen, A. W. Cummings, and S. Roche. Anisotropic behavior of quantum transport in graphene superlattices: Coexistence of ballistic conduction with anderson insulating regime. *Phys. Rev. B*, 89:165401, Apr 2014.

[198] D. van Tuan. *Charge and spin transport in disordered graphene-based materials*. PhD thesis, Catalan institute of nanoscience of nanotechnology, 2014.

[199] R. Haydock. The recursive solution of the schrdinger equation. *Computer Physics Communications*, 20(1):11 – 16, 1980.

[200] A. Weiße, G. Wellein, A. Alvermann, and H. Fehske. The kernel polynomial method. *Reviews of Modern Physics*, 78(1):275–306, March 2006.

[201] J. G. Pedersen, A. W. Cummings, and S. Roche. Anisotropic behavior of quantum transport in graphene superlattices: Coexistence of ballistic conduction with anderson insulating regime. *Phys. Rev. B*, 89:165401, Apr 2014.

[202] S. Roche, N. Leconte, F. Ortmann, A. Lherbier, D. Soriano, and J.-C. Charlier. Quantum transport in disordered graphene: A theoretical perspective. *Solid State Communications*, 152(15):1404 – 1410, 2012. Exploring Graphene, Recent Research Advances.

[203] N. Leconte, F. Ortmann, A. Cresti, J.-C. Charlier, and S. Roche. Quantum transport in chemically functionalized graphene at high magnetic field: defect-induced critical states and breakdown of electron-hole symmetry. *2D Materials*, 1(2):021001, 2014.

[204] F. Ortmann, N. Leconte, and S. Roche. Efficient linear scaling approach for computing the kubo hall conductivity. *Phys. Rev. B*, 91:165117, Apr 2015.

[205] P. Soven. Coherent-potential model of substitutional disordered alloys. *Physical Review*, 1017, 1967.

[206] T. Aktor, A.-P. Jauho, and S. R. Power. Electronic transport in graphene nanoribbons with sublattice-asymmetric doping. page 5, April 2015.

[207] B. Velicky. Theory of Electronic Transport in Disordered Binary Alloys: Coherent-Potential. *Physical Review*, 321(3), 1969.

[208] B. Velicky. Single-Site Approximations in the Electronic Theory of Simple Binary Alloys. *Physical Review*, 1(3), 1968.

[209] Y. Zhu, L. Liu, and H. Guo. Quantum transport theory with nonequilibrium coherent potentials. *Physical Review B*, 88(20):205415, November 2013.

[210] Y. Ke, K. Xia, and H. Guo. Disorder scattering in magnetic tunnel junctions: Theory of nonequilibrium vertex correction. *Phys. Rev. Lett.*, 100:166805, Apr 2008.

[211] Z. Wang, Y. Ke, D. Liu, H. Guo, and K. H. Bevan. Low bias short channel impurity mobility in graphene from first principles. *Applied Physics Letters*, 101(9):093102, 2012.

[212] Z. Wang, H. Guo, and K. H. Bevan. First principles modeling of disorder scattering in graphene. *Journal of Computational Electronics*, 12(2):104–114, February 2013.

[213] A. Lherbier, X. Blase, Y.-M. Niquet, F. M. C. Triozon, and S. Roche. Charge transport in chemically doped 2d graphene. *Phys. Rev. Lett.*, 101:036808, Jul 2008.

[214] E. R. Mucciolo, A. H. Castro Neto, and C. H. Lewenkopf. Conductance quantization and transport gaps in disordered graphene nanoribbons. *Phys. Rev. B*, 79:075407, Feb 2009.

[215] L. Zhao, R. He, K. T. Rim, T. Schiros, K. S. Kim, H. Zhou, C. Gutirrez, S. P. Chockalingam, C. J. Arguello, L. Plov, D. Nordlund, M. S. Hybertsen, D. R. Reichman, T. F. Heinz, P. Kim, A. Pinczuk, G. W. Flynn, and A. N. Pasupathy. Visualizing individual nitrogen dopants in monolayer graphene. *Science*, 333(6045):999–1003, 2011.

[216] R. Lv, Q. Li, A. R. Botello-Méndez, T. Hayashi, B. Wang, A. Berkdemir, Q. Hao, A. L. Elías, R. Cruz-Silva, H. R. Gutiérrez, Y. A. Kim, H. Muramatsu, J. Zhu, M. Endo, H. Terrones, J.-C. Charlier, M. Pan, and M. Terrones. Nitrogen-doped graphene: beyond single substitution and enhanced molecular sensing. *Scientific reports*, 2:586, January 2012.

[217] L. Zhao, M. Levendorf, S. Goncher, T. Schiros, L. Plov, A. Zabet-Khosousi, K. T. Rim, C. Gutirrez, D. Nordlund, C. Jaye, M. Hybertsen, D. Reichman, G. W. Flynn, J. Park, and A. N. Pasupathy. Local atomic and electronic structure of boron chemical doping in monolayer graphene. *Nano Letters*, 13(10):4659–4665, 2013. PMID: 24032458.

[218] A. Zabet-Khosousi, L. Zhao, L. Plov, M. S. Hybertsen, D. R. Reichman, A. N. Pasupathy, and G. W. Flynn. Segregation of sublattice domains in nitrogen-doped graphene. *Journal of the American Chemical Society*, 136(4):1391–1397, 2014.

[219] J. A. Lawlor, P. D. Gorman, S. R. Power, C. G. Bezerra, and M. S. Ferreira. Sublattice imbalance of substitutionally doped nitrogen in graphene. *Carbon*, 77(0):645 – 650, 2014.

[220] A. Lherbier, A. R. Botello-Mndez, and J.-C. Charlier. Electronic and transport properties of unbalanced sublattice n-doping in graphene. *Nano Letters*, 13(4):1446–1450, 2013.

[221] I. Deretzis and A. La Magna. Origin and impact of sublattice symmetry breaking in nitrogen-doped graphene. *Phys. Rev. B*, 89:115408, Mar 2014.

[222] J. A. Lawlor and M. S. Ferreira. Sublattice asymmetry of impurity doping in graphene: A review. *Beilstein journal of nanotechnology*, 5:1210–7, January 2014.

[223] S. Timoshenko. *Theory of elasticity*. Mcgraw-Hill, 1970.

[224] E. Ventsel and T. Krauthammer. *Thin plates and shells*. Marcel Dekker, 2001.

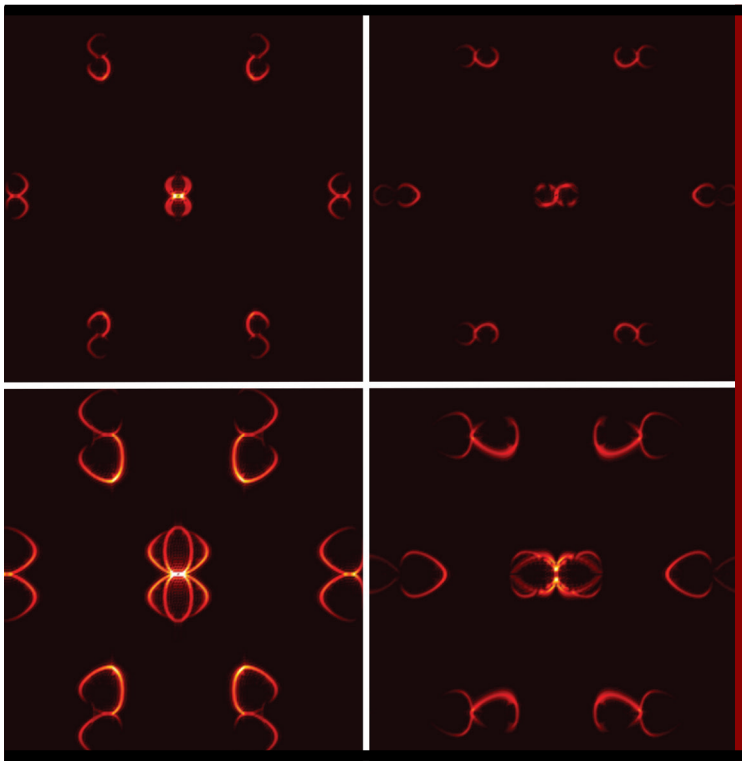

Copyright: Mikkel Settnes
All rights reserved

Published by:
DTU Nanotech
Department of Micro- and Nanotechnology
Technical University of Denmark
Ørsteds Plads, building 345B
DK-2800 Kgs. Lyngby